

Department of Electrical and Computer Engineering

Smoothing of Photovoltaic Generation

Mojtaba Saleh

This thesis is presented for the Degree of
Doctor of Philosophy
of
Curtin University

September 2017

Declaration

To the best of my knowledge and belief this thesis contains no material previously published by any other person except where due acknowledgment has been made. This thesis contains no material which has been accepted for the award of any other degree or diploma in any university.

Mojtaba Saleh
27/09/2017

A handwritten signature in blue ink, appearing to read 'Saleh', with a horizontal line underneath.

“To those who have taught us in one way or another”

Acknowledgments

I would like to express my gratitude to my supervisor, Prof Mohammad A.S. Masoum, whose valuable insights and recommendations added considerably to my postgraduate experience. Without his guidance and persistent help this dissertation would not have been possible.

I gratefully acknowledge the generous financial support toward my PhD study from Curtin International Postgraduate Scholarship (CIPRS)/Magellan Power Conversion Scholarship.

I would like to extend my thanks to the staff of Magellan Powertronics Pty Ltd, Perth, Australia, especially Mr Masoud Abshar, M.D., and Mr Lindsay Meek, CTO, for their technical assistance and contribution in conducting the experiments for the research.

Abstract

Distributed photovoltaic generation (PVG) and associated interconnection requirements are fast becoming a disruptive technological challenge to the existing regulated electric industry. The inherent intermittency of the solar photovoltaic (PV) resources, caused by cloud passing, tends to exceed the response time of the operational reserve of the power system or place an excessive burden on that. To pave the way for hosting a larger amount of the grid-tied solar PVG resources, in the areas with high penetration level utilities have introduced a restriction on the ramp rate (RR) of the PVG output power, referred to as smoothing. Battery storage (BS) devices can reliably absorb the sudden PVG dips and rises as the passing clouds cast a shadow over the solar plant while the RR requirements are maintained. On the other hand, the BS significantly increases the price of solar PVG and challenges its commercial viability.

This study aims to contribute to this growing field of research by investigating two key elements which virtually justify the BS solution: extending its life cycle and reducing the required capacity. Generally, the BS technologies are designed to undertake relatively long and stable charge and discharge cycles rather than supplying short-term and momentary energy demands. This creates a motivation for using BS chemistries of higher energy density, e.g. Li-FePO₄, as well as incorporating ultra-capacitor (UC) technology to construct a hybrid storage system (HSS). Hence, the structure of the power electronic converters and required control system for the HSS-based PVG smoothing is addressed in this dissertation. Another matter of concern is that the Li-FePO₄ cells suffer the issue of the state of charge (SOC) imbalance particularly in series connected strings for relatively high voltage applications. An active cell balancing algorithm is proposed to mitigate the growing SOC gap between the cells during the charge and discharge cycles using bidirectional flyback converters.

Seen from a wider perspective, the required BS capacity could be remarkably reduced, if the ramp down process is initiated prior to occurrence of the sudden

dip in PVG output. This raises a key question that whether a battery-optimised PVG smoothing is accomplished by means of the prior knowledge about timing and characteristics of the clouds projected to obscure the sun. To this end, a real-time imagery based short-term cloud prediction approach is proposed to serve as a conservative early warning of the passing clouds. Afterwards, the cloud prediction information is incorporated into a conventional storage based PVG smoothing system to examine the amount of reduced storage capacity. The results obtained through an experimental test confirms the hypothesis of the battery-optimised smoothing approach using the prediction information produced from the live images taken from a sky-facing roof-top camera.

The present study makes several contributions to the field of the generation smoothing of the solar PV:

- It looks into an HSS-based smoothing approach accounting for the structure of the power electronic converters as well as the control strategy.
- A control algorithm is proposed for a flyback active battery cell balancer with an interleaved connection of the transformers. This provides a safe and efficient utilisation of the entire capacity of a large battery stack while eliminates any premature termination of the charge/discharge cycles attributed to SOC imbalance of the series-connected battery cells.
- An improved PVG smoothing approach based on real-time cloud prediction information is proposed and examined for the amount of required BS backup. It is eventually indicated that the storage-optimised PVG smoothing process is technically viable by the means of an imagery-based cloud forecasting method.

Statement of Originality

This thesis includes two original studies published as one conference paper and one peer reviewed journal article which are incorporated in chapter 3 and chapter 4, respectively.

- "Control Algorithm for Bidirectional Fly-Back Active Cell Balancer with Interleaved Transformer Connections," in *2016 IEEE Power and Energy Society General Meeting (PESGM)*, July 2016, pp. 1-5.
- "Battery-Less ShortTerm Smoothing of Photovoltaic Generation Using Sky Camera," *Industrial Informatics, IEEE Transactions on*, vol. 14, no. 2, pp. 403-414, Feb. 2018. (doi: 10.1109/TII.2017.2767038)

The full-text version of the papers is available in Appendix-D. Moreover, in a formal statement presented in Appendix-E, the co-authors of published papers have endorsed my contribution.

This research work was supported by a joint scholarship awarded by Curtin International Postgraduate Research Scholarship (CIPRS) and Magellan Powertronics, Ltd, Pty. Hence, this work was conducted in collaboration with the research and development (R&D) team in Magellan Powertronics, Mr Lindsay Meek (CTO) and Mr Masoud Abshar (MD). This study was essentially conceptualised in Magellan Powertronics to address the technical challenges involved in the rapidly increasing integration of the solar energy in the Western Australian regional electricity grid.

I made a substantial contribution in the design and coordination of the project and carried out data collection and analysis as well as the drafting of the publications and thesis manuscript. I conducted this PhD research project under the consistent guidance from my academic Curtin supervisor Prof Mohammad A.S. Masoum who provided invaluable inputs to this work and actively assisted with revising the manuscript of my publications and this thesis. Moreover, in the course of my research, Magellan Powertronics shared their advanced industrial

facilities and engineering capabilities which significantly helped me to develop an industrial prototype of the *Cloud Camera* system and practically verify its functionality within the stipulated time frame of my PhD project.

Contents

Declaration	ii
Acknowledgments	iv
Abstract	v
Statement of Originality	vii
List of Figures	x
List of Tables	xi
List of Acronyms	xii
List of Roman Symbols	xiv
1 Introduction	1
1.1 Background	1
1.1.1 Static Effects	2
1.1.2 Dynamic Effects	6
1.1.3 Storage System	9
1.1.4 Cell Equalisation of Battery Storage	10
1.1.5 Short-Term Cloud Prediction	11
1.2 Main Objectives	12
1.3 Structure of Thesis	13
1.4 Publications Incorporated in Thesis	14

2	Storage-Based Smoothing of PV Generation	15
2.1	Introduction	15
2.2	Structure of Power Electronic Converter	17
2.3	Smoothing Controller	20
2.4	Controller of Power Electronic Converters	24
	2.4.1 AC Coupled Smoother	24
	2.4.2 DC-Coupled Smoother	30
2.5	Simulation Results	31
2.6	Summary	36
3	Cell Balancing Control in Battery Storage Systems	38
3.1	Introduction	38
3.2	Active Cell Balancer	42
	3.2.1 Active Cell Balancing Algorithm	45
	3.2.2 Active Cell Balancing Simulation and Analysis	53
3.3	Passive Cell Balancer	64
	3.3.1 Passive Cell Balancing Algorithm	65
	3.3.2 Passive Cell Balancing Simulation	66
3.4	Summary	68
4	Storage-Optimised Smoothing of PV Generation	
	Using Short-Term Imagery-Based Cloud Prediction	69
4.1	Introduction	69
4.2	Solar Prediction Methods	70
	4.2.1 Statistical Models	70
	4.2.2 Numerical Weather Prediction	71
	4.2.3 Ground-Based Camera and Satellite Cloud Imagery	71
4.3	Proposed Averaged Cloud Prediction Algorithm	73
	4.3.1 Correcting Lens Distortion	73
	4.3.2 Sun Positioning	73
	4.3.3 Cloud Segmentation	74
	4.3.4 Cloud Motion	74

4.3.5	Cloud Forecasting	75
4.4	Proposed PVG Smoothing Approach	78
4.4.1	Conventional Storage Backup Smoothing Strategy	78
4.4.2	Ideal Export Prediction Smoothing Strategy	79
4.4.3	Proposed Smoothing Method-I: Using Output Estimation .	80
4.4.4	Proposed Method-II: Smoothing Using Binary Cloud Pre- diction	81
4.5	Developed Testbed and Experimental Setup	82
4.6	Evaluation and Analysis	83
4.7	Summary	99
5	Conclusion	100
5.1	Summary and Findings	100
5.2	Limitations	103
5.3	Challenges	103
5.4	Recommendations	104
	Appendix A Linkage Matrices of Active Cell Balancer	106
	Appendix B Calibration of the Fisheye Lens	108
	Appendix C Refraction Parameter of the Fish-Eye Lens	110
	Appendix D Full-Text of the Publications	113
	Appendix E Statements of the Co-Authors	130
	Bibliography	133

List of Figures

1.1	Variations of PVG output power in different time scales.	3
1.2	The CAISO duck chart.	3
1.3	Totalised areal equalising effect in a 25 MW PVG plant. (a) The output power of one PV panel. (b) The observed variations for different combinations of PV arrays.	7
1.4	The diagram of a PVG output smoothing controller.	8
2.1	Ragone plot of energy and power characteristics for storage technologies.	16
2.2	Various composition of power electronic interface for PVG plants.	17
2.3	Different variants of incorporating the BS into a grid-tied PVG system. (a) Direct connection to the DC link. (b) Connection to the DC link through DC-DC converter. (c) Connection at the AC side.	17
2.4	Different variants of integrating BS and UC for PVG output smoothing application. (a) UC directly coupled to DC link and BS via DC-DC converter. (b) BS directly coupled to DC link and UC via DC-DC converter. (c) UC and BS coupled through DC-DC converter.	18
2.5	Different structures of the PVG plant accompanied with an HSS for output smoothing, (a) coupling at DC side, (b) coupling at AC side.	19
2.6	Response to step change for (a) RR limiter filter, and (b) first-order low-pass filter.	20
2.7	The diagram of the PVG output smoothing controller. (a) Without UC voltage regulator. (b) With UC voltage regulator.	21

2.8	Reference power generation for PVG output smoothing using HSS: (a) PV produced power and reference output power, (b) HSS reference power decomposed into the reference power for the BS and UC, and (c) the smoothing energy delivered by the BS and the UC.	22
2.9	Simulation results of the PVG output smoothing using HSS: (a) PV produced power and reference output power, (b) allocated smoothing power to the BS and the UC, and (c) the smoothing energy delivered by the BS and the UC.	23
2.10	The diagram of the AC-coupled HSS-based PVG output smoothing.	25
2.11	The diagram of the MPPT controller and the boost converter's control loop.	26
2.12	The single-phase equivalent circuit diagram of the grid-connected VSI.	26
2.13	The control diagram of the grid-connected PVG inverter.	27
2.14	The control diagram of the grid-connected HSS VSI.	28
2.15	The control diagram of the bidirectional parallel DC-DC converters.	29
2.16	The diagram of the DC-coupled HSS-based PVG output smoothing.	30
2.17	The output current of the PVG inverter; (a) three-phase values, and (b) in synchronous dq reference frame.	32
2.18	The smoothing current injected by the AC-coupled HSS inverter; (a) three-phase values, and (b) in synchronous dq reference frame.	32
2.19	The regulated current delivered to the utility grid by AC-coupled smoother; (a) three-phase values, and (b) in synchronous dq reference frame.	33
2.20	DC link voltage stabilisation in AC-coupled smoother, (a) the current injected by BS and UC in DC link of HSS, (b) DC link voltages for PVG and HSS VSIs.	33
2.21	PVG smoothing process at DC side; (a) DC link currents, and (b) decomposed components of HSS current.	34
2.22	DC link voltage of the PVG-VSI with DC-coupled HSS during the smoothing process.	34
2.23	PVG output current for smoothing at DC side; (a) three-phase values, and (b) in synchronous dq reference frame.	35

3.1	Effective utilisation of battery bank capacity by SOC equalisation.	39
3.2	Comparison on energy efficiency of the two categories of balancing approaches; passive and active.	40
3.3	The interleaved structure of flyback active cell balancer.	43
3.4	(a) flyback converter topology, and (b) waveforms of transformer currents during charge and discharge operation.	44
3.5	The discharge curve of a 100 [Ah] Li-FePO ₄ cell under various discharge currents.	45
3.6	Three-level hysteresis cell voltage interpreter.	46
3.7	The diagram of energy transfer between adjacent subsets, (a) when over-charged cells are being discharged, and (b) non-overcharged cells are being charged.	48
3.8	Flowchart of the proposed balancing algorithm for n^{th} subset.	52
3.9	Diagram of the proposed simulation model for active cell balancer.	55
3.10	The simulation results of Case-I in charge cycle, (a) cell voltages, (b) subset mean voltages, (c) cell SOC's, and (d) charger current I_{charge} .	57
3.11	The simulation results of Case-I in discharge cycle, (a) cell voltages, (b) subset mean voltages, (c) cell SOC's, and (d) discharge current $I_{discharge}$.	58
3.12	The simulation results of Case-II in charge cycle, (a) cell voltages, (b) subset mean voltages, (c) cell SOC's, and (d) charger current I_{charge} .	59
3.13	The simulation results of Case-II in discharge cycle, (a) cell voltages, (b) subset mean voltages, (c) cell SOC's, and (d) discharge current $I_{discharge}$.	60
3.14	The simulation results of Case-III in charge cycle, (a) cell voltages, (b) subset mean voltages, (c) cell SOC's, and (d) charger current I_{charge} .	61
3.15	The simulation results of Case-III in discharge cycle, (a) cell voltages, (b) subset mean voltages, (c) cell SOC's, and (d) discharge current $I_{discharge}$.	62
3.16	The structure of the passive cell balancer.	64
3.17	Two-level hysteresis cell voltage interpreter.	65
3.18	Flowchart of the passive cell balancing controller.	66

3.19	The simulation results of passive balancer in charge cycle, (a) cell voltages, (b) cell SOCs, and (c) charge current I_{charge}	67
4.1	Classification of solar radiation prediction models according to temporal and spatial resolution.	71
4.2	(a) fisheye image captured by the sky camera. (b) Undistorted image in flat coordination. (c) False colour representation of RBR image. (d) Binary segmented image. (e) Outlines of cloud regions and solar area. (f) Scattered outline overlayed on the sky image. (g) Displacement of the most suitable features in the sky image. (h) The effective range of displacement prediction.	77
4.3	Energy balance in PVG smoothing. (a) Conventional smoothing. (b) Based on Cloud Prediction.	79
4.4	Photo of the testbed for PVG smoothing based on the proposed cloud prediction techniques.	82
4.5	Smoothing results for 4 December 2015. (a) Storage-based. (b) Ideal Prediction. (c) Estimation-based. (d) Binary Prediction. . .	88
4.6	Smoothing signals for 4 December 2015. (a) Total SO_i . (b) Total CO_i . (c) Export toggle command to solar inverter.	89
4.7	Smoothing results for 6 December 2015. (a) Storage-based. (b) Ideal Prediction. (c) Estimation-based. (d) Binary Prediction. . .	90
4.8	Smoothing signals for 6 December 2015. (a) Total SO_i . (b) Total CO_i . (c) Export toggle command to solar inverter.	91
4.9	Smoothing results for 7 December 2015. (a) Storage-based. (b) Ideal Prediction. (c) Estimation-based. (d) Binary Prediction. . .	92
4.10	Smoothing signals for 7 December 2015. (a) Total SO_i . (b) Total CO_i . (c) Export toggle command to solar inverter.	93
4.11	Smoothing results for 8 December 2015. (a) Storage-based. (b) Ideal Prediction. (c) Estimation-based. (d) Binary Prediction. . .	94
4.12	Smoothing signals for 8 December 2015. (a) Total SO_i . (b) Total CO_i . (c) Export toggle command to solar inverter.	95
4.13	Smoothing results for 9 December 2015. (a) Storage-based. (b) Ideal Prediction. (c) Estimation-based. (d) Binary Prediction. . .	96
4.14	Smoothing signals for 9 December 2015. (a) Total SO_i . (b) Total CO_i . (c) Export toggle command to solar inverter.	97

4.15 Segregated energy balance for different smoothing approaches.	
(a) Energy yield. (b) Engagement of the BS. (c) Energy curtailed.	98
B.1 The fisheye chessboard photos with detected corners points in 640×480 resolution.	109
B.2 The undistorted chessboard photos in 640×480 resolution.	109
C.1 The diagram of ray refraction in fish-eye lens.	111
C.2 The calibration plane with sectoral marking.	111
C.3 The angular calibration photo.	112

List of Tables

2.1	Parameters of the simulation model.	31
3.1	Simulation set points.	56
3.2	Duration of cell equalisation.	63
3.3	Energy loss in cell balancing approaches.	68
4.1	Specifications of testbed.	84
4.2	Smoothing set points.	87

List of Acronyms

AC	alternating current
AI	artificial intelligent
ANN	artificial neural network
ARIMA	auto regressive integrated moving average
ARMA	auto regressive moving average
BMS	battery management system
BS	battery storage
CAISO	California Independent System Operator
CARDS	coupled auto regressive and dynamical system
CBH	cloud base height
CSI	current source inverters
DC	direct current
DCM	discontinuous conduction mode
DOD	depth of discharge
FACTS	flexible alternating current transmission system
HSS	hybrid storage system
HV	high voltage
IGBT	insulated gate bipolar transistors
LAN	local area network
LV	low voltage
MOSFET	metal-oxide-semiconductor field-effect transistor
MPP	maximum power point
MPPT	maximum power point tracking
MV	medium voltage
NWP	Numerical weather prediction
OC	over-charged

OD	over-discharged
P&O	perturb and observe
PF	power factor
PI	proportional-integral
PLL	phase locked loop
PV	photovoltaic
PVG	photovoltaic generation
PWM	pulse width modulation
RBR	red to blue ratio
RR	ramp rate
SMES	super-conducting magnetic energy system
SOC	state of charge
SVPWM	space vector pulse width modulation
UC	ultra-capacitor
UPS	uninterruptible power supply
VOC	voltage oriented control
VSI	voltage source inverter
WDR	wide dynamic range
WNN	wavelet neural network

List of Roman Symbols

A	linkage matrix of the active balancer
C_{Base}	shut-Off coefficient of PV plant during passing clouds
C_{PV}	input capacitor of boost converter
D	duty cycle of the boost converter
FF	fill-factor of PV cell
I_d^G	direct component of grid current
I_{DC}^{PVG}	DC side current of the PVG inverter
I_d^{PVG}	direct component of PVG inverter current
I_q^{PVG}	quadrant component of PVG inverter current
I_{DC}^{PVG}	incoming current to DC link of PVG inverter
I_q^{*PVG}	reference value of quadrant component of PVG inverter current
I_{DC}^{*HSS}	reference value of incoming current to DC link of HSS inverter
I_G	grid current
I_{PV}	PV array current
I_{SC}	short-circuit current of PV cell
$I_{balancing}$	reduced charge current of the battery stack during balancing
I_{charge}	charge current of battery stack
$I_{discharge}$	discharge current of battery stack
I_d^{*HSS}	reference value of direct component of HSS inverter current
I_q^{*HSS}	reference value of quadrant component of HSS inverter current
L_f	inductive component of filter
L_{boost}	inductor of the boost converter

N	number of cells in the stack
P_G^*	reference value of output power of PVG system
P_{BS}^*	reference value of output power of BS system
P_{HSS}^*	reference value of output power of HSS system
$P^{n \rightarrow (n+1)}$	power transferred from n^{th} to $(n+1)^{th}$ subset
$P_P(t_i)$	predicted generation level at t_i
P_{BS}	output power of BS system
P_G	output power of PVG system
P_{HSS}	output power of the HSS system
P_{MPP}	power of PV array at MPP
P_{PV}	output power of PV plant
P_{STC}	PV output power in standard test conditions (STC)
$R(t_0)$	instantaneous observed ramp rate of the PVG at t_0
$R_O(t_0)$	RR command to the PV system at t_0
$R_c(t_0)$	the most critical RR to predicted PVG output values
R_f	resistive component of filter
$R_i(t_0)$	the RR from PVG output value at t_0 to i^{th} predicted value
R_b	bleeding resistor
R_s	maximum allowable ramp rate of output power
S	insolation on PV cell surface
S	number of cells in a subset
T	turn ratio of flyback transformer
T_P	effective prediction range
T_{cell}	temperature of PV cell
V_C^B	hysteresis band for maximum permissible cell voltage
V_D^B	hysteresis band for minimum permissible cell voltage

V_d^G	direct component of grid voltage
V_{DC}^{PVG}	DC link voltage of the PVG inverter
V_{DC}^{*PVG}	reference value of DC voltage of the PVG inverter
V_C	maximum permissible cell voltage
V_D	minimum permissible cell voltage
V_{BS}	nominal voltage of BS system
V_{DC}	DC voltage of the DC-coupled PVG inverter
V_{DC}^{HSS}	DC link voltage of HSS inverter
V_{DC}^{*HSS}	reference value of DC link voltage of HSS inverter
V_G	grid voltage
V_{HV}	voltage across HV side of flyback
V_{LV}	voltage across LV side of flyback
V_{OC}	oper-circuit voltage of PV cell
V_{UC}	nominal voltage of UC system
V_{cell}	cell voltage
V_{inv}	output voltage of inverter
V_{max}	maximum permissible cell voltage
V_{mean}	battery stack mean cell voltage
V_{min}	minimum permissible cell voltage
\bar{I}_{HV}^C	mean charge current at HV side of flyback
\bar{I}_{HV}^D	mean discharge current at HV side of flyback
\bar{I}_{LV}^C	mean charge current at LV side of flyback
\bar{I}_{LV}^D	mean discharge current at LV side of flyback
$\bar{V}(n)$	mean voltage of n^{th} subset
$\vec{V}(t_0)$	principal velocity vector of the clouds at t_0
\vec{C}	charge vector of the converters
\vec{D}	discharge vector of the converters
$\vec{D}_{t_0}^{t_1}$	projected displacement value between t_0 and t_1
$\vec{V}(t_0)$	clouds' velocity vector at t_0
\vec{d}_n	n^{th} clouds' displacement vector

\vec{L}_P	effective displacement prediction
\vec{SOC}_{init}	initial SOC vector of the battery stack
\vec{I}_{HV}^C	mean current vector in charge mode at HV side
\vec{I}_{HV}^D	mean current vector in discharge mode at HV side
\vec{I}_{LV}^C	mean current vector in charge mode at LV side
\vec{I}_{LV}^D	mean current vector in discharge mode at LV side
\vec{I}_{cell}	mean current vector of cells
f_G	grid voltage frequency
f_{SW}	switching frequency
t_f	prediction span
t_r	observation instant
t_{SP}	split prediction ange
t_{h1}	minimum distance between observation time and prediction time
t_{h2}	maximum range of historic observation
I_{HV}	HV side current of flyback
I_{HV}^P	peak current value at HV side of flyback
I_{LV}	LV side current of flyback
I_{LV}^P	peak current value at LV side of flyback

Chapter 1

Introduction

1.1 Background

The growing concerns about energy crises and climate changes have created a motivation for extensive deployment of renewable energy resources displacing the conventional power plants. On the other hand, due to the reducing trend in manufacturing cost of photovoltaic (PV) panel and recent advances in power electronic converters, PV power plants have been broadly deployed in a wide range of rated power as standalone generation plants in remote areas as well as grid-connected applications. The integration of the PVG plants into electric power system either as relatively low voltage (LV) small rooftop plants or medium voltage (MV) utility-scale PV farms has raised a new area of investigation among electrical scholars, utility grid operators as well as PV solution manufacturers; the advantageous and detrimental effects of these systems on the utility grid. Since the distribution power systems have been traditionally designed for unidirectional power-flow from the main substation into downstream loads, the presence of the PV systems close to the consumption points might violate these assumptions and introduce unprecedented changes in power-flow direction, power factor, transmission losses, voltage magnitude, and harmonic distortion. These might be either detrimental or beneficial for the distribution network. The severity of these changes is a function of power system's characteristics, and the variations in consumers' demand as well as amount of PVG units installed across the network. These variations affect the power system in different ways depending on the time span they occur. The day-long variations, that mostly follow a predictable parabolic trend, shift the operating point of the power system which are commonly referred to as "static effects". Whereas, "dynamic effects" are

those created by stochastic and short-term indeterminacy of the PVG. Different aspects of both dynamic and static effects will be discussed in this chapter.

1.1.1 Static Effects

As the PVG plants are increasingly taking over a remarkable portion of the total demand in distribution level, a larger capacity will be released either in distribution or transmission network. To some extent, this makes up for the regular demand growth of the clients without any infrastructural upgrade. Moreover, it provides an opportunity for exporting electric energy to the neighbouring networks as a potential long-term benefit [1]. By the reduction of power-flow in the distribution system, the current in the power lines is decreased correspondingly which results in reduced losses in the power lines (RI^2 term) [2]. On the other hand, when in a load point the generation exceeds the amount of demand, the power will flow in reverse direction from end users to other load points or main substation that brings about voltage swell, malfunction of voltage drop compensator devices, and runaway condition in the transformer tap changers [3]. This phenomenon in terms of severity and extent exacerbates as the deployment level of PVG systems increases. To this end, utilising the PVG systems beyond 25% of customers' demand is usually regarded as high penetration level that noticeably affects network operation [4]. The apparent mismatch between the daily trend in energy demand of the residential clients and output power of the PVG plants implies a higher likelihood of over-generation during the mid-day time. This long-term mismatch between PVG power and the demand is illustrated in Fig. 1.1 for a household customer. The over-generation causes reverse power-flow and the voltage swell issues in distribution networks which occasionally propagate into the upstream transmission level, as well. The reactive power control of the PV inverters as well as utilising the flexible alternating current transmission system (FACTS) devices have been indicated as effective solutions to alleviate the static effects [5]. Although reverse power-flow and the resulting voltage rise are regarded as the immediate static effect of the distributed PVG, it will not be critically troublesome for power grids unless in weak power feeders [6]. A similar deduction has been made by [7] according to a simulation probability study of voltage amplitude in several sample buses as well as the averaged value for all consumers in a test network against the penetration level of PVG which indicated conformity with EN BS 50160 up to 30% of penetration level. The excessive level of PVG deployment also changes the unit commitment model of the power system.

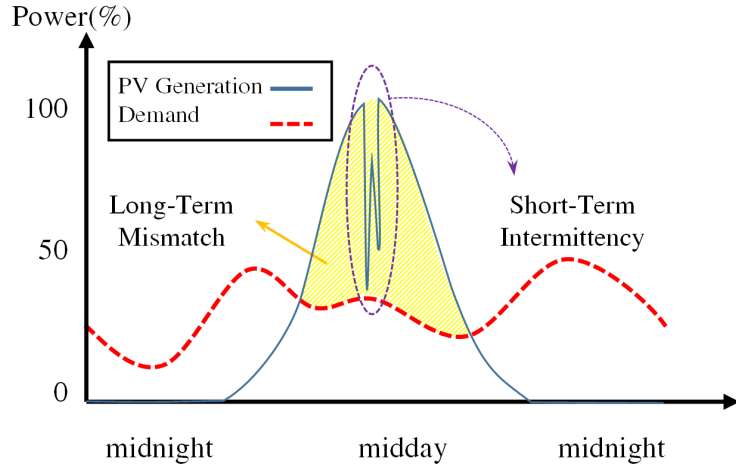


Figure 1.1: Variations of PVG output power in different time scales.

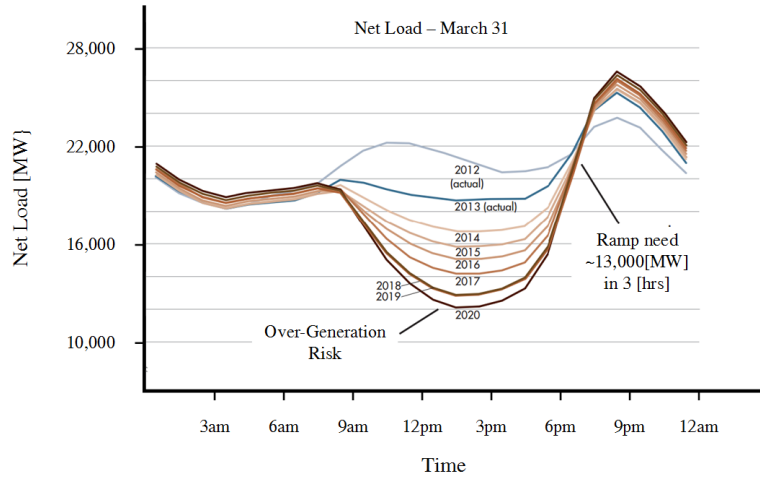


Figure 1.2: The California Independent System Operator (CAISO) duck chart [8].

The PVG integration can dramatically change the pattern of net load demand need to be met by the utility. Due to the parabolic trend in the daily generation of the PV, the net demand would experience a significant reduction during the mid-day production peak. This may result in over-generation which violates the economic dispatch and raises the generation cost. Fig. 1.2, referred to as "duck chart", shows how the growing level of PV integration could change the shape of net load demand and poses the potential risk of mid-day over-generation [8]. The power system security is also a critical factor to determine the financial evaluation of the large-scale PV plants. Even if the PV generation capacity well matches the peak demand, the location of the plant should be chosen as such the bus voltages and line capacity limits are not violated and the power system is able

to withstand the contingencies [9, 10]. Different solutions have been outlined to reduce the mismatch between the amount of demand and the total output power of the PVG systems. Changing the orientation of the PV panels toward east or west will slightly level off the peak area of the generation curve and relatively expand that toward morning and evening hours, respectively, however at the cost of the reduction in the overall daily production. As indicated in [11] this does not completely compensate the generation consumption imbalance yet the mid-day generation's peak is reduced by 30%. Alternatively, the control strategy of the PVG system could be modified to have it working below maximum power point (MPP) and curtail the excess power [12]. Moreover, this may be achieved by employing a dump load to consume the excess output power while the PVG system is operating at MPP. From the perspective of grid operation, the large scale PV generation plants could significantly benefit the utility grid in terms of the stability and reliability provided that the essential grid interactive capabilities are properly incorporated, e.g. voltage control, active power controls, regulating ramp-rate, fault ride through, and frequency control. This requires the instantaneous management of active and reactive power as well as ramp rate control similar to large conventional generation plants. The PV plant, as such, operates in a more reliable and profitable manner [13]. The energy storage systems are also capable of addressing the discrepancy issue by matching up generation and demand over time without any energy curtailment [14–17]. Thus, BS have been indicated to be a promising option [18–21] and the only feasible solution for household clients, while for utility-scale applications super-conducting magnetic energy system (SMES) [22, 23], flywheel kinetic energy storage [24], UC [25], and fuel-cell systems [26, 27] have been proposed as well. With the exception of SMES the other solutions have been also practically utilised. From a financial point of view, the virtually high price of BS becomes more justifiable when it is allocated to serve other functions along with PVG shifting. As a generation shifter the BS stores the generated energy over the off-pick demand period (noon) and contributes in supplying the load during the on-pick period (evening) when increased tariff is applied. This practice is termed as peak shaving. In addition, the BS can reshape the demand profile to a comparatively leveler daily pattern which referred to as load levelling. If it is allowed in the regulatory framework the energy surpasses the consumption of the household client could be purchased by the utility in on-pick periods. It is provided that an amount of generation, which is predefined by the operator, is supplied by PVG in a timely manner. This is manifested as dispatch-ability which may not be accomplished unless the

PVG is accompanied by a BS system. The BS could also serve other auxiliary applications such as uninterruptible power supply (UPS), grid frequency stabilisation, reduction of transmission losses, increasing the reliability, spinning reserve, peak-shaving, load levelling, etc. [14–16, 18, 28–33]. The integration of PVG units with utility grid requires compliance with the regulations adopted by grid operators. In the case of rooftop scale, PV systems are allowed to inject active power up to the nominal rating, while reactive power is often restricted to the value of *zero* meaning no contribution in voltage control of the network [34, 35]. Consequently, over the hours when PVG has a considerable share in supplying active power demand of consumers, the utility only delivers the reactive power. Therefore, the power factor will drop to a level as low as 0.5, which conventional measures usually fail to perfectly compensate that. The situation becomes more crucial when reactive power supply to the endpoint loads is interrupted due to a power line or a generator outage. Therefore the customers are subject to more serious voltage disturbances [6, 36]. Hence, incorporating reactive power control in PVG solutions might subside these power factor issues [7]. In this regard, the advent of smart-grid enables a more comprehensive control strategy on distributed generation units. Another matter of concern about the high penetration of PVG is system stability which has been in focus of attention in few previous research works. Different scenarios of the PVG deployment in the power system, namely centralised PV farm with constant output of active and reactive power (PQ), centralised PV farm with constant active power generation and voltage amplitude (PV), and distributed installation of PV systems in residential area, have been analysed in [1] which revealed an improvement in loading capability of the network in the case of distributed installation. Whereas, no significant changes were observed in two other cases. The integration of PVG into utility grid can positively affect the transient stability of the transmission network, as well. As penetration level of the PVG increases, characteristic eigenvalues of the power system varies slightly while all are still located in the left-hand area of the s-plane which guarantee the stability of the system [1]. Moreover, the transient post-fault behaviour of a test distribution network is examined in [36]. Depending on the type of fault and its location with respect to the major generator units as well as PVG systems, the presence of the PVG systems could improve or deteriorate transient response of the generator speed, its relative angle, and also the voltage magnitude in different buses. A positive effect of distributed PVG plants on the stability of the transmission system has been observed when a power line outage isolates the generation units from the rest of network with insufficient

generation. In this case, the stability is seriously compromised unless the severity of the post-fault disturbances is alleviated as a result of the contribution of PVG systems.

1.1.2 Dynamic Effects

The primary matter of concern raised in relation to wide-spread deployment of the PVG systems is stemmed from intermittent nature of the solar irradiance caused from passing clouds and atmospheric phenomena so that the generated electric power will fluctuate proportionally. In particular when the PVG units are allowed to operate in MPP with no restriction from utility operator. As Fig. 1.1 illustrates, compared with the aforementioned long-term daily variations passing clouds create very fast and unpredictable generation dips with significant amplitude. This requires that the ordinary operational reserves of the power system make up for the variability of the PVG plants as well avoiding the frequency deviations. Therefore, the reserve generation plants will suffer an extensive operational burden or even fail to deliver the required backup due to insufficient capacity which may lead to undesired frequency deviations. The variations in the PV output may propagate to the upstream transmission network and increase the tie-line power fluctuations [17,37–39]. To avoid the frequency fluctuation and subsequent power outages, one solution is to adapt the conventional economic load dispatching scheme tentatively to allow any unit with available capacity participate in the load-following regardless of the fuel price. However, this may increase the operational cost of the power system [40–42].

The analysis and quantification of fluctuations in solar radiation, its amplitude and periodicity have been the topic of many research papers. The localised spectral analysis of instantaneous clearness index is carried out by meant of wavelet transform in [43] and then the "fluctuation power index" and "fluctuation energy index" are introduced to characterise the variations in clearness index of the atmosphere. The results have revealed that although the clearness index is subject to fluctuations ranging from a few seconds to an hour of duration, the remarkable variations primarily occur in a time frame of few minutes. In another work, the clouds have been simulated in order to quantify their effect on PVG level [44]. This research revealed that the worst cases of generation losses usually occur during the mid-day PVG peak by Cumulus clouds which surprisingly are not as dark and dense as Squall Line ones, yet they pass more frequently over a specific location. Moreover, the wider be the area that PVG systems are

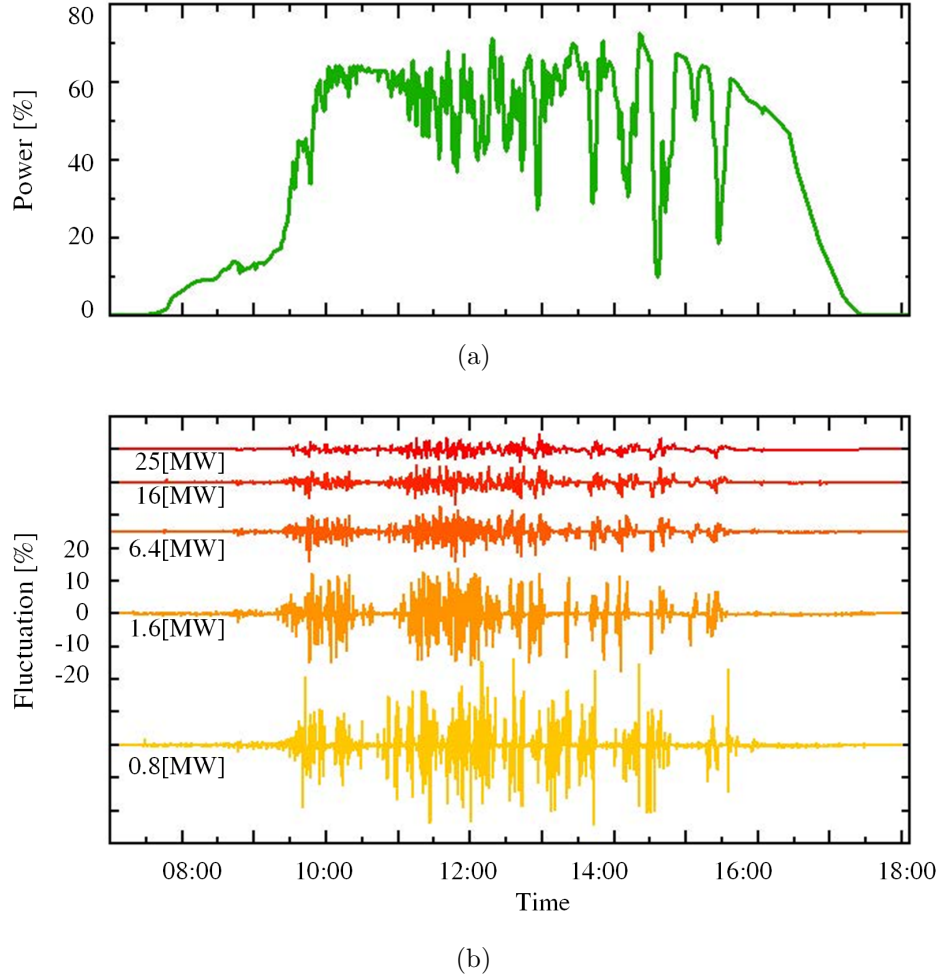


Figure 1.3: Totalised areal equalising effect in a 25[MW] PVG plant [50]. (a) The output power of one PV panel. (b) The observed variations for different combinations of PV arrays.

dispersed throughout; the less total generation will be affected. For areas larger than few hundreds km^2 , the maximum generation changes were also shown to occur mainly in 1-2 [min] intervals. The relation between the total PVG output and vastness of the area PVG systems are located has been evaluated in [45–48]. Where a significant reduction has been identified in the amplitude of the power fluctuations particularly the short-time components. This effect is termed as the equalising effect of totalised areal irradiance [49, 50]. Fig. 1.3 represents the short-term variability of a 25 [MW] PVG plant observed across a different number of arrays. The more PV arrays are included, the fewer disturbances are observed in the generated power as a result of totalised areal equalising effect. This explains the financial and technical benefits of implementing the equalising

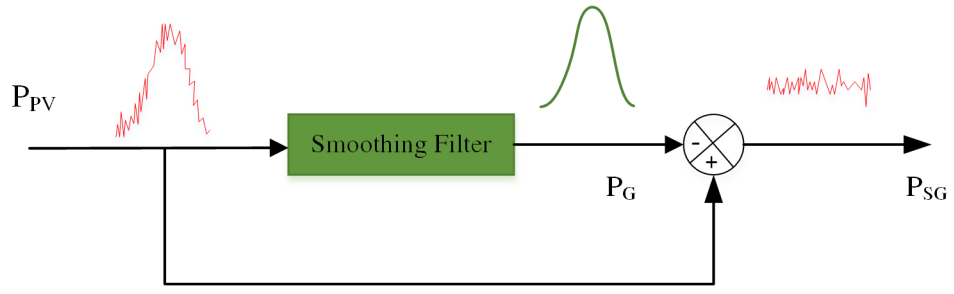


Figure 1.4: The diagram of a PVG output smoothing controller.

measures in upstream level especially for locationally dispersed and small-scale PVG plants [47,48]. Whereas the requirement for the equalising the PVG output is unavoidable. In particular, this is comparatively more crucial for centralised PVG plants in industrial or utility-scale capacity. Therefore, different solutions have been outlined to address the output power fluctuations of the PVG systems attributed to the solar radiation intermittency and passing clouds which are referred as "smoothing" hereafter. The key element for smoothing the PVG output power is a storage system which serves as an energy buffer and suppresses the short-term generation fluctuations. The main objective is to maintain the RR of the output power variations within a pre-defined limit. This is usually requested by the utility operators in the percentage of the rated output power per minute, e.g 10% per minute, which determines the required energy storage capacity.

Regardless of the technology and characteristics of the storage system, the strategy of controlling the smoothing storage device has a significant influence on the performance of the smoothing process as well as the optimal capacity of the storage system and its amount of engagement. The primary function of the smoothing controller is generating a reference quantity for the regulated PVG output power. This defines how the storage backup operates to make up for the fast variations. Fig. 1.4 represents a simplified diagram of a smoothing controller. Given the output variability of the wind power generation systems as well as wind-PV hybrid plants, the smoothing techniques for these systems share similar principles to the PVG output equalising, with the exception of relatively different characteristics of disturbances. A number of studies have proposed low-pass filtering, moving window averaging and other linear filtering approaches to segregate the fluctuating component of the output power [51,52]. In these techniques, the maximum allowable RR of output power may be violated momentarily since it is not the directly under control. Hence, direct control on the RR of the variations has proved to exhibit a more satisfactory smoothing performance in

the hybrid wind-PV generation plants. In the literature, linear signal processing approaches, e.g. Kalman, and Fuzzy wavelet filtering have been also proposed to mitigate the output power variability of the wind and hybrid wind/PVG systems. Moreover, Refs. [53, 54] have suggested Fuzzy logic SOC controller to ensure the optimal operation of the BS. In general, the energy storage devices account for a significant share of the total price in a PVG plant. Therefore the optimal operation of the BS would be of great financial benefit. For this purpose, some of the recent research works discussed incorporating the SOC in the smoothing control to prevent the lifetime depletion caused by overcharge and over-discharge of the BS [31, 32, 55, 56]. Previous studies have reported the geographical dispersion as a critical factor which can significantly reduce the amount of required BS. It was identified that the centralised smoothing approach can efficiently function using half the amount of BS needed in distributed smoothing approach, in terms of capacity and power [47]. Moreover, in [39] a Fuzzy-based output controller was proposed for a PV-Diesel hybrid isolated electricity grid where the PV generation level was determined using the Fuzzy reasoning based on the average insolation, insolation changes, and frequency fluctuations. This approach minimised the battery involvement by allocating the frequency control to the PV inverters using a Fuzzy controller. In another research work, two techniques were suggested to optimise the amount of BS required for smoothing action. It was proposed that the ramp up events be regulated by limiting the PV inverters export. This effectively halves the BS capacity needed for the smoothing operation. Moreover, it was identified that the required BS capacity could be also reduced by adjusting the SOC based on the instantaneous export of the PVG plant [57].

1.1.3 Storage System

In the electric networks, BS has proven a versatile solution for a wide range of applications which could be expanded to the RR control of the PVG output as well [21, 31, 51, 55, 56]. The BS generally suits the applications which involve virtually long-term and stable intervals of energy exchange. Whereas, in comparison to the PVG peak-shifting, in smoothing process during the sudden output variations the BS backup is subject to an excessive stress due to the recurrent, short-term and shallow charge/discharge cycles. Therefore the BS technologies of higher power density, e.g. Li-FePO₄, serve as more efficient solutions to this application [58]. Moreover, the UC technology could be combined with the BS to bridge fast and intense power fluctuations [59, 60]. UC has been recently introduced and gained

a considerable attention as a short-time energy storage in the power system. In spite of the BS technologies, which operate based on the electrochemical reactions, in UC the principal is storing the energy via electric charge which is similar to the ordinary capacitors and enables delivering higher pulses of energy. Furthermore, a new type of lead-acid battery cells integrated with UC in a unified package termed as ultra-battery has been commercialised in recent years which can be deployed for both the smoothing and energy shifting applications in a PVG system [44,61]. For an effective handling of the HSS consisting of BS and UC the appropriate considerations should be taken into account in power conversion stage as well as control system.

1.1.4 Cell Equalisation of Battery Storage

Battery cells are usually utilised as series connected strings to build up a voltage level which suits the relatively high voltage applications such as utility grid. However, in this arrangement, the cells tend to develop unequal SOC due to manufacturing tolerances, irregular distribution of temperature, and differences in the ageing and self-discharge characteristics of particular cells. The cell degraded in capacity are subject to excessive stress due to overcharge and over-discharge which leads to premature failure of the affected cells. In particular the Li-FePO₄ chemistry it manifested as irreversible chemical reactions in the electrodes and the electrolyte. On the other hand, Li-FePO₄ feature a comparatively superior energy and power density than the lead-acid chemistry. Therefore, this technology is widely deployed for the applications which involve short-term and high power energy demand, e.g. PVG output power smoothing. The cell equalising measures are the key solution to this issue and prevent any possible damage to the Li-FePO₄ cells in the series connected battery stacks which prolong the lifespan of the battery cells. Moreover, this enables a more efficient utilisation of the entire capacity of the stack by preventing immature termination of the charge or discharge cycle once only a few outlier cells are reached an over-charged or over-discharged condition [62]. Passive balancing approaches are common solutions which shunt the overcharged cells with bleeding resistors during charge cycle until all cells concurrently reach the full charge state. The shunt resistors dissipate the excess power as heat during the balancing process. Therefore, this solution is not of a superior efficiency and can create a significant temperature gradient between the cells and negatively affect the balancing process. In contrast in active cell balancing approaches the charge imbalance is addressed by routing the surplus

charge from the over-charged cells to those of lower SOC level [63–68]. The methods which are based on switched capacitor/inductor primarily allows charge transfer between adjacent cells and suffer prolonged balancing time until the cell voltages are converged [69–73]. Bidirectional DC-DC converters such as flybacks can expand the charge routing scheme, i.e. between cells and the entire battery stack or smaller group of cells [74–77].

1.1.5 Short-Term Cloud Prediction

Incorporating the BS into the PVG system for smoothing purpose involves several deterrent factors, i.e. relatively high capital price, regular maintenance, additional considerations in power conversion and control design. Therefore, considerable attention has been paid to weather prediction information for more efficient management of solar energy resources and enables accommodating higher levels of these variable generation resources while comparatively less amount of storage backup is required. There is a wide range of forecasting methods and data sets with different temporal and spatial scales [78]. Long-term weather prediction approaches are of potential benefits in scheduling the unit commitment as well as economic dispatch of generation plants up to a day ahead while a significant amount of distributed PVG systems are also taken into consideration [41, 79–81]. From a short-term perspective, the load balancing operation is considerably enhanced by incorporating the information on the projected output of PVG units. Therefore, a precise information about timing and optical characteristics of the clouds which are projected to shade a PVG plant enables a predictive smoothing approach. Therefore, prior to the shading event, the output power begins a downward slope so that it reaches the low point by the time the passing clouds occlude the sun. In the ideal case, this mitigates the sudden generation drop while the storage backup is not required. Meanwhile, the comparatively gentle slope of the output power satisfies the RR limitation of the existing operational reserves. Given the scheduled time scale of the reserve capacity, forecasting approaches with sub-hour temporal range exhibit a more precise accuracy. Hence, the ground-based real-time observations using the sky-cameras [82–85] and the network of radiometric sensors [86–88] has been recently in the focus of many research works on the PVG output smoothing. There is a wide range of forecasting methods and data sets with different temporal and spatial scales [78]. Long-term weather prediction approaches are of potential benefits in scheduling the unit commitment as well as economic dispatch of generation plants up to a

day ahead while a significant amount of distributed PVG systems are also taken into consideration [41, 79–81]. From a short-term perspective, the load balancing operation is considerably enhanced by incorporating the information on the projected output of PVG units. Therefore, a precise information about timing and optical characteristics of the clouds which are projected to shade a PVG plant enables a predictive smoothing approach. Therefore, prior to the shading event, the output power begins a downward slope so that it reaches the low point by the time the passing clouds occlude the sun. In the ideal case, this mitigates the sudden generation drop while the storage backup is not required. Meanwhile, the comparatively gentle slope of the output power satisfies the RR limitation of the existing operational reserves. Given the scheduled time scale of the reserve capacity, forecasting approaches with sub-hour temporal range exhibit a more precise accuracy. Hence, the ground-based real-time observations using the sky-cameras [82–85] and the network of radiometric sensors [86–88] has been recently in the focus of many research works on the PVG output smoothing.

1.2 Main Objectives

The main objectives of the conducted research study are as follows:

- Examination of the storage based smoothing scheme for an industrial scale grid connected PVG system, including suitable structures for the power electronic converters, and design and simulation of the respective control system.
- Further investigation of the storage based PVG smoothing using the HSS and considering the contribution of the UC for a more efficient utilisation of the BS.
- Proposing an equalising algorithm for a bidirectional flyback based active cell balancer to address the SOC mismatch issue which occurs in the series connected battery banks in both charge and discharge cycles.
- Discussing the hypothesis of storage-optimised PVG output smoothing approach by means of the short-term cloud prediction data produced by real time processing of the sky images.
- Proposing a robust imagery based cloud prediction method and developing a preliminary prototype to evaluating the experimental results and find out

whether it is a viable storage-optimised PVG smoothing solution.

1.3 Structure of Thesis

The remainder of this thesis is organised as follows:

Chapter-2 first describes the double-stage structure of the power electronic converter including a DC-DC and DC-AC converter to serve as an interface between a general DC power resource and the utility grid. Two different ways to integrate the HSS into the PVG converter for export smoothing purpose, i.e. AC-coupled and DC-coupled structured are studied. In AC coupled configuration, the HSS is tied into the grid through an independent DC-AC converter with two parallel DC-DC converters for the BS and UC. Whereas, the parallel DC-DC converters are directly connected to the DC link of the PVG converter in DC-coupled structure. The smoother controller splits up the HSS reference power in a low-pass filter. The high-frequency component is sent out to the UC and the rest is supplied by the BS. Lastly, the performance of the designed control system is verified and compared on both of the structures through a simulation study.

Chapter-3 investigates a bidirectional flyback active cell balancer with interleaved arrangement of high voltage (HV) side of the transformers. It proposes an active cell balancing control algorithm which is able to handle the cell equalisation during either charge or discharge cycle. It is also examined that how the interleaved arrangement of the transformers affects the performance of this method. It follows a simulation study confirms the appropriate performance of the proposed active balancing algorithm.

Chapter-4 demonstrates a storage-optimised PVG smoothing approach using the short-term imagery based cloud prediction data from real-time observations. Given the limitations and inaccuracies involved in this approach, a robust and reliable PVG smoothing strategy is proposed. This chapter is also concerned with the implementation of a prototype including a sky camera and two solar inverters to evaluate the performance of the designed algorithm. Where the PVG smoothing controlled is applied to one of the inverters and the other one is always working at MPP. Comparing the experimental results show that the sudden rise and dips appear in the

output power of the uncontrolled inverter are significantly compensated by the smoothing algorithm in the controlled inverter.

Chapter-5 A summary of the main findings and observations on the present research are presented in the final chapter. Moreover, the principal issues and limitations arisen in this research are discussed. It follows the suggestions for the future investigations in the field of PVG output smoothing.

1.4 Publications Incorporated in Thesis

Two papers derived from this body of work, including a conference presentation and a peer reviewed journal article:

1. M. Saleh, M. AS. Masoum, L. Meek, and M. Abshar, Control Algorithm for Bidirectional Fly-Back Active Cell Balancer with Interleaved Transformer Connections, in *2016 IEEE Power and Energy Society General Meeting (PESGM)*, July 2016, pp. 1-5. (Chapter-3)
2. M. Saleh, L. Meek, M. AS. Masoum, and M. Abshar, Battery-Less Short-Term Smoothing of Photovoltaic Generation Using Sky Camera, *Industrial Informatics, IEEE Transactions on*, vol. 14, no. 2, pp. 403-414, Feb. 2018. (Chapter-4)

The full-text of publications is given in Appendix-D. Moreover, the role of candidate is formally endorsed by the co-authors and presented in Appendix-E.

Chapter 2

Storage-Based Smoothing of PV Generation

2.1 Introduction

BS systems have been long deployed in electric transmission and distribution networks for grid stabilisation, operational support, power quality and reliability, load shifting, etc [89]. There is an escalating trend in the deployment of the solar electricity in the distribution networks to meet the growing amount of demand. Fast output variability is typical of the PVG resources, which is mainly attributed to the clouds obscuring the sun and substantial insolation fluctuations. These sudden over/under generation of the PVG plants are treated as ordinary load variations which may lead to an extra burden on the conventional operational reserve of the power system, in terms of the incidence of operation as well as required capacity [40]. This has prompted the utility operators to consider some restrictions on the output RR of distributed PVG systems [90–92]. Therefore, the application of BS has been expanded to mitigate the extensive and fast variability in the output of the dispersed PVG plants at the downstream feeders. Compared to the typical energy storage purposes, for PVG smoothing applications relatively higher power level and shorter cycling intervals, e.g. 10 [min] versus 1 [hr] are required. Fig. 2.1 is an illustrative comparison between the performance characteristics of various energy storage technologies. The proportion of the energy density and power density is indicated by sloped lines which allow evaluation of the typical cycle time for of storage technologies. As seen battery technologies deliver a typical cycling of 1 [hr], while Li-Ion chemistry tends to exhibit a greater discharge current (or power [kW]) than Lead-Acid and Ni-Cd

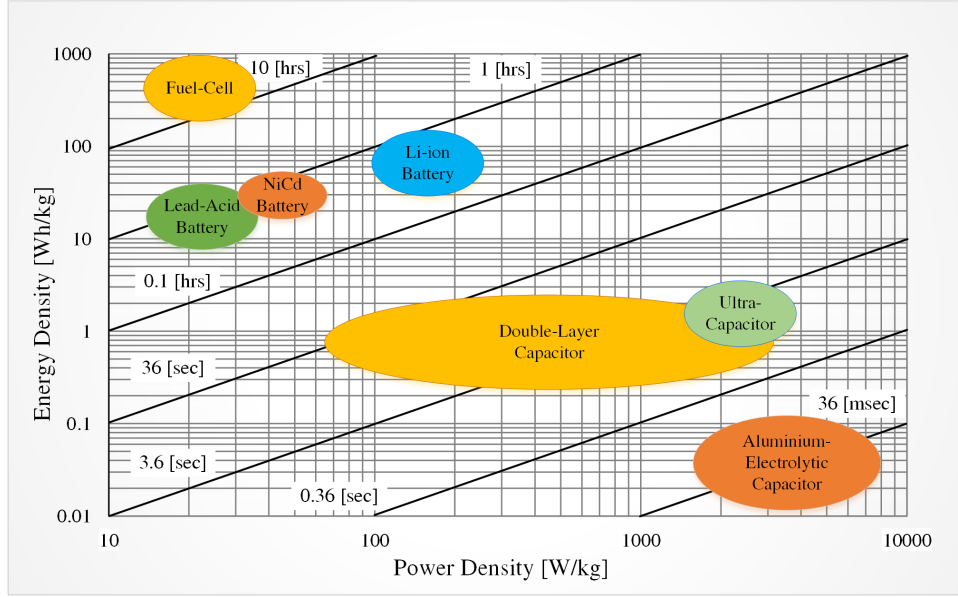


Figure 2.1: Ragone plot of energy and power characteristics for storage technologies [58].

in a similar capacity ([kWh]) which makes that a better candidate for undertaking sub-hour cycles. Given the time frame of the intermittency in the solar electricity generation, which is in few minute range, there is a noticeable gap between the typical cycle time of the BS technologies in the Ragone plot and the required cycle time. Therefore, a PVG output smoothing technique that solely relies on the BS is not the financially optimal solution, since the BS should be over-sized in energy capacity to meet the power rating requirement. This is the main motivation to combine the BS and UC technologies as an HSS for PVG output smoothing application while the desired energy and power characteristics are achieved using a reduced BS size. In the HSS the short-term power impulses are allocated into the UC which presents a higher power density, shorter time constant, and less round-trip loss. This virtually mitigates the recurring and shallow charge/discharge cycles of the BS and extends its lifetime, consequently [93–99]. Hence, this chapter discusses and describes the PVG output smoothing technique by means of the HSS. It begins with a brief overview of various configurations of the power electronic converters for grid-connected PVG plants accompanied with BS devices. Afterwards, the incorporation of the UC is surveyed and a closed-loop controller is designed for an HSS to regulate the short-term PVG output power variations. Finally, two different structures for integrating the HSS into the PVG system, at the AC and DC side, are examined and compared in terms of performance through a simulation study.

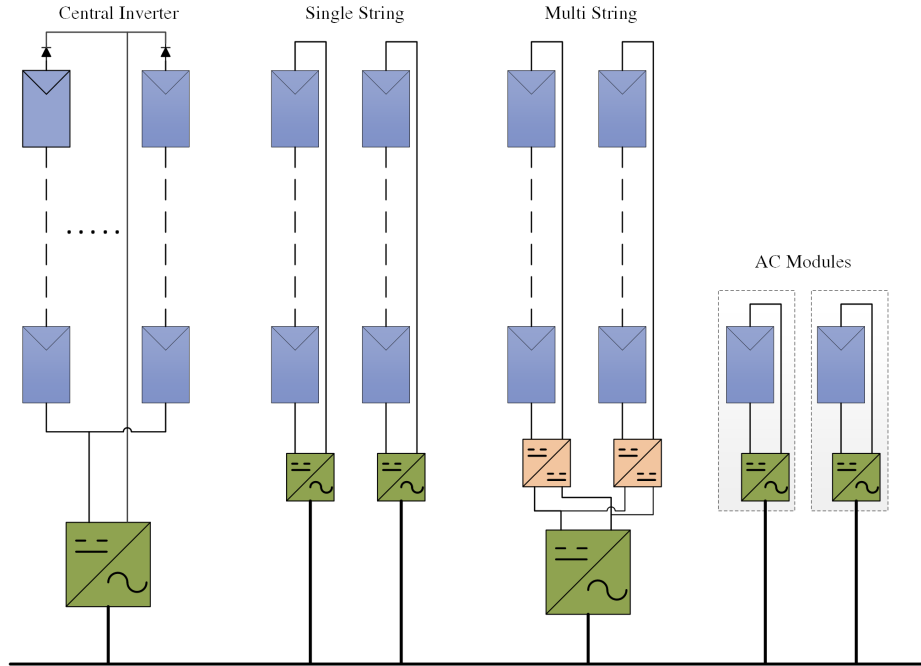


Figure 2.2: Various composition of power electronic interface or PVG plants [100].

2.2 Structure of Power Electronic Converter

Fig. 2.2 represents a concise overview of the various structures for grid-connected PVG inverters. Centralised structure only allows single maximum power point tracking (MPPT) for the whole PV array which is not of the highest solar electricity yield for sizable plants. On the other hand, due to expandability and multi-MPPT features, the two-stage multi-string configuration is widely deployed for industrial and utility scale PVG plants [100]. Therefore, the two-stage structure is a suitable candidate for PVG smoothing application. Fig. 2.3 demonstrate the various possible adaptations for including BS in the two-stage configuration.

For small-scale applications, i.e. residential rooftop PVG plant, the BS can be connected directly to the direct current (DC) link [101]. However, the variable BS voltage as a function of the SOC is not favourable for large-scale applications. Hence, using a DC-DC converter as an interface between the BS and DC link will ensure constant and stable DC link voltage and improves the reliability and performance of the voltage source inverter (VSI) and provides a more flexible control on charge and discharge process of the storage system. Coupling the BS at the alternating current (AC) side and using an independent DC-AC converter for that enables a modular structure with a superior reliability as well as expansion capability [102]. This structure features a reduced operational loss as well

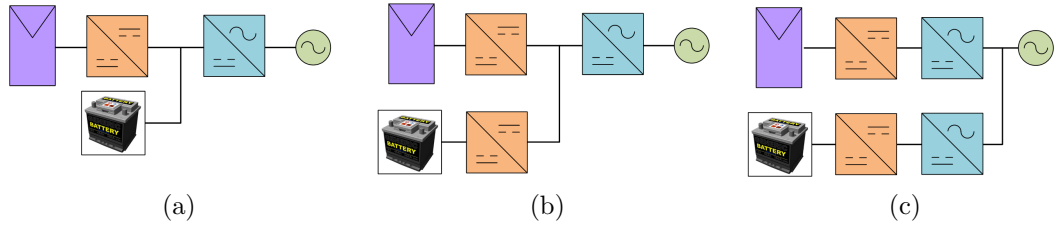


Figure 2.3: Different variants of incorporating the BS into a grid-tied PVG system. (a) Direct connection to the DC link. (b) Connection to the DC link through DC-DC converter. (c) Connection at the AC side.

since the parallel operation of multiple converters in a fraction of rated power is comparatively more efficient. Furthermore, this structure gives a flexibility in the location that PVG output smoothing is implemented. In particular, to take advantage of the equalising effect of the dispersed PVG plants throughout a region the AC side coupling of the BS system allows that PVG output smoothing is performed at upstream level, i.e. the incoming of a feeder or substation location [103]. From HSS perspective the UC could complement the BS system to achieve a more optimised PVG smoothing operation. In order to include the UC in the independent DC-AC structure, various feasible alterations are demonstrated in Fig. 2.4. The UC voltage varies as a linear function of the charge, therefore its stored energy couldn't be fully utilised due to VSI DC link voltage limitation. This makes the structure in Fig. 2.4(a) less suitable for HSS application. Since the direct connection of the BS in DC link arises a similar issue in smaller extent (Fig. 2.4(b)) deploying DC-DC converters for interfacing the BS and UC will prevent substantial variations in DC link voltage and improves the VSI operation in transient conditions (Fig. 2.4(c)). The next section deals with

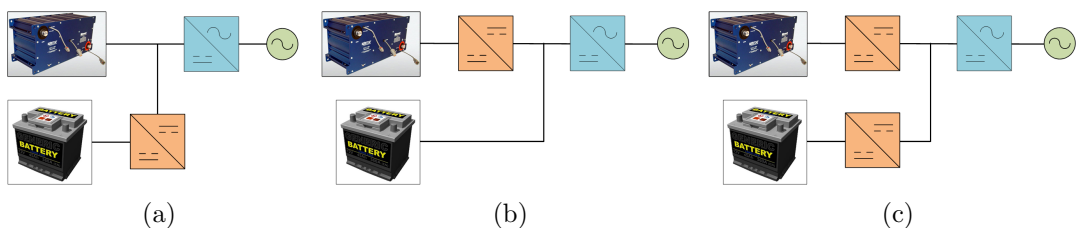
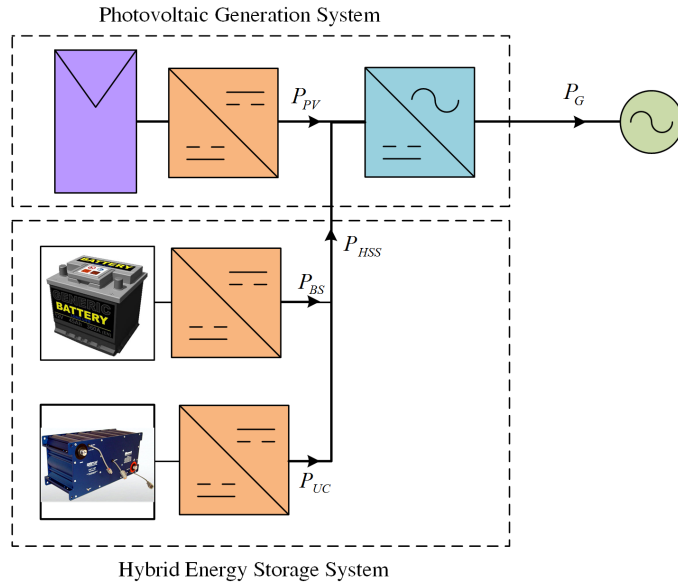
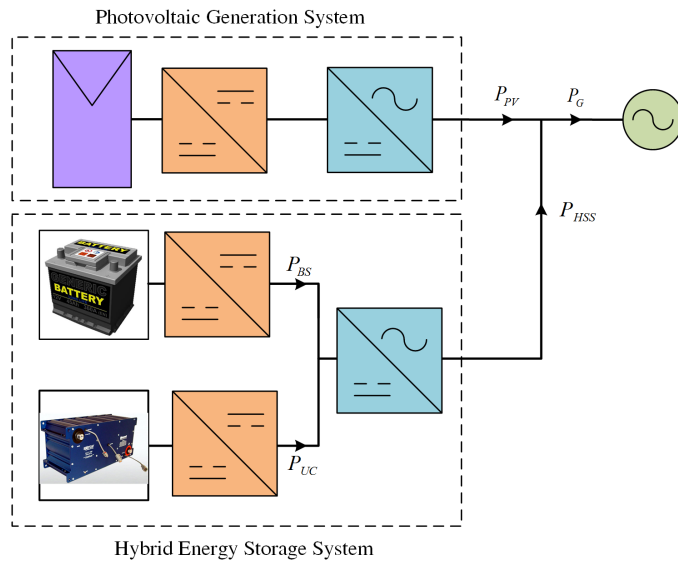


Figure 2.4: Different variants of integrating BS and UC for PVG output smoothing application. (a) UC directly coupled to DC link and BS via DC-DC converter. (b) BS directly coupled to DC link and UC via DC-DC converter. (c) UC and BS coupled through DC-DC converter.

two different configurations of power electronic converter for PVG smoothing as illustrated in Figs. 2.5(a)-(b), referred as "AC Smoother" and "DC Smoother" hereafter.



(a)



(b)

Figure 2.5: Different structures of the PVG plant accompanied with an HSS for output smoothing, (a) coupling at DC side, (b) coupling at AC side.

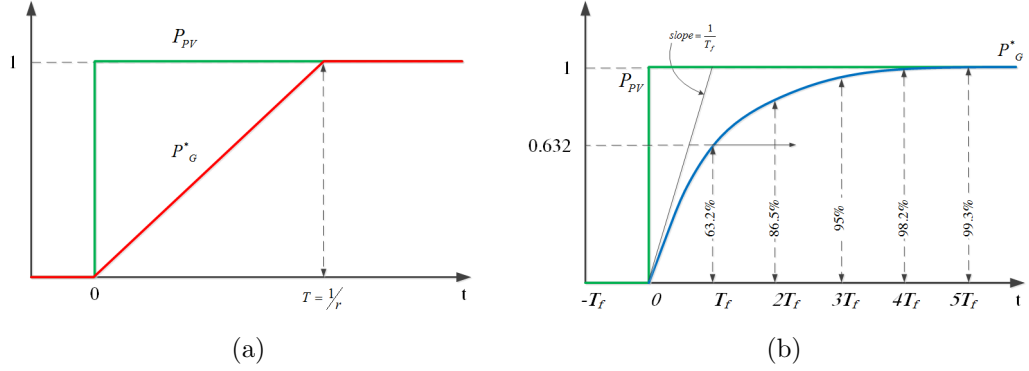


Figure 2.6: Response to step change for (a) RR limiter filter, and (b) first-order low-pass filter.

2.3 Smoothing Controller

The main objective of the smoothing controller is to detect and compensate the undue variations in the PVG output power. Hence, the reference output power is generated through processing the present and previous output power information. The desired smoothing effect could be achieved using various linear filters. Fig. 2.6 illustrates the response of the first-order low-pass filter and the ramp limiter to a step change in the input. Given the bounded area between the step input and the output power curve represents the required amount of the storage backup for the smoothing process, the linear ramp limiter filter is comparatively more optimised in terms of required storage capacity. Moreover, the RR is maintained within the desired limit all the time, whereas the low-pass filter generates a reference power with a varying RR. Hence, the smoothed output reference value is generated by a simple RR limiter and its discrete time representation is expressed in Eq. (2.1):

$$P_G^*(t + \tau_s) = \begin{cases} P_G(t) + R_s \cdot \tau_s & \text{if } P_{PV}(t) - P_G(t) > R_s \cdot \tau_s \\ P_G(t) & \text{if } -R_s \cdot \tau_s \leq P_{PV}(t) - P_G(t) \leq R_s \cdot \tau_s \\ P_G(t) - R_s \cdot \tau_s & \text{if } P_{PV}(t) - P_G(t) < -R_s \cdot \tau_s \end{cases} \quad (2.1)$$

where P_G and P_G^* are the sampled smoothed PVG output power and the reference value for next sampling interval of τ_s , respectively. Moreover, P_{PV} denotes the generated power of the PV plant and R_s is the maximum allowable RR of the PVG output.

As Fig. 2.6(b) demonstrates the step response of the first-order low-pass filter shows a gradually decaying RR which is suitable for decomposing the reference

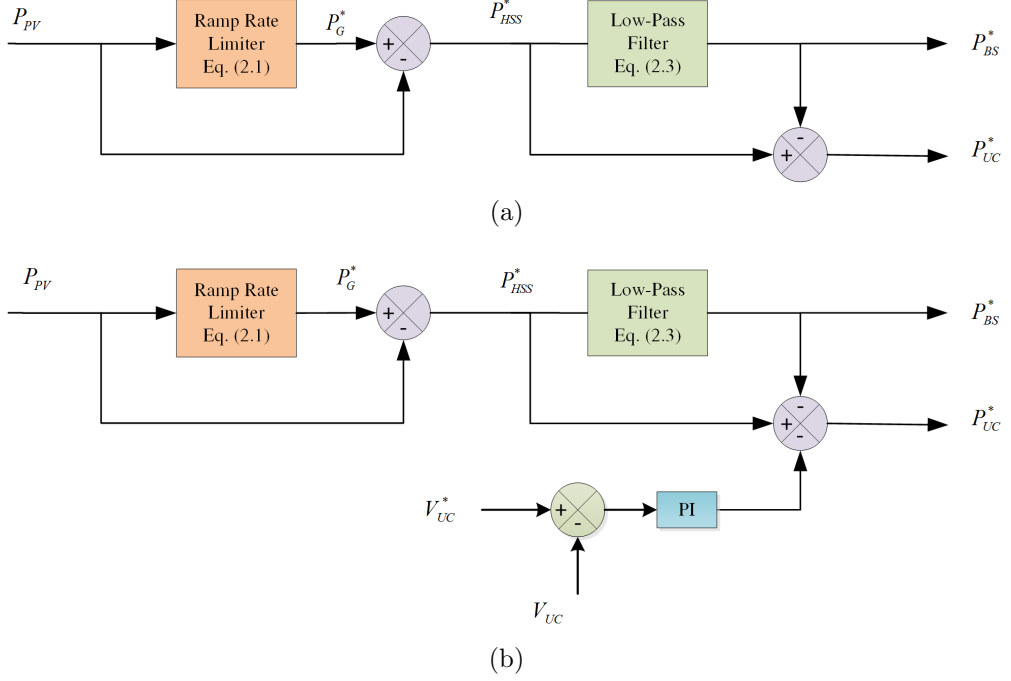


Figure 2.7: The diagram of the PVG output smoothing controller. (a) Without UC voltage regulator. (b) With UC voltage regulator.

power of the BS from the HSS reference power and allocating the fast changing component to the UC in order to keep the BS from supplying high impulse power. Eq. (2.2) defines the HSS reference power and (2.3) gives the exponentially smoothed reference power for the BS using a low-pass filter:

$$P_{HSS}^*(t + \tau_s) = P_G^*(t + \tau_s) - P_{PV}(t) \quad (2.2)$$

$$P_{BS}^*(t + \tau_s) = \frac{\tau_f}{\tau_s + \tau_f} \cdot P_{BS}(t) + \frac{\tau_s}{\tau_s + \tau_f} \cdot P_{HSS}^*(t + \tau_s) \quad (2.3)$$

where P_{HSS} and P_{BS} denote the sampled quantity of HSS and BS power, respectively. Moreover, P_{HSS}^* and P_{BS}^* stands for the corresponding reference values. τ_s is the discrete sampling time and the time constant of τ_f determines the filtering performance, $\tau_f = 0$ results in "no filtering" while as $\tau_f \rightarrow \infty$ the P_{HSS}^* command is completely ignored. The diagram of the HSS decomposed reference power generator is demonstrated in Fig. 2.7(a). In order to verify the functionality of the controller, its simulated response to a 1 [kW] sudden decline in the PVG output is shown in Fig. 2.8, where the RR limit of 0.1 [kW·min⁻¹] is applied. Using a

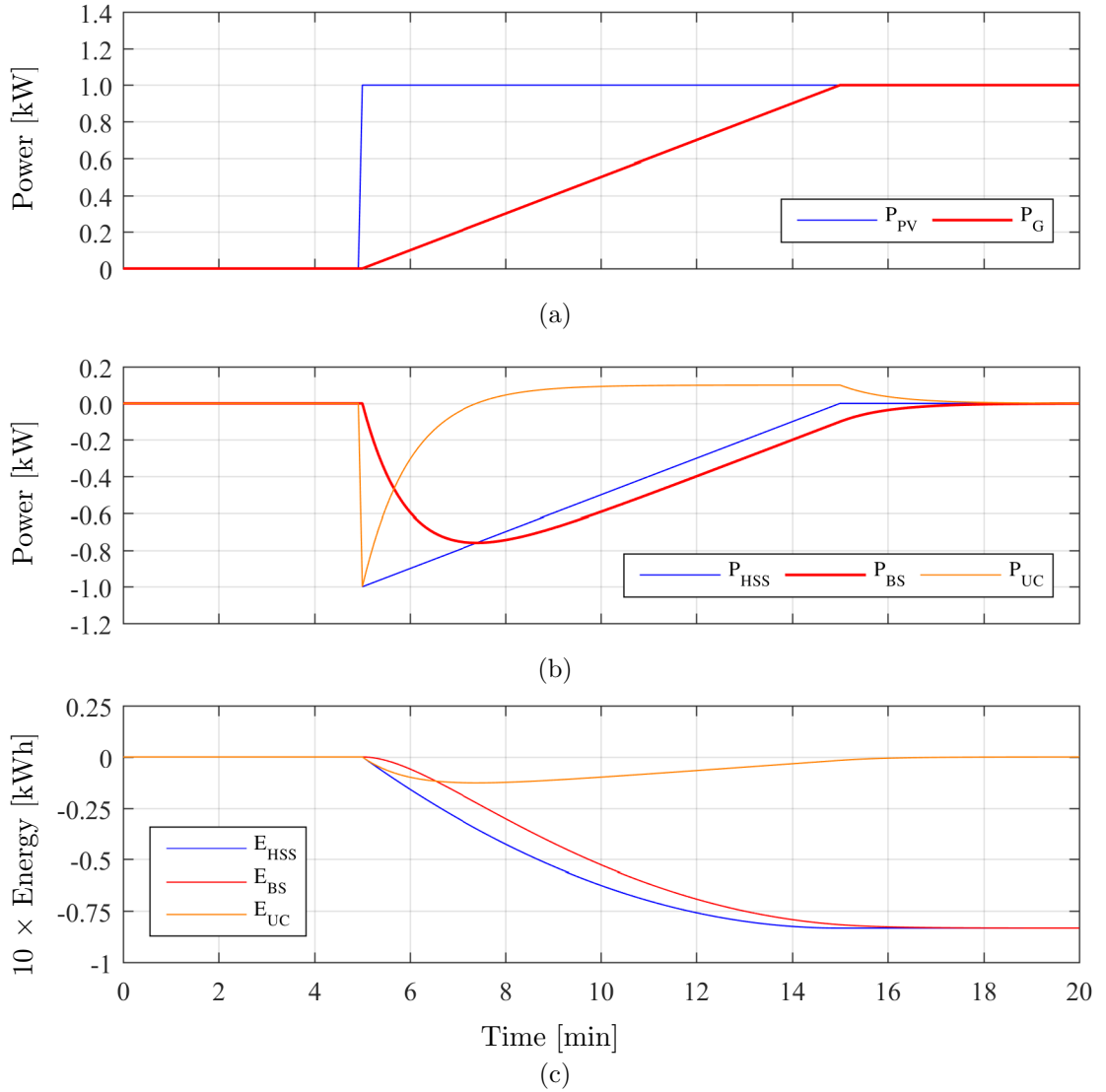


Figure 2.8: Reference power generation for PVG output smoothing using HSS: (a) PV produced power and reference output power, (b) HSS reference power decomposed into the reference power for the BS and UC, and (c) the smoothing energy delivered by the BS and the UC.

low-pass filter with time a constant of 60 [sec], the smoothing reference power is divided into the low and high-frequency components to be allocated to the BS and the UC, respectively. Since the DC component of the smoothing power is entirely assigned to the BS the net energy exchange by the UC is zero. However, considering the power losses in the UC and power electronic converters as well as self-discharge rate of the UC a charge regulator is required to adjust its charge level at a specific value. For this purpose, a proportional-integral (PI) regulator

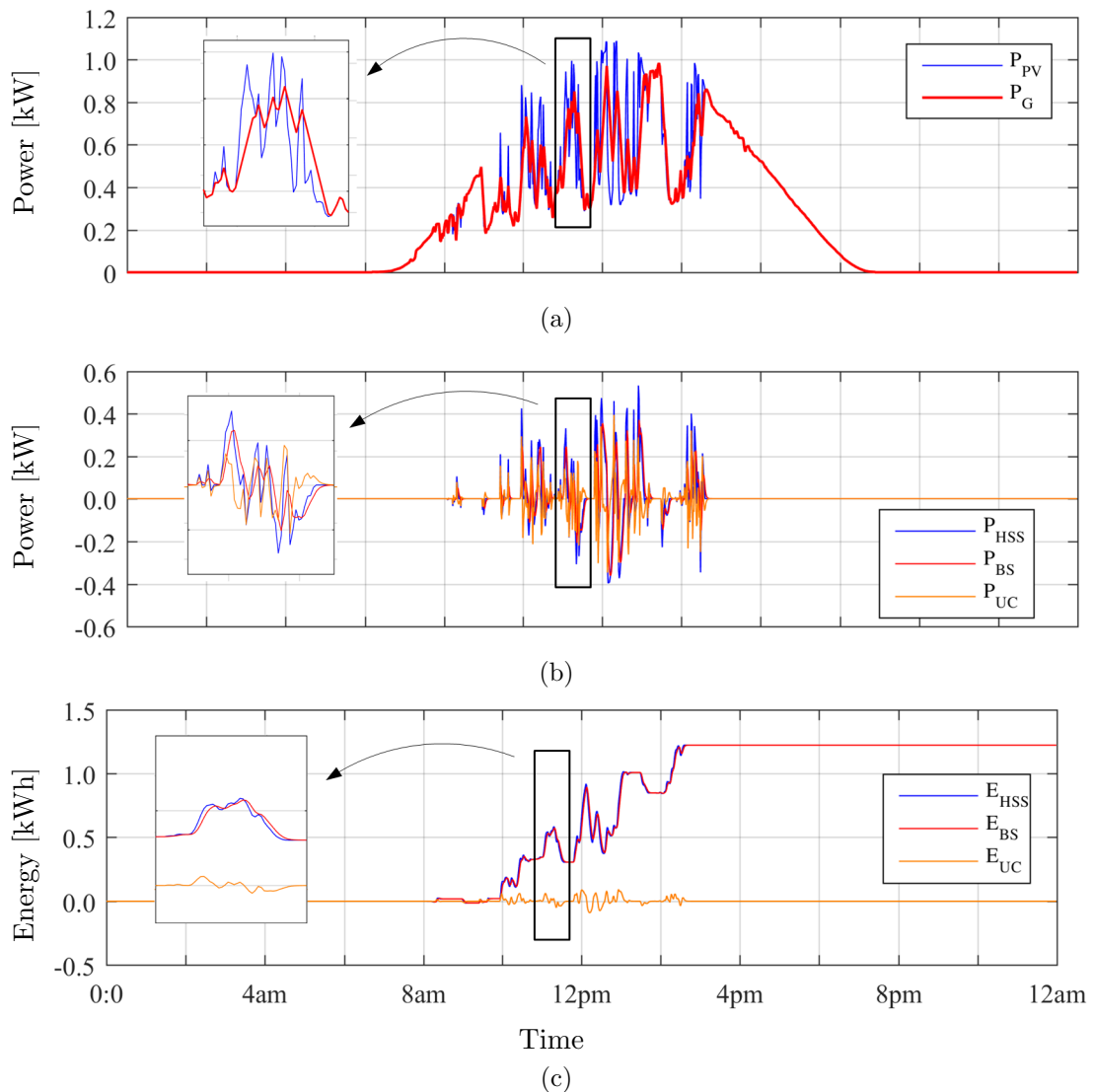


Figure 2.9: Simulation results of the PVG output smoothing using HSS: (a) PV produced power and reference output power, (b) allocated smoothing power to the BS and the UC, and (c) the smoothing energy delivered by the BS and the UC.

is also incorporated in the smoothing controller to compensate the UC's voltage error. The time constant of the UC charge regulator should be much greater than that of the decomposing filter in order to prevent any interference between these two controller loops. Fig. 2.7(b) shows the diagram of the PVG power smoothing with UC voltage regulator. A simulation study is conducted to examine the performance of the HSS based PVG output power smoothing using real insolation data captured on a day with passing clouds in Western Australia. It is assumed that the PVG plant is rated at 1 [kW] maximum output power and the desired

maximum RR of 10% rated power per minute is considered. Moreover, the time constant τ_f of the decomposing low-pass filter is 90 [sec]. The simulation results are shown in Fig. 2.9. It's observed that upon the fast variations of the output power the UC starts supplying the smoothing power and the BS gradually takes over the supply as the time passes. Meanwhile, the overall energy exchanged by the UC is maintained at zero. The longer is the time constant of the low-pass filter, the more the UC contributes in smoothing the power fluctuations so that the BS supplies relatively stable energy demands.

2.4 Controller of Power Electronic Converters

In this section, the implementation of the output smoothing for a grid-connected PVG plant using HSS is addressed in terms of the structure and controller design of the power electronic converters, i.e. AC and DC smoother. Various topologies have been proposed for three-phase PV inverters. In terms of DC to three-phase AC power electronic converter, the VSIs have gained the monopoly in the market as well as industry, especially in LV applications, while current source inverters (CSI) have not found significant appeal practically in this area of the application so far. This is primarily due to the ease of control and more abundant supply of conventional self-commutating power electronic switches, e.g. insulated gate bipolar transistors (IGBT), which is a key component of the VSI topology. Given the inherent buck characteristics of the VSI its proper operation is provided that the DC link voltage is greater than the line voltage at AC side. This necessitates deploying a boost DC-DC converter between the PV array and DC link or alternatively a step-up transformer to accommodate the voltage level at AC side [100, 104].

2.4.1 AC Coupled Smoother

Fig. 2.10 illustrates the composition of the power electronic stage for the AC-coupled HSS-based PVG. The PV-VSI control loop aims at delivering the maximum attainable solar power into the utility grid, while the objective of the HSS-VSI control loop is to meet the smoothing expression defined by Eqs. (2.1)-(2.2). Meanwhile, for both VSIs the AC output current is required to be synchronised with the grid voltage with *zero* phase shift to ensure the unity power factor (PF) [105]. The two parallel bidirectional bulk-boost converters essentially provide bi-directional active power-flow that the smoothing process requires. Next

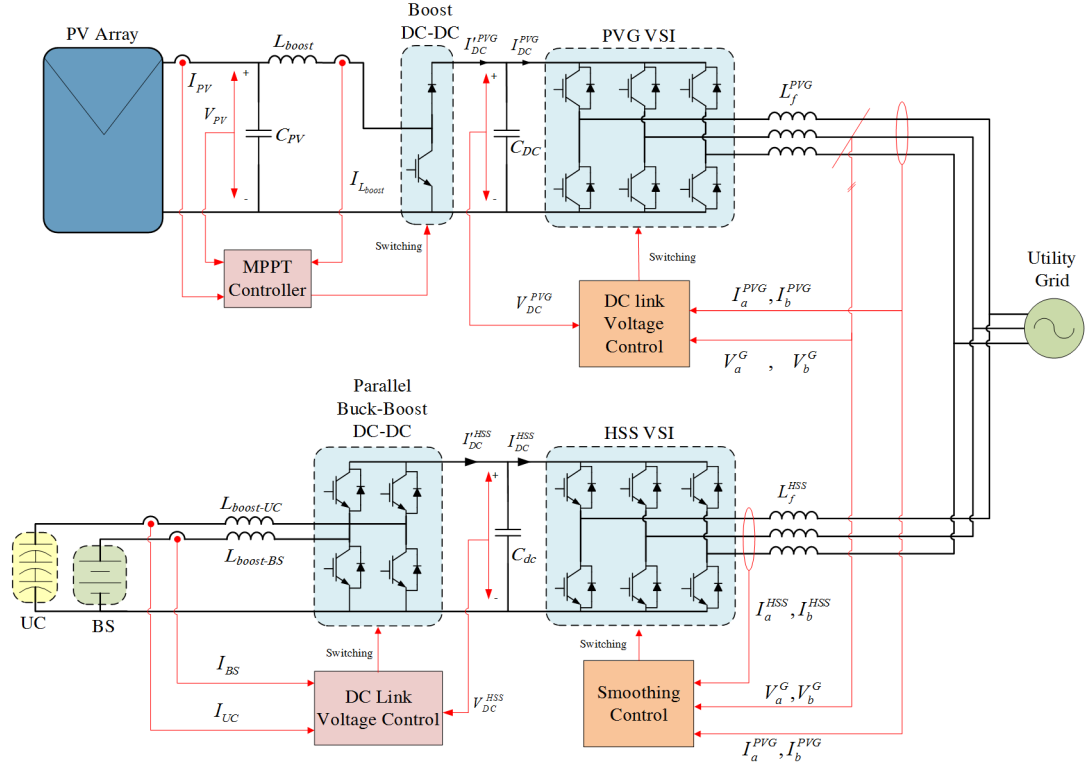


Figure 2.10: The diagram of the AC-coupled HSS-based PVG output smoothing.

parts move on to describe the control system arrangement in further detail.

Maximum Power Point Tracking Control (MPPT)

From a financial perspective, the operation of the PV array at the MPP should be guaranteed. In the two-stage structure of Fig. 2.10, where a DC-DC boost converter interfaces the PV array and the grid-connected VSI, this is the main function of the DC-DC boost converter to handle the MPPT control by manipulating the operation point of the PV array to capture P_{MPP} independent of DC link voltage. The boost converter essentially scales up the voltage of the PV array to an LV utility level at the DC link. Moreover, the inductor of the boost converter, L_{boost} , along with the capacitor C_{PV} behave as a low-pass filter which stabilises the current drawn from the PV array, I_{PV} . Among various MPPT algorithms have been proposed so far perturb and observe (P&O) is widely deployed for the majority of applications [106]. A basic control diagram of the MPPT to be performed by a boost converter is illustrated in Fig. 2.11. The MPPT algorithm determines the reference inductor current for the control loop of the boost converter which compensates the error by a PI regulator. The output of

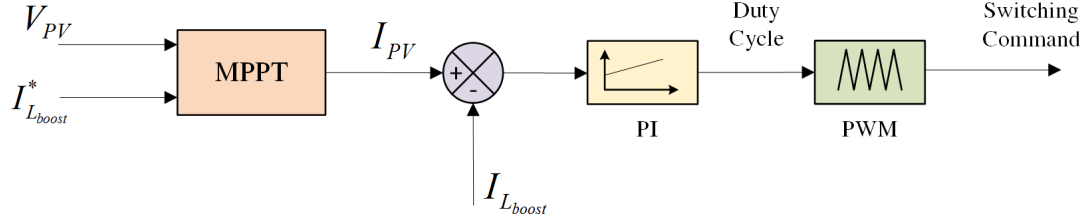


Figure 2.11: The diagram of the MPPT controller and the boost converter's control loop.

this control loop is the switching duty cycle which is converted into switching command using pulse width modulation (PWM). In the steady state condition the duty cycle D is adjusted so as to satisfy the input to output voltage ratio:

$$\frac{V_{DC}^{PVG}}{V_{PV}} = \frac{1}{1 - D} \quad (2.4)$$

where V_{DC}^{PVG} and V_{PV} are PV array voltage and DC link voltage of the PVG inverter, respectively.

Control of the Grid-Tied Voltage Source Inverters

In grid-connected PVG applications, the control method for the VSI is voltage oriented control (VOC) which deploys a grid voltage aligned rotating reference frame to convert three-phase AC parameters to DC parameters. This enables using ordinary PI compensators in the control loops as well as decoupled control of the active and reactive power export of the inverter. The controller is designed based on the principal circuit Eq. (2.5) which is derived from the equivalent circuit shown in Fig. 2.12.

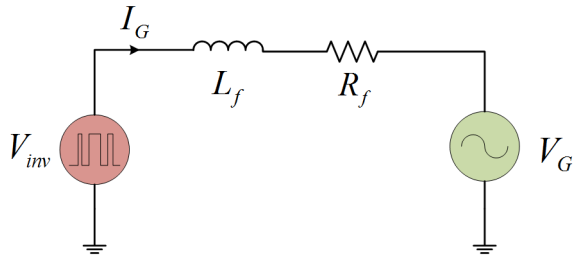


Figure 2.12: The single-phase equivalent circuit diagram of the grid-connected VSI.

$$V_{inv} = V_G + L_f \frac{d}{dt} I_G + R_f I_G \quad (2.5)$$

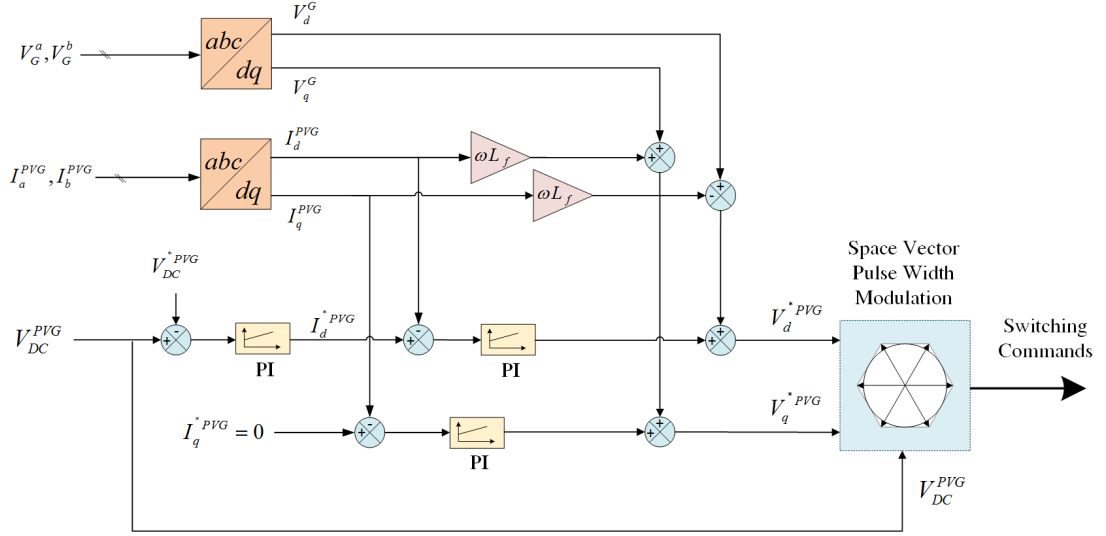


Figure 2.13: The control diagram of the grid-connected PVG inverter.

where V_G and V_{inv} are the utility grid and converter's output voltage, respectively. Moreover, R_f and L_f are resistive and inductive components of the output filter and I_G stands for the current injected into the grid. For the ease of calculations and processing the measurements for a three-phase balanced system a synchronously rotating reference frame is used hereafter [107]. Applying the dq transformation on Eq. (2.5) yields decomposed equations as:

$$V_d^{inv} = R_f I_d^G + L_f \frac{d}{dt} I_d^G - \omega L_f I_q^G + V_d^G \quad (2.6)$$

$$V_q^{inv} = R_f I_q^G + L_f \frac{d}{dt} I_q^G + \omega L_f I_d^G + V_q^G \quad (2.7)$$

where ω is the speed of the rotating reference frame which is synchronised with the grid voltage. Moreover, for each variable, the subscript d and q denote the corresponding direct and quadrature components in the reference frame, respectively. As the reference frame is in-line with the grid voltage vector we have:

$$V_q^G = 0 \quad (2.8)$$

Neglecting the converter's losses the active power equilibrium holds for the VSI. The active and reactive power export of the VSI in the rotating reference frame are:

$$P_{PVG} = V_{DC}^{PVG} I_{DC}^{PVG} = \frac{3}{2} (V_d^G I_d^{PVG} + V_q^G I_q^{PVG}) = \frac{3}{2} V_d^G I_d^{PVG} \quad (2.9)$$

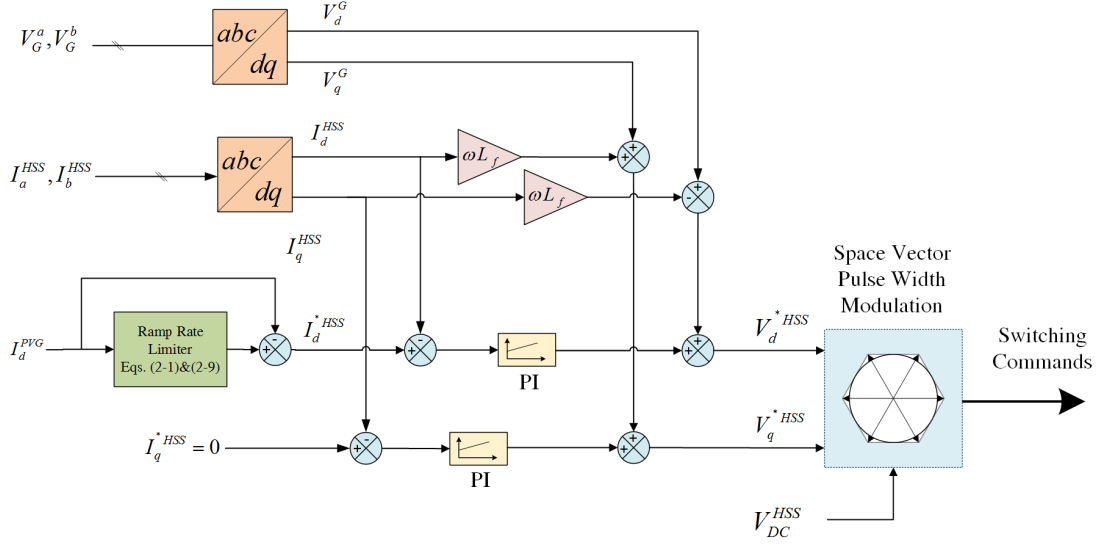


Figure 2.14: The control diagram of the grid-connected HSS VSI.

$$Q_{PVG} = \frac{3}{2}(V_d^G I_q^{PVG} - V_q^G I_d^{PVG}) = \frac{3}{2}V_d^G I_q^{PVG} \quad (2.10)$$

where V_{DC}^{PVG} and I_{DC}^{PVG} are the voltage and current at DC side of the VSI. Moreover, I_d^{PVG} , I_q^{PVG} are the PVG inverter current in dq reference frame.

Eq. (2.9) implies that the output active power can be controlled through I_d^{PVG} , as the grid voltage vector V_d^G is virtually constant. Moreover, the DC link voltage V_{DC}^{PVG} can be adjusted through active power control because:

$$C_{DC} \frac{d}{dt} V_{DC}^{PVG} = I_{DC}^{PVG} - I_{DC}'^{PVG} \quad (2.11)$$

where $I_{DC}'^{PVG}$ is the incoming DC current to the DC link. In a similar way I_q^{PVG} determines the reactive power export (Eq. (2.10)) which allows the power factor to be maintained at unity all the time as the reference quantity of I_q^{*PVG} is set to zero.

Given Eqs. (2.6)-(2.7), in order to provide an independent active/reactive power control (or alternatively I_d^{PVG} and I_q^{PVG}) compensating decoupling quantities of $\omega \cdot L_f \cdot I_d^{PVG}$ and $\omega \cdot L_f \cdot I_q^{PVG}$ are introduced to each control loop as feed-forward. In order to obtain ω the phase angle of the grid voltage is determined using a phase locked loop (PLL) controller. This is required for calculating decoupling feed-forward coefficients as well as for transferring the three-phase quantities into the rotating reference frame. Finally, the resulting reference values

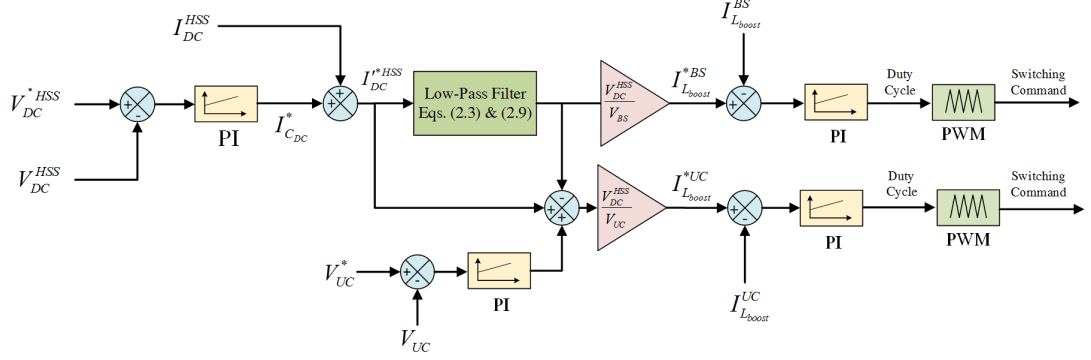


Figure 2.15: The control diagram of the bidirectional parallel DC-DC converters.

of the VSI output voltage along with the DC link voltage are incorporated to generate the gate control commands using the space vector pulse width modulation (SVPWM) technique [108]. The control system for the grid-tied PVG inverter is illustrated in Fig. 2.13. In the case of the other VSI which interfaces the HSS to the utility grid, the control system is rather different in terms of active power reference. Where the active power-flow is determined by the smoothing power reference as per Eq. 2.2. Given the constant ratio of exported power and direct component of the output current of the PVG inverter in steady state (Eq. (2.9)), the measurement value of I_d^G is used to generate smoothing reference current for HSS inverter, I_d^{*HSS} , and to prevent any reactive power contribution the quadrant component I_q^{*HSS} is set to *zero*. Fig. 2.14 illustrates the block diagram of the control system for the HSS inverter.

Control of the HSS DC-DC Converters

In the HSS system, the DC-DC converters deal with the charging and discharging process of the storage devices to meet the smoothing active power demand of the HSS inverter. As Fig. 2.15 illustrates, given a similar expression to Eq. (2.10) holds for the HSS inverter, the DC link voltage error is compensated using a PI regulator to obtain the reference value of incoming current I_{DC}^{*HSS} to the DC link capacitor. The high-frequency content of this reference current is supplied by the UC and the remainder is allocated to the BS. Finally, the error quantities of this input current components are regulated to obtain the duty cycle of the respective DC-DC converter. Then, the PWM technique is deployed to generate the switching commands for each leg of the H-bridge in a complementary manner. This enables bidirectional power-flow of the DC-DC converters for charge and discharge cycles.

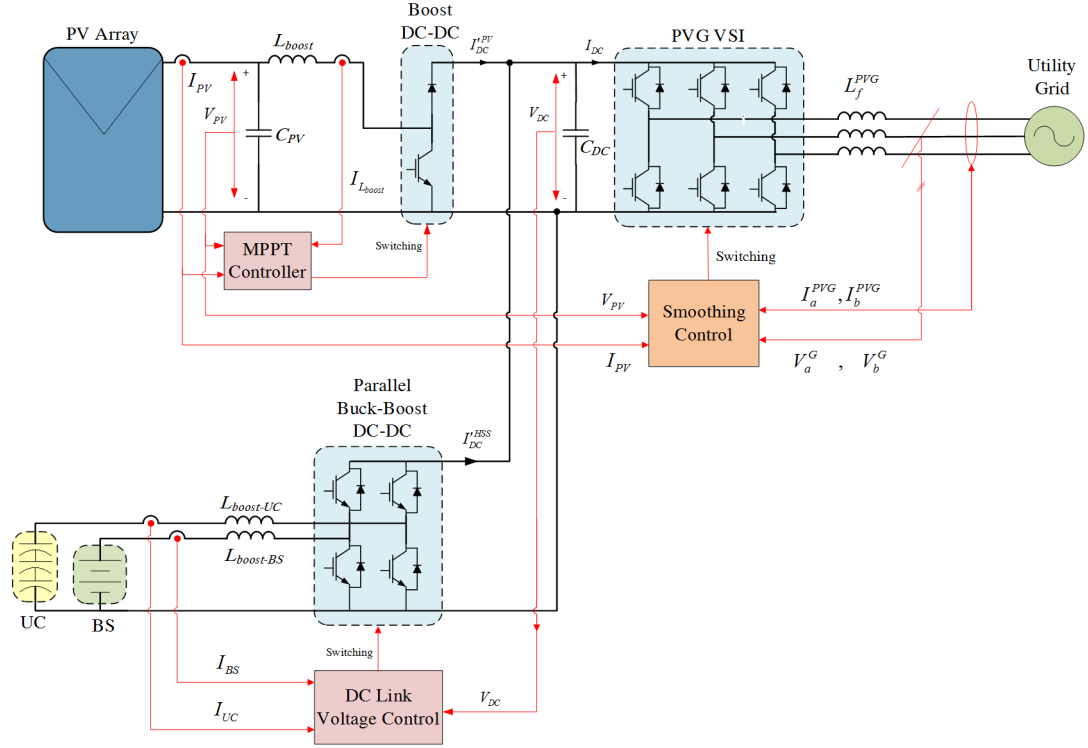


Figure 2.16: The diagram of the DC-coupled HSS-based PVG output smoothing.

2.4.2 DC-Coupled Smoother

In this section, the HSS-based PVG coupled at the DC side is described. As Fig. 2.16 shows and the term "DC-coupled" suggests, the HSS injects the smoothing power directly into the DC link of the PVG-VSI. The fundamentals of the control approach are essentially similar to the AC-coupled smoothing, while less power conversion is involved. The boost DC-DC converter fulfils MPPT operation of the PV array (Fig. 2.11) and the PVG-VSI is governed by Eq. (2.1) to ensure the smoothing requirement (Fig. 2.14). Therefore, the smoothing power during the sudden ramp-up/down in the P_{PV} is compensated by the HSS. This is achieved by regulating the DC link voltage as shown in the Fig. 2.15.

Compared to the AC-coupled smoother, in the DC-coupled smoother the P_{PV} is observed and regulated in the DC link before it is processed by the VSI. This makes the smoothing performance relatively more responsive and stable in short-term scale.

2.5 Simulation Results

In order to examine the performance of the designed control system as well as comparing the operation of the DC-coupled and AC-coupled smoother a simulation study is carried out in Matlab/Simulink. The specifications of the created simulation model are presented in Table. 2.1. Since the simulation intends to study dynamic operation of the controllers the time step is required to be as small as a fraction of the switching period of the converters, e.g. 50 [μsec], and a simulation duration up to 10 [sec] is usually sufficient. To include an entire ramp event in a realistic time scale, e.g. 10 [min], an extremely high calculation capability, as well as memory capacity, is required. Hence, a very steep smoothing RR is chosen so that a few ramp events could be observed within simulation time of few seconds. In the simulation study, a sudden PV power variation occurs at 1 [sec] where it declines from 16.25 [kW] to *zero*. After a no-export period, it recovers to the output power of 13 [kw] at 2 [sec].

AC-Coupled Smoother

In this structure, the PV-VSI delivers the P_{MPP} to the utility grid. Therefore, the sudden variations in the P_{PV} creates an immediate and corresponding change

Table 2.1: Parameters of the simulation model.

Parameter	Symbol	Value
Grid Line Voltage	V_G	380 [V]
Grid Frequency	f_G	50 [Hz]
Filter Inductance	L_f	10 [mH]
PVG DC Link Voltage	V_{DC}^{*PVG}	650 [V]
HSS DC Link Voltage	V_{DC}^{*HSS}	750 [V]
DC Link Capacitor	C_{DC}	470 [μF]
Boost Inductor	L_{boost}	5 [mH]
Battery Voltage	V_{BS}	450 [V]
Ultracapacitor Voltage	V_{UC}	450 [V]
Inverter Rated Power	P_{nom}	10 [kW]
Switching Frequency	f_{SW}	5 [kHz]
Permissible RR	R_S	35 [kW.sec ⁻¹]
Low-Pass Filter Time Constant	τ_f	50 [msec]

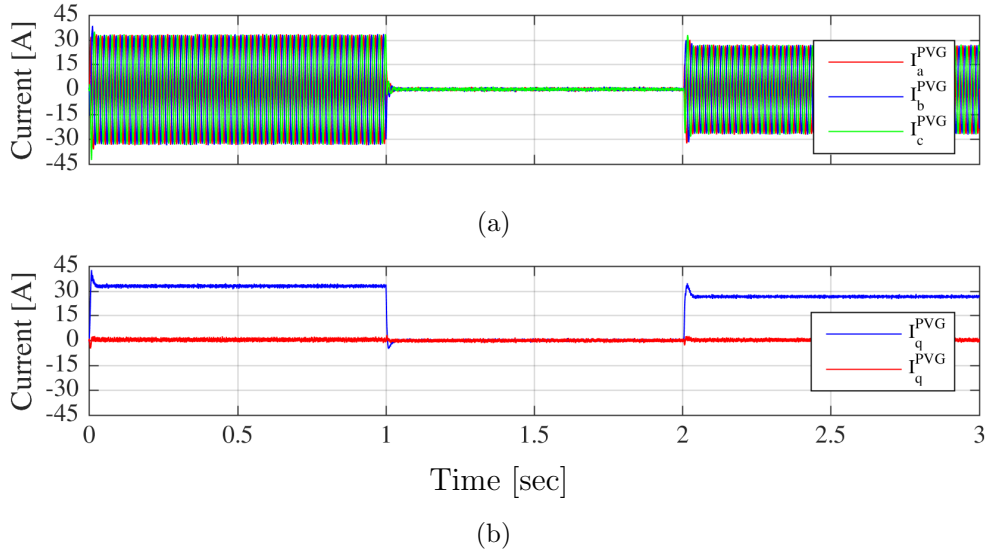


Figure 2.17: The output current of the PVG inverter; (a) three-phase values, and (b) in synchronous dq reference frame.

in the export of the PV-VSI. Fig. 2.17 illustrates the variations in the output current represented as three-phase quantities as well as dq equivalents. There is no reactive power exchange as the quadrant component of the output current I_q^{PVG} is always *zero*. The direct component I_d^{PVG} is proportional to the output active

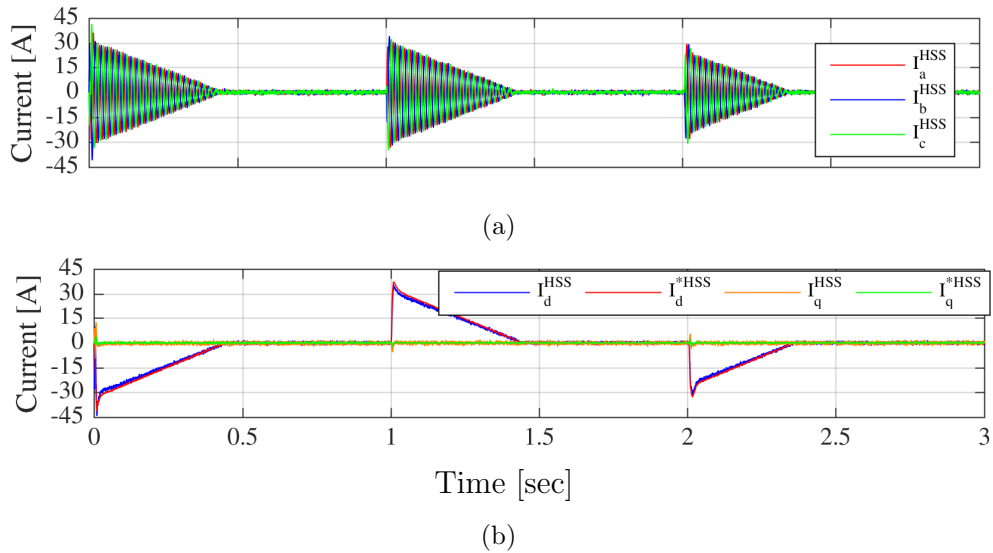


Figure 2.18: The smoothing current injected by the AC-coupled HSS inverter; (a) three-phase values, and (b) in synchronous dq reference frame.

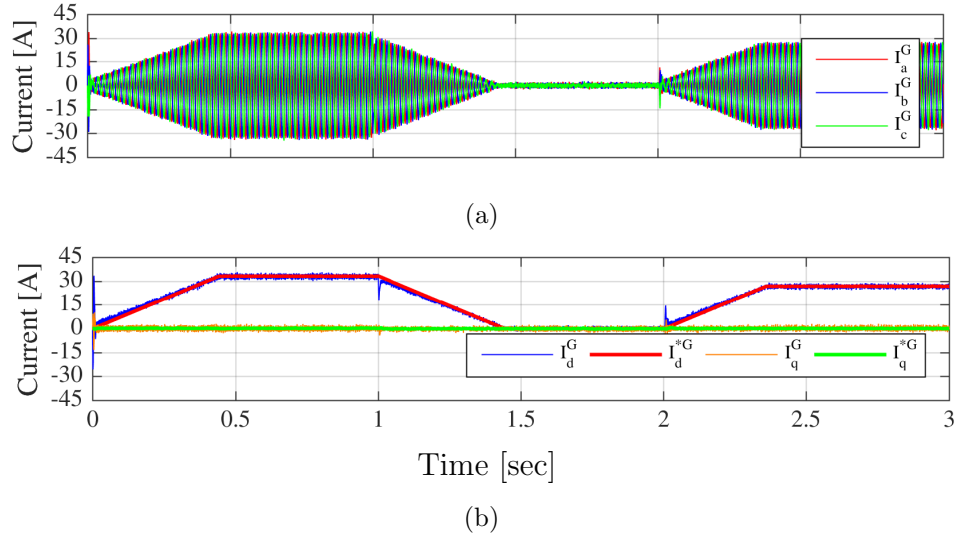


Figure 2.19: The regulated current delivered to the utility grid by AC-coupled smoother; (a) three-phase values, and (b) in synchronous dq reference frame.

power and as shown in Fig. 2.14, it is observed to identify the smoothing export of the HSS-VSI. Fig. 2.18 represents the smoothing currents, where the reference quantities are denoted with asterisk superscript (*). The close agreement between measured and reference quantities implies satisfactory behaviour of the closed-loop control system in transient circumstances as well as steady state.

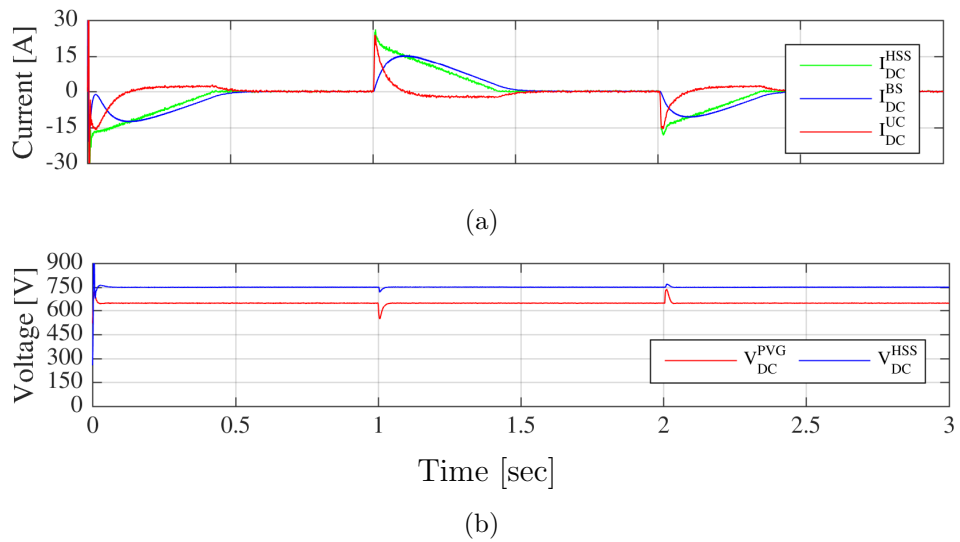


Figure 2.20: DC link voltage stabilisation in AC-coupled smoother, (a) the current injected by BS and UC in DC link of HSS, (b) DC link voltages for PVG and HSS VSIs.

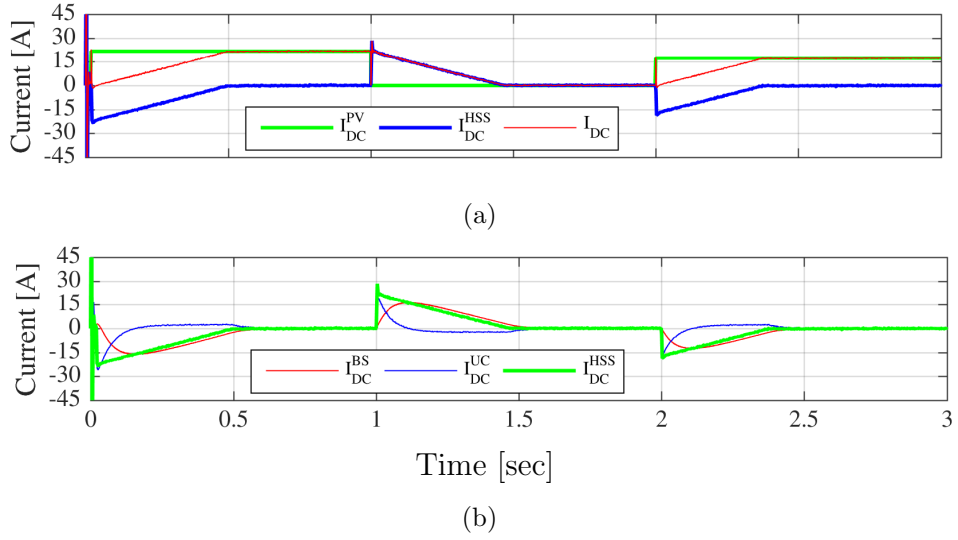


Figure 2.21: PVG smoothing process at DC side; (a) DC link currents, and (b) decomposed components of HSS current.

Fig. 2.19 depicts the injected currents into the utility grid which closely match the reference quantities so that RR of the output power variations is maintained within the acceptable limit. This highlights the performance of the smoothing controller (Eq. (2.1)) as well as the closed-loop controller of the HSS inverter (Fig. 2.15). The decomposition of the smoothing power at the DC link of the HSS inverter is illustrated in Fig. 2.20(a) where the UC supplies the sudden smoothing power demands and then phases out gradually as the contribution of the BS is increasing until it takes over the entire DC link current I_{DC}^{PVG} (Eq. (2.3)). This ensures the active power balance in the DC link of the HSS inverter and, consequently, the DC link voltage V_{DC}^{HSS} is maintained at the reference value of 750 [V] in Fig. 2.20(b).

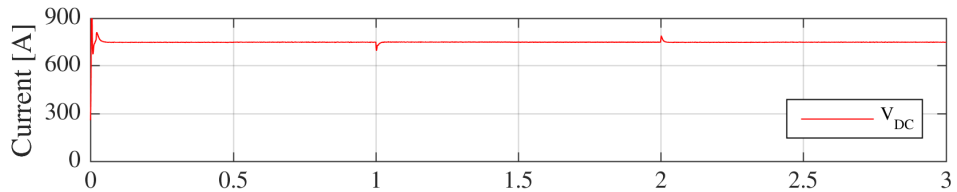


Figure 2.22: DC link voltage of the PVG-VSI with DC-coupled HSS during the smoothing process.

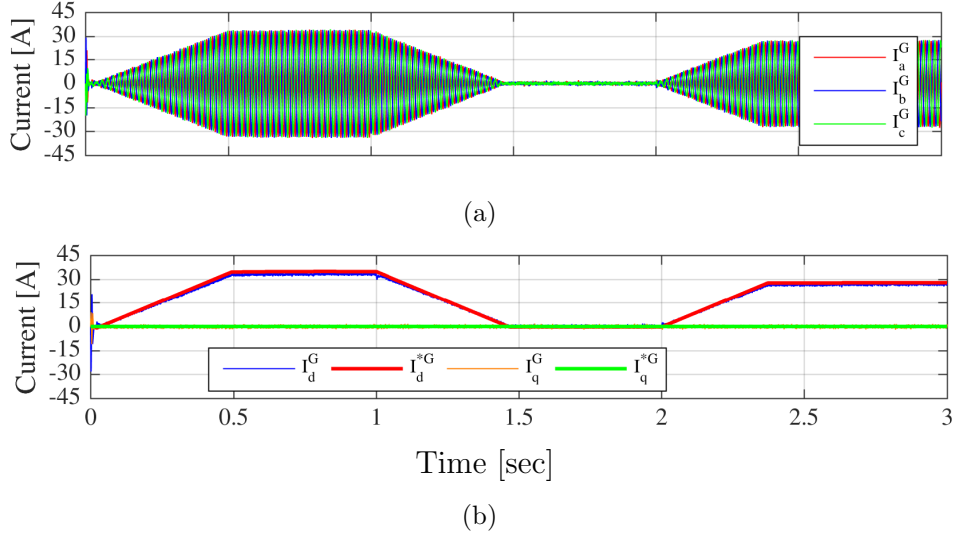


Figure 2.23: PVG output current for smoothing at DC side; (a) three-phase values, and (b) in synchronous dq reference frame.

DC-Coupled Smoother

In this configuration, as shown in Fig. 2.16, the boost converter conducts the MPPT and transfers the P_{MPP} into the DC link and the front-end VSI exports this power to the utility grid while the smoothing criteria are maintained (Eq. 2.1). The required smoothing power, P_{HSS} , is then determined by the imbalance between P_{PV} and P_G (Eq. (2.2)), which exhibits in the DC link voltage V_{DC} variations. Therefore, compensating the DC link voltage error defines the reference value of incoming smoothing current I_{DC}^{*HSS} to the DC link capacitor. As described earlier, Fig. 2.15 represents the control diagram of the HSS bidirectional DC-DC converters. Fig. 2.21 illustrates how the smoothing requirement is achieved at the DC link of the PVG-VSI by HSS meanwhile the DC link voltage is stabilised at the desired value of 750 [V] as shown in Fig. 2.22. The regulated output at AC side is shown in Fig. 2.23 which confirms the appropriate performance of this system.

Compared with the AC-coupled structure, the smoothing at the DC side tends to react relatively faster with fewer fluctuations at the grid side during the sharp transients. It is mainly due to the two additional power stages between the source of the variations in P_{PV} and the smoothing source P_{HSS} in the AC-coupled structure. As Fig. 2.10 suggests, the variations first appear in the DC link voltage of the PVG-VSI, which is then compensated by a corresponding change in the AC side current where it is observed by the smoothing controller. The HSS-VSI sup-

plies the smoothing current instantly. This creates a power imbalance between AC and DC sides of the HSS-VSI which reflects in the DC link voltage to be regulated by the bidirectional DC-DC converters that define the respective operation of BS and UC. Therefore, the AC-smoother reacts rather slower which results in some small over/under-shoots during the transients (compare Fig. 2.19(b) and Fig. 2.23(b) at 1[sec] and 2[sec]). On the other hand, as Fig. 2.16 shows, in the DC-coupled structure the PVG-VSI always fulfils the smoothing criteria so that any sudden variation in the solar generation creates a power imbalance in the DC link and immediately follows a corresponding change in the DC link voltage V_{DC} which will be compensated by the HSS. This enables a direct smoothing reaction right at the point it occurs. Therefore, the P_{PV} variations are treated before it is observed on the AC side. However, from a practical point of view, where the required ramp rate (RR) is normally 8-10% rated power per minute there is not any substantial distinction between the operation of the AC-coupled and the DC-coupled smoother. Therefore, the smoothing structure is technically decided based on the level of the rated power and locational constraints of the solar PVG unit. In low-power applications ranging 5-10[kW] the off-the-shelf hybrid PV inverters are suitable candidates for smoothing operation. Whereas, utility-scale PVG plants generally include multiple parallel PV inverters where the AC-coupled structure would be of much technical reliability and financial advantages.

2.6 Summary

In this chapter, various configurations of the grid-tied PV inverters are presented and investigated in order to point out a suitable option for incorporating an HSS. AC-coupled and DC-coupled smoother structures were modelled and simulated in MATLAB/Simulink to allow a comparative analysis on the performance of the smoother controller. Afterwards, the conventional RR controller is upgraded to decompose the required smoothing power and allocate the fast variations into the UC and the BS handles the less varying component of the smoothing power. Two parallel bidirectional DC-DC converters interfaced the storage systems into the DC link of the respective inverter. The control system included few local sections, i.e. grid-tied inverters inverter, and DC-DC converters of the HSS, which were coordinated by the smoothing RR control unit. VOC in rotating reference frame was deployed for the grid-connected inverters and the DC-DC

converters were under closed-loop control with PWM switching. The overall performance of the designed control system was verified through the simulation study where the sudden PVG output variations were smoothed out by the storage system. Meanwhile, the controller of the DC-DC converters split up the reference DC link current to be supplied by the BS and UC. The simulation results also implied that treating the power variations either at DC or AC side of the PVG inverter fulfils the smoothing requirements. While in the AC-coupled structure more power stages are involved which makes the smoothing controller slightly slower. This creates few small over/under-shoots during the transients which is not a substantial issue in practical terms.

Chapter 3

Cell Balancing Control in Battery Storage Systems

3.1 Introduction

Due to comparatively superior energy density, high cell voltage, low memory effect, and extended life cycle the Li-ion batteries are of a wide range of application, i.e. utility grid and electric vehicles. For the purpose of voltage elevation, the battery cells are stacked in large strings which arise a key issue of cell characteristic mismatch. It is mainly attributed to the manufacturing tolerances in the characteristics such as capacity, internal resistance, self-discharge rate, and thermal response of the cells, which diverge by the ageing. The temperature difference between cells widens this mismatch and exacerbates the SOC imbalance. This is mainly due to the ineffective ventilation and uneven heat dissipation in the battery packs. In particular, the thermal dependency of the electrochemical reactions involved in the battery operation follows the Arrhenius Law which suggests that the reaction rate doubles for each 10°[C] the temperature increases from 25°[C] , as a rule of thumb. More accurate coefficients of the Arrhenius formula could be derived empirically for each particular battery cell. Based on this formula, even among battery cells of similar characteristics those exposed to a higher temperature generally exhibit a higher rate of self-discharge and faster capacity degradation [109, 110]. Therefore, those cells with reduced capacity level usually experience an over-charge/discharge condition at the end of a charge/discharge cycle, unless the battery management system (BMS) is equipped with individual cell monitoring and terminates the charge/discharge cycle prior to any irreversible damage to the cells or an incidence of explosion, in the worst case scenario. This

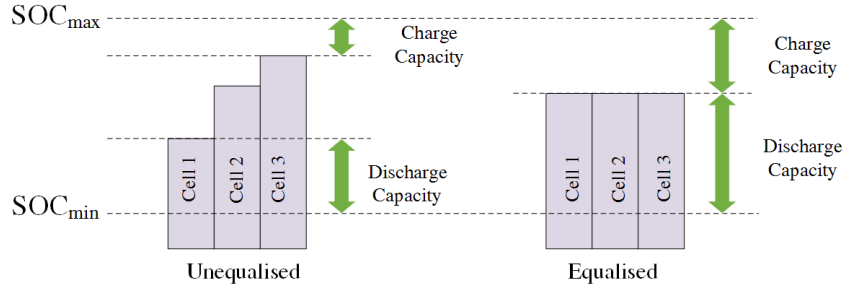


Figure 3.1: Effective utilisation of battery bank capacity by SOC equalisation.

could prevent full utilisation of the battery bank capacity; basically, the cells with extreme SOC level determine the charge/discharge capacity of the battery bank. Fig. 3.1 illustrates how cell equalisation expands the amount of charge a battery bank can deliver/absorb. Meanwhile, the destructive over-charge/over-discharge condition is prevented. Therefore, a charge balancing solution should be incorporated into the traditional BMS devices to ensure a safe and efficient utilisation of the entire capacity of the battery stack while any premature charge/discharge termination is avoided [62].

“In terms of energy recovery capability, the balancing approaches are categorised into two main groups: passive and active. The former primarily involves dissipating excess charge of the over-charged cells as heat through bleeding resistors until every single cell reaches the full charge point, concurrently” [68]. In the case of large SOC gap in a battery bank, the excessive balancing heat dissipation should be considered in ventilation design, as well. In spite of the charge cycle, during the discharge cycle, the passive approach fails to deal with imbalanced cells and the cycle might need to be stopped before all cells are fully discharged. Whereas, active balancing solutions manage the SOC mismatch by charge transit between cells and thus exhibit significantly higher efficiency. This is illustrated in Fig. 3.2 wherein the dissipated energy in passive approach is hatched in red. Moreover, the energy recovery in active balancing is shown from blue hatched area to the green. Different active balancing methods have been proposed so far. Those based on switched capacitor or inductor take advantage of the voltage imbalance between cells to enable an automatic charge exchange and achieve an even SOC distribution in the battery bank [63–73]. These approaches are primarily based on shuttling the charge between adjacent cells and suffer from relatively low charge transfer rate. In particular between those cells located faraway in the stack which are more prone to charge imbalance due to the

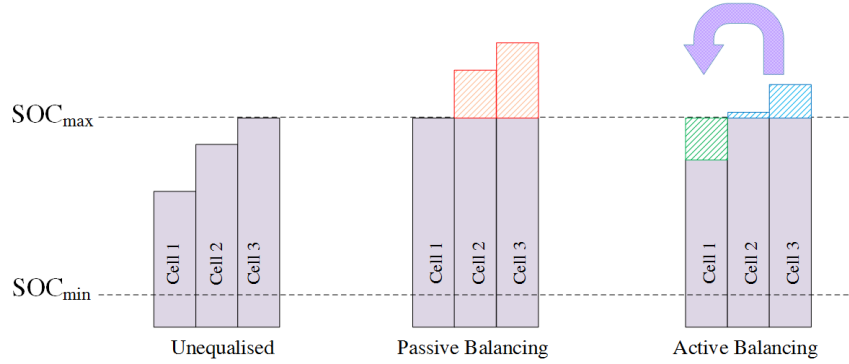


Figure 3.2: Comparison on energy efficiency of the two categories of balancing approaches; passive and active.

gradient of ambient temperature. Reference [70] has examined two solutions to this issue including the double tier structure as well as chain configuration which both over-performed the conventional switched capacitor configuration. Cassani et.al. have presented a switched inductor configuration where the balancing current of each cell is decided by regulating the corresponding voltage error with respect to the adjacent cells in the stack. This has been shown to improve the equalising performance in terms of balancing time and stability [64]. Furthermore, the double tiered switched capacitor cell balancer is studied in [72] which concluded despite the improved sensitivity toward variation in the parameters of this technique, it is still susceptible to increasing the capacitance. Ewanchuk et.al. in [63] have proposed a modular charge balancing structure which equalises the charge inside two-cell modules with a multi-winding transformer based DC-DC converter. The adjacent modules are coupled through extra windings of the respective transformers which provide an inter-module equalising as well. The balancing is accomplished automatically by a PWM switching with 50% duty cycle and the voltage sensing facility is no longer required. The charge routing process in these methods is highly reliant on cell-to-cell voltage difference which causes the voltages converge rather slowly. Furthermore, solid-state switches exhibit a forward voltage drop which creates a lasting voltage gap between cells. Hence, a switched capacitors based approach with quasi-resonance zero-current switching has been proposed utilising metal-oxide-semiconductor field-effect transistor (MOSFET) switches instead of diodes to achieve zero voltage gap in an extremely high efficiency [73].

By means of bidirectional DC-DC converters, a more effective active cell balancing approach could be achieved which offers more flexible charge transfer be-

tween cells. In particular, a transformer component creates a galvanic isolation which enables various balancing scenarios, such as charge exchange between each cell and the entire battery stack or any arbitrary smaller set of series cells [74–77]. A multiphase interleaved active cell balancing structure has been investigated in [76]. Where each phase consists of a buck-boost converter assigned to a specific battery cell to facilitate charge transfer between the respective subset, including the cell itself through the bottommost one, and the whole battery stack. This structure effectively performs a normal cell balancing without any voltage or current sensing providing a predefined duty cycle is adopted for each phase. The forced balancing is also feasible if inductor currents are regulated by the duty cycle of each phase. Moreover, it is proposed to use two inductors for each phase one is coupled with those of adjacent phases in top and bottom, respectively. Therefore, the DC component of the flux in inductors will be compensated and the magnetic cores could be reduced in dimensions. Einhorn *et al.* have surveyed a flyback based active cell balancing using one multi-winding transformer that provides a charge exchange between every single cell and the whole stack. Different balancing scenarios have been examined, i.e. voltage, and capacity equalisation. In the case of unequal cells in capacity and initial SOC the voltage based balancing tends to cause unnecessary charge exchange and prolonged equalising time. Whereas, estimating the cells' capacity and only discharging those with the lowest capacity ensures a faster and more efficient equalising [77]. This structure is of utmost balancing control flexibility at the cost of higher voltage rating of the power electronic switches, since it deals with the entire battery stack at HV side of the converts. However, the interleaved arrangement of the transformers across the sub-stacks proportionally reduces the voltage stress on the power electronic components while the balancing effectiveness is slightly sacrificed and a more sophisticated control technique is required.

This chapter introduces a control method for the bidirectional flyback active cell balancer with interleaved connection of the transformers. An active balancer system is modelled and the performance of this approach is investigated through a simulation study. In order to provide a more conclusive benchmark, the ordinary passive balancer approach is also simulated to evaluate the performance of the proposed active balancer method in terms of energy efficiency.

3.2 Active Cell Balancer

Several types of flyback based active cell balancing modules designated for a wide range of applications which are currently available in the market [111,112]. In order to provide a reliable SOC equalising operation, the balancer modules perform the gate drives, accurate current sensing, and required fault detections. Hence, a similar topology is investigated herein and the governing equations are obtained. Fig. 3.3 demonstrates a typical interleaved flyback active balancer configuration. The cells are divided into subsets of S cells where the HV side of the transformers are paralleled across a sub-stack, which consists of the subset itself and the one just above that. This structure facilitates the charge exchange between adjacent subsets which is a key factor to achieve the fully equalised SOC throughout the entire stack. This stackable structure is repeated for the whole series connected battery bank of N cells [112]. As an exception in the control algorithm, the topmost subset is regarded as the last sub-stack. The flybacks operate in discontinuous conduction mode (DCM) by peak current sensing at LV and HV sides of the transformers (I_{LV}^P and I_{HV}^P). The circuit diagram of the flyback converter is illustrated in Fig. 3.4(a). In each cycle of discharge operation mode, once LV side current I_{LV} hits *zero* the SW_{LV} turns on (at t_0 and t_2) and the off-time t_1 is detected as I_{LV} reaches I_{LV}^P . Likewise, during the charge operation mode, SW_{HV} starts conduction as I_{HV} drops to *zero* (at t_3 and t_5) and it is switched off as soon as I_{HV} hits I_{HV}^P (at t_4). The current waveforms of the flyback are shown in Fig. 3.4(b) and Eqs. (3.1)-(3.4) determine the mean current values in different operation modes [112]:

$$\bar{I}_{LV}^C = -\frac{I_{HV}^P}{2} \left(\frac{V_{HV} \cdot T}{V_{HV} + V_{LV} \cdot T} \right) \eta^C \quad (3.1)$$

$$\bar{I}_{HV}^C = \frac{I_{HV}^P}{2} \left(\frac{V_{LV} \cdot T}{V_{HV} + V_{LV} \cdot T} \right) \quad (3.2)$$

$$\bar{I}_{LV}^D = \frac{I_{LV}^P}{2} \left(\frac{V_{HV}}{V_{HV} + V_{LV} \cdot T} \right) \quad (3.3)$$

$$\bar{I}_{HV}^D = -\frac{I_{LV}^P}{2} \left(\frac{V_{LV}}{V_{HV} + V_{LV} \cdot T} \right) \eta^D \quad (3.4)$$

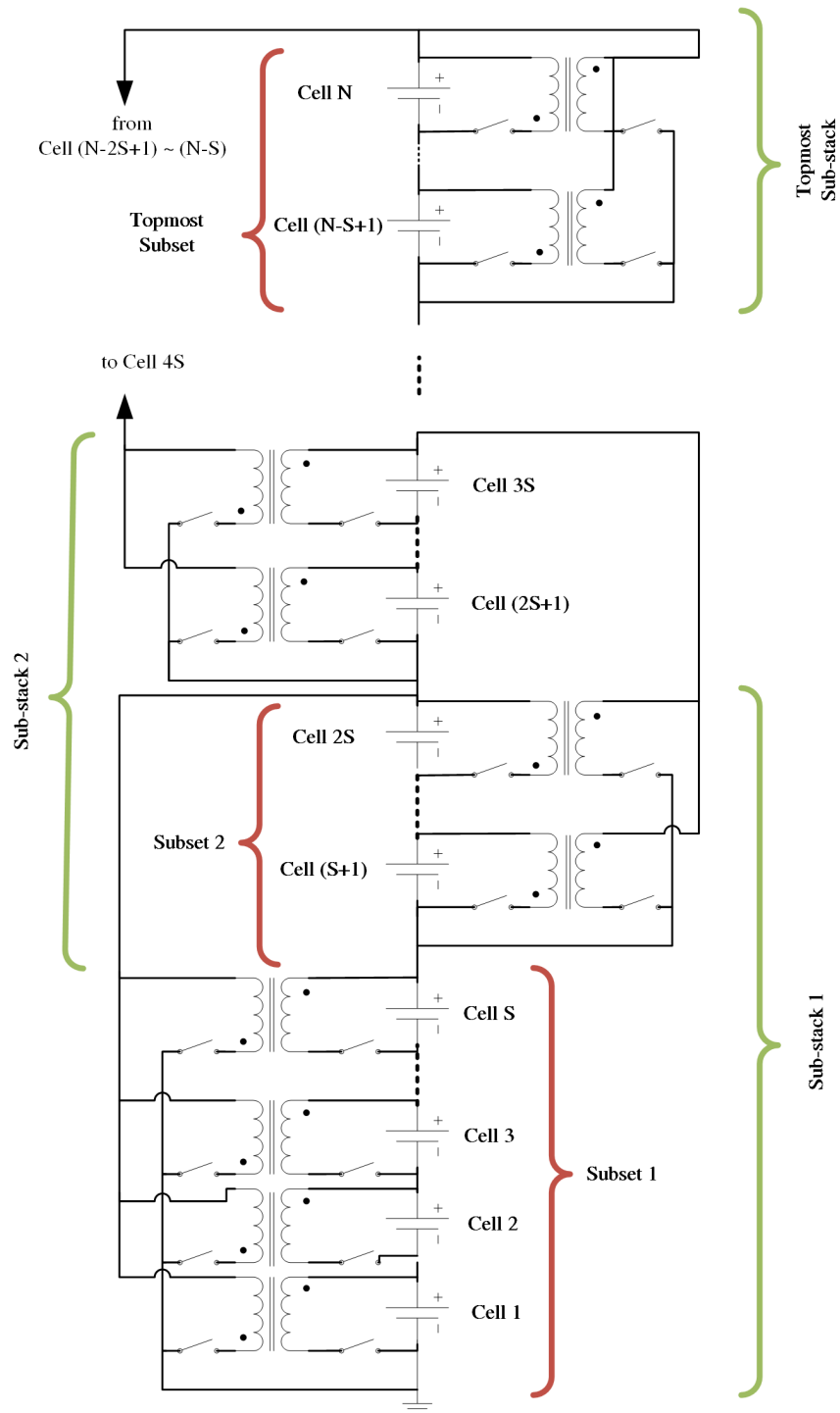


Figure 3.3: The interleaved structure of flyback active cell balancer [112].

where \bar{I}_{LV}^C , \bar{I}_{LV}^D , \bar{I}_{HV}^C , and \bar{I}_{HV}^D denote the mean currents during discharge and charge operation of the flyback, at LV and HV side, respectively. V_{LV} and V_{HV} are the voltage across the LV and HV side of the converter, respectively. Moreover,

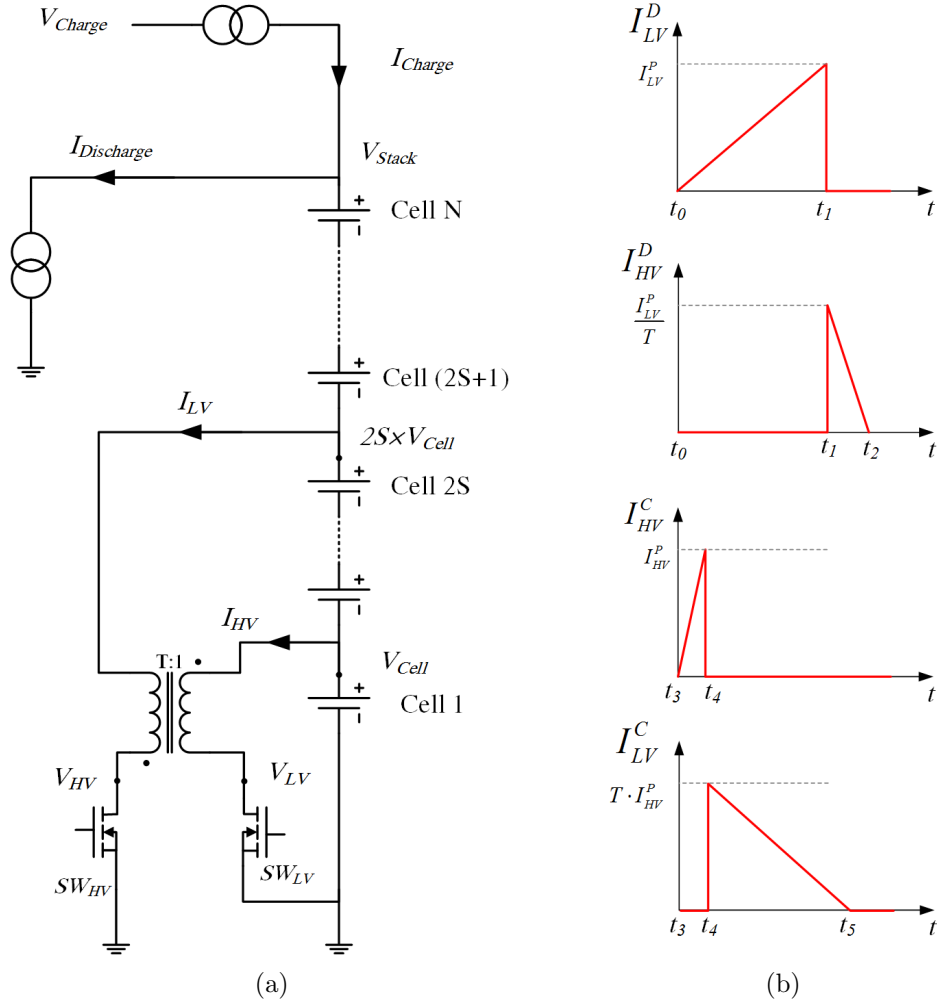


Figure 3.4: (a) flyback converter topology, and (b) waveforms of transformer currents during charge and discharge operation [112].

T , η^C , and η^D stand for transformers' turn ratio, and flyback efficiency in charge and discharge modes, respectively. For the purpose of further simplification it is assumed that all cells are in equal voltage of V_{cell} which yields:

$$V_{LV} = V_{cell} \quad \text{and} \quad V_{HV} = S \cdot V_{cell} \quad (3.5)$$

where S is the cell count of the subset. Substitution of relations (3.5) into Eqs. (3.1)-(3.4) the simplified equations are obtained:

$$\bar{I}_{LV}^C = -\frac{I_{HV}^P}{2} \left(\frac{S \cdot T}{S + T} \right) \eta^C \quad (3.6)$$

$$\bar{I}_{HV}^C = \frac{I_{HV}^P}{2} \left(\frac{T}{S + T} \right) \quad (3.7)$$

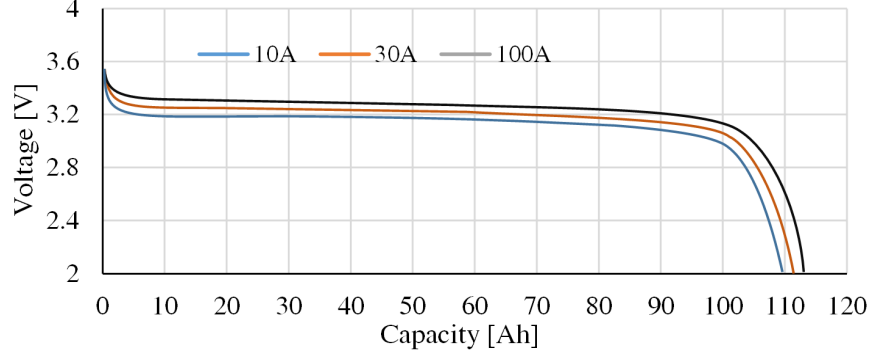


Figure 3.5: The discharge curve of a 100 [Ah] Li-FePO₄ cell under various discharge currents.

$$\bar{I}_{LV}^D = \frac{I_{LV}^P}{2} \left(\frac{S}{S+T} \right) \quad (3.8)$$

$$\bar{I}_{HV}^D = -\frac{I_{LV}^P}{2} \left(\frac{1}{S+T} \right) \eta^D \quad (3.9)$$

In the following section, we move on to the control approach for the flyback active cell balancer based on the operation principle explained here.

3.2.1 Active Cell Balancing Algorithm

The main objective of the balancing control is to keep the SOC mismatch between all series connected cells within acceptable bounds over the charge as well as the discharge cycle. Consequently, the run time of the battery bank will be extended by preventing any premature termination of the charge/discharge cycle before the stack is fully charged/discharged [68]. This requires that the SOC of all cells are monitored and compared so that the outlying values can be identified to be equalised. In extreme charge conditions, the Li-Ion cells exhibit a quadratic SOC versus voltage characteristic. This implies that at the end of charge or discharge cycle the voltage difference between the cells could distinctly indicate the SOC mismatch. Fig. 3.5 shows the characteristic curves of a Li-FePO₄ battery cell. For the purpose of identifying the outlier cells in SOC a three-level hysteresis voltage interpreter is deployed as shown in Fig. 3.6. Where V_C and V_D represent the maximum and minimum allowable V_{cell} , respectively. While V_C^B and V_D^B are the associated hysteresis bands. $OC(k)$, $NC(k)$, and $OD(k)$

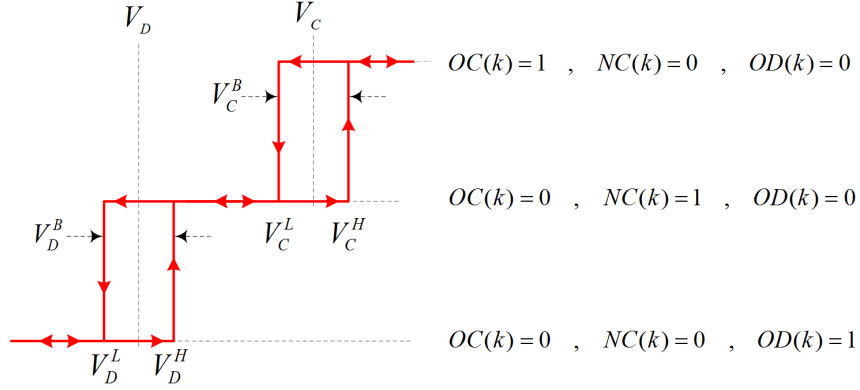


Figure 3.6: Three-level hysteresis cell voltage interpreter [68].

exclusively indicate the k^{th} cells charge status, i.e. *over – charge*, *normal*, and *over – discharge* states, respectively. Once the unbalanced cells are indicated the charge equalising process is initiated. The balancing algorithm manipulates bidirectional charge transfer between each cell and the corresponding sub-stack by operating the flyback converters. “Considering the charge and discharge mode of a flyback converter in the n^{th} subset, the total power in HV and LV side of all flybacks could be obtained by the following summations” [68]:

$$P_{LV}^n = \left(\sum_{k=S \times (n-1)+1}^{S \times (n+1)} V_k \right) \times \sum_{k=S \times (n-1)+1}^{S \times n} (D_k \cdot I_{HV}^D + C_k \cdot I_{HV}^C) \quad (3.10)$$

$$P_{HV}^n = \sum_{k=S \times (n-1)+1}^{S \times n} [(D_k \cdot I_{LV}^D + C_k \cdot I_{LV}^C) \times V_k] \quad (3.11)$$

where V_k stands for the k^{th} cell voltage, and C_k and D_k are exclusively assigned a value of *one* corresponding to the *charge* and *discharge* operation of the k^{th} flyback, respectively. Given the interleaved connection at the HV side of the flybacks, Eqs. (3.12)-(3.13) explain how the energy is divided in the n^{th} subset

[68].

$$\begin{aligned}
P_{HV}^{n \rightarrow n} &= P_{HV}^n \times \frac{\left(\sum_{k=S(n-1)+1}^{S \times n} V_k \right)}{\left(\sum_{k=S(n-1)+1}^{S(n+1)} V_k \right)} \\
&= \left(\sum_{k=S(n-1)+1}^{S \times n} V_k \right) \times \sum_{k=S(n-1)+1}^{S \times n} (D_k \cdot I_{HV}^D + C_k \cdot I_{HV}^C) \quad (3.12)
\end{aligned}$$

$$\begin{aligned}
P_{HV}^{n \rightarrow (n+1)} &= P_{HV}^n \times \frac{\left(\sum_{k=S \times n+1}^{S(n+1)} V_k \right)}{\left(\sum_{k=S(n-1)+1}^{S(n+1)} V_k \right)} \\
&= \left(\sum_{k=S \times n+1}^{S(n+1)} V_k \right) \times \sum_{k=S(n-1)+1}^{S \times n} (D_k \cdot I_{HV}^D + C_k \cdot I_{HV}^C) \quad (3.13)
\end{aligned}$$

where $P_{HV}^{n \rightarrow n}$ and $P_{HV}^{n \rightarrow (n+1)}$ are transferred power from the HV side of flybacks in n^{th} subset which returns to n^{th} subset itself, and $(n+1)^{th}$ subset, respectively. The $P_{HV}^{n \rightarrow (n+1)}$ signifies the energy transfer between two adjacent subsets and its notation is contracted as $P^{n \rightarrow (n+1)}$ hereafter. The relation (3.13) could be simplified assuming all cell are of the equal voltage of V_{cell} and inserting Eqs. (3.1)-(3.4) [68]:

$$P^{n \rightarrow (n+1)} = \left(\frac{S \cdot V_{cell}}{S + T} \right) \sum_{k=S(n-1)+1}^{S \times n} \left(C_k \cdot T \cdot \frac{I_{HV}^P}{4} - D_k \cdot \frac{I_{LV}^P}{4} \cdot \eta^D \right) \quad (3.14)$$

which indicates that discharging a cell in the n^{th} subset leads to a negative $P^{n \rightarrow (n+1)}$. This implies charge transfer from n^{th} to $(n+1)^{th}$ subset and likewise charge will move in a reverse direction from $(n+1)^{th}$ to n^{th} subset as a cell is charged in n^{th} subset. This phenomenon is shown in Fig. 3.7 by the way of illustration. The relative charge status of a cell with respect to the associated subset is a fair indication of the required equalising intra-subset charge routing. “Hence, over-charged (OC) and over-discharged (OD) indexes (OCI and ODI) are defined for n^{th} subset as below” [68]:

$$\left\{ \begin{array}{l} OCI(n) = \sum_{k=S(n-1)+1}^{S \cdot n} OC(k) \\ ODI(n) = \sum_{k=S(n-1)+1}^{S \cdot n} OD(k) \end{array} \right. \quad (3.15)$$

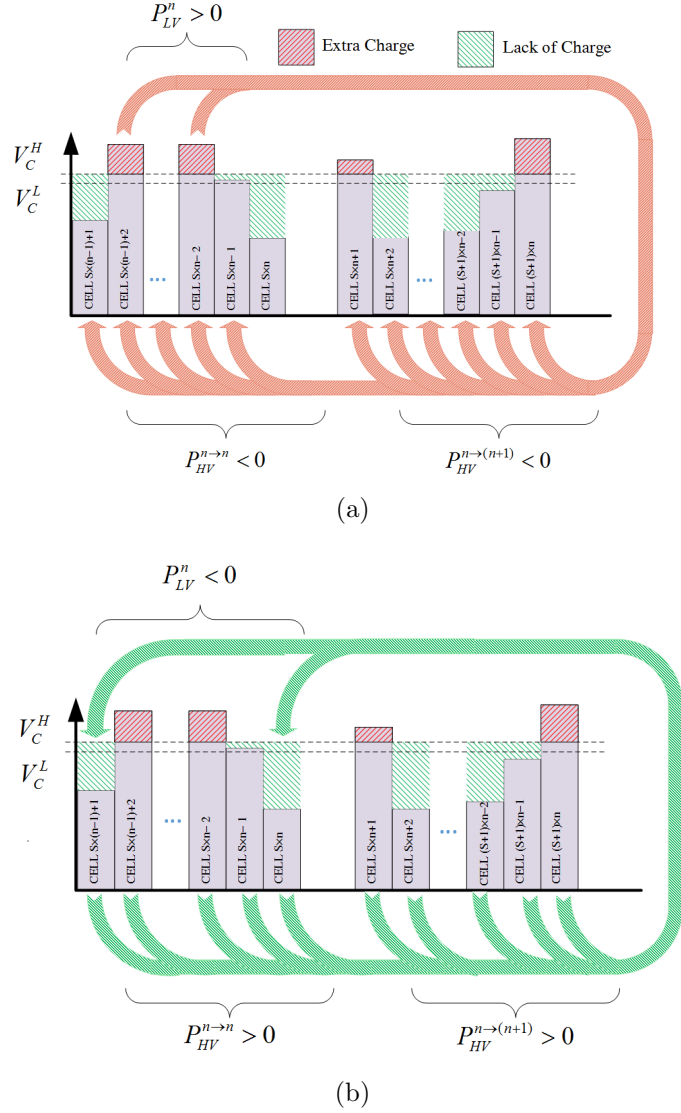


Figure 3.7: The diagram of energy transfer between adjacent subsets, (a) when over-charged cells are being discharged, and (b) non-over-charged cells are being charged [68].

In the following, a three-stage balancing method is discussed which examines charge status of the cells, and the *OCI* and *ODI* of the subsets to determine the appropriate operation mode of the flybacks [68].

Stage-I: Inter-Subset Equalisation of OC/OD Cells

To mitigate the irreversible damages to battery cells as well as hazardous situations attributed to excessive undue SOC, addressing the OC/OD cells are the main priority in the balancing procedure. Meanwhile, the inter-subset charge exchange for each subset is decided based on its relative *OCI/ODI* to the subsets

just above that [68].

Charge Cycle: During the charge cycle the algorithm deals with OC status of the cells and OCI of the subsets. If the subset is of greater OCI than the subset just above that, $OCI(n) > OCI(n + 1)$, the OC cells of that subset need to be discharged. By contrast, the non-OC cells have to be charged, if $OCI(n) < OCI(n + 1)$. As soon as the subsets are equal in OCI the mean voltage of the subsets is considered, alternatively. Ultimately, in the case of concurrent non-zero and equal OCI , as well as mean voltage gap within the hysteresis band of δ_S the non-OC cells are charged to facilitate the equalisation [68].

Discharge Cycle: During the discharge cycle the OD status of the cells and the ODI of the subsets are targeted. The OD cells of that subset need to be charged if the subset has a greater ODI compared with the one above that ($ODI(n) > ODI(n + 1)$). Whereas, if $ODI(n) < ODI(n + 1)$ the non-OD cells have to be discharged. When the subset is equal to the one above that in ODI their mean voltages are compared, alternatively. Finally, in the case of concurrent non-zero and equal ODI , as well as mean voltage gap within the hysteresis band of δ_S the non-OD cells are discharged to facilitate the equalisation [68].

Stage-II: Inter-Subsets Equalisation of Mean Voltage

This stage starts when there is no OC or OD cell in the associated sub-stack. This means that the subset and the one above that are of *zero* value of ODI or OCI . Therefore, the inter-subset equalisation is determined the associated mean voltages. If the subset is lower in mean voltage compared with the subset just above ($\bar{V}(n) - \bar{V}(n + 1) < \delta_S$) a negative inter-subset charge exchange is adopted ($P^{n \rightarrow (n+1)} < 0$) and all cells in the subset need to be charged. In contrast, if the subset is higher in mean voltage compared with the subset just above ($\bar{V}(n) - \bar{V}(n + 1) > \delta_C$) a positive inter-subset charge exchange is adopted ($P^{n \rightarrow (n+1)} > 0$) which requires all cells in the subset are discharged. This stage continues until absolute mismatch of subset mean voltages converge within a specific hysteresis band ($|\bar{V}(n) - \bar{V}(n + 1)| < \delta_S$) [68].

Stage-III: Intra-Subset Cell Voltages Equalisation

A more rigorous intra-subset cell voltage balancing is initiated once the subset gets into equalised state relative to the upper subset. This is identified by equal *OCI* or *ODI*, and the difference in the subset mean voltages is bounded within the hysteresis band of δ_S . During the intra-subset cell voltage balancing the inter-subset charge exchange is kept minimum. The state of the intra-subset charge balance is defined by the highest cell voltage gap inside the subset. Therefore, based on the voltages the cells are sorted in an ascending order and the upper half are discharged while the rest are charged. “This stage continues, as long as the maximum cell voltage difference in the subset is out of the respective hysteresis band ($|V^{max}(n) - V^{min}(n)| > \delta_C$)” [68].

Equalisation of the Topmost Subset

The different connection of HV side of the transformers in the topmost subset only allows intra-subset energy exchange ($P^{n \rightarrow (n+1)} = 0$). Therefore, an effective balancing control could be adopted in a relatively simpler way:

Charge Cycle: During the charge cycle the OC are discharged and the non-OC ones are charged.

Discharge Cycle: During the discharge cycle the OD cells are charged and the non-OD ones are discharged.

Furthermore, if all cells are in *NC* state, the intra-subset cell voltage equalisation (section 3.2.1) is deployed to achieve a higher degree of balancing [68].

Battery Stack Charge/Discharge Control

the effective performance of the balancer requires an operating current greater than the battery stack charge/discharge current (I_{charge} and $I_{discharge}$ in Fig. 3.4). On the other hand, using power electronic converters rated at the charge/discharge current is not feasible in practice due to the system volume and cost constraints. Alternatively, upon the start of the balancing operation, the BMS reduces the charger current I_{charge} to $I_{balancing}$ which is a value close to the mean current of flybacks. Moreover, the control of discharge current $I_{discharge}$ is not practically feasible. Therefore, in a similar way during the discharge cycle, the BMS disconnects the load as soon as the first over-discharged cell is detected. Upon completion of the equalisation, the battery stack could continue with supplying

the load until it reaches the maximum depth of discharge (DOD) limit. The BMS also monitors mean cell voltage of the entire stack V_{mean} and compare that with V_C and V_D to decide the termination of the charge and discharge cycle, respectively [68].

Fig. 3.8 illustrates the flowchart of the proposed balancing algorithm for n^{th} subset during charge and discharge cycles. This algorithm is repeated for every subset to determine the operation mode of the respective flyback converters.

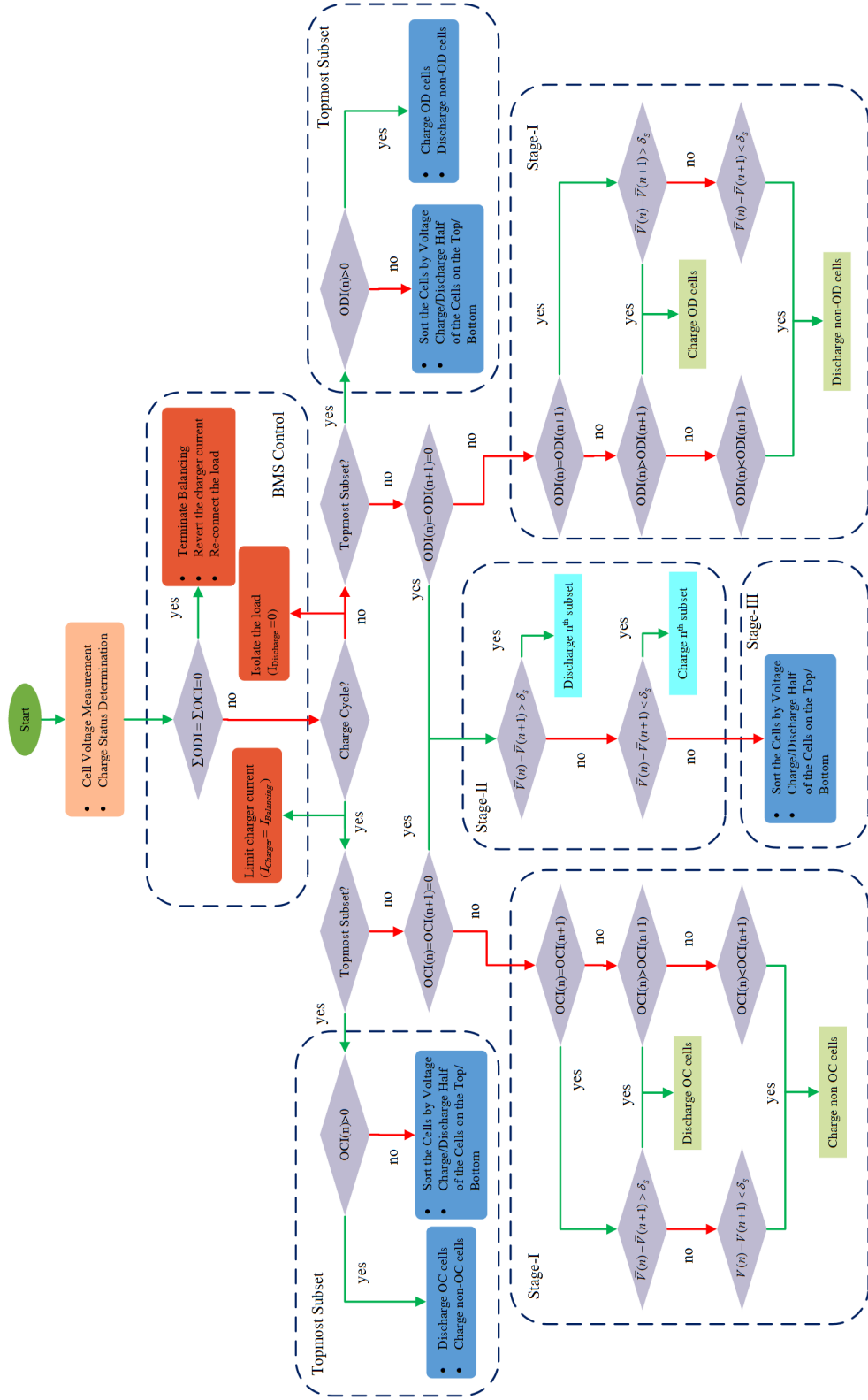


Figure 3.8: Flowchart of the proposed balancing algorithm for n^{th} subset.

3.2.2 Active Cell Balancing Simulation and Analysis

This section analyses the performance of the proposed balancing algorithm and then validates its functionality through a series of simulation studies in Matlab/Simulink. The simulation model is composed of a 24-cell stack of 100 [Ah] Li-FePO₄ batteries. The characteristic curve of the battery cells is shown in Fig. 3.5. In order to investigate how the arrangement of the subsets affects the balancing operation three different configurations are considered:

Case-I: *four* subsets of *six* cells (4×6).

Case-II: *three* subsets of *eight* cells (3×8).

Case-III: Asymmetric structure consisting subsets of *six*, *four*, *eight*, and *six* cells.

The following subsection looks into the modelling of the flyback converters and the structure of the balancer for the purpose of the simulation studies.

flyback Converters Modeling

The simulation study of the flyback active cell balancer deals with multiple identical DC-DC converters which their operation needed to be observed over a sample balancing operation. In comparison with the switching frequency of the DC-DC converters, the balancing process takes exceedingly longer time. Therefore, to prevent excessive computation burden the flyback converters are modelled as controlled DC current sources at LV side and similarly, parallel HV windings are aggregated and modelled as a single DC current source. The associated current quantities at HV and LV side of the flyback converters have to be calculated using Eqs. (3.1)-(3.4) while vector quantities are deployed instead of scalars. For the purpose of improving the precision of the simulation model, the simplifying assumption of equal cell voltages is not considered in the modelled stage in spite of the design process of the balancer algorithm. Therefore, the arrangement of the interleaved structure determines the actual HV side voltage of the converters. For this purpose, a linkage matrix A is defined to indicate which cells are included in the HV side of the flyback converter respective to each battery cell. Where the value of the element in the i^{th} row and j^{th} column, $a_{i,j}$, is determined as:

$$a_{i,j} = \begin{cases} 0 & \text{if } j^{th} \text{ cell is included in the HV side of } i^{th} \text{ flyback,} \\ 1 & \text{otherwise.} \end{cases} \quad (3.16)$$

The linkage matrix for the three different configurations is given in Appendix-A. Therefore the proposed unified model can emulate different HV side structures only by displacing the respective linkage matrix while it offers the superior simplicity of vector calculation as well.

The LV and HV voltage vector of the flybacks are obtained as below:

$$\vec{V}_{LV} = \vec{V}_{cell} \quad (3.17)$$

$$\vec{V}_{HV} = A^T \cdot \vec{V}_{cell} \quad (3.18)$$

where the overhead arrow denotes the vector representation of respective quantities. \vec{V}_{cell} is the vector of cell voltages and A^T represents the transpose of the linkage matrix. We can now proceed analogously to Eqs. (3.1)-(3.4) and insert Eqs. (3.17)-(3.18) to derive the flyback current vectors as below [68]:

$$\vec{I}_{LV}^C = - \left(A \cdot \vec{V}_{cell} \oslash \left(\vec{V}_{cell} \cdot T + A \cdot \vec{V}_{cell} \right) \right) \cdot \left(\frac{I_{HV}^P \cdot \eta^C \cdot T}{2} \right) \quad (3.19)$$

$$\vec{I}_{HV}^C = \left(\vec{V}_{cell} \oslash \left(\vec{V}_{cell} \cdot T + A \cdot \vec{V}_{cell} \right) \right) \cdot \left(\frac{I_{HV}^P \cdot T}{2} \right) \quad (3.20)$$

$$\vec{I}_{LV}^D = \left(A \cdot \vec{V}_{cell} \oslash \left(\vec{V}_{cell} \cdot T + A \cdot \vec{V}_{cell} \right) \right) \cdot \left(\frac{I_{LV}^P}{2} \right) \quad (3.21)$$

$$\vec{I}_{HV}^D = - \left(\vec{V}_{cell} \oslash \left(\vec{V}_{cell} \cdot T + A \cdot \vec{V}_{cell} \right) \right) \cdot \left(\frac{I_{LV}^P \cdot \eta^D}{2} \right) \quad (3.22)$$

where the symbol \oslash denoted element-wise division. Each element of \vec{I}_{LV}^C and \vec{I}_{HV}^C represent the mean current produced at LV and HV side of the corresponding converter when it operates in *charge* mode. Likewise, \vec{I}_{LV}^D and \vec{I}_{HV}^D correspond to *discharge* operation mode.

Active Balancer Modeling

In order to calculate the vector of cell currents \vec{I}_{cell} during the balancing process a governing relation is developed which superimposes three components:

$$\begin{aligned} \vec{I}_{cell} &= \left(\vec{I}_{LV}^D + A^T \cdot \vec{I}_{HV}^D \right) \otimes \vec{D} \\ &+ \left(\vec{I}_{LV}^C + A^T \cdot \vec{I}_{HV}^C \right) \otimes \vec{C} \\ &+ (I_{discharge} - I_{charge}) \cdot \vec{1} \end{aligned} \quad (3.23)$$

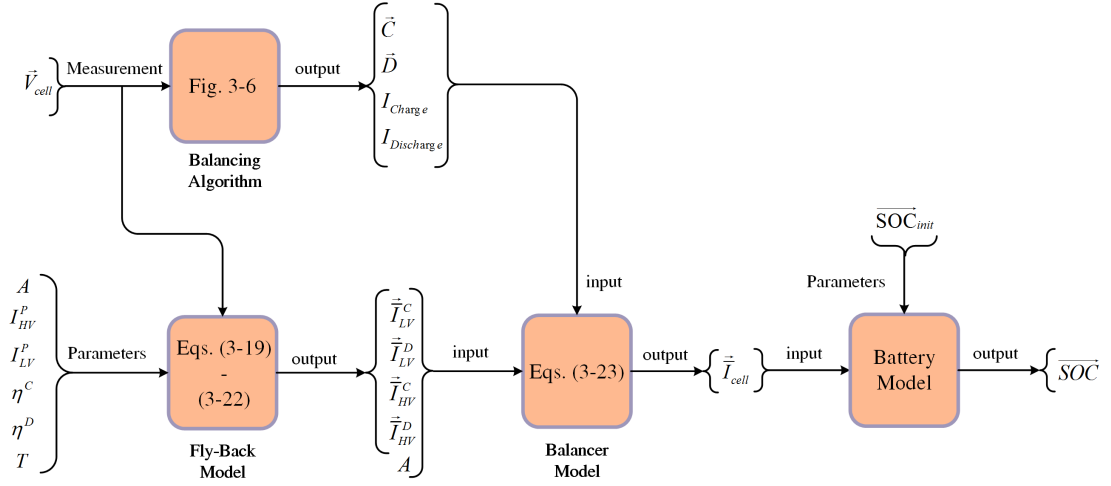


Figure 3.9: Diagram of the proposed simulation model for active cell balancer.

In Eq. (3.23), the symbol \otimes denotes element-wise multiplication and $\vec{1}$ stands for a vector the size of cell count with all *one* entries. A^T is the transposed linkage matrix which determines the energy routeing between the cells and the subsets during *charge* and *discharge* operation of flybacks. \vec{C} and \vec{D} are the *charge* and *discharge* vectors of the converters which are generated by the balancing algorithm (Fig. 3.6). Each row of \vec{C} and \vec{D} exclusively take on a *one* entry to indicate *charge* and *discharge* operation of the associated flyback, respectively. Therefore, the first segment of Eq. (3.23) represents the currents produced by the flybacks operating in *charge* mode. In a similar way, the second line corresponds to the *discharge* operation of the converters. Moreover, the charge or discharge current of the battery stack is considered in the last segment (Fig. 3.4) [68].

The diagram of the proposed simulation model is illustrated in Fig. 3.9. At the start time of the simulation, the initial SOC values (SOC_{init}) are randomly distributed between 10% and 22% to create an exaggerated condition of unequal SOC. The set points and parameters of the simulated model are presented in Table 3.1. The operation of the proposed control algorithm is simulated over the charge and discharge cycles for three different combinations of subsets. The simulation results are illustrated in Figs. 3.10-3.15. Moreover, the time span of the balancing procedure for different cases are compared in Table 3.2 including the ratio of the balancing duration in discharge cycle to the charge cycle. the results verify that the proposed balancing algorithm has successfully handled the extreme SOC unbalance among the cells in both charge and discharge cycles [68]. Upon the start of the cell equalising during the charge cycle, the I_{charge}

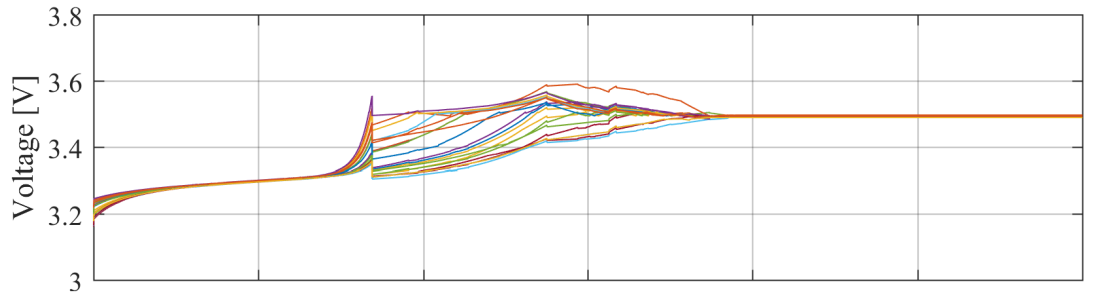
Table 3.1: Simulation set points [68].

	Parameter	Symbol	Value
	Cell Capacity	C	100 [Ah]
	Cells in Stack	n	24
FlyBack	LV Side Peak Current	I_{LV}^P	6.25 [A]
	HV Side Peak Current	I_{HV}^P	3.125 [A]
	Transformer Turn Ratio	T	1:2
	Charge Efficiency	η^C	92%
	Discharge Efficiency	η^D	92%
	Charger Current	$I_{charger}$	50 [A]
	Charger Current During Balancing	$I_{balancing}$	4 [A]
	Discharge (Load) Current	$I_{discharge}$	20 [A]
	Subset Mean Voltage Hysteresis Band	δ_S	5 [mV]
	Cell Voltage Hysteresis Band	δ_C	5 [mV]
	Cell Charge Cut-Out Voltage	V_C	3.5 [V]
	Maximum Cell Voltage	V_{max}	3.7 [V]
	Cell Discharge Cut-Out Voltage	V_D	2.8 [V]
	Minimum Cell Voltage	V_{min}	2.7 [V]
	Over-Charge Hysteresis Band	V_C^B	12 [mV]
	Over-Discharge Hysteresis Band	V_D^B	12 [mV]

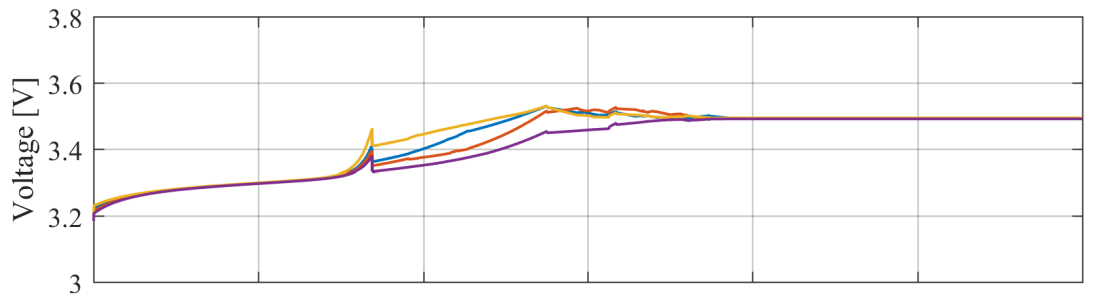
steps down to $I_{balancing}$. This prevents OC cells from violating the impermissible level of charge. Meanwhile, the cells of lower SOC are gradually charged and their SOC level is gradually lifted up toward the fully balanced condition which happens at the full-charged state. This virtually accelerates the balancing process of the whole battery stack. Given the reduced charge current of $I_{balancing}$ it takes approximately 1 [hr] that the stack's mean SOC of 93% reaches to 96.6% corresponding to the cell cut-off voltage of V_C [68]:

$$\frac{96.6 - 93}{100} \times \frac{100[Ah]}{4[A]} = 0.9[hr] \approx 1[hr] \quad (3.24)$$

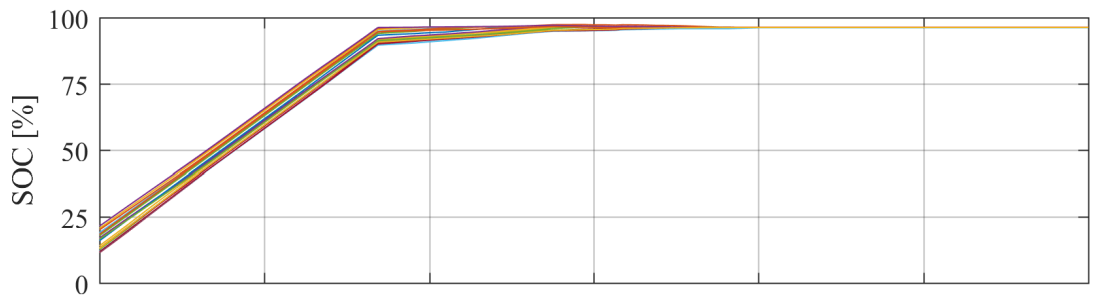
Afterwards, I_{charge} further declines to *zero* if the stack nearly reaches the full-charged state, which is detected by comparing mean cell voltage of the stack V_{mean} and the cell cut-off voltage V_C , or the maximum permissible voltage of V_{max} is violated by a cell. The results pertaining to the charge cycle show how the equalising process is improved after I_{charge} is restricted. In particular, after



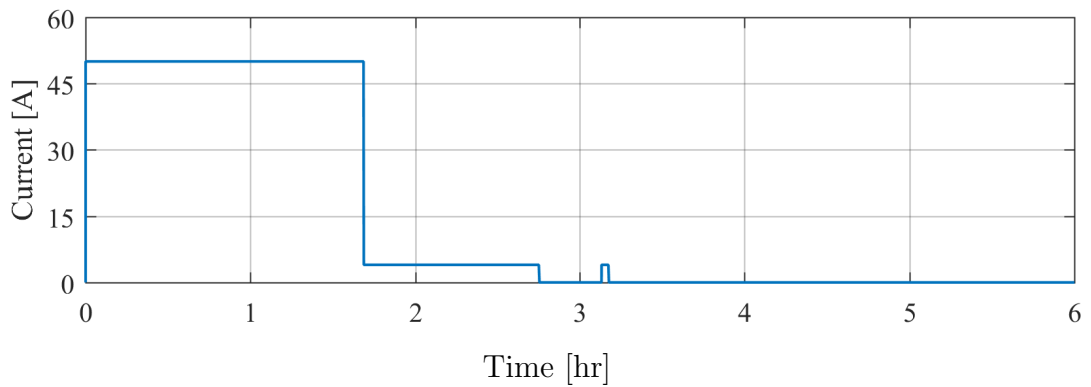
(a)



(b)

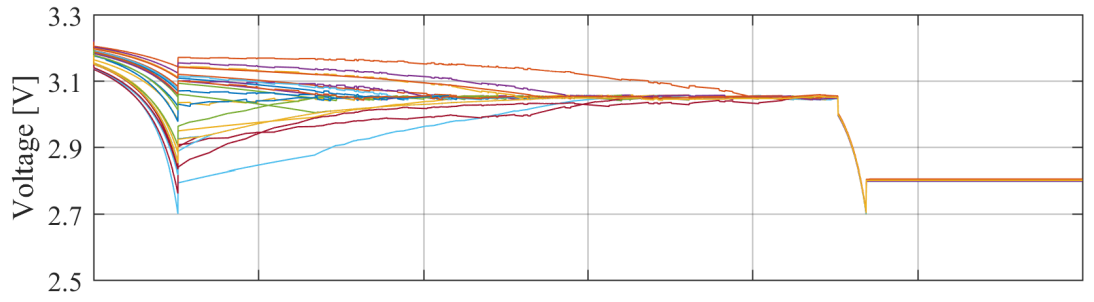


(c)

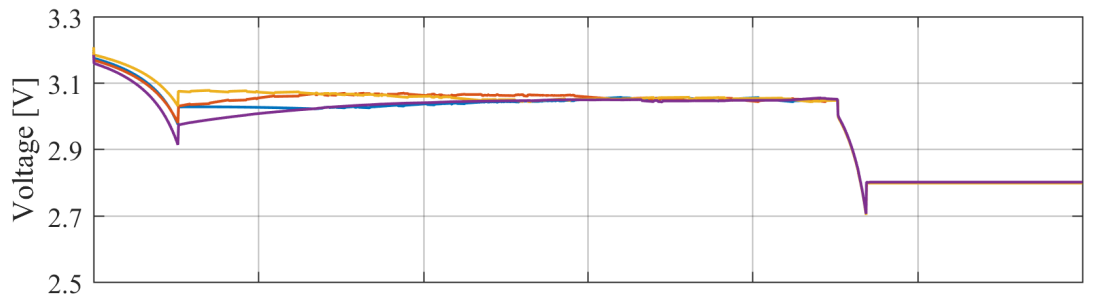


(d)

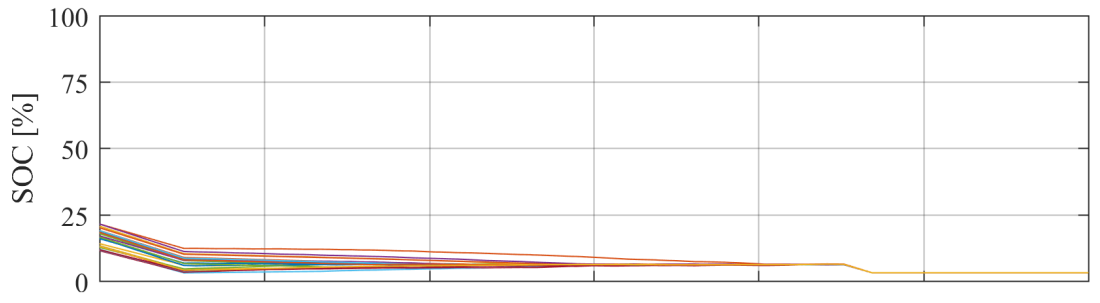
Figure 3.10: The simulation results of Case-I in charge cycle, (a) cell voltages, (b) subset mean voltages, (c) cell SOC, and (d) charger current I_{charge} [68].



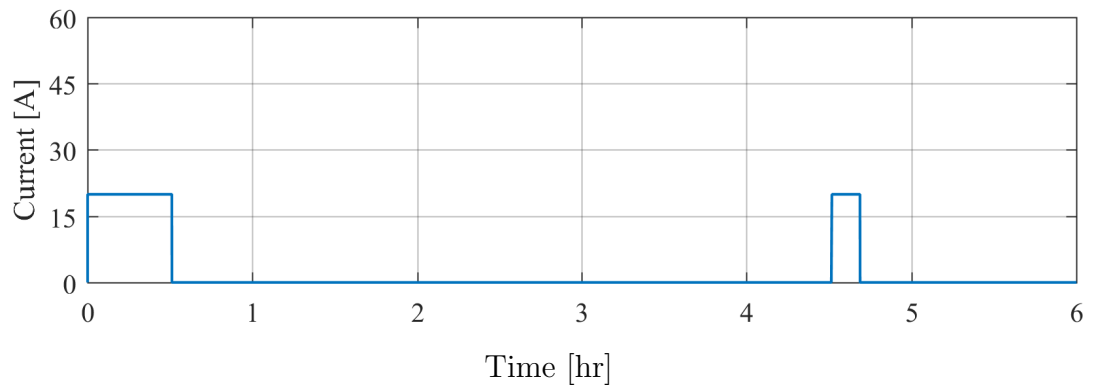
(a)



(b)

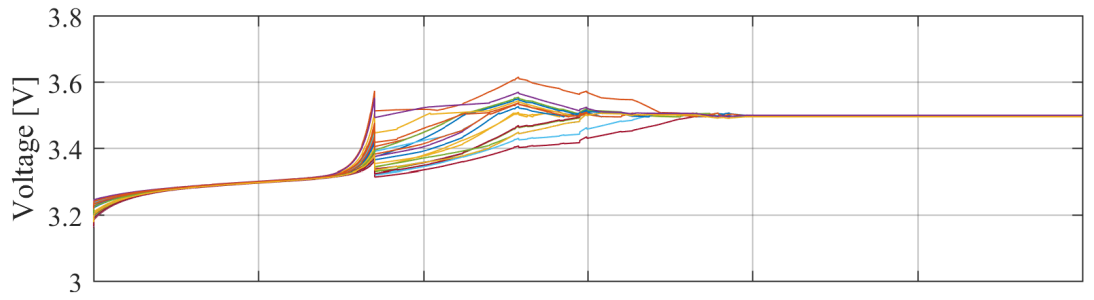


(c)

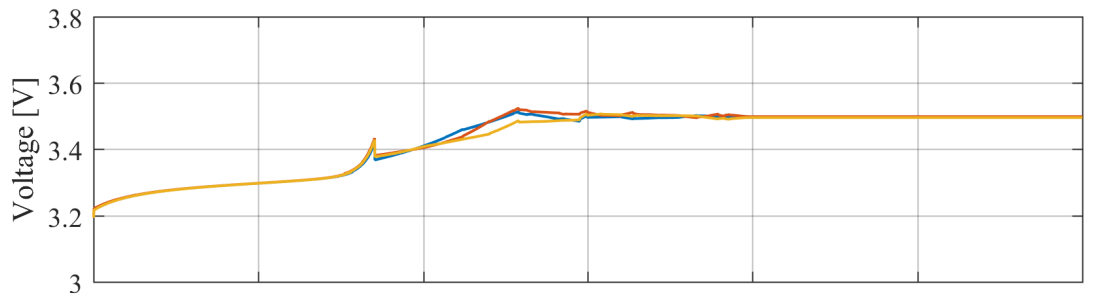


(d)

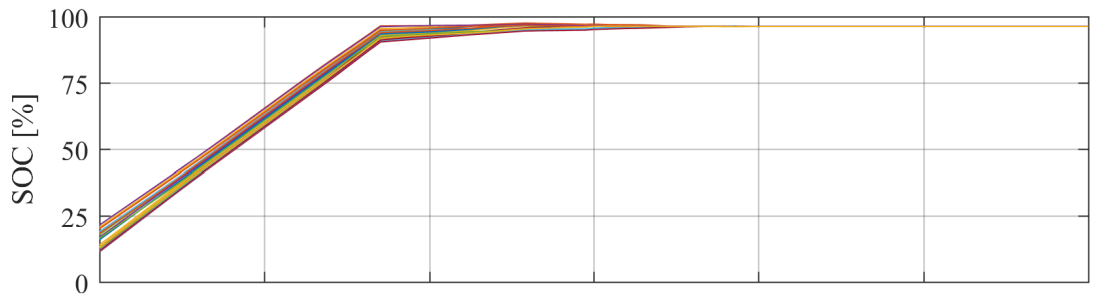
Figure 3.11: The simulation results of Case-I in discharge cycle, (a) cell voltages, (b) subset mean voltages, (c) cell SOC, and (d) discharge current $I_{discharge}$ [68].



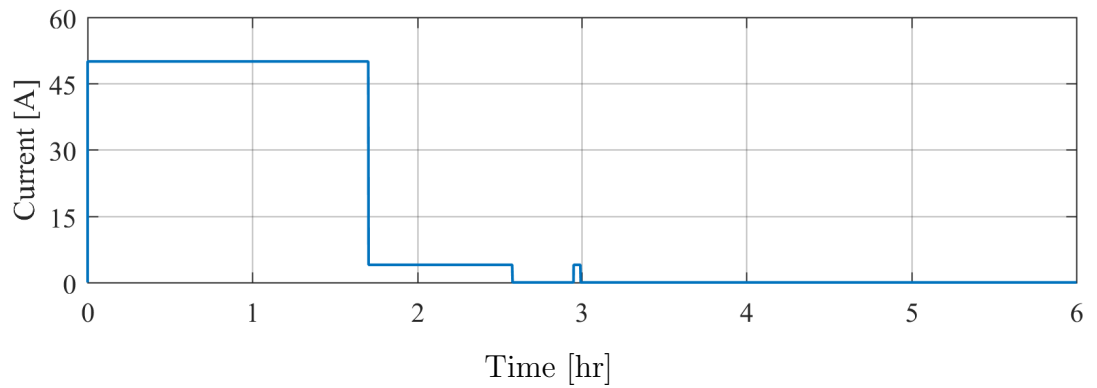
(a)



(b)

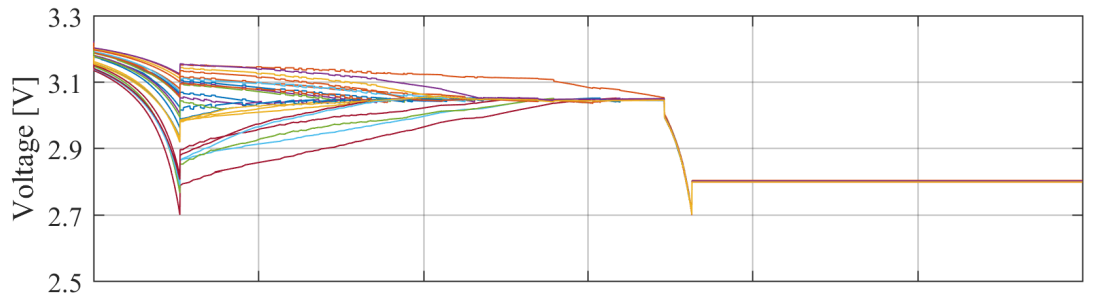


(c)

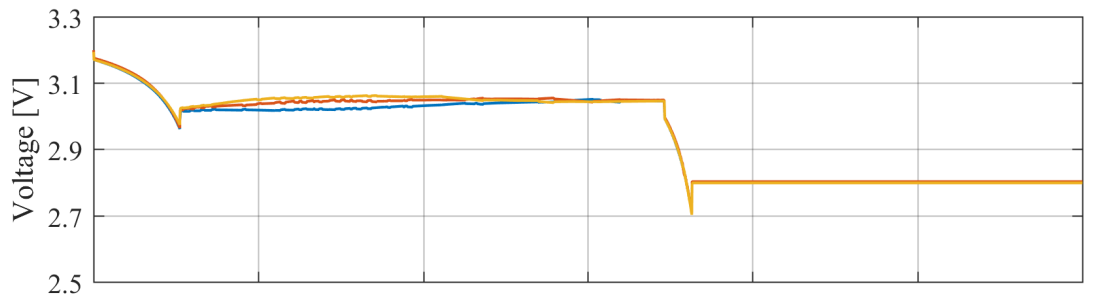


(d)

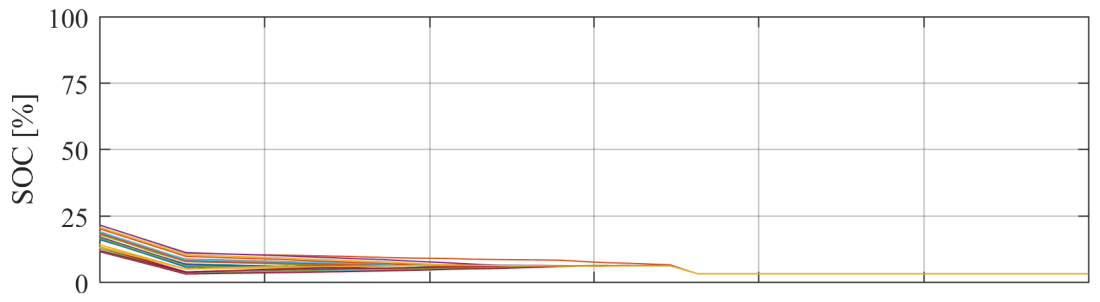
Figure 3.12: The simulation results of Case-II in charge cycle, (a) cell voltages, (b) subset mean voltages, (c) cell SOC, and (d) charger current I_{charge} .



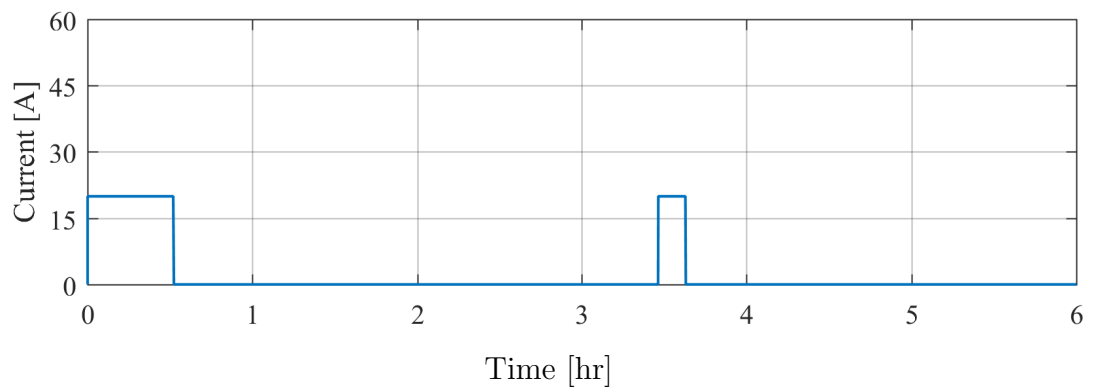
(a)



(b)

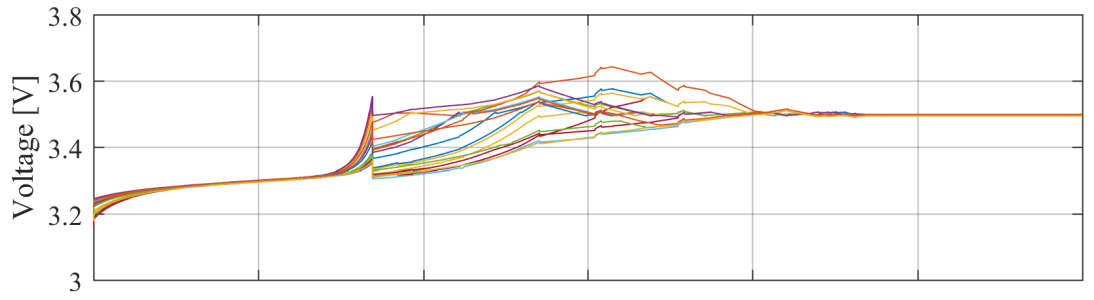


(c)

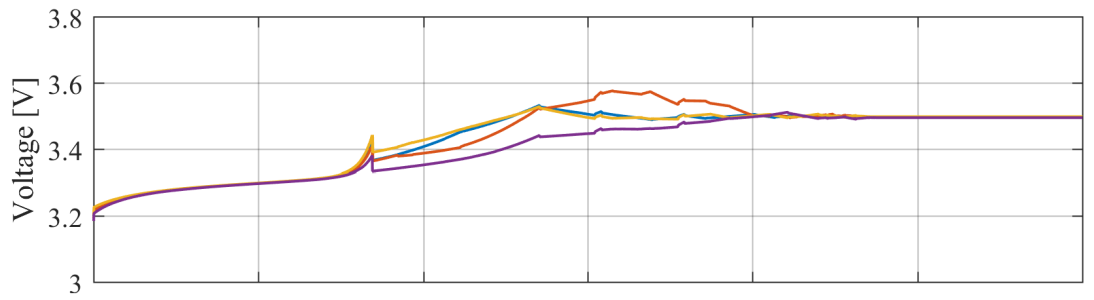


(d)

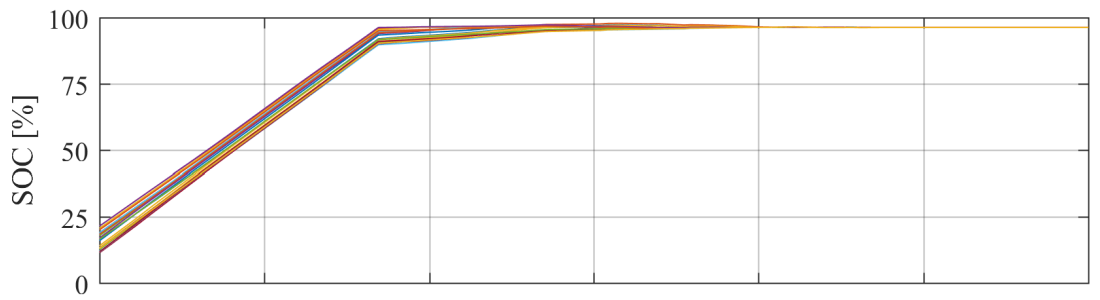
Figure 3.13: The simulation results of Case-II in discharge cycle, (a) cell voltages, (b) subset mean voltages, (c) cell SOC, and (d) discharge current $I_{discharge}$.



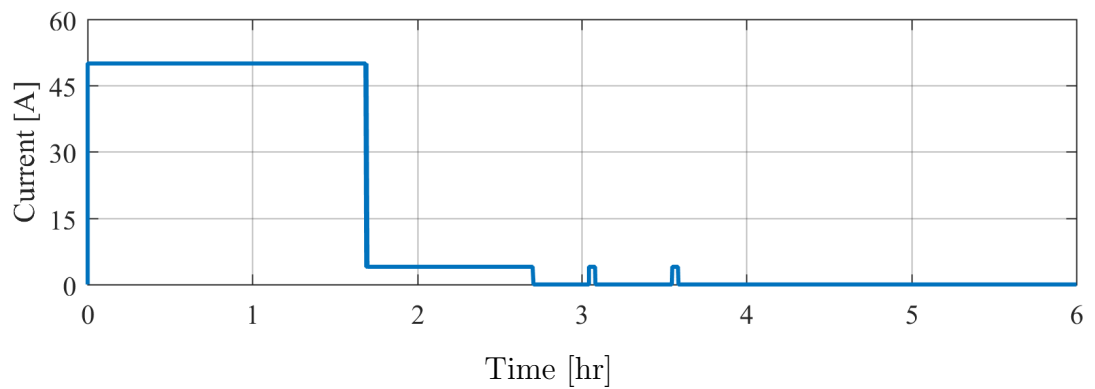
(a)



(b)

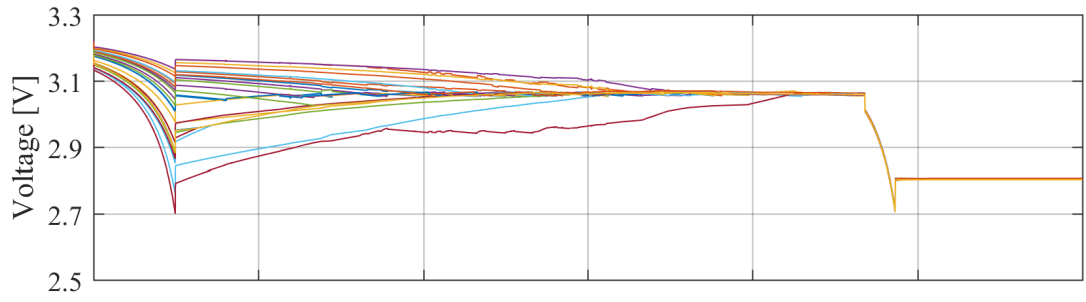


(c)

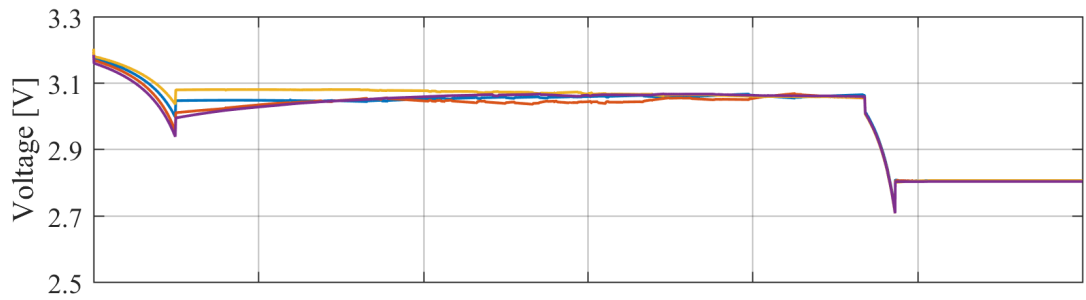


(d)

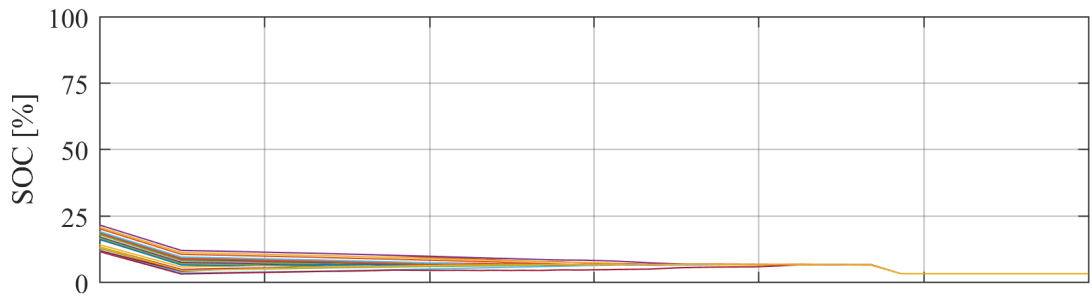
Figure 3.14: The simulation results of Case-III in charge cycle, (a) cell voltages, (b) subset mean voltages, (c) cell SOCs, and (d) charger current I_{charge} .



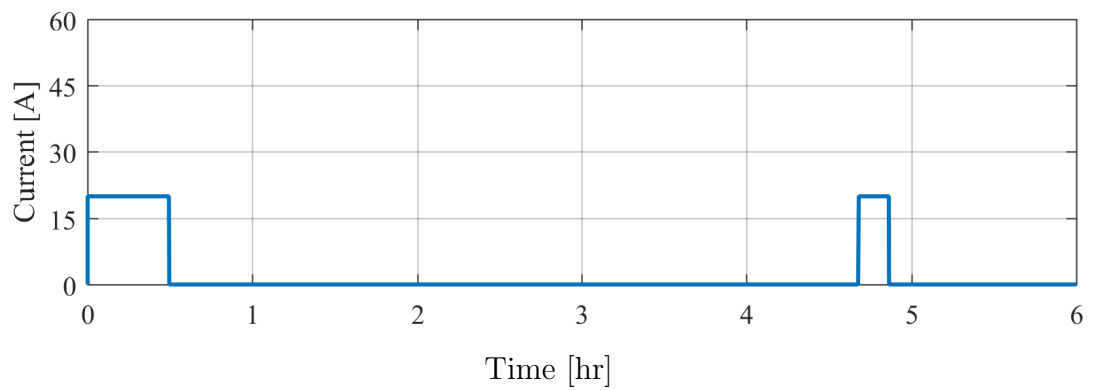
(a)



(b)



(c)



(d)

Figure 3.15: The simulation results of Case-III in discharge cycle, (a) cell voltages, (b) subset mean voltages, (c) cell SOC's, and (d) discharge current $I_{discharge}$.

Table 3.2: Duration of cell equalisation.

	Charge Cycle	Discharge Cycle	Ratio
Case-I	2.32 [hr]	4.00 [hr]	1.72
Case-II	1.93 [hr]	2.60 [hr]	1.34
Case-III	2.87 [hr]	4.18 [hr]	1.50

it dropped to *zero* the charge balancing is further escalated and the convergence rate of the cell voltages is remarkably increased. In contrast, to facilitate OD equalisation, the discharge current $I_{discharge}$ is cut-off right away by isolating the load once the first cell voltage is detected less than a predefined discharge cut-out threshold V_D . This continues until both inter-subset and intra-subset balancing criteria are met, i.e. cell voltages laid within the respective hysteresis bands δ_S and δ_C . Therefore, the *zero* stack current during the OD cell equalising rather than a *non – zero* value during some parts of OC cell balancing can remarkably lengthen the balancing process during discharge cycle up to 70%. The values of *Raito* in Table 3.2 confirm this fact. During the discharge cycle, balancing due to the *zero* current of the stack its final charge level in fully balanced condition does not necessarily correspond to the discharge cut-out voltage V_D . Therefore, after the first OD cell is detected the initial value of V_D will be continuously updated by the average cell voltage of the stack. This dynamic target balancing process finishes as soon as the fully equalised condition is achieved. Afterward, any remaining stored energy can be retrieved by resuming the discharge cycle. The Table 3.2 also implies that the balancing process tends to take longer for the structures of smaller subsets, e.g. Case-I (4×6). In other words, when more battery cells are included in the subsets the charge imbalance will be distributed over a larger group of cells which leads to a faster balancing process, consequently. Comparing the symmetric structures of Case-I and Case-II suggests that for the 3×8 composition the fully equalised condition is achieved 20% and 53% faster during charge and discharge cycles, respectively. Since the $I_{discharge}$ is cut-off during the balancing the effect of HV side structure is more distinctly manifested in the discharge cycle. The unsymmetrical structure of Case-III (6-4-8-6) also suffers the relatively longer balancing time than Case-II (3×8) due to larger subset count. Moreover, the asymmetric composition of subsets further lengthens the inter-subset equalisation in stage-II due to inconsistent rate of the charge transfer between the 8-cell subset and adjacent subsets. As seen in Fig. 3.14(a) from

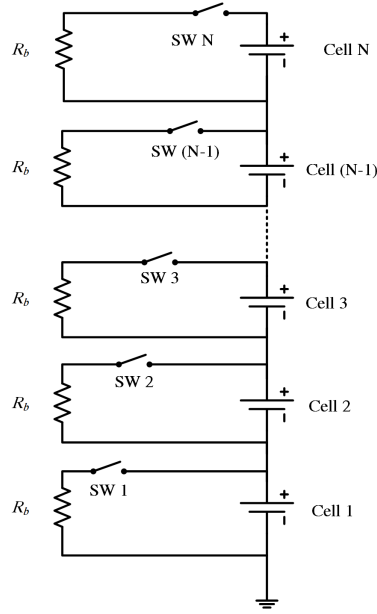


Figure 3.16: The structure of the passive cell balancer.

4 to 4.5[hr] the cell voltages are well converged while the equalisation process still continues until the ultimate balanced condition is achieved. The SOC gap between individual cells and how it is distributed over the battery stack somehow determine the total balancing time. As rule of thumb, the 12% SOC mismatch is expected to take roughly 2 [hr] to be rectified by the active balancer operating in approximately 2.5 [A] (Eq. (3.6) and (3.8)) of balancing current:

$$\frac{0.5 \times 12}{100} \times \frac{100[Ah]}{2.5[A]} = 2.4[hr] \approx 2[hr] \quad (3.25)$$

3.3 Passive Cell Balancer

Basically, the main function of the passive cell balancer is to monitor the SOC of each cell, identify and protect the cells approaching the over-charge condition. The passive cell equalising approach essentially bypasses the energy flow across the over-charged cells during the charge cycle. For this purpose, a bleeding resistor shunts across those cells whereby the surplus energy is dissipated mitigating the destructive effects due to excessive over-charge. Fig. 3.16 depicts the structure of the passive cell balancer.

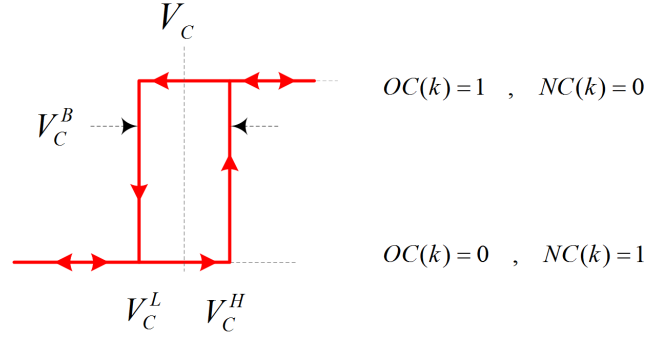


Figure 3.17: Two-level hysteresis cell voltage interpreter.

3.3.1 Passive Cell Balancing Algorithm

The SOC estimation is a key function in the passive balancing algorithm. As discussed in section 3.2.1, according to the cells' characteristic curve, the cell voltages are used to identify the critical SOC level and initiate the appropriate equalising operation. Since the passive equalisation approach only operates during the charge cycle only over-charge condition of each cell has to be determined based on the respective cell voltage V_{cell} using a two-level hysteresis interpreter. Fig. 3.17 shows how the charge status of a cell is identified, wherein $OC(k)$ and $NC(k)$ signify the k^{th} cell *over-charge* and *normal* states, respectively. Afterwards, the passive balancer controller activates the resistive bypass across the cell recognised as *OC*. Eq. (3.26) explains the operation principle of the passive balancing method.

$$SW(n) = \begin{cases} 1 & \text{if } OC(n) = 1 \\ 0 & \text{otherwise.} \end{cases}, n \in 1 \cdots N \quad (3.26)$$

This expression applies to all cells $1 \cdots N$ and upon detection of any over-charge cell $OC(n) = 1$, the respective bypass switch is closed which is represented as $SW(n)=1$, otherwise the switch remains open $SW(n)=0$. From a practical perspective, during the charge cycle in order to bypass a large charge current I_{charge} through bleeding resistors appropriate ventilation has to be adopted to avoid excessive heat builds up. Reducing the I_{charge} during the balancing process could effectively limit the heat produced by the bleeding resistors. Therefore, the BMS decreases the charge current to $I_{balancing}$ as soon as the first cell is detected as *OC* and revert that back to I_{charge} once all cells are *NC*. At the end of charge cycle once all cells are fully charged ($V_{mean} = V_C$) the BMS stops the charge current, $I_{charge}=0$. Fig. 3.18 illustrates the flowchart of the passive cell balancer controller.

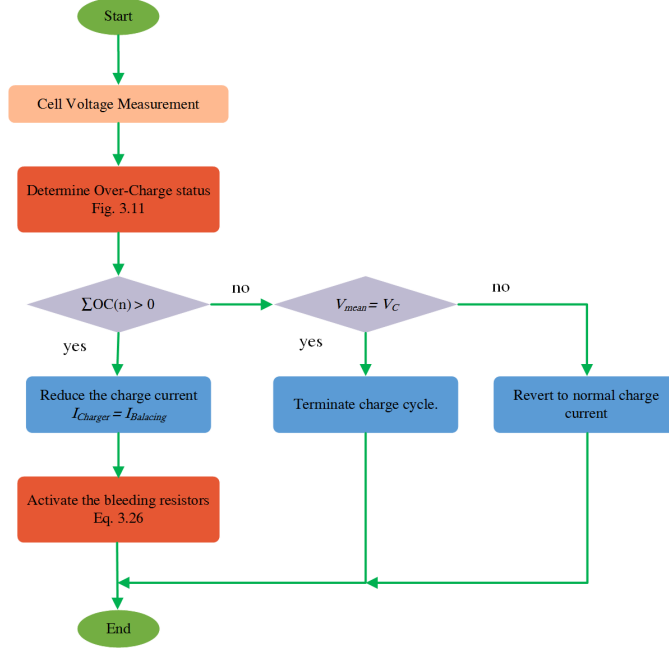


Figure 3.18: Flowchart of the passive cell balancing controller.

3.3.2 Passive Cell Balancing Simulation

In order to demonstrate the performance of the passive cell balancer, a simulation model is developed in Matlab/Simulink based on the schematic shown in Fig. 3.16 and the control algorithm illustrated in Fig. 3.18. The battery bank consists of $24 \times \text{LiFePO}_4$ cell of 100 [Ah] capacity. The simulation model specifications, the respective set points, and $S\vec{O}C_{init}$ are chosen similar to the active balancer model in Table 3.1. The value of the bleeding resistors R_b are chosen so as to bypass the whole $I_{balancing}$ once the respective switch is closed.

$$R_b = \frac{V_C}{I_{balancing}} = 1.14\Omega \quad (3.27)$$

Fig. 3.19 illustrates the simulation results of the passive balancer approach. As seen, as soon as the first cell reaches the critical cell voltage V_{max} , the I_{charge} is restricted to $I_{balancing}$ and the respective bypass resistors are engaged to prevent extra charge is delivered to those cells. Meanwhile, the charge cycle continues until the rest of cells are fully charged. Comparing the Fig. 3.19 to Figs. 3.10, 3.12, and 3.14 confirms the equalisation process is relatively faster in active cell balancer. The passive method exhibits an equalising time of 2.96 [hrs] in charge cycle which is almost 50% longer than that of the active balancer approach with 3×8 configuration (Case-II in Table 3.2) but not much longer than the unsym-

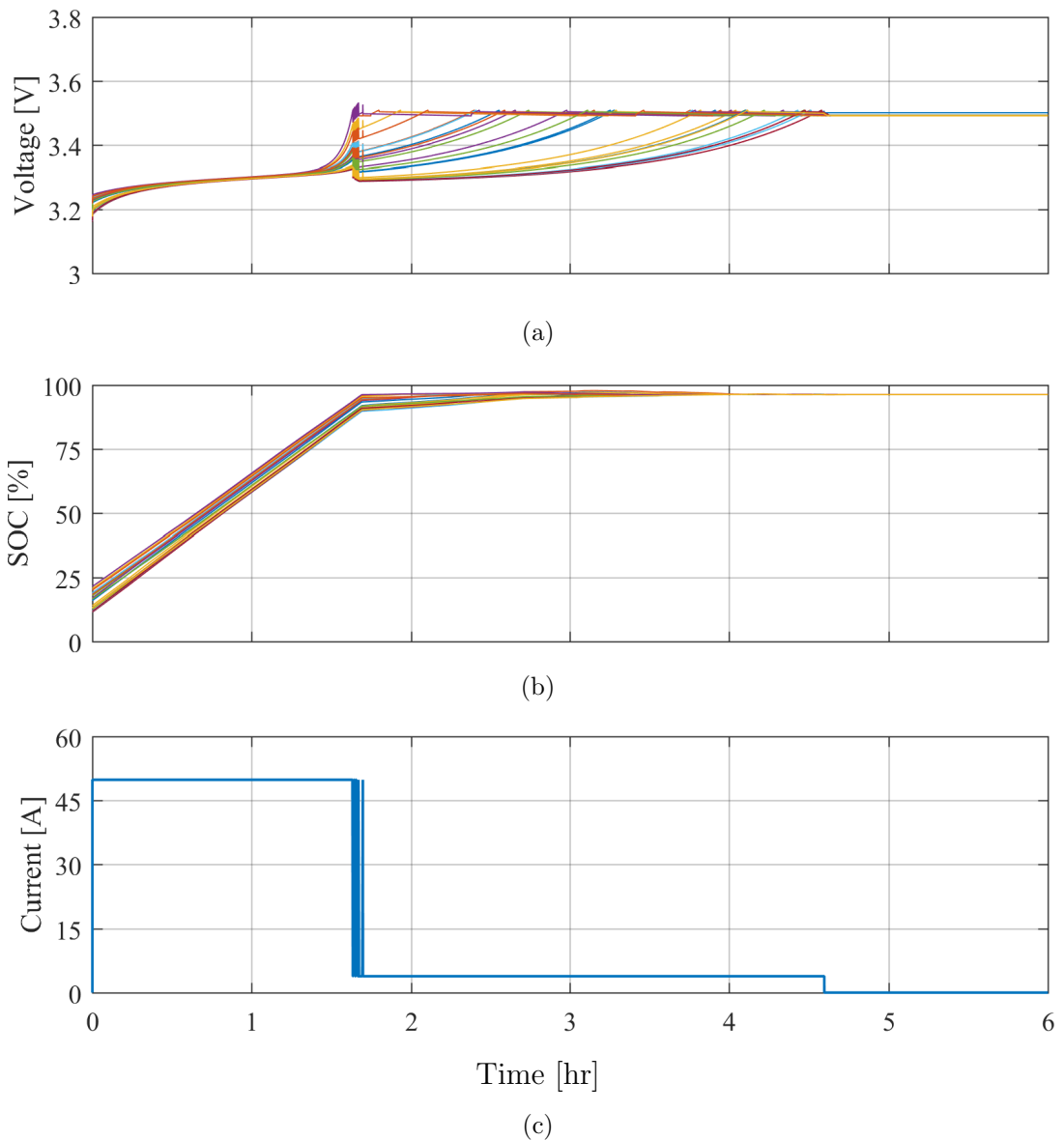


Figure 3.19: The simulation results of passive balancer in charge cycle, (a) cell voltages, (b) cell SOC, and (c) charge current I_{charge} .

metrical configuration (Case-III in Table 3.2). In terms of energy efficiency, Table 3.3 gives an account of the energy loss of different methods. The energy delivered to the battery stack in excess of the amount required to full charge is normalised by the battery bank capacity. In active balancer approaches the energy loss is primarily attributed to the operational loss of the flyback converters, the more charge routing is required, the more energy loss is involved. Whereas in the passive balancer the power dissipation in the bleeding resistors results in a higher

amount of energy loss and inferior efficiency.

Table 3.3: Energy loss in cell balancing approaches.

	Balancing Method	Energy Loss [%]
<i>Active</i>	Case-I	3.33
	Case-II	3.36
	Case-III	3.56
	passive	8.03

3.4 Summary

In this chapter, the structure of a bidirectional flyback active cell balancer with interleaved HV connections was investigated and the governing relations were obtained. Based on the inter-subset and intra-subset charge routeing a cell equalising algorithm was proposed for series connected battery stacks. In order to examine the performance of the proposed method, a simulation model was implemented in Matlab/Simulink. Moreover, the linkage sparse matrix was introduced which defines the energy routing respective to any composition of the subsets in the simulation model. The simulation study was conducted for three different combinations of subsets. Where the results confirmed the effectiveness of the proposed algorithm as the fully equalised condition was successfully achieved in all cases. Whereas the duration of the balancing process was remarkably affected by several factors, i.e. stack current, and the number and cell count of the subsets. The larger the subsets, the faster charge imbalance is disappeared across the battery stack. Especially, in the case of a significant charge mismatch between the cells faraway in the stack, because this requires the charge is shuttling across more cells. In order to evaluate the energy efficiency, the active balancing approaches were compared to the passive cell balancer. It was concluded that in spite of almost similar energy efficiency in different structures of active cell balancer, those exhibits a superior efficiency compared to the passive approach.

Chapter 4

Storage-Optimised Smoothing of PV Generation

Using Short-Term Imagery-Based Cloud Prediction

4.1 Introduction

Solar irradiance forecasting and information on projected generation of PV plants could offer significant reliability and power quality advantages to the power system, i.e. serve to improve the ability to dispatch utility-scale PVG units, enabling less variable PVG in urban feeders and alleviate the operation of voltage regulation equipment, and allow efficient and smart control of storage systems integrated into PV plants. There are a wide range of solar forecasting methods available which typically differ in the temporal and spatial domain. They range from a very short-term time frame of 1 [min] to a full day ahead, with a spatial accuracy ranging from very coarse 50 [km] down to a more precise 1 [km] domain. Among various methods ground-based cloud imagery approaches offer comparatively higher resolutions in both temporal and spatial domains, making them good candidates for PVG smoothing applications that require identifying rapid irradiance variations [78]. In this approach, hemispherical sky images are captured and analysed to identify the characteristics and motion information of the clouds. Insolation variations could be interpreted from this information while a certain amount of forecasting inaccuracies are inevitable. Therefore, an averaged cloud prediction approach is proposed in this chapter that considers multiple historical observations to arrive at a single projected cloud region. Furthermore, this method is applied to generate a series of equally spaced prediction information to improve robustness as well as addressing the occasional inaccuracies of the algorithm in identifying of the shape, dimensions, or motion of the clouds. Ultimately,

the cloud prediction information is introduced into a conventional storage based PVG regulating algorithm as a supplementary input for the purpose of minimizing the reliance on the BS in terms of the required engagement and capacity. The proposed algorithm is then evaluated through comparative simulation studies as well as experimental trials conducted on a developed prototype.

Hence the remainder of this chapter is organised as the following: section 4.2 briefly goes over various techniques of solar irradiance prediction. Section 4.3 is devoted to the proposed imagery cloud prediction algorithm, and this is followed by a detailed explanation of different smoothing approaches in section 4.4. Afterward, the structure of developed experimental testbed is described in section 4.5 and the performance of several smoothing approaches are comparatively surveyed through experimental measurements and simulation studies in section 4.6. Ultimately, the conclusion of this chapter is reported in section 4.7.

4.2 Solar Prediction Methods

Based on the scale of input information and the principle of operation, the accuracy of solar irradiance forecasting methods varies over the temporal as well as spatial horizons of prediction. Fig. 4.1 depicts the regions of the most accurate operation for different techniques of solar insolation forecasting in terms of the effective temporal and spatial domain.

4.2.1 Statistical Models

Many forecasting methods have been proposed based on historical solar radiation data, including linear and nonlinear approaches. The core component of the linear models is a time series which is obtained using the statistical methods. Then, the model predicts solar radiation based on the time series and input variables. Auto regressive moving average (ARMA), and its extension auto regressive integrated moving average (ARIMA), and coupled auto regressive and dynamical system (CARDS) are categorised as linear models. The input data for time series based methods is required to be stationary which implies that any trend and seasonality should be removed from the input through a pre-processing stage. Accordingly, two transmissivity indexes have been introduced; clearness index and clear sky index. The former only reflects the irradiance attenuation by clouds and atmospheric constitutions while the latter takes the effect of air mass into account as well. In non-linear approaches, different variants of artificial intel-

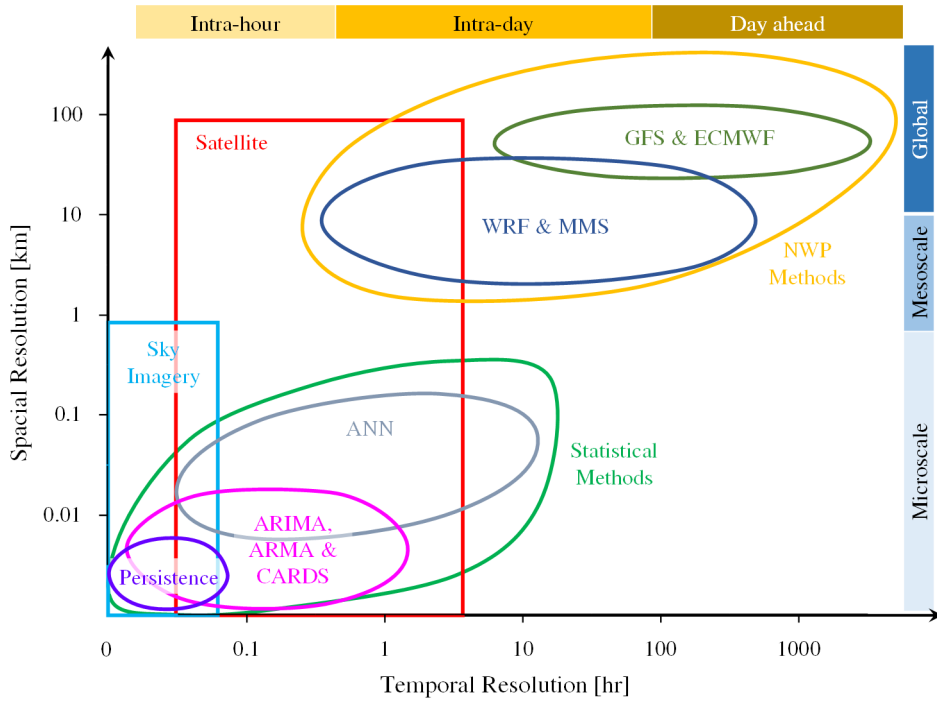


Figure 4.1: Classification of solar radiation prediction models according to temporal and spatial resolution [78].

light (AI) technique such as artificial neural network (ANN) and wavelet neural network (WNN) could be employed to recognise the historical pattern of data and estimate the solar irradiance [78].

4.2.2 Numerical Weather Prediction

Numerical weather prediction (NWP) models use basic differential equations to model the governing physical rules which determine atmospheric behaviours. The weather condition could be predicted up to 15 days ahead. The global NWP models are mostly used by large weather service organisations and have quite coarse spatial resolution of 16-50 [km]. A more accurate local forecasting is possible using mesoscale or regional models to downscale the NWP output data. For short-term applications, NWP is less suitable, due to inevitable errors in clouds timing and positioning [78].

4.2.3 Ground-Based Camera and Satellite Cloud Imagery

Satellite and ground-based images usually give useful information about cloud characteristics over time and space. Since the irradiance at the surface level is

highly influenced by the cloud condition and its spatial motion, the satellite information or sky images are recorded and analysed using image processing schemes to obtain the cloud cover and its movement over time. Afterwards, the future surface irradiance is estimated by extrapolating the recorded data [78, 113]. The satellite imagery method suffers from the low rate of image capture, navigation errors, and parallax effect. Therefore, it may not serve as a promising short-term solar forecasting option for precise spatial scales. On the other hand, the ground-based sky imaging and the grid of irradiance sensors offer superb temporal and spatial resolution suitable for regulating the short-term PVG variations. Whereas the sky-camera technique seems more suitable choice for localised PV plants due to less component count and smaller communication link [85]. There is a series of publications available on terrestrial imagery based solar irradiance forecasting [82–85, 114] which to some extent describe similar fundamentals. The acquired image is first captured by a whole-sky camera, and transformed into a red to blue ratio (RBR) image. Then, it is compared with a corresponding reference image of the clear sky, where the difference in RBR values is used to distinguish cloud regions. This is used to generate a cloud map, which in conjunction with the cloud base height (CBH) information yields a ground shadow map with up to 5 [km] range from the observation spot [84, 85, 114]. West *et al.* [83], have deployed an artificial neural network to make an estimation on the respective degree of cloudiness of each pixel while [82] proposed a fixed value Ref. RBR thresholding approach augmented by cloud texture filters to identify the cloudy areas. Another key element investigated in different approaches is the cloud motion, i.e. the cross-correlation of consecutive images [84, 85, 114] and dense optical-flow [83] as well as a non-rigid registration method which takes the local deformation of clouds into account [82]. Insolation prediction is conclusively conducted according to the present cloud regions and their prevailing movements. In a traditional method as used by [84, 85, 114], the cloud map is advected by extrapolating the observed cloud motion to identify a projected cloud map and then by means of ray-tracing a shadow map is calculated. However, Ref. [83] correlates the occlusion of the sun to the cloudiness figure of an annulus area with radii proportional to forecast range. Bernecker *et al.* [82], have defined and examined an area in which the clouds have the potential of obscuring the sun to generate an occlusion probability which is used to estimate the projected insolation information. Aside from the inherent inaccuracies arising from the cloud formation and evaporation, the perspective error, and the limited field of view, the extensive evaluative results presented in [84] implies an inconsistency in the incidence and

magnitude of erroneous predictions from day to day. These inconsistencies call for more robust and improved approaches.

4.3 Proposed Averaged Cloud Prediction Algorithm

The cloud prediction procedure is primarily an image processing operation which considers successive whole sky images captured by a fisheye camera, and generates projected cloudiness figures which are interpreted as a reliable indication of projected PVG power downward ramps. In this section, the major contribution is a multi-target prediction technique that examines the cloud prediction information associated to a series of prediction instants within a prediction range of interest. This allows an averaged prediction that improves the overall performance of the algorithm in terms of robustness and accuracy.

4.3.1 Correcting Lens Distortion

A fisheye lens has an ultra-wide view angle which makes that an appropriate solution for aerial observations, while produces strong visual distortion. In order to remove these spherical distortions and obtain a flat projection of the image in linear coordinates a camera calibration toolbox is deployed [115]. First, several photos should be taken from a chessboard template. Afterwards, the toolbox extracts the coordinate of the corner points in each photo to obtain the inherent characteristic coefficients of the lens. The respective coefficients are then used to produce the mapping lookup arrays which enable instant conversion of the fisheye hemispherical view into an undistorted flat image. The chessboard photos and the output of the calibration toolbox are presented in Appendix-B. Figs. 4.2(a)-(b) depict the hemispheric and undistorted views of the sky, respectively.

4.3.2 Sun Positioning

The solar forecasting process requires the position of the sun in the sky images which is accurately indicated and updated over successive time intervals. One solution is scanning the sky image to identify the solar disk by the relatively higher value of its brightness. However this approach may not work perfectly in all weather conditions, e.g. the optically thin clouds can be intensely illuminated by the sun and considerably deviate the sun-locating procedure. Therefore, a

computational approach is deployed which yields zenith and azimuth angle of the sun corresponding to the geographical information, date, and time [116]. By means of refraction parameters of the fisheye lens, the coordinates of the solar disk on the fisheye image is identified and then translated into undistorted coordinates using the undistortion mapping arrays. Accordingly, the solar area is reconstructed to be used in the cloud prediction algorithm. The procedure of obtaining the refraction parameters is briefly discussed in Appendix-C.

4.3.3 Cloud Segmentation

Different optical properties of atmospheric aerosols and constituent particles of the clouds create a relatively marked visual distinction between clear and cloudy regions of the sky. Hence, thresholding the RBR value of each pixel has proven to be an effective approach to generate the cloud mask by discriminating the cloud pixels from the clear sky [117]. To prevent computational burden, the undistorted image is averaged block-wise and the corresponding RBR value is calculated for each block. Fig. 4.2(c) illustrates the RBR image represented in false colour. The cutting value, θ_{RBR} , is decided based on the absolute maximum and minimum of daily observed RBR values to segment out areas with excessive RBR values as cloud regions, as shown in Fig. 4.2(d). The solar area always exhibits a RBR value similar to the clouds, which is consequently recognised as a cloudy region in segmentation. Using a scattered outline allows the solar region to be excluded from cloud mask in the following steps of the algorithm. Figs. 4.2(e)-(f) present the plane cloud outline and where the scattered honeycomb pattern is overlayed onto the sky image, respectively. The excluded solar area is marked in a different colour.

4.3.4 Cloud Motion

Motion analysis is carried out by identifying the most distinctive points in the undistorted image and then searching for the corresponding points in the next captured image using the iterative sparse optical-flow method of Lucas-Kanade to calculate the motion vectors [118]. Displacement values are then processed to eliminate the erroneous ones far away from the more recurrent observed values. Fig. 4.2(g) gives an example of the motion vectors resulting from two successive samples. Using a simplifying assumption that all visible clouds are single layer making a uniform motion in a horizontal plane, the instantaneous velocity vector

$\vec{V}(t_0)$ is obtained by averaging the validated collection of motion vector [119]:

$$\vec{V}(t_0) = \frac{1}{t_c} \sum_{i=1}^n \frac{\vec{d}_i}{n} \quad (4.1)$$

where t_0 and t_c are sample instants and cycling time of the algorithm, respectively, over which n displacement values of \vec{d}_1 through \vec{d}_n have been observed. Afterwards, to smooth out the turbulent movement of the clouds or any occasional passing object within effective view of the camera, previous instantaneous motions corresponding to r recent cycles of algorithm are averaged to obtain the principal velocity vector $\bar{\vec{V}}(t_0)$ which is introduced into the forecasting section of the proposed algorithm [119].

$$\bar{\vec{V}}(t_0) = \frac{1}{r} \sum_{i=-r}^0 \vec{V}(i \cdot t_c) \quad (4.2)$$

To ease the deployment of observation data for future predictions, in each cycle an observation structure containing the associated time tag t_r , cloud mask, and principal velocity vector is created as below [119]:

$$obs(t_r) = \begin{cases} \text{reference time:} & t_r \\ \text{cloud outline:} & C \\ \text{velocity vector:} & \bar{\vec{V}}(t_r) \end{cases} \quad (4.3)$$

4.3.5 Cloud Forecasting

Given the key assumption of the persistent movement of the clouds, the projected displacement value of $\vec{D}_{t_0}^{t_1}$, associated with a time interval of t_0 to t_1 , is obtained by extrapolating the principal velocity vector from the time origin [119].

$$\vec{D}_{t_0}^{t_1} = \bar{\vec{V}}(t_0) \times (t_1 - t_0) \quad (4.4)$$

In order to make a more reliable prediction which is less susceptible to occasional errors in segmentation and optical-flow, a series of historical observations are incorporated. Respective to each prediction time t_f a suitable range for the reference time of historic observation is defined as below:

$$t_0 - t_{h2} < t_r < t_f - t_{h1} \quad (4.5)$$

Excluding the circumsolar area in the segmentation stage makes the very short-term predictions impossible. Therefore, a minimum space of t_{h1} is considered

between the observation time t_r and prediction time t_f . Moreover, due to the limited effective prediction range (viewing angle of the camera) the outdated observations spaced back farther than t_{h2} prior to the present time t_0 are ignored. Afterwards, the cloud outlines respective to the eligible observations (Eq. (4.5)) are overlaid and the resulting normalised monochrome image is thresholded by the middle-intensity value of $\theta_{avg} = 256 \div 2 = 128$ to generate an averaged predicted cloud outline. The averaged prediction processing produces a binary cloud mask which is overlaid onto the solar disc templates to obtain the predicted cloudiness indexes. The solar disc template consists of a circle equal in size to the sun as observed in the undistorted image and centred on the calculated coordinate of the sun. The pixel count of the projected cloud mask that overlaps the solar disc template is then normalised by the solar disc area to produce the solar occlusion index, SOi , which is a fair indication of the predicted attenuation of solar insolation. Similarly, a circumsolar template is an annulus with an inner radius equal to the size of the solar disc, and an outer radius twice that size. The circumsolar occlusion index, COi , is the normalised conjunction of the circumsolar annulus and the cloud mask, which could be interpreted as a moderate likelihood of sunlight obstruction in future time. However, when it comes to fast moving intermittent clouds, it is more challenging to predict a shading event that is occurring relatively far away from current time. The effective prediction range T_P is defined as the time a cloud segment takes to travel the effective displacement prediction \vec{L}_P at the velocity and orientation of the observed principal motion. As shown in Fig. 4.2(h), \vec{L}_P is the shortest trajectory from the margin of viewing field to the position of the sun [119].

$$T_P = \frac{\vec{L}_P}{\vec{V}(t_0)} \quad (4.6)$$

Hence, the cloud prediction algorithm is capable of indicating occlusion of the sun for a prediction time up to the effective range and fails when that time exceeds T_P . This is a motivation for proposing multi-point forecasting, as opposed to a single target, in which prediction is performed at a series of evenly spaced prediction instants [119]:

$$\{t_0 + t_{SP}, t_0 + 2 \cdot t_{SP}, \dots, t_0 + n \cdot t_{SP}\} \quad (4.7)$$

$$n \times t_{SP} = t_f \quad (4.8)$$

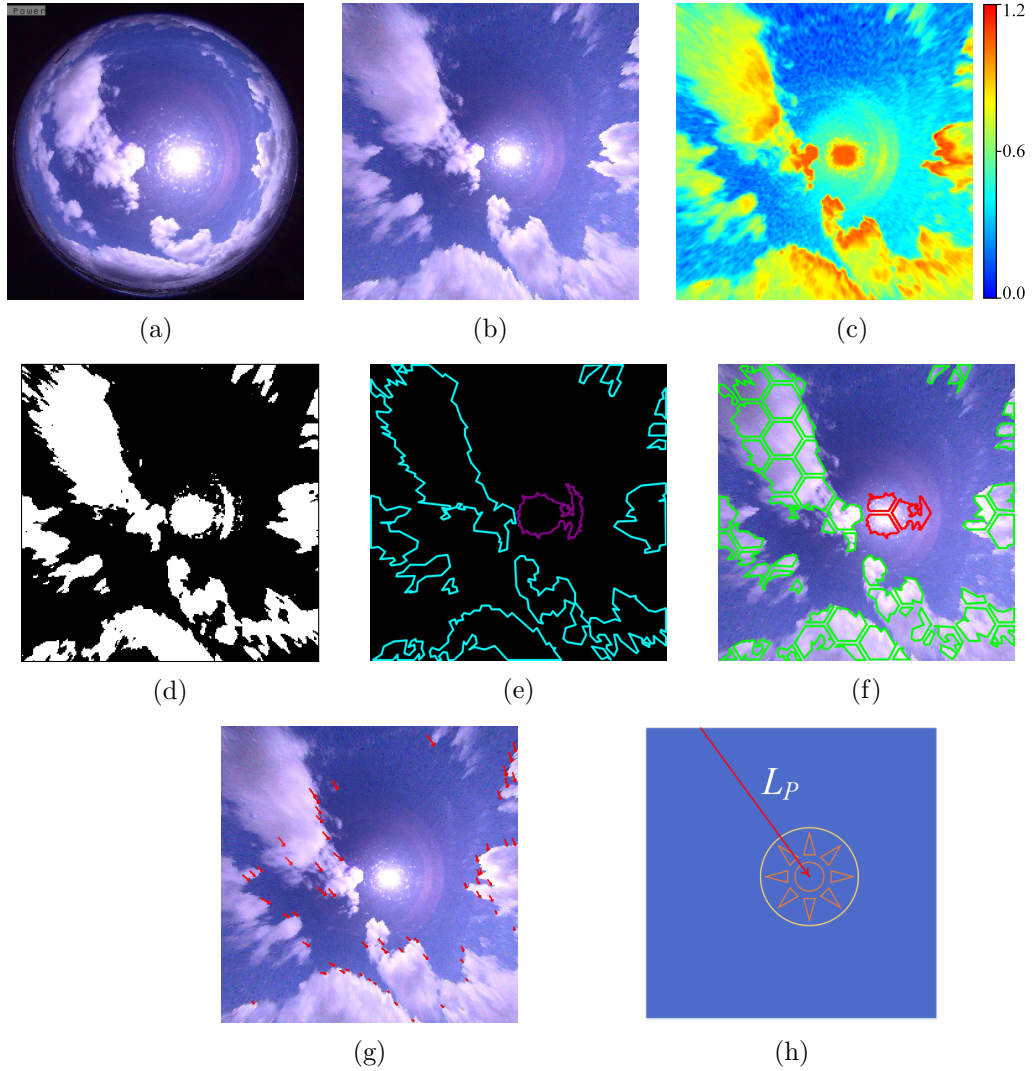


Figure 4.2: (a) fisheye image captured by the sky camera. (b) Undistorted image in flat coordination. (c) False colour representation of RBR image. (d) Binary segmented image. (e) Outlines of cloud regions and solar area. (f) Scattered outline overlaid on the sky image. (g) Displacement of the most suitable features in the sky image. (h) The effective range of displacement prediction.

where t_f and t_{SP} are total and split forecast ranges, respectively. Moreover, n stands for the total number of prediction instants. This is a solution to address the all-or-nothing nature of the individual target prediction i.e. a shading event out of an effective range will be still identified prior to its occurrence yet not at a perfect time. Therefore, pointing to a specific time forward, the multi-point prediction generates a series of SO_i and CO_i values corresponding to the elements of prediction time series as per Eq. (4.7).

4.4 Proposed PVG Smoothing Approach

For the grid-tied PVG systems compliance with operators RR requirements, e.g. 10% per minute RR tolerance as per [90], ensures that grid is not significantly disturbed and power quality criteria are satisfied. Sudden variations in the generation of a PV plant, which are primarily attributed to passing clouds and their shading characteristics, can be addressed in different ways. This section presents the conventional storage backup compensation approach followed by cloud prediction assisted strategies. In the end, a new battery-optimised smoothing technique using conservative cloud prediction by the sky-camera is explained [119].

4.4.1 Conventional Storage Backup Smoothing Strategy

This method works based on the assumption that the PV plant is continuously operating at the MPP, while the generation is monitored and undue RR is compensated by means of a storage backup such as a BS system. Eqs. (4.9)-(4.11) elucidate the cooperation between PVG plant and BS, and how power export of the BS is determined [119].

$$P_G(t_0) = P_{PV}(t_0) + P_{BS}(t_0) \quad (4.9)$$

$$R(t_0) = \frac{P_{PV}(t_0) - P_G(t_0 - \tau_s)}{\tau_s} \quad (4.10)$$

$$P_{BS}(t_0 + \tau_s) = \begin{cases} [R_S - R(t_0)] \cdot \tau_s & \text{if } R(t_0) > R_S, \\ -[R_S + R(t_0)] \cdot \tau_s & \text{if } R(t_0) < -R_S, \\ 0 & \text{otherwise .} \end{cases} \quad (4.11)$$

where P_{PV} , P_{BS} , and P_G are PV plant generation, storage export power and the resulting smoothed power, respectively. t_0 and τ_s stand for present time and sampling rate, respectively. Moreover, $R(t_0)$ and R_s represent instantaneous RR of the PVG at t_0 and its associated extreme allowable value, respectively.

Fig. 4.3(a) depicts an appropriate upward and downward ramps over a severe 100% under-generation follows a full recovery, while the smoothing process is initiated upon detection of the sudden changes. During the ramp-down period, the BS has to provide as much energy as the area marked by a_1 while ramp up

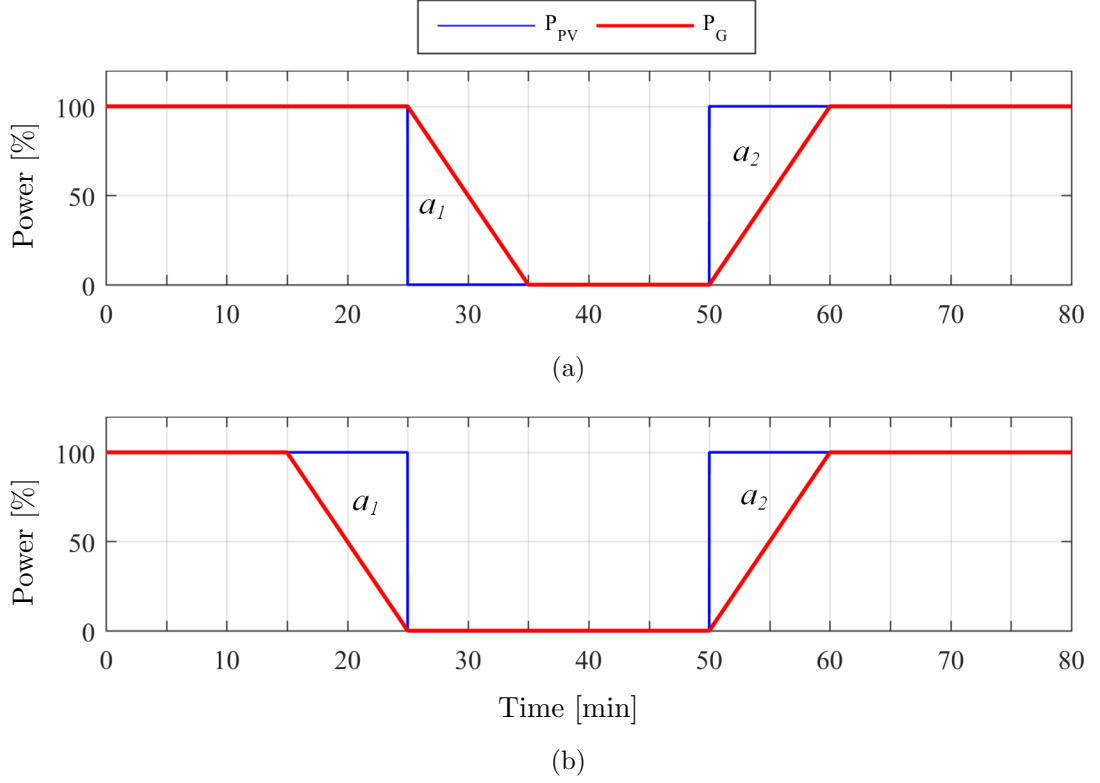


Figure 4.3: Energy balance in PVG smoothing. (a) Conventional smoothing. (b) Based on Cloud Prediction. [119]

smoothing requires energy absorption equal to the area a_2 . Given the upward ramps could be simply (yet not utmost efficiently) handled by curtailment of surplus power instead of charging the BS, battery-optimised PVG regulation is feasible provided the ramp down procedures are started sufficiently prior to the occurrence of the PVG fall off period. This requires an algorithm that accurately predicts the timing and amplitude of sudden under generations caused by passing clouds. Fig. 4.3(b) illustrates the battery-less predictive regulation and as seen it only involves energy curtailment and no backup is required.

In the following section, the storage based smoothing is examined in conjunction with cloud prediction information to investigate whether it results in a satisfactory storage-optimised smoothing approach, given the limitations and relative deficiencies of imagery based cloud prediction [119].

4.4.2 Ideal Export Prediction Smoothing Strategy

Smoothing approach purely based on prediction is ideally defined on the assumption that valid projected PVG output data up to the desired prediction range

is available all the time and then respective RR is obtained accordingly. Eqs. (4.12)-(4.13) are applied to all projection points within the prediction range in order to generate the most critical RR and the appropriate restricted RR for PVG is determined by Eq. (4.14) [119].

$$R_i(t_0) = \frac{P_P(t_i) - P_G(t_0)}{t_i - t_0} \quad i \in (1 : n) \quad (4.12)$$

$$R_c(t_0) = \min\{R_1(t_0), R_2(t_0), \dots, R_n(t_0)\} \quad (4.13)$$

$$R_O(t_0) = \begin{cases} R_s & \text{if } R_c(t_0) > R_s, \\ -R_s & \text{if } R_c(t_0) < -R_s, \\ R_c(t_0) & \text{otherwise .} \end{cases} \quad (4.14)$$

where $R_i(t_0)$ is the required RR to bridge the present PVG value $P_G(t_0)$ to the expected generation level at the i^{th} prediction point $P_P(t_i)$ and n denotes the number of prediction instants. Moreover, $R_c(t_0)$ is the most critical RR which has to be used in order to achieve a smooth P_G only by allowing energy curtailment and without any engagement of storage. R_s and $R_O(t_0)$ are the extreme allowed RR and the RR command to the PV system, respectively.

An effective storage-less PVG smoothing approach requires a precise prediction of P_{PV} by estimating the solar insolation, incidence angle, and temperature of the PV panels. Any inaccuracy arising from the prediction process should be compensated by the storage backup. Alternatively, the lack of desired precision could be appropriately dealt with to mitigate the required storage backup. In the following sections, two different attempts to develop prediction based PVG output smoothing are examined and compared in their effectiveness and functionality [119].

4.4.3 Proposed Smoothing Method-I: Using Output Estimation

With the simplifying assumptions of virtually constant open-circuit voltage V_{OC} , PV cell temperature T_{cell} , and fill-factor of FF , the generated power is proportional to insolation, S :

$$\begin{aligned} P_{MPP} &= FF \cdot V_{OC} \cdot I_{SC} \\ I_{SC} &\propto S, \quad FF = cte, \quad V_{OC} = cte, \quad T = cte \\ \therefore P_{MPP} &\propto S \end{aligned} \quad (4.15)$$

where I_{SC} and P_{MPP} stand for short-circuit current and maximum attainable power of the PV cell, respectively. Furthermore, the angle of incident for direct component of the solar irradiance can be obtained using the coordinate of the sun that generated by solar positioning procedure [116] and alignment of the PV array. This allows a relatively coarse approximation of the PVG forecast [119]:

$$P_{PV} = P_{MPP} = P_{STC} \cdot S_{STC} \cdot \cos(\alpha) \cdot SOi \quad (4.16)$$

where P_{STC} is PVG output in standard test conditions (STC), α is the solar incident angle, and SOi is the respective solar occlusion factor. The simplified estimation of Eq. (4.16) is used to obtain the projected generation values, $P_P(t_i)$, and the governing principle of the ideal prediction, Eqs. (4.12)-(4.14), are applied to meet the appropriate RR requirement. As the smoothing control primarily relies on sudden variations, rather than precise estimation of the export power of the PV plant, these simplifications and resultant inaccuracies will not cause a remarkable deterioration of this proposed smoothing approach [119].

4.4.4 Proposed Method-II: Smoothing Using Binary Cloud Prediction

In order to address the limitations discussed earlier with respect to the PVG output estimation, a PVG export smoothing strategy based on a binary conservative cloud prediction is proposed. The conservative approach restricts the export power during critical situations with a high likelihood of solar occlusion. This condition is determined based on the SOi and COi figures and an estimated PVG output value of $P_P(t_1)$ which is obtained from Eq. (4.17) [119]:

$$P_1 = \begin{cases} P_{Base} & \text{if } \sum SOi > \theta_{SO}, \\ P_{Base} & \text{if } \sum COi > \theta_{CO}, \\ P_{MPP} & \text{otherwise .} \end{cases} \quad (4.17)$$

where θ_{SO} and θ_{CO} are threshold values associated with aggregated SOi and COi values, respectively. Furthermore, P_{Base} is the target amount of generated power during shut-off condition which is determined as a percentage of the nominal amount of expected generation in clear sky condition at the time ($P_{STC} \cdot \cos(\alpha)$). The transmissivity characteristic of the obscuring clouds is a decisive factor in subsequent incident radiation, which barely causes the PVG output to decline by more than 75%-80% [120]. Hence, the shut-off coefficient of C_{Base} is assigned a

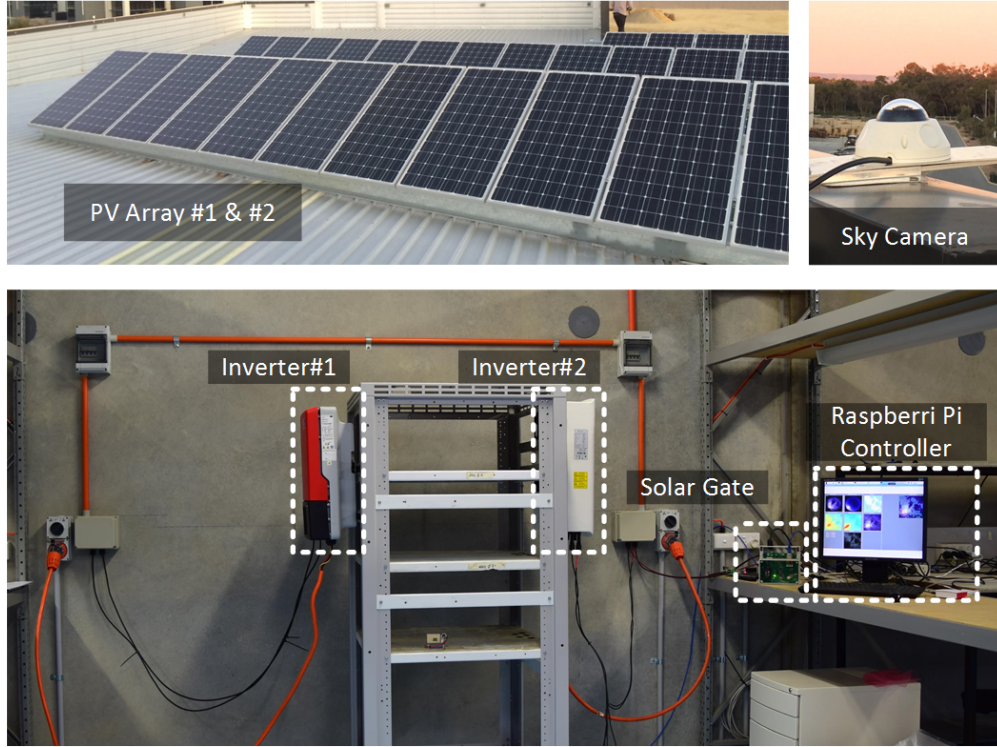


Figure 4.4: Photo of the testbed for PVG smoothing based on the proposed cloud prediction techniques.

value of 20% which enables efficient utilisation of the PVG yield while smooth power generation is maintained [119]:

$$P_{Base}(t) = C_{Base} \cdot P_{STC} \cdot \cos(\alpha) \quad (4.18)$$

4.5 Developed Testbed and Experimental Setup

This section sets out the configuration of hardware components of the testbed developed for conducting a series of evaluative trials on the proposed PVG smoothing approach. The key component of the developed system is a weather proof fisheye security camera with a wide dynamic range (WDR) to accommodate the extremely broad extent of pixel brightness in the sky image, ranging from the sun disc to relatively dark cloud regions, without a considerable level of saturation in the image. The IP camera is mounted upright facing the sky in an outdoor area and communicated through a local area network (LAN). Based on the proposed strategy discussed in section 4.4.4 a cloud prediction software is developed and

implemented on a Linux operating Raspberry Pi computer which acquires snapshots from the sky camera in regular time steps and then generates and archives recent cloud segmentation and optical-flow data used for the solar occlusion forecast. Meanwhile, for the purpose of future analysis all key data are logged, i.e. image processing results, SO_i and CO_i figures. Ultimately, the RR command is generated and sent out to a Solar Gate [121], which is an intermediate device to enable external control of the PV power export by overriding the MPPT operation of the grid-tied solar inverter #1. The solar inverter #2 is used with no export smoothing control to allow a comparative evaluation of the proposed PVG smoothing algorithm. Fig. 4.4 makes a visual presentation of the composition of the testbed while Table 4.1 gives further details about that [119].

4.6 Evaluation and Analysis

This section aims at establishing a benchmark to assess performance and eligibility of the previously discussed PVG smoothing schemes. They are compared with the conventional storage-based method in terms of required capacity of the storage backup and the frequency of its usage. A preliminary trial experiment was conducted at Magellan Power in Western Australia, including different meteorological conditions, i.e. fully sunny, overcast, and partly cloudy. The collected data set includes all the critical prediction data including SO_i , CO_i , incident angle α , and the export power of the uncontrolled solar inverters #2. It allows trying different set points of Eq. (4.17) on the simulation model of the proposed PVG smoothing algorithm in Matlab/Simulink to obtain the most suitable values. An evaluative trial was also carried out over 10 days in December 2015 to demonstrate the practicality of the proposed smoothing algorithm. In this experiment, inverter #1 was subject to the export smoothing based on the proposed binary prediction approach of section 4.4.4 and the set points in Table 4.2 while inverter #2 was operating normally with no smoothing controls. As representative samples, the measurement results of the proposed binary cloud prediction based PVG smoothing approach are presented accompanied with the simulation results associated with the other methods using ideal export prediction and storage backup. Figs. 4.5, 4.7, 4.9, 4.11, and 4.13 illustrate the comparative results for 4th, 6th, 7th, 8th, and 9th of December, 2015 with scattered fast-moving clouds, as well as mostly clear sky. Furthermore, the respective aggregated SO_i and CO_i figures and the resultant smoothing command are illustrated in Figs. 4.6, 4.8,

Table 4.1: Specifications of testbed [119]

	Parameter	Value
Camera	Model	ACTi E925
	Communication	TCP/IP
	Viewing Angle	189°(overview), 115.3°(high detail)
	Focal Length	Fixed, f1.19 [mm]
	Dynamic Range	Basic WDR 74 [dB]
Controller	Model	Raspberry Pi 2 Model B
	CPU	900MHz quad-core ARM Cortex-A7
	RAM	1 [GB]
	Storage	16 [GB]
Inverter #1	Model	SMA Sunny Boy 5000TL
	Rated power	4.6 [kW]
	Nominal AC voltage	210 ··· 230 [V]
	MPP voltage range	100 ··· 500 [V]
	Max. input current	15 [A]
Inverter #2	Model	Solis-4K-2G
	Rated power	4 [kVA]
	Nominal AC voltage	180 ··· 270 [V]
	MPP voltage range	100 ··· 500 [V]
	Max. input current	15 [A]
PV Array #1 / #2	Module	ESM200S-125 Monocrystalline
	Open Circuit Voltage- V_{OC}	388.8 [V]
	Short Circuit Current- I_{SC}	6.3 [A]
	Peak Power Watts- P_{MPP}	1.8 [kW] @ 314.1 [V] , 5.73 [A]
	Panel Azimuth Angle	0°N
	Panel Tilt Angle	34°
Location	Latitude	32.1°S
	Longitude	115.81°E
	Elevation	31 [m]

4.10, 4.12, and 4.14, respectively. The energy balance profile, i.e. energy yield, the contribution of the BS backup, and curtailed energy, for different approaches are summarised and compared in Fig. 4.15. The BS backup is considered in the prediction based methods as well to compensate the probable inaccurate prediction of under generation events. During the ramp-up conditions, the smoothing

energy is recovered into the BS and the remainder is curtailed [119].

The following remarks could be concluded from the comparative results:

- The BS assisted PVG smoothing (section 4.4.1; Eqs. (4.9)-(4.11)) involves bidirectional supporting energy exchange during ramp events. Hence, to maintain the RR criterion the energy injection and absorption are necessary during the ramp down and ramp up events, respectively. This is illustrated in Figs. 4.5(a), 4.7(a), 4.9(a), 4.11(a), and 4.13(a), where P_{Inj} and P_{Abs} represent the injected and absorbed power, respectively. The inevitable reliance on the storage support is a financial barrier to vast deployment of PV resources across the areas that RR regulation is mandated by the grid operator. In particular, the BS system has to be oversized in energy capacity to deliver the required smoothing power over a relatively short duration of 10 [min] [58]. As Fig. 4.15(c) implies this method doesn't need much energy curtailment which explains its comparatively superior energy yield in Fig. 4.15(a). Nevertheless, the capital cost and the maintenance of the BS has created a motivation for exploring more economical alternatives.
- As Figs. 4.5(b), 4.7(b), 4.9(b), 4.11(b), and 4.13(b) implies, the ideal export prediction PVG smoothing (section 4.4.2; Eqs. (4.12)-(4.14)) mostly relies on power curtailment and power injection is no longer required. Fig. 4.15(b) also confirms the viability of storage-free smoothing method provided the occurrence of the rapid generation variations are accurately predicted and the resulting export power is precisely estimated. However, in order to achieve the maximum yield the energy absorption P_{Abs} has to be handled by BS and delivered to the grid while the RR requirement is maintained. Since this approach doesn't necessarily rely on the energy absorption, the BS could be eliminated at the cost of reduced energy efficiency, as indicated in Fig. 4.15(a). From a financial point of view, mitigating the storage distinctly outweighs the reduced revenue due to the lower yield. The capital price of the BS system normally accounts for a significant portion of the total cost of a BS assisted PV plant, e.g. it adds up to 50% to price of the PVG plant, as of 2012 in US [122]. On the other hand, in Perth, Western Australia, only 30% of the days are cloudy in average which are not of high yield compared to an ordinary sunny day [123]. Moreover, during the cloudy days, only a portion of the generation is curtailed in the smoothing treatment. This suggests that deployment of the BS can potentially recover less than 30% of annual yield while it raises the initial cost of the plant up

to 50% which is not financially justified compared to the prediction based PVG smoothing approach.

- The proposed PVG smoothing based on output estimation (section 4.4.3; Eqs. (4.15)-(4.16)) shows a virtually varying performance depending on the degree of cloudiness. As seen in Figs. 4.5(c), 4.7(c), 4.9(c), 4.11(c), and 4.13(c), this method suffers from the lack of perfect accuracy in the presence of fast moving clouds. Although, the relative inaccuracy is a typical drawback to the imagery based cloud prediction approaches, in the case of highly cloudy days with substantially intermittent generation level it still saves a remarkable amount of required backup power required for smoothing process. In contrast, during the mostly clear days with occasional brief shading events, its poor performance is more evident (Fig. 4.15(b)). This is mainly due to the erroneous estimation during the clear-sky periods. Moreover, the simplifications made in the calculation of projected generation level in Eq. (4.15) may create an offset estimation error during the clear sky periods and unnecessary energy absorption. Hence, this method doesn't show an excellent energy yield when compared to the ideal export prediction (Fig. 4.15(a)). Overall, this method reduces the amount of injected smoothing energy, while the required bidirectional energy exchange makes the storage backup unavoidable.
- The proposed binary prediction based PVG smoothing approach (section 4.4.4; Eqs. (4.17)-(4.18)), in essence, operates by restricting PVG export power once passing clouds are projected to obscure either the solar disc or the circumsolar region. The latter compensates for the inherent imperfect accuracy in the cloud prediction process. Compared to the ideal generation prediction, this approach involves a higher level of energy curtailment during the cloudy days which deteriorates its performance in terms of energy harvest (Fig. 4.15(a)). According to the experimental results, the amount of required BS backup is reduced to an inconsiderable level in only a few infrequent instances in cloudy days which is negligible when compared with the conventional storage based method (Figs. 4.5(d), 4.7(d), 4.9(d), 4.11(d), and 4.13(d)). In particular, slight violation from the required RR up to a certain extent is allowed by most network operators, e.g. the Horizon Power Corporation in Western Australia permits for a 10% non-linearity in the RR of PVG power export [124]. Therefore, since the required backup power injection doesn't exceed 10% of rated power ($10\% \times 1.8$ [kW]), those

Table 4.2: Smoothing set points [119].

Parameter	Symbol	Value
Permissible RR	R_s	180 [Wmin ⁻¹]
Min Observation Range	t_{h1}	120 [s]
Max Observation Range	t_{h2}	155 [s]
Forecast Range	t_f	10 [min]
Split Forecast Range	t_{SP}	30 [s]
SOi Threshold	θ_{SO}	0.15
COi Threshold	θ_{CO}	0.15
Shut-Off Coefficient	C_{Base}	20%

could be well accommodated by the existing spinning reserves of the utility. This suggests that by excluding the supporting BS this method still shows a satisfactory smoothing performance.

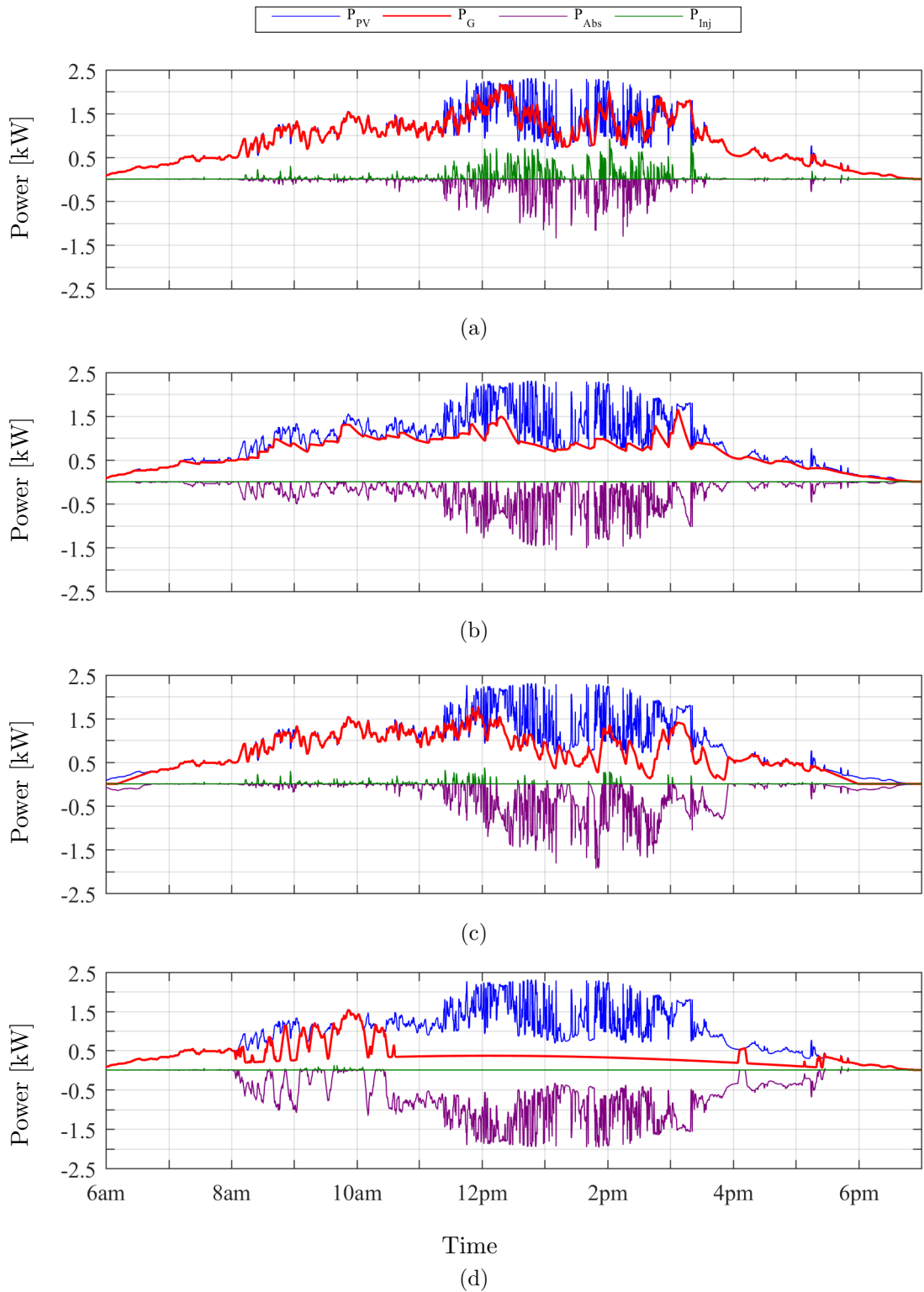


Figure 4.5: Smoothing results for 4 December 2015. (a) Storage-based. (b) Ideal Prediction. (c) Estimation-based. (d) Binary Prediction [119].

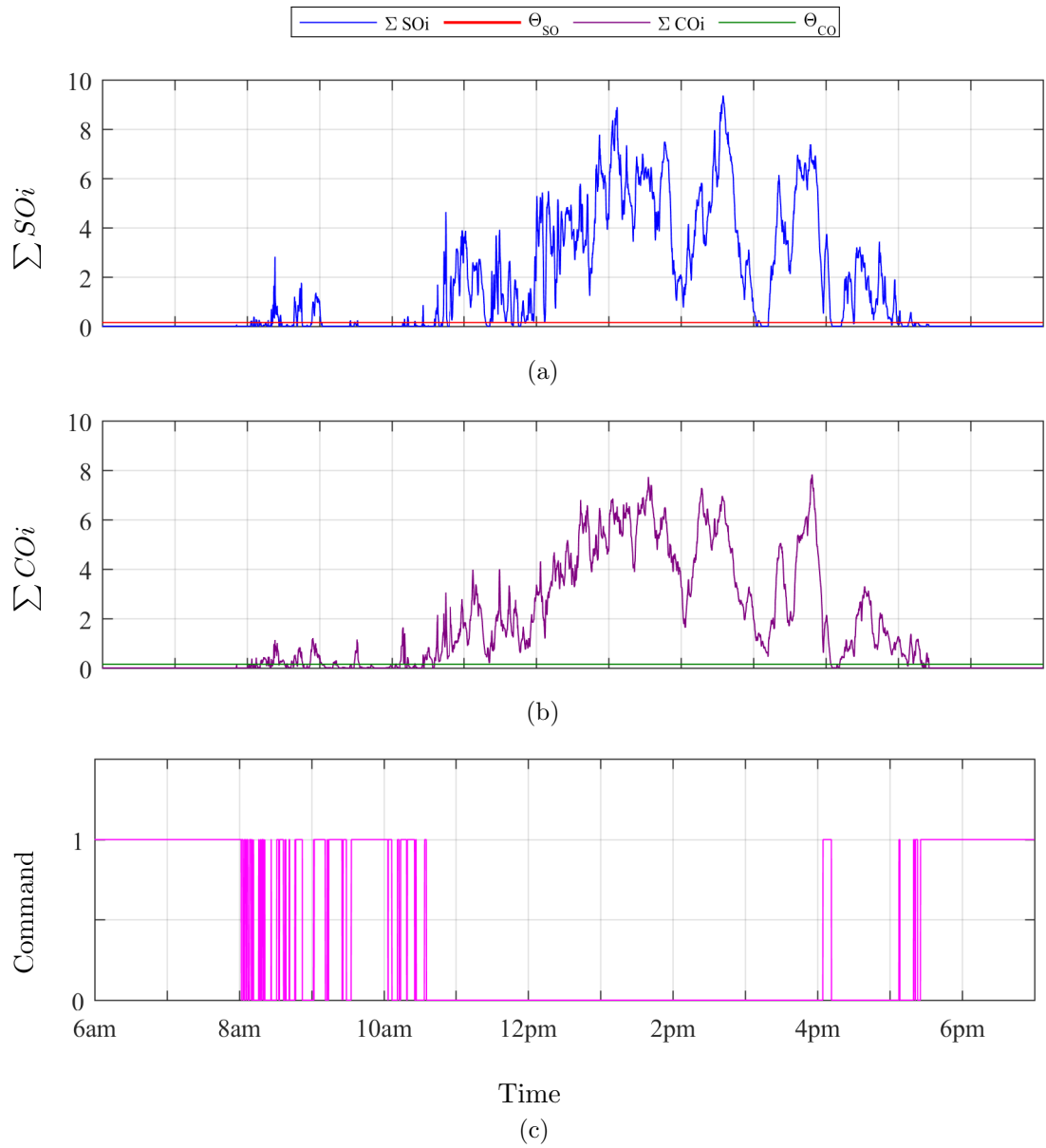


Figure 4.6: Smoothing signals for 4 December 2015. (a) Total SO_i . (b) Total CO_i . (c) Export toggle command to solar inverter [119].

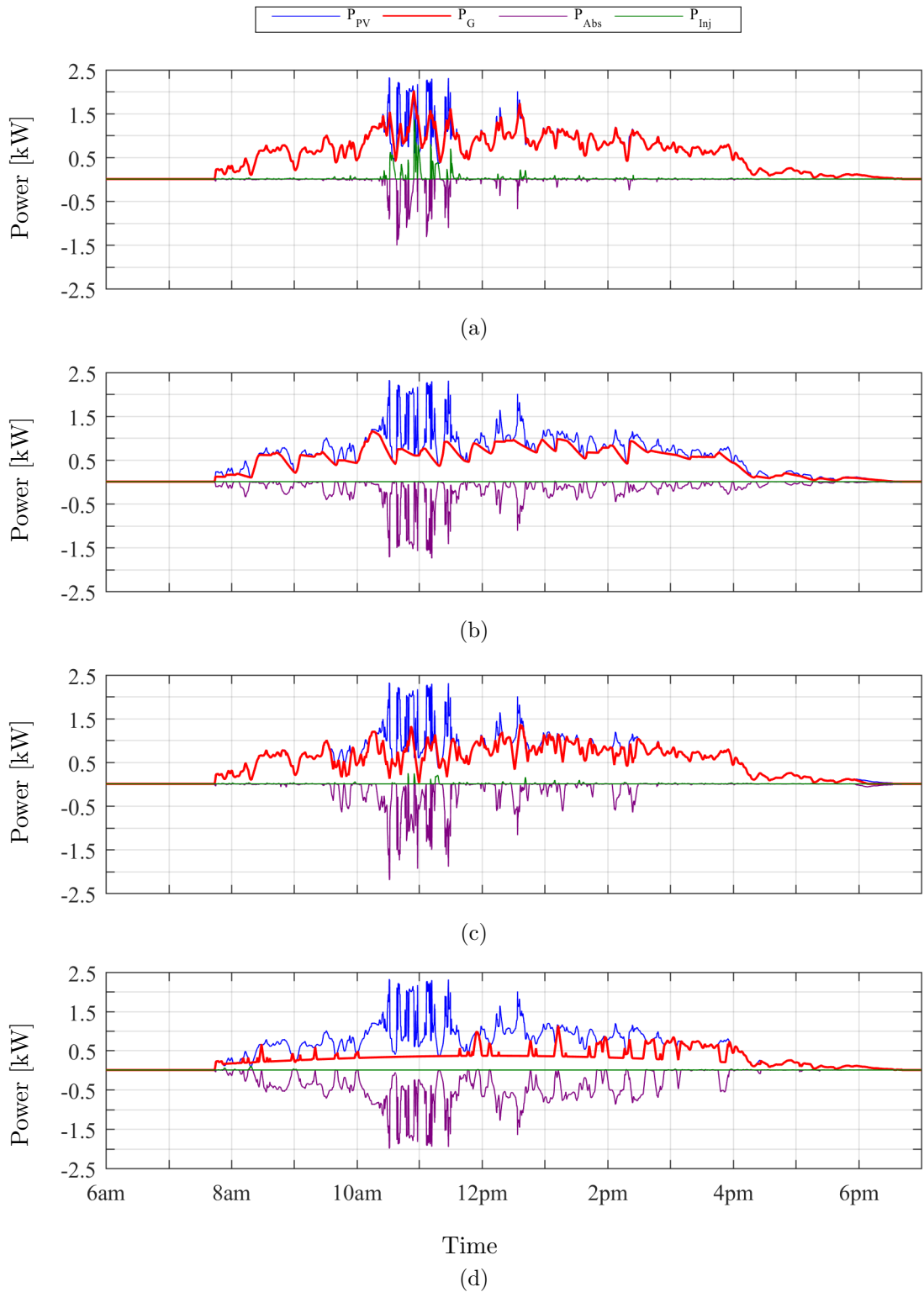


Figure 4.7: Smoothing results for 6 December 2015. (a) Storage-based. (b) Ideal Prediction. (c) Estimation-based. (d) Binary Prediction.

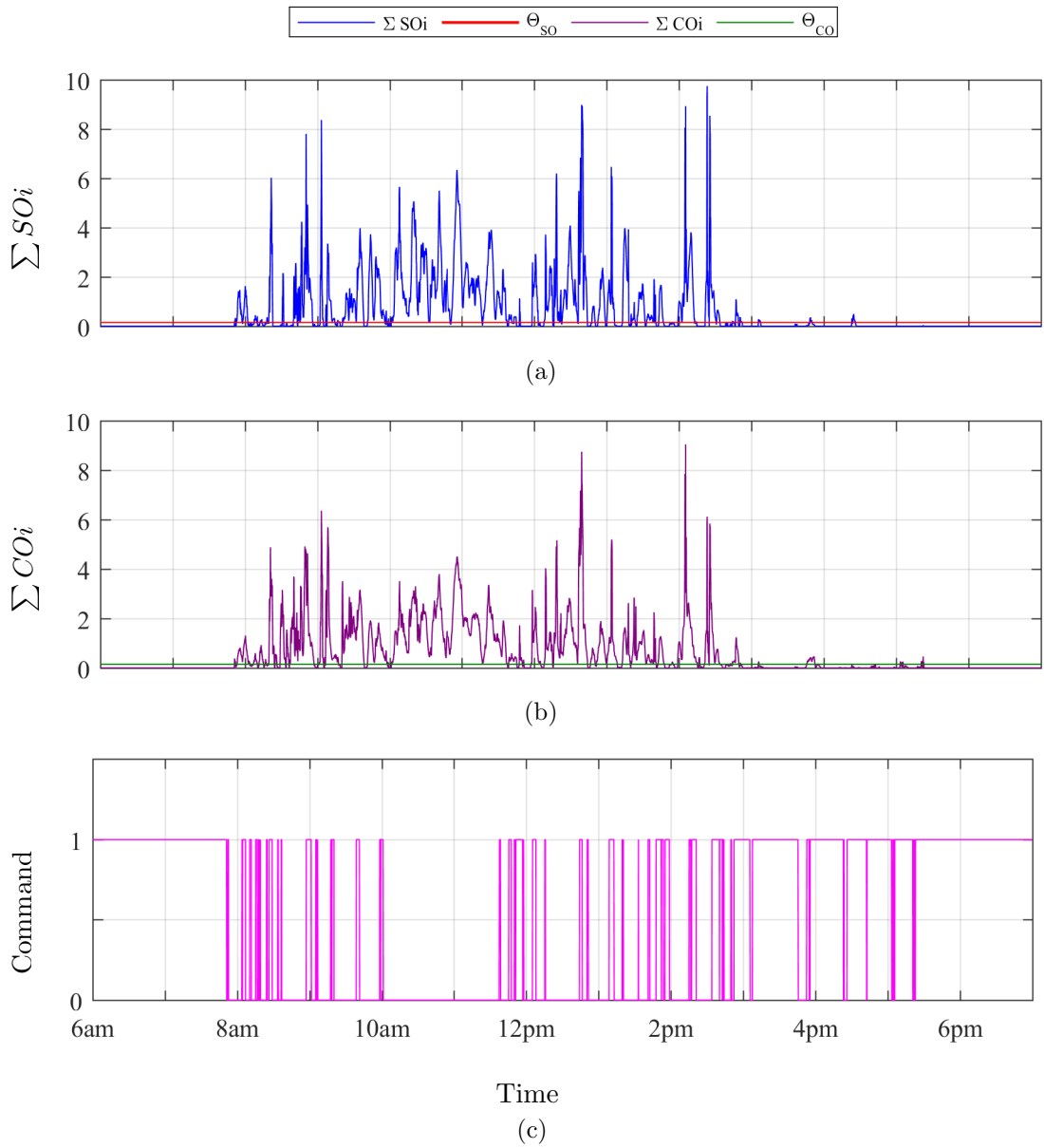


Figure 4.8: Smoothing signals for 6 December 2015. (a) Total SO_i . (b) Total CO_i . (c) Export toggle command to solar inverter.

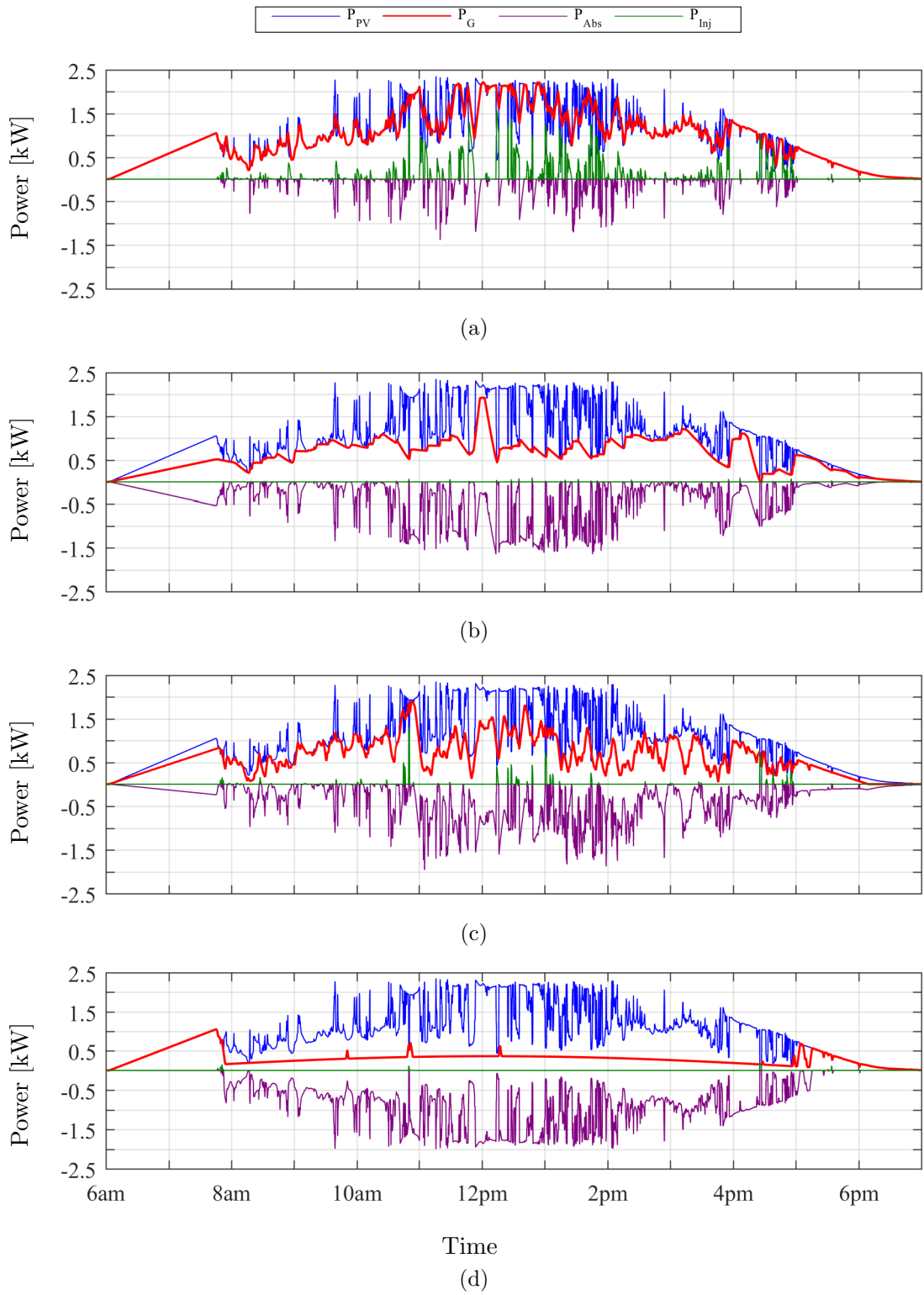


Figure 4.9: Smoothing results for 7 December 2015. (a) Storage-based. (b) Ideal Prediction. (c) Estimation-based. (d) Binary Prediction.

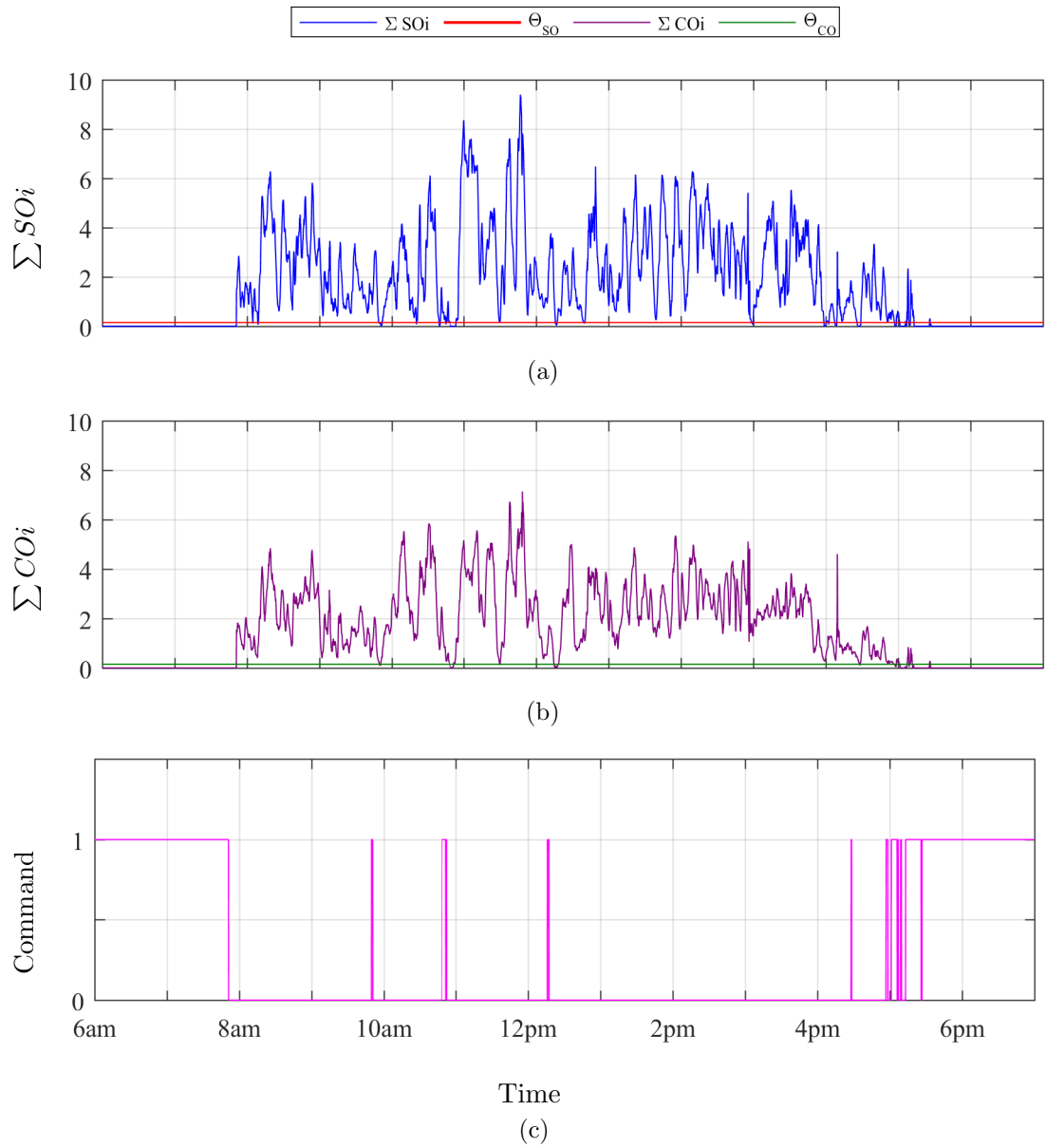


Figure 4.10: Smoothing signals for 7 December 2015. (a) Total SO_i . (b) Total CO_i . (c) Export toggle command to solar inverter.

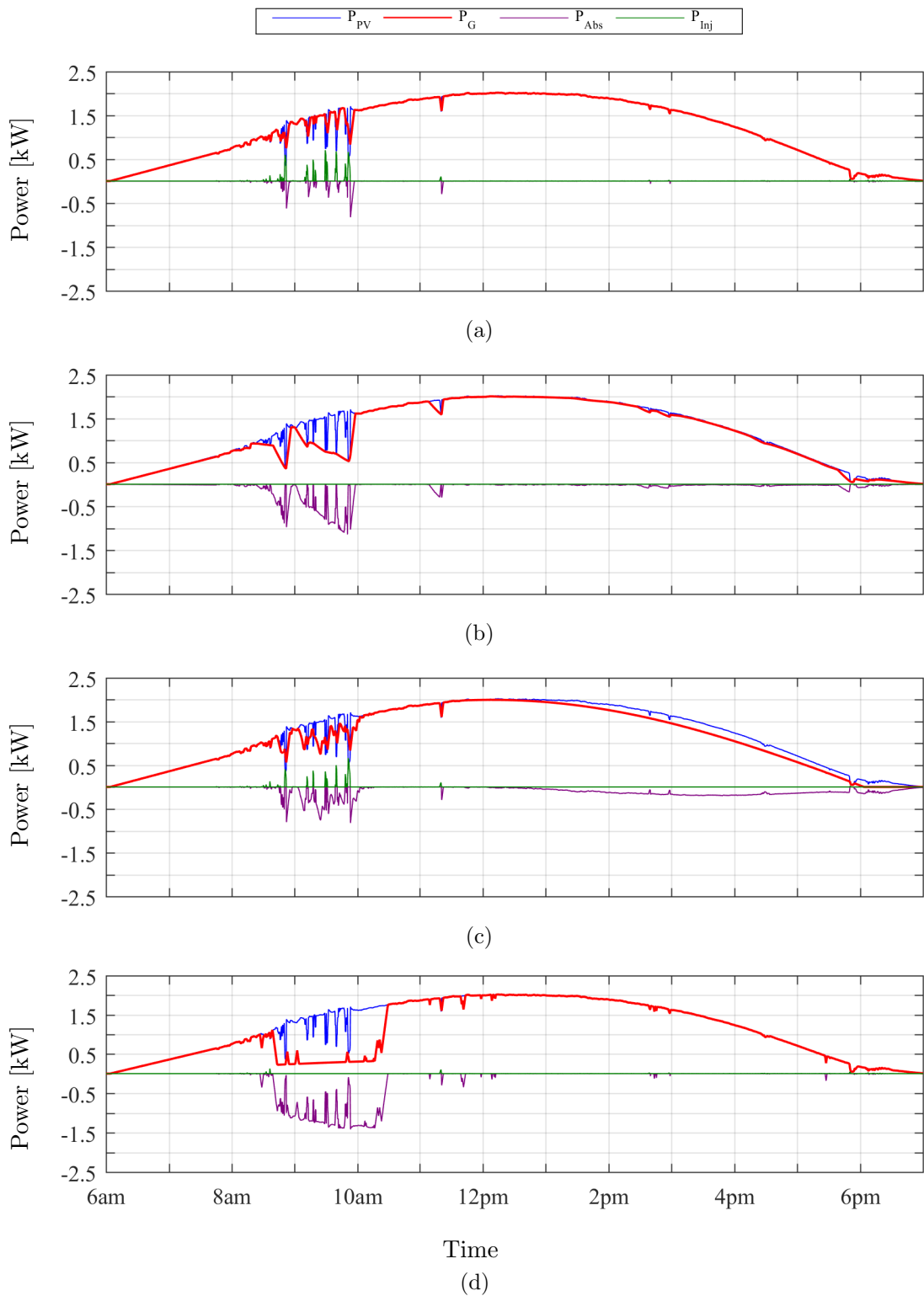


Figure 4.11: Smoothing results for 8 December 2015. (a) Storage-based. (b) Ideal Prediction. (c) Estimation-based. (d) Binary Prediction [119].

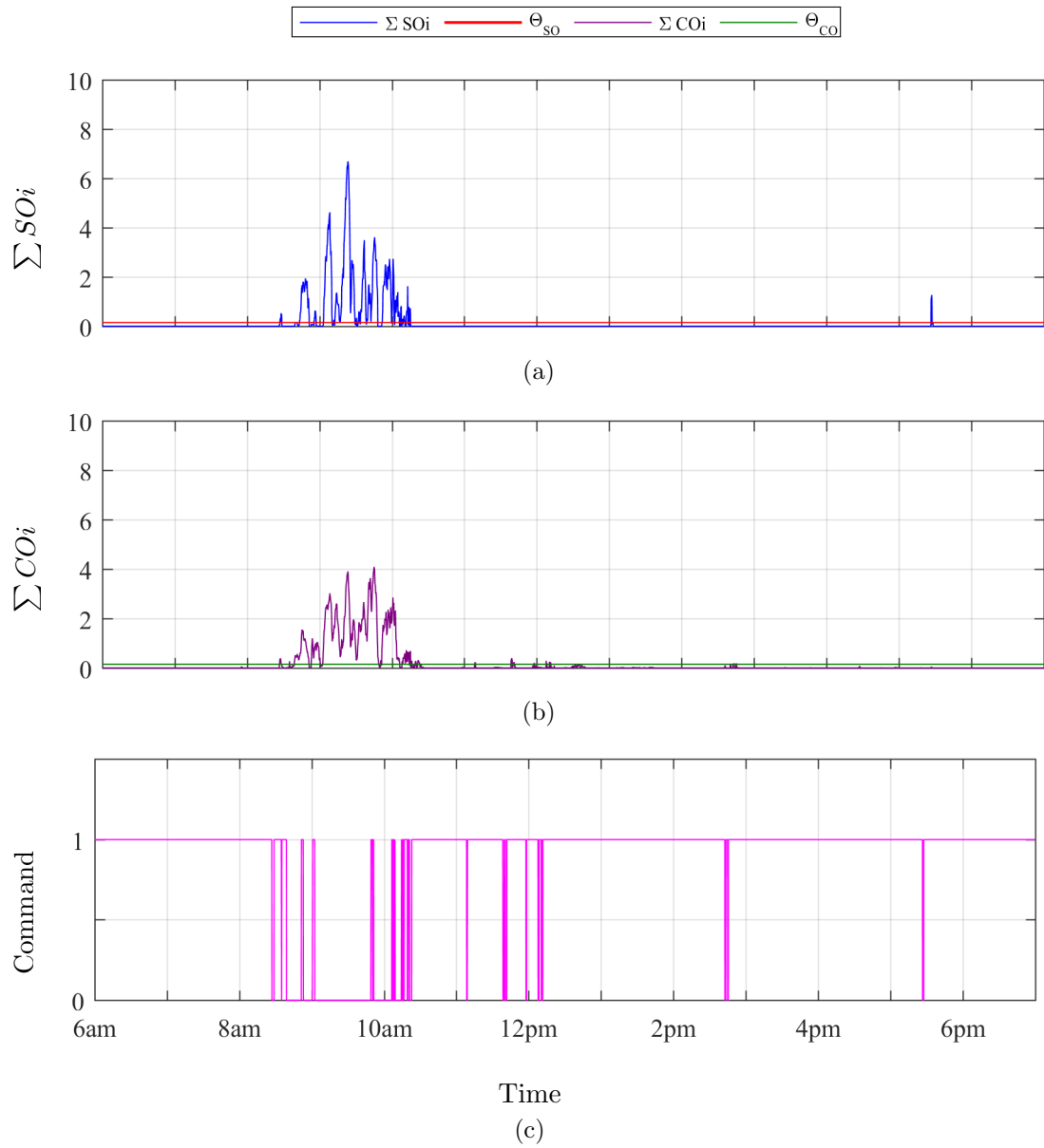


Figure 4.12: Smoothing signals for 8 December 2015. (a) Total SO_i . (b) Total CO_i . (c) Export toggle command to solar inverter [119].

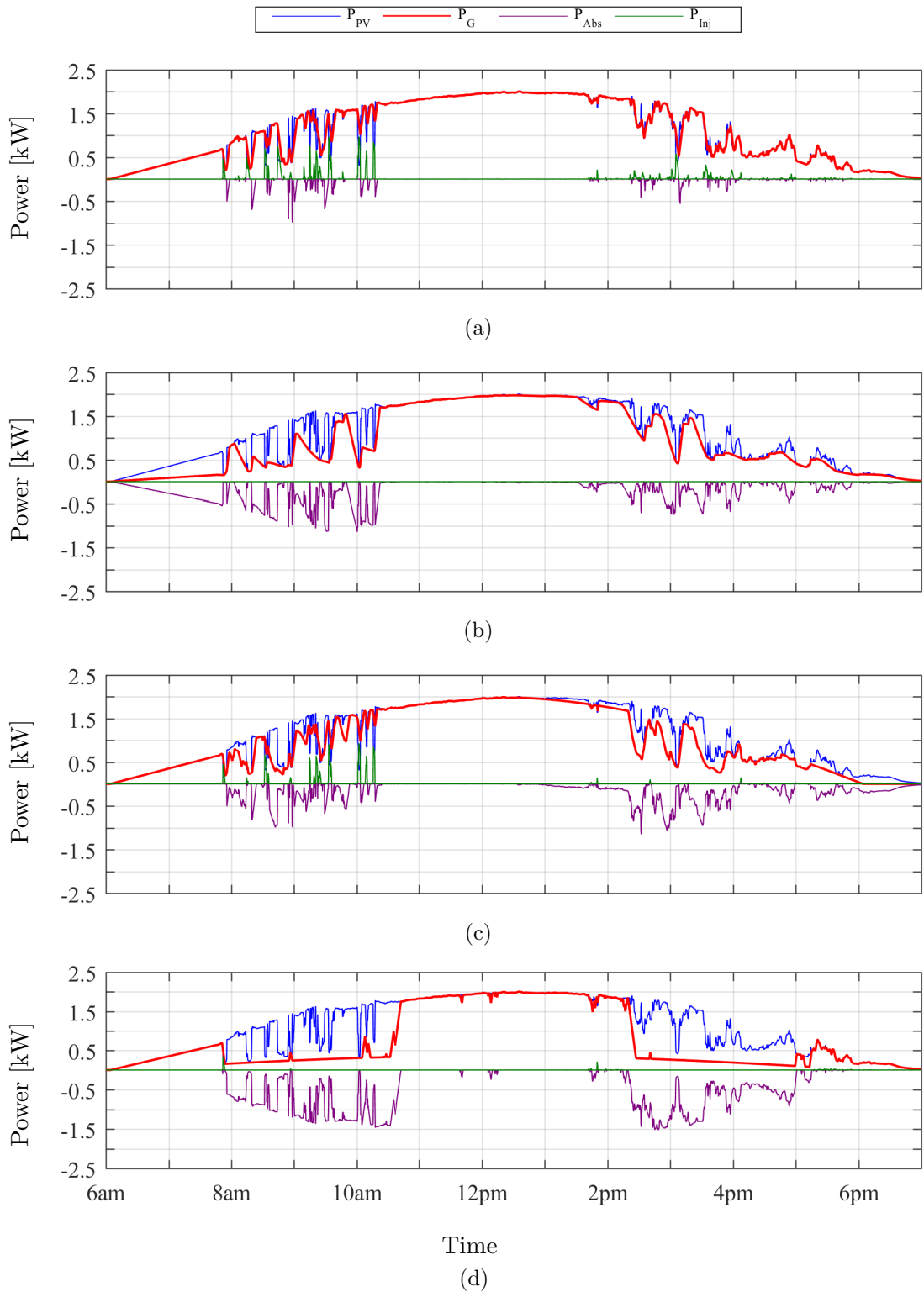


Figure 4.13: Smoothing results for 9 December 2015. (a) Storage-based. (b) Ideal Prediction. (c) Estimation-based. (d) Binary Prediction.

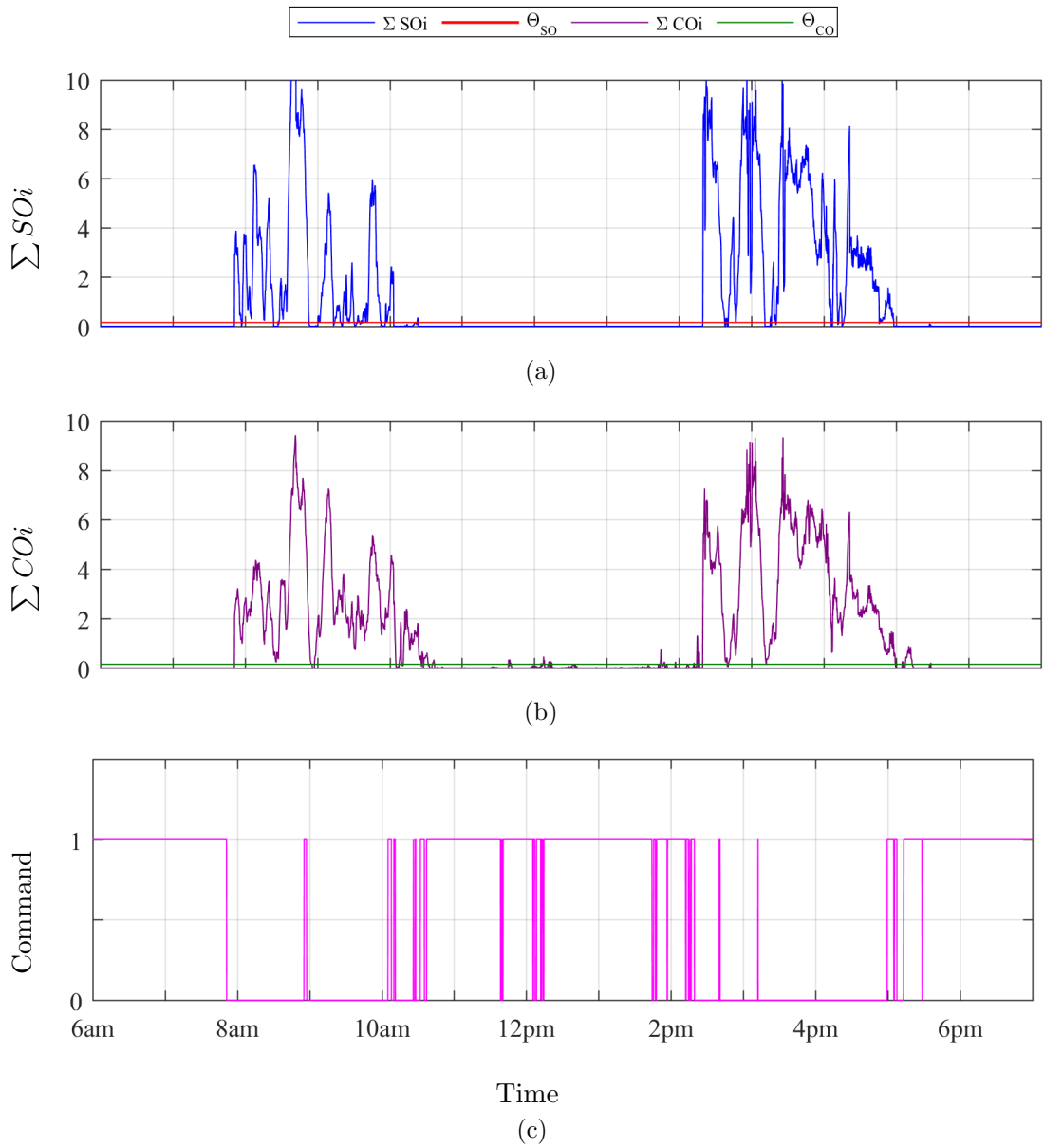


Figure 4.14: Smoothing signals for 9 December 2015. (a) Total SOi . (b) Total COi . (c) Export toggle command to solar inverter.

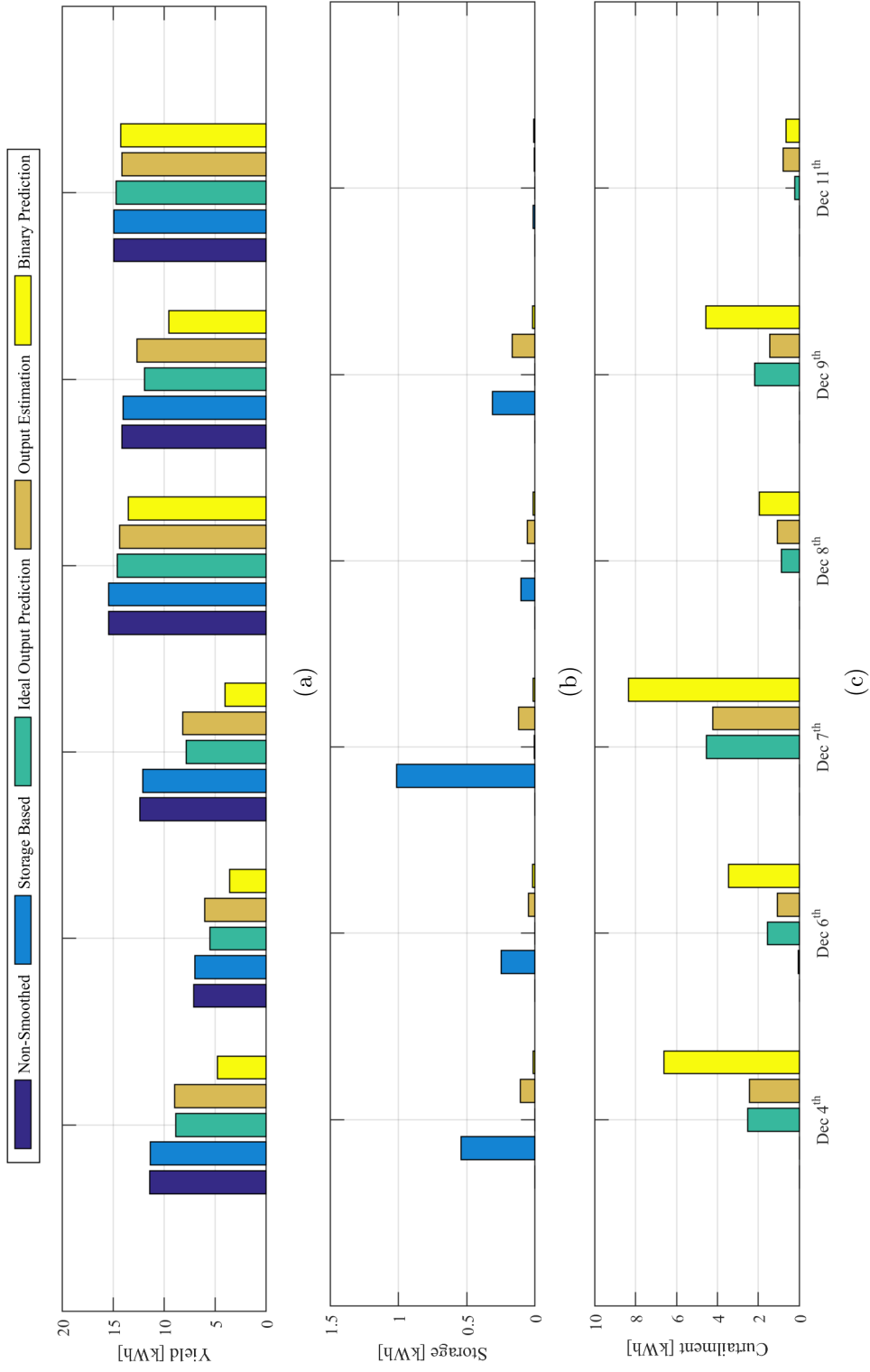


Figure 4.15: Segregated energy balance for different smoothing approaches.
 (a) Energy yield. (b) Engagement of the BS. (c) Energy curtailed.

4.7 Summary

This chapter proposes a practical battery-optimised approach for PVG export smoothing that relies on real-time images captured by a sky camera to address the utility concerns about the intermittent short-term fluctuations in output power due to environmental factors such as passing clouds. The performance of the proposed smoothing approach is evaluated through a series of experimental tests on a prototype that has been constructed at Magellan Power in Western Australia. The system includes two grid-connected solar inverters where one is controlled by the proposed smoothing software and the other operates without an external RR controller. The experimental results are also compared with the associated results of the conventional BS-based smoothing strategy simulated in Matlab/Simulink. A perfectly accurate PVG output prediction results in a regulation method with no reliance on the BS back-up while yield energy is not remarkably compromised. Given the inherent shortcomings of the imagery-based prediction approaches, a novel averaged cloud prediction scheme with improved robustness is proposed that is capable of indicating occlusion of the sun sufficiently ahead of its incidence. The proposed binary cloud prediction using a sky camera could significantly mitigate the reliance of the conventional PVG smoothing strategy on the BS backup. Accordingly, this allows a remarkable reduction in the required BS for in the smoothing process. However due to the conservative design of the cloud prediction algorithm, for some operating conditions the approach may suffer from an inferior energy harvest profile when compared with the ideal prediction technique. Although deployment of the BS could potentially recover a portion of curtailed energy and improve the amount of yield, the gained benefit doesn't outweigh the initial expenditure on the BS. From a technical perspective, the experimental outcomes of the proposed prediction assisted PVG smoothing method support the feasibility of a reliable battery-optimised RR smoothing solution [119].

Chapter 5

Conclusion

5.1 Summary and Findings

The present dissertation sought to review the detrimental effects that the distributed grid-connected solar PV plants create in the highly penetrated electric distribution grids. It primarily focused on the intermittent and short-term variations in the output power of the PV generators. These variations potentially disturb the balance between generation and demand unless an appropriate smoothing measure is adopted. Otherwise, an additional amount of operational reserve should be utilised to handle the imbalance associated with the short-term variability of PV generation plants. The PVG smoothing solutions compensate the fast variations, primarily caused by passing clouds, and maintain the RR of the generated power within a specified limit. This enables further deployment of the distributed solar PV plant throughout the electric power network, eliminating the financial burden of upgrading the reserve capacity. BS can absorb the fast dips and rises of the PV generated power and meet the respective RR requirements. Whereas the prohibitive price of this solution makes that financially less viable. From a technical perspective, the capacity of the BS should be overestimated to provide the sufficient backup power for the smoothing purpose. On the other hand, the BS technologies of higher power density, e.g. Li-FePO₄, are more prone to the SOC imbalance in the series connection of battery cells for HV applications. The PV generation forecast offers a more cost-effective smoothing strategy. Where the output power is gradually reduced under the required RR when a cloud is predicted to shade the PV array. As soon as the cloud is cleared, the generation level ramps up on an appropriate slope. This effectively eliminates the sudden under-generations attributed to passing clouds, while power

curtailment during the controlled ramp events is unavoidable.

In the following a brief synopsis of the key investigations in each chapter is presented:

Chapter-1 presented a detailed literature review on how the distributed PVG plants influence the operation of the electric power systems. Moreover, it discussed different solutions to eliminate the intermittency of the dispersed PVG plants. This allows hosting higher level of these generation resources without upgrading the existing power plants.

Chapter-2 was a detailed discussion on the design and control of the power electronic converters for a PVG output smoother with HSS. A double-stage DC-DC-AC converter was deployed as an interface between the PV array and the utility grid. Two different structures i.e. AC-coupled and DC-coupled were investigated. For AC-coupled HSS smoother another DC-DC-AC converter with two bidirectional input ports was also dedicated to the smoothing process using a BS and UC. Whereas, in the DC-coupled structure the two parallel DC-DC converters were directly connected to the DC link of the DC-DC-AC converter. Simulation models and closed-loop controllers were developed for both configurations. The simulation results confirmed the reliable cooperation of the PV plant with the HSS-based smoothing facility in both configurations. In the DC-coupled smoother the control objective is stabilising the DC link voltage which causes AC side current transients during the rapid PVG variations. In contrast, the AC-coupled smoother exhibits more stable AC current.

Chapter-3 was concerned with an active equalising solution to the SOC imbalance in Li-FePO₄ battery stacks. The circuitry of a bidirectional flyback based active cell balancer with interleaved transformer connection was modelled and a control algorithm was proposed for that. During the charge/discharge cycle, the outlier cells were identified and the charge/discharge operation of the flybacks were decided so that the SOC imbalance was eliminated and all battery cells eventually came in parity. It was also pointed out that the interleaved arrangement of the transformers remarkably affects the speed of the equalising process. An additional equalising effect was achieved when more cells were included on the HV side of the transformers. To evaluate the energy efficiency of the active cell balancer, the passive cell equalisation was also modelled and simulated which pointed out

lower level of energy loss in the active balancer approach.

Chapter-4 looked into a PVG smoothing approach based on the short-term cloud prediction information. An ideal forecasting approach was simulated and it proved to completely eliminate the storage backup. It followed the proposed imagery-based method to indicate when the passing clouds cast a shadow on the PV arrays, well ahead of its occurrence. The proposed strategy deployed a sky-facing fish-eye camera to produce wide-angle sky images. Afterwards, the position of the sun, the cloud regions and their principal motion were identified to estimate the upcoming shading events in a timely manner. Moreover, the algorithm was implemented on a prototype and the generated prediction information was incorporated into a traditional storage-based PVG output smoothing system. The experimental results suggested that the designed algorithm successfully compensated the undesired short-term variability of the PVG output, although on very rare occasions it failed to predict a passing cloud at the right time. However, the resulting disturbances were of a negligible magnitude as small as the amount allowed for by the utility operators as a non-linearity error of the smoothing process. This confirmed the technical viability of the storage-less PVG output smoothing.

The present study made several contributions to the field of the generation smoothing of the solar PV:

- It looks into an HSS-based smoothing approach accounting for the structure of the power electronic converters as well as the control strategy.
- A control algorithm is proposed for a flyback active battery cell balancer with interleaved connection of the transformers. This provides a safe and efficient utilisation of the entire capacity of a large battery stack while eliminates any premature termination of the charge/discharge cycles attributed to SOC imbalance of the series-connected battery cells.
- An improved PVG smoothing approach based on real-time cloud prediction information is proposed and examined for the amount of required BS backup. It is eventually indicated that the storage-less PVG smoothing process is technically viable by the means of an imagery-based cloud forecasting method.

5.2 Limitations

Few limitations of this research need to be acknowledged. The PVG smoother is essentially a solution to mitigate the adverse effects of the intermittency in the PVG output power on the utility grid which is mainly manifested as a deviation in the critical parameters, i.e. frequency and bus voltages. However, the present work was not particularly designed to quantify the performance of the storage based and the prediction based PVG smoother in terms of the grid stabilisation. The scope of this research was limited to incorporating the imagery based cloud prediction information in the conventional BS based PVG smoothing algorithm and evaluate its performance through the practical trials.

5.3 Challenges

The major difficulty I faced during this study lies in the fact that the experimental setup was developed in Magellan Power premise. Therefore, in order to conduct the trials, I had to commute long distance off campus to Magellan Power office. Due to the user-friendly and block diagram environment of the Matlab/Simulink it has been widely used by researchers in the fields of computer vision and image processing. Moreover, the state-of-the-art hardware interfacing devices, e.g. DSpace, allow rapid prototyping and practical verification of the designed models. When it comes to industrial manufacturing, the Simulink Coder toolbox offers automatic low-level code generation for implementing on a suitable target platform. The produced C/C++ code usually requires further manual modifications for probable troubleshooting and improving its efficiency. To this end, implementing an algorithm in C/C++ from scratch proved to be a promising alternative with a unified structure, optimised processing burden, easier troubleshooting, and increased cross-platform productivity. Due to the industrial orientation of this research the cloud prediction software, discussed in chapter 4, was developed in C++ deploying the open-source image-processing library of OpenCV. From an academic perspective, this option may not serve as a time efficient prototyping solution, as extra effort and time should be allowed to facilitate the visual presentation and comparison of the results. Moreover, for the purpose of evaluation and visualisation, the collected data was manually imported to Matlab/Simulink which was a time-consuming process. Another problem I faced in the development of the prototype was building the outdoor fisheye camera system which was a mechanical design process, in particular, it

had to withstand the adverse weather conditions.

5.4 Recommendations

There are few potential areas of research which have not been investigated in this research. It is recommended that further research is undertaken in the following areas:

- In the present research, the operation of the flyback converters were decided based on the relative SOC of the adjacent subsets. A potential area of future research would be to investigate an improved active cell balancing algorithm taking the relative SOC of each subset with respect to all subsets.
- The sources of the SOC imbalance, i.e. uneven thermal distribution and manufacturing tolerance, and their effect could be modelled and taken into account in the cell balancing process.
- In the proposed cloud prediction algorithm it was assumed that the clouds are single-layer making persistence motion in the sky. Further research is required to account for cloud classification according to the visual characteristics as well as long-term NWP information. The estimated optical transmissivity and light scattering properties of the clouds enable a more precise irradiance-predictive PVG smoothing approach with improved energy yield.
- The effective viewing angle in a fisheye image is somewhat compromised through the undistortion process. Therefore, multiple projections from different cameras could be stitched together to obtain a wide undistorted projection with a potential to distinguish between different cloud layers. This creates a great potential to develop a central controller collecting the real-time images from a network of sky-facing cameras distributed across a wide area to obtain a region-wide cloud map and produce the respective smoothing commands for all PVG plants.
- The cloud prediction algorithm could be further improved in functionality and accuracy if ANN processing approach is incorporated for cloud identification and classification, and resulting irradiance estimation.
- The long-term regional weather prediction data from the meteorological satellites as well as NWP models could be also incorporated to improve the accuracy and reliability of the short-term imagery based cloud prediction data.

- The stabilisation of the power systems with high PVG penetration level using the proposed imagery based smoothing solution.
- A central controller for multiple predictive PVG smoothing solutions geographically distributed over the utility grid.
- The financial advantages of the proposed solution over the conventional BS based approach.

Appendix A

Linkage Matrices of Active Cell Balancer

The linkage matrices of the fly-back active cell balancer for different arrangements of subsets are presented here:

$$A_{(4 \times 6)} = \left[\begin{array}{ccc|ccc|ccc|ccc}
 1 & \dots & 1 & 1 & \dots & 1 & 0 & \dots & 0 & 0 & \dots & 0 \\
 \vdots & \ddots & \vdots & \vdots & \ddots & \vdots & \vdots & \ddots & \vdots & \vdots & \ddots & \vdots \\
 1 & \dots & 1 & 1 & \dots & 1 & 0 & \dots & 0 & 0 & \dots & 0 \\
 \hline
 0 & \dots & 0 & 1 & \dots & 1 & 1 & \dots & 1 & 0 & \dots & 0 \\
 \vdots & \ddots & \vdots & \vdots & \ddots & \vdots & \vdots & \ddots & \vdots & \vdots & \ddots & \vdots \\
 0 & \dots & 0 & 1 & \dots & 1 & 1 & \dots & 1 & 0 & \dots & 0 \\
 \hline
 0 & \dots & 0 & 0 & \dots & 0 & 1 & \dots & 1 & 1 & \dots & 1 \\
 \vdots & \vdots & 0 & \vdots & \ddots & \vdots & \vdots & \ddots & \vdots & \vdots & \ddots & \vdots \\
 0 & \dots & 0 & 0 & \dots & 0 & 1 & \dots & 1 & 1 & \dots & 1 \\
 \hline
 0 & \dots & 0 & 0 & \dots & 0 & 0 & \dots & 0 & 1 & \dots & 1 \\
 \vdots & \ddots & \vdots & \vdots & \ddots & \vdots & \vdots & \ddots & \vdots & \vdots & \ddots & \vdots \\
 0 & \dots & 0 & 0 & \dots & 0 & 0 & \dots & 0 & 1 & \dots & 1
 \end{array} \right] \begin{array}{l} \left. \vphantom{\begin{array}{c} \vdots \\ \vdots \\ \vdots \end{array}} \right\} 6 \\ \left. \vphantom{\begin{array}{c} \vdots \\ \vdots \\ \vdots \end{array}} \right\} 6 \\ \left. \vphantom{\begin{array}{c} \vdots \\ \vdots \\ \vdots \end{array}} \right\} 6 \\ \left. \vphantom{\begin{array}{c} \vdots \\ \vdots \\ \vdots \end{array}} \right\} 6 \end{array} \quad (A-1)$$

$\underbrace{\hspace{2em}}_6$

$\underbrace{\hspace{2em}}_6$

$\underbrace{\hspace{2em}}_6$

$\underbrace{\hspace{2em}}_6$

$$A_{(3 \times 8)} = \left[\begin{array}{ccc|ccc|cc}
1 & \dots & 1 & 1 & \dots & 1 & 0 & \dots & 0 \\
\vdots & \ddots & \vdots & \vdots & \ddots & \vdots & \vdots & \ddots & \vdots \\
1 & \dots & 1 & 1 & \dots & 1 & 0 & \dots & 0 \\
\hline
0 & \dots & 0 & 1 & \dots & 1 & 1 & \dots & 1 \\
\vdots & \ddots & \vdots & \vdots & \ddots & \vdots & \vdots & \ddots & \vdots \\
0 & \dots & 0 & 1 & \dots & 1 & 1 & \dots & 1 \\
\hline
0 & \dots & 0 & 0 & \dots & 0 & 1 & \dots & 1 \\
\vdots & \ddots & \vdots & \vdots & \ddots & \vdots & \vdots & \ddots & \vdots \\
0 & \dots & 0 & 0 & \dots & 0 & 1 & \dots & 1
\end{array} \right] \left. \begin{array}{l} \vphantom{A_{(3 \times 8)}} \\ \vphantom{A_{(3 \times 8)}} \\ \vphantom{A_{(3 \times 8)}} \end{array} \right\} \begin{array}{l} 8 \\ 8 \\ 8 \end{array} \tag{A-2}$$

$\underbrace{\hspace{10em}}_8$
 $\underbrace{\hspace{10em}}_8$
 $\underbrace{\hspace{10em}}_8$

$$A_{(6-8-4-6)} = \left[\begin{array}{ccc|ccc|cc|cc}
1 & \dots & 1 & 1 & \dots & \dots & 1 & 0 & \dots & 0 & 0 & \dots & 0 \\
\vdots & \ddots & \vdots & \vdots & \ddots & \ddots & \vdots & \vdots & \ddots & \vdots & \vdots & \ddots & \vdots \\
1 & \dots & 1 & 1 & \dots & \dots & 1 & 0 & \dots & 0 & 0 & \dots & 0 \\
\hline
0 & \dots & 0 & 1 & \dots & \dots & 1 & 1 & \dots & 1 & 0 & \dots & 0 \\
\vdots & \ddots & \vdots & \vdots & \ddots & \ddots & \vdots & \vdots & \ddots & \vdots & \vdots & \ddots & \vdots \\
\vdots & \ddots & \vdots & \vdots & \ddots & \ddots & \vdots & \vdots & \ddots & \vdots & \vdots & \ddots & \vdots \\
0 & \dots & 0 & 1 & \dots & \dots & 1 & 1 & \dots & 1 & 0 & \dots & 0 \\
\hline
0 & \dots & 0 & 0 & \dots & \dots & 0 & 1 & \dots & 1 & 1 & \dots & 1 \\
\vdots & \ddots & \vdots & \vdots & \ddots & \ddots & \vdots & \vdots & \ddots & \vdots & \vdots & \ddots & \vdots \\
0 & \dots & 0 & 0 & \dots & \dots & 0 & 1 & \dots & 1 & 1 & \dots & 1 \\
\hline
0 & \dots & 0 & 0 & \dots & \dots & 0 & 0 & \dots & 0 & 1 & \dots & 1 \\
\vdots & \ddots & \vdots & \vdots & \ddots & \ddots & \vdots & \vdots & \ddots & \vdots & \vdots & \ddots & \vdots \\
0 & \dots & 0 & 0 & \dots & \dots & 0 & 0 & \dots & 0 & 1 & \dots & 1
\end{array} \right] \left. \begin{array}{l} \vphantom{A_{(6-8-4-6)}} \\ \vphantom{A_{(6-8-4-6)}} \\ \vphantom{A_{(6-8-4-6)}} \\ \vphantom{A_{(6-8-4-6)}} \\ \vphantom{A_{(6-8-4-6)}} \end{array} \right\} \begin{array}{l} 6 \\ 8 \\ 4 \\ 6 \end{array} \tag{A-3}$$

$\underbrace{\hspace{10em}}_6$
 $\underbrace{\hspace{10em}}_8$
 $\underbrace{\hspace{10em}}_4$
 $\underbrace{\hspace{10em}}_6$

Appendix B

Calibration of the Fisheye Lens

The OcamCalib toolbox provides a convenient way to extract the intrinsic parameters of an omnidirectional camera through a few photos taken from a chessboard in different positions and orientations. The toolbox then extracts the corners points of the photos. The calibration parameters are then calculated and stored in a file. The toolbox also includes a number of functions which create the mapping arrays which are used for the conversion between fisheye and undistorted coordinates. Fig. B.1 shows the collection of fisheye photos of the chessboard and detected corners by the toolbox. The calculated parameters of the fisheye then are then used to verify library functions developed for removing the hemispherical distortion of the photos. Fig. B.2 illustrates the undistorted chessboard photos where all lines appear straight.

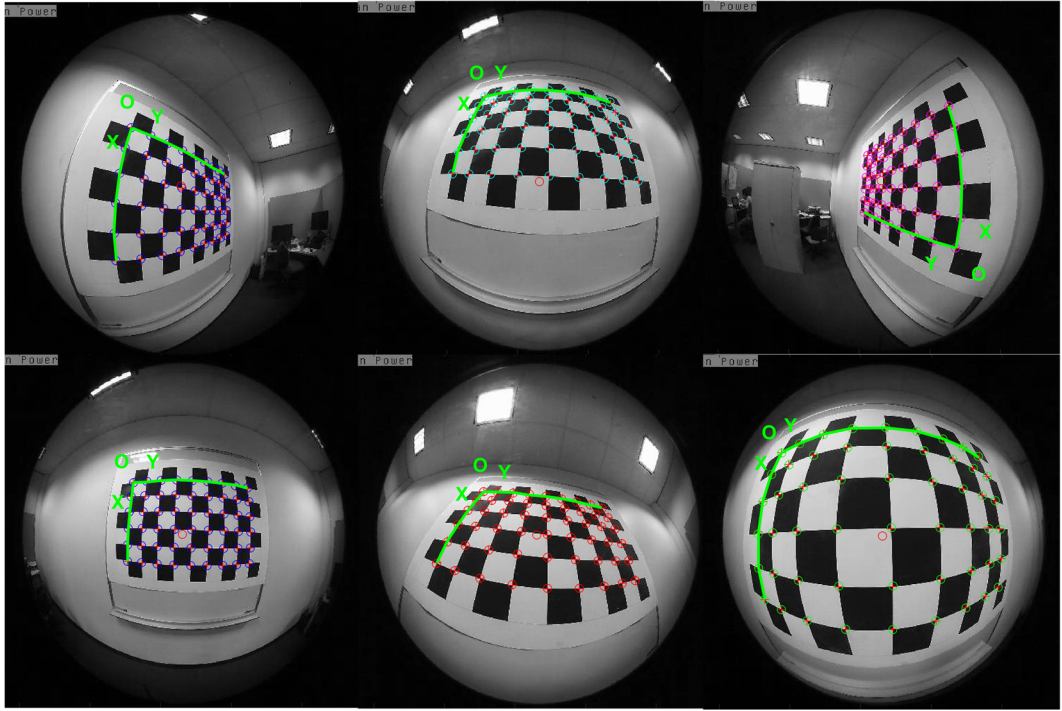


Figure B.1: The fisheye chessboard photos with detected corners points in 640×480 resolution.



Figure B.2: The undistorted chessboard photos in 640×480 resolution.

Appendix C

Refraction Parameter of the Fish-Eye Lens

In fish-eye lenses, the projection is based on a linear correlation between the angular position of the object and the projected point in the image [125]. Fig. C.1 shows the refraction diagram of a fish-eye lens. This yields the principle refraction relation:

$$\begin{aligned}d_2 &= \frac{d_1}{\alpha_1} \times \alpha_2 \\ &= r \times \alpha_2\end{aligned}\tag{C.1}$$

Given the linear behaviour of the fish-eye lens, the parameter r can be extracted from a series of photos taken from an object located at different angular positions with respect to the optical axis. This requires a plane with sectoral markings as Fig. C.2 to produce the calibration photo of Fig. C.3. The calibration results are plotted in Fig. C.4 which shows a linear trend over the whole radial extent of the image. Therefore the conversion coefficient of r is 2.5 [pixel/degree] in the resolution of 640×480 .

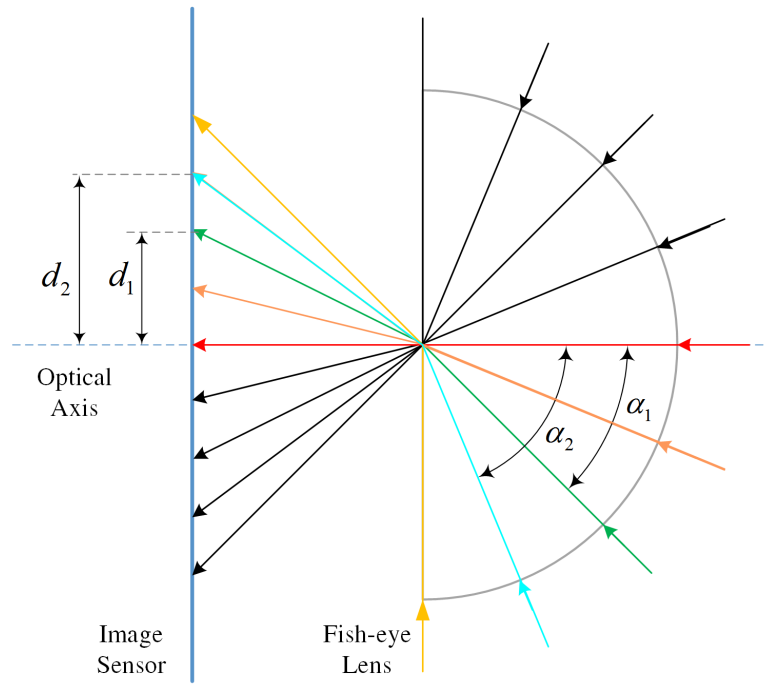


Figure C.1: The diagram of ray refraction in fish-eye lens [125].

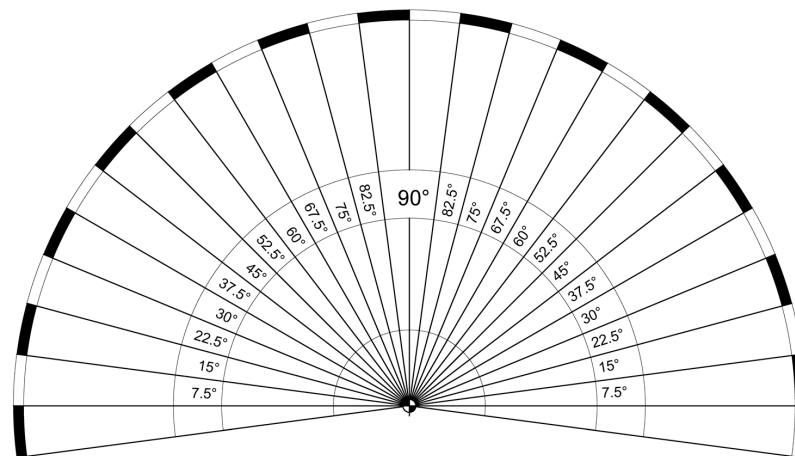


Figure C.2: The calibration plane with sectoral marking.

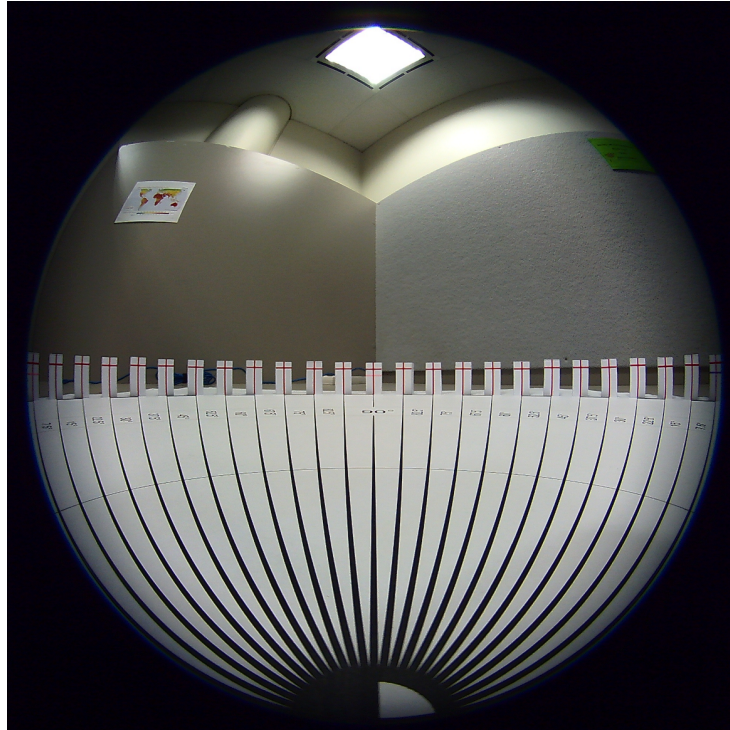


Figure C.3: The angular calibration photo.

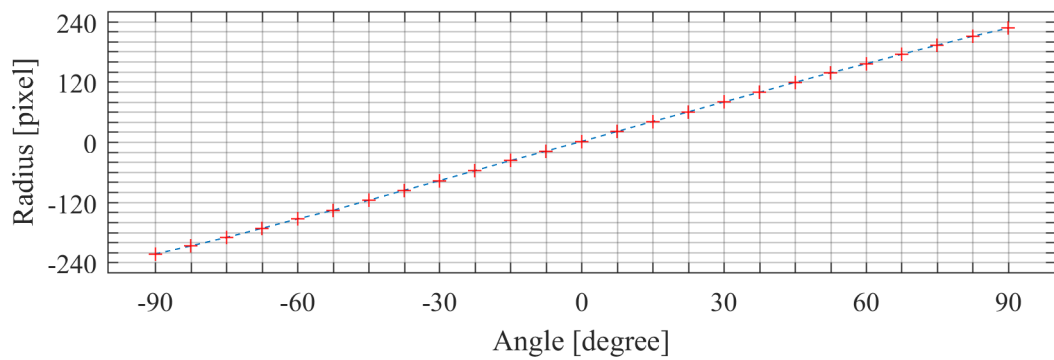


Figure C.4: The angular calibration curve in 640×480 resolution.

Appendix D

Full-Text of the Publications

Control Algorithm for Bidirectional Fly-back Active Cell Balancer with Interleaved Transformer Connections

Mojtaba Saleh, Mohammad A.S Masoum

mojtaba.saleh@postgrad.curtin.edu.au, m.masoum@curtin.edu.au,

Department of Electrical and Computer Engineering
Curtin University, Perth, WA, Australia

Lindsay Meek, Masoud Abshar

lmeek@magellanpower.com.au, mabshar@magellanpower.com.au

Magellan Powertronics Pty Ltd.
Perth, WA, Australia

Abstract— Fly-back converter has proved a promising option for effective bidirectional active cell balancing in series connected battery stacks. The stack could be organized as a number of subsets to facilitate an interleaved connection across consecutive subsets at the high-voltage side of transformers so that the voltage rating of components will be reduced accordingly. This structure features expandable modular attribute, however, creates more complicated charge transfer between cells which has to be taken into account in the control scheme. This paper sets out the operation principals and proposes a control strategy handling intra-subset imbalance as well as inter-subset uneven charge distribution. The results of simulation study confirms the effectiveness of the proposed control method in both charge and discharge cycles.

Index Terms—Active cell balancer, charge equalization, series-connected battery string, fly-back converter.

I. INTRODUCTION

The rapid progresses in battery technology and deployment of cells featuring high power and energy density, i.e. LiFePO₄, necessitate a state-of-the-art battery management system (BMS). In series-connected battery packs cell state of charge (SOC) imbalances, generally, accounts for slight mismatches in internal resistance, capacity, self-discharge rate, and temperature characteristics of cells due to manufacturing variations, which diverges by cell aging. Ineffective ventilation and uneven heat dissipation in battery packs moreover cause temperature difference between cells which widens this mismatch and exacerbate the SOC imbalance significantly. To ensure batteries' safe operation and prevent over-run damage, BMSs traditionally terminate charge/discharge cycles when the first cell reaches its maximum/minimum SOC, this by no means leads to fully utilization of battery stack capacity, unless all the cells are effectively equalized in SOC to achieve fully charge/discharge simultaneously.

Balancing methods are categorized into two main groups: passive and active. The former primarily involves dissipating excess charge of over-charged cells in heat through bleeding resistors until every single cell reaches the full charge point. This might end up with unevenly distributed temperature rise in battery pack unless it is taken into account in ventilation design. Active balancing, however, manages the imbalance by

charge transit between cells and thus features significantly higher efficiency. The active balancing methods based on switched capacitor or inductor enable either direct cell-to-cell or adjacent cell-to-cell equalization achieved automatically by the charge flow initiated by voltage imbalance between cells without any voltage sensing requirement [1-6]. The charge flow in this approaches is tightly dependence on cell-to-cell voltage mismatch which leads to relatively slow voltage convergence. The inherent forward voltage drop on solid state switches, moreover, results in a persistence non-addressable voltage gap among cells. Quasi-resonance switched capacitors have been proposed to achieve zero voltage gap and extremely high efficiency in zero-current switching [7-10]. Fly-back converters could also provide a more flexible bidirectional charge transfer between cells as the galvanic isolation allows each cell to exchange charge with either the whole stack or any arbitrary smaller set of series cells [11-13]. This requires interleaved arrangement of transformers across sub-stacks which remarkably reduces the voltage rating of power electronic components at the cost of slightly inferior effectiveness and more complicated control requirements.

This paper sets out the structure and operation principle of a bidirectional fly-back active cell balancer and a control strategy is proposed afterwards. Eventually, the performance of the balancing algorithm is evaluated through simulation study.

II. CONVERTER TOPOLOGY

Several kinds of fly-back converter based active cell balancing modules for varied applications are on the market nowadays [14, 15], which provide all gate drives, accurate current sensing, and fault detections required for reliable operation of converters to equalize the charge level of series connected battery cells. Fig. 1 illustrates a typical interleaved fly-back active balancer configuration which is repeated for each subset consisting of S cells. In each subset, fly-back converters rout the charge into two subsets constituting a sub-stack. The topmost subset is exceptionally considered as the last sub-stack, which should be taken into account in control method. The fly-backs are controlled in Discontinuous Conduction Mode (DCM) by peak current sensing at primary and secondary sides of the transformer (I_{Peak}^{Pri} and I_{Peak}^{Sec}).

The authors would like to acknowledge sponsorship of this research by Magellan Powertronics Pty Ltd, Perth, WA, Australia.

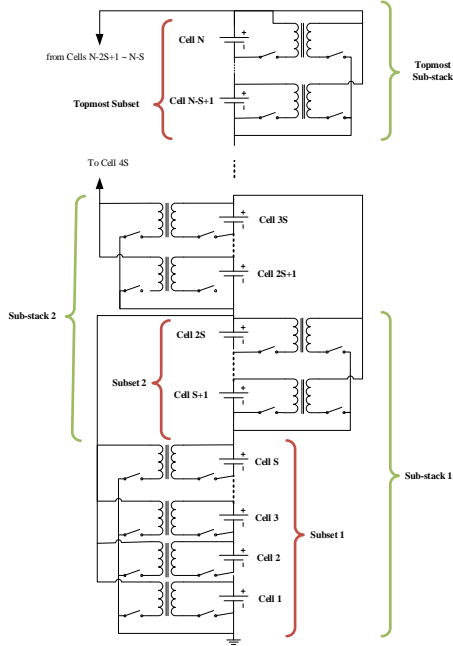


Figure 1. Interleaved connection of transformers [15].

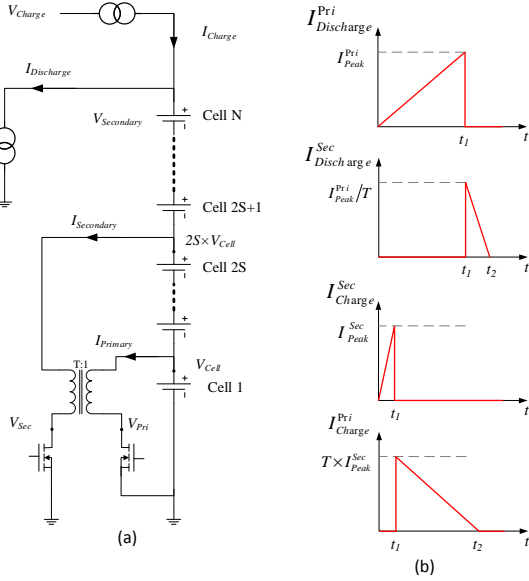


Figure 2. (a) Fly-back converter topology, (b) Current waveforms in charge and discharge operation [15]

Where $\bar{I}_{Discharge}^{Sec}$, $\bar{I}_{Discharge}^{Pri}$, \bar{I}_{Charge}^{Sec} , and \bar{I}_{Charge}^{Pri} are mean discharge and charge currents at secondary (sub-stack) and primary (battery cell) side, respectively. S and T stand for number of cells in subset and transformer turn ratio, respectively.

III. CONTROL STRATEGY

The balancing control objective is to maintain the charge difference between all series connected cells in an acceptable range over either charge or discharge cycles. This consequently extends the storage's run time by preventing premature termination of charge/discharge cycle before the stack is fully charge/discharged. The cells' SOC's are then required to be compared in order to identify the unbalanced cells. As Fig. 3 illustrates, the SOC mismatch could be distinctly identified with voltage difference in quadratic sections of the SOC vs voltage curve, which implies the end of charge or discharge cycles where the equalizing is supposedly performed.

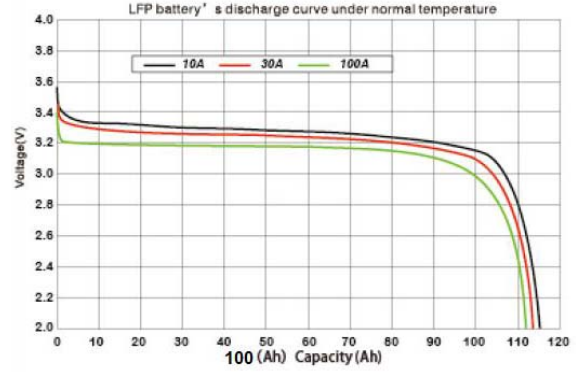


Figure 3. Cell's voltage variation over discharge cycle.

A bidirectional active balancer operates by manipulating bidirectional charge transfer between each cell and the associated sub-stack. Considering the charge and discharge operation of fly-backs in n^{th} subset, the total power in primary and secondary sides of all fly-backs could be obtained by the following summations:

$$P_n^{Sec} = \left(\sum_{S \times (n-1) + 1}^{S \times n} (D_k \cdot I_{Discharge}^{Sec} + C_k \cdot I_{Charge}^{Sec}) \right) \times \left(\sum_{S \times (n-1) + 1}^{S \times (n+1)} V_k \right) \quad (5)$$

$$P_n^{Pri} = \sum_{S \times (n-1) + 1}^{S \times n} \left[(D_k \cdot I_{Discharge}^{Pri} + C_k \cdot I_{Charge}^{Pri}) \times V_k \right] \quad (6)$$

$$C_k = \begin{cases} 1, & \text{Charging} \\ 0, & \text{otherwise} \end{cases}, \quad D_k = \begin{cases} 1, & \text{Discharging} \\ 0, & \text{otherwise} \end{cases} \quad (7)$$

Given the interleaved arrangement of fly-backs, Eqs. 8-9 yield the energy division at the secondary sides of fly-backs in n^{th} subset.

$$P_{n,n}^{Sec} = \left(\sum_{S \times (n-1) + 1}^{S \times n} V_k \right) \times P_n^{Sec} = \left(\sum_{S \times (n-1) + 1}^{S \times n} (D_k \cdot I_{Discharge}^{Sec} + C_k \cdot I_{Charge}^{Sec}) \right) \times \left(\sum_{S \times (n-1) + 1}^{S \times n} V_k \right) \quad (8)$$

$$P_{n,n+1}^{Sec} = \left(\sum_{S \times (n-1) + 1}^{S \times (n+1)} V_k \right) \times P_n^{Sec} = \left(\sum_{S \times (n-1) + 1}^{S \times n} (D_k \cdot I_{Discharge}^{Sec} + C_k \cdot I_{Charge}^{Sec}) \right) \times \left(\sum_{k=S \times (n-1) + 1}^{S \times (n+1)} V_k \right) \quad (9)$$

Where $P_{n,n}^{Sec}$ and $P_{n,n+1}^{Sec}$ are transferred power from the secondary side of fly-backs in n^{th} subset which returns to n^{th} subset itself, and $(n+1)^{\text{th}}$ subset, respectively. Therefore, Eq. 10 presents the energy transfer between the two adjacent subsets:

$$P_{n,n+1} = P_{n,n+1}^{Sec} = \left(\sum_{S \times (n-1) + 1}^{S \times n} (D_k \cdot I_{Disch}^{Sec} + C_k \cdot I_{Ch}^{Sec}) \right) \times \left(\sum_{k=S \times n + 1}^{S \times (n+1)} V_k \right) \quad (10)$$

To simplify Eq. 10, it is presumed that all cell voltages are the same and equal to V . Substituting Eqs. 1-4 in Eq. 10 yields:

$$P_{n,n+1} = P_{n,n+1}^{Sec} = \left(\frac{S \cdot V}{S+T} \right) \sum_{S \times (n-1) + 1}^{S \times n} \left(C_k \cdot \frac{T \cdot I_{Peak}^{Sec}}{4} - D_k \cdot \frac{I_{Peak}^{Pri}}{4} \eta_{Discharge} \right) \quad (11)$$

Equation 11 indicates that discharging a cell in the n^{th} subset will result in negative $P_{n,n+1}$ which implies charge transfer from n^{th} to $(n+1)^{\text{th}}$ subset and likewise charge will move in reverse direction from $(n+1)^{\text{th}}$ to n^{th} subset as a cell is being charging in n^{th} subset. Fig. 4 shows this phenomenon by the way of illustration.

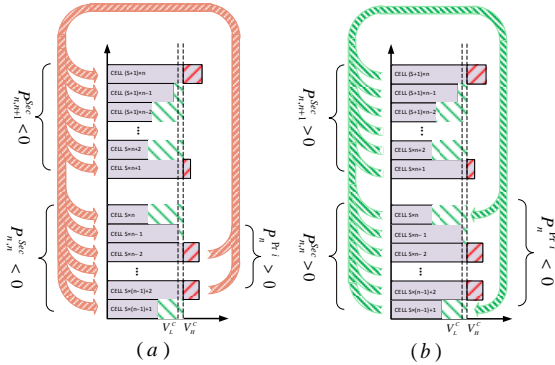


Figure 4. Energy transfer diagram while (a) over-charged cells are being discharged, and (b) non-over-charged cells are being charged.

IV. CHARGER CONTROL

The balancer cannot perform effectively unless it operates at a current greater than the battery stack charge/discharge current. In most of the cases using power electronic converters with this rating is not viable due to system volume or cost limitations. Alternatively, the charge current will be reduced to less than balancing current as balancing operation starts. However, in the end of discharge cycle the BMS isolates the load once the first cell is detected over-discharged as discharge current control is not practically feasible. After the completion of equalization, the BMS might resume supplying the load until all cells reach the maximum DOD (depth of discharge) limit.

As shown in Fig. 5, a three-level hysteresis voltage interpreter can be employed to determine SOC status of each cell based on its voltage.

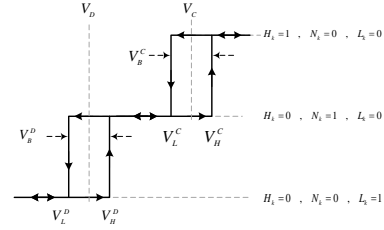


Figure 5. Hysteresis voltage interpreter.

In Fig. 5, V_C and V_D represent the maximum and minimum permissible cell voltages, respectively, while V_B^C and V_B^D are the associated hysteresis bands. “ $H_k=I$ ”, “ $N_k=I$ ”, and “ $L_k=I$ ” indicate the k^{th} cell’s charge status, i.e. “over-charged” (OC), “normal” (NC), and “over-discharged” (OD) states, respectively. Hence, the intra-subset charge routing is decided according to corresponding cells’ charge status with respect to other cells in subset. To handle inter-subset charge exchange, over-charge and over-discharge indexes (OCI and ODI) are defined for each subset as below:

$$OCI(n) = \sum_{k=S \times (n-1) + 1}^{S \times n} (H_k) , \quad ODI(n) = \sum_{k=S \times (n-1) + 1}^{S \times n} (L_k) \quad (12)$$

In the remaining parts of this section, a three-stage balancing approach is explained, utilizing cells’ charge status, and subsets’ OCI and ODI .

A. Stage-I: Equalizing Over-Charged/Discharged Cells

To mitigate cells’ irreversible damages at the end of charge/discharge cycle, the over-charged/over-discharged (OC/OD) cells have to be equalized while the inter-subset charge exchange is targeted at rectifying OCI/ODI inequality of adjacent subsets. In the case of non-zero and equal OCI/ODI , inter-subset charge routing could be decided based on the subsets’ mean voltage. Eventually, in each sub-set the inter-subset equalization criteria are met, as the associated subsets are equal in OCI/ODI and mean voltage, concurrently. Afterwards, the intra-subset equalizing will be adopted with minimum inter-subset charge exchange.

B. Stage-II: Equalising Subsets’ Mean Voltage

When OCI/ODI is zero for both subsets in a sub-stack, the corresponding mean voltages determine the inter-subset equalization, until subsets’ mean voltage absolute mismatch converges within a specific hysteresis band of δ_S .

C. Stage-III: Intra-Subset Cell Voltages Equalising

After a subset achieves a relatively equalized state with respect to the upper subset, which is identified by equal OCI/ODI and mean voltage difference within the hysteresis band of δ_S , a more precise intra-subset cell voltage balancing with minimum inter-subset charge exchange will be set out. The gap between the highest and lowest cell voltages is a good indication of intra-subset charge balance. Hence, the cells are sorted in a sequence by their corresponding voltage and in either charge or discharge cycle the highest-voltage half of cells are discharged and the rest are charged. This stage continues, as long as the maximum cell voltage difference in the subset is out of a hysteresis band of δ_C .

Fig. 6 illustrates the flowchart of the proposed balancing algorithm for charge and discharge cycles.

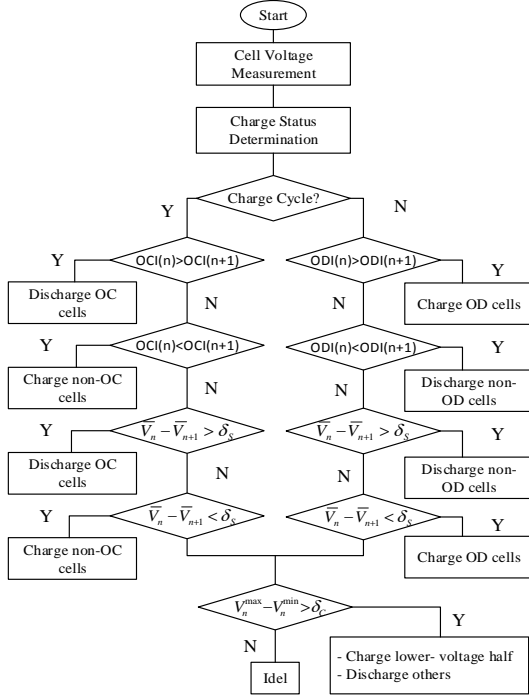


Figure 6. flowchart of the proposed balancing algorithm.

V. SIMULATION RESULTS AND ANALYSES

In this section the performance of the proposed balancing control is evaluated through simulation studies. A simulation model has been developed in Matlab/Simulink consisting of a battery stack made up of 24 LiFePO₄ cells of 100Ah capacity arranged as 4×6-cell subsets in cases-1, and 3×8-cell subsets in case-2. The cells' characteristic curve is illustrated in Fig. 3 and the specifications of simulated model are presented in Table I. The simulation starts with initial cells' SOC that are randomly distributed between 10% and 22% in both cases. As simulation results suggest in Fig. 7, this extreme charge unbalance has been successfully managed by the proposed balancing control in both charge and discharge cycles. Moreover, it is concluded that when more cells are included in subsets, charge distribution will take place over larger sub-stacks and fully balanced state is achieved in shorter time, consequently. Comparing the two cases, equalizing takes 68% and 37% longer in 4×6 arrangement with respect to 3×8 over charge and discharge cycles, respectively.

It is observed that by the time the first cell is detected over-charged at the 96% of SOC, the charger current is reduced to 2A, a value less than balancing current, and it takes almost 1 hours until stack reaches from mean SOC of 93.1% to fully charge state of 96.4% ($0.033 \times 100\text{Ah} / 4\text{A} = 0.83\text{hrs}$). Among all cells in the stack those with the minimum and maximum SOC at the starting time of the balancing needed the longest balancing time around 2.5hrs ($0.06 \times 100\text{Ah} / 2.5\text{A} = 2.4\text{hrs}$).

Figs. 7(b) and (d) represent cell voltages as well as their SOC, and load current over a balancing procedure. To facilitate over-discharge equalization, the discharge current is cut off by load isolation by the time the first cell voltage is detected less than a predefined threshold, 2.7V, until cell voltages laid within an acceptable range, 0.02V. During over-discharge balancing the stack's neither charged nor discharged but its overall charge level is unknown therefore the threshold values of the hysteresis interpreter couldn't be strictly defined and should be determined by average cell voltage, alternatively. To utilize the remaining stack's stored energy, a discharge cycle continues afterwards until the stack is fully discharged.

The current control in fly-back converters is performed at supplying side of the transformer (primary in discharge mode and secondary in charge mode). Hence, the cell's charge and discharge current are slightly different. The cell's charging current and the lowest SOC among the cells will determine the balancing time which is around 2.5hrs ($0.06 \times 100\text{Ah} / 2.46\text{A} = 2.43\text{hrs}$).

TABLE I. SPECIFICATIONS OF SIMULATED MODEL IN SIMULINK.

Parameter	symbol	Value		
		Case-1	Case-2	
cell capacity	C	100Ah		
cells in stack	N	24		
Cells in sub-stack	M	12	16	
Cells in subset	S	8	6	
Fly-back	Primary side Peak current	I_{Peak}^{Pri}	6.25A	6.25A
	Secondary side Peak current	I_{Peak}^{Sec}	3.125A	3.125A
	Primary side mean discharge current	$I_{Discharge}^{Pri}$	2.67A	2.78
	Secondary side mean discharge current	$I_{Discharge}^{Sec}$	-0.2A	-0.16
	Primary side mean charge current	I_{Charge}^{Pri}	-2.46A	-2.55
	Secondary side mean charge current	I_{Charge}^{Sec}	0.22A	0.17
	Transformer turn ratio	T	1:2	
	charge efficiency	η_{Charge}	92%	
discharge efficiency	$\eta_{Discharge}$	92%		
Charger Current	I_{Charge}	50A		
Charger Current during balancing	$I_{Balancing}$	4A		
Discharge (load) current	$I_{Discharge}$	20A		
Subset mean voltage threshold	δ_s	5mV		
Cell voltage threshold	δ_c	5mV		
Cell charge cut-out voltage	V_c	3.5V		
Cell discharge cut-out voltage	V_D	2.8V		
Over-charge hysteresis band	V_c^B	12mV		
Over-discharge hysteresis band	V_D^B	12mV		

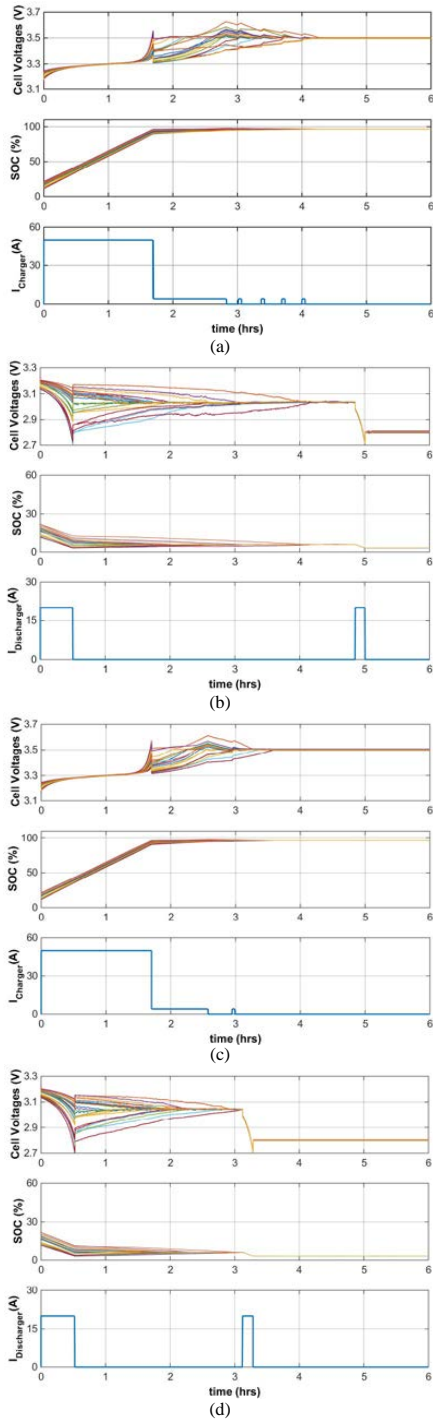


Figure 7. Simulation results for cell voltages, SOC, and charge/discharge current; (a)-(b) Charge and discharge cycles in 4x6 arrangement, respectively, (c)-(d) Charge and discharge cycles in 3x8 arrangement, respectively.

VI. CONCLUSION

A control method is proposed and implemented for the bidirectional fly-back active balancer with interleaved transformer arrangement at high voltage side. Simulation results suggest that by means of inter-subset and intra-subset charge routing an effective global balancing will come about in both charge and discharge cycles. Moreover, it was pointed out that as the subsets become smaller in size, the lower voltage rating of power electronic switches will be required whereas the ultimate equalized state takes longer time to be accomplished. In particular, if a significant charge imbalance exists between faraway cells in the stack as this involves charge to be transferred through more subsets in between.

VII. REFERENCES

- [1] P. Thanh Hai, A. Collet, and J. C. Crebier, "An Optimized Topology for Next-to-Next Balancing of Series-Connected Lithium-ion Cells," *Power Electronics, IEEE Transactions on*, vol. 29, no. 9, pp. 4603-4613, 2014.
- [2] K. Moon-Young, K. Chol-Ho, K. Jun-Ho, and M. Gun-Woo, "A Chain Structure of Switched Capacitor for Improved Cell Balancing Speed of Lithium-Ion Batteries," *Industrial Electronics, IEEE Transactions on*, vol. 61, no. 8, pp. 3989-3999, 2014.
- [3] J. Ewanchuk, and J. Salmon, "A Modular Balancing Bridge for Series Connected Voltage Sources," *Power Electronics, IEEE Transactions on*, vol. 29, no. 9, pp. 4712-4722, 2014.
- [4] K. Moon-Young, K. Jun-Ho, and M. Gun-Woo, "Center-Cell Concentration Structure of a Cell-to-Cell Balancing Circuit With a Reduced Number of Switches," *Power Electronics, IEEE Transactions on*, vol. 29, no. 10, pp. 5285-5297, 2014.
- [5] P. A. Cassani, and S. S. Williamson, "Design, Testing, and Validation of a Simplified Control Scheme for a Novel Plug-In Hybrid Electric Vehicle Battery Cell Equalizer," *Industrial Electronics, IEEE Transactions on*, vol. 57, no. 12, pp. 3956-3962, 2010.
- [6] A. C. Baughman, and M. Ferdowsi, "Double-Tiered Switched-Capacitor Battery Charge Equalization Technique," *Industrial Electronics, IEEE Transactions on*, vol. 55, no. 6, pp. 2277-2285, 2008.
- [7] Y. Ye, K. W. E. Cheng, and Y. P. B. Yeung, "Zero-Current Switching Switched-Capacitor Zero-Voltage-Gap Automatic Equalization System for Series Battery String," *Power Electronics, IEEE Transactions on*, vol. 27, no. 7, pp. 3234-3242, 2012.
- [8] L. Kyung-Min, C. Yoo-Chae, S. Chang-Hyeon, and K. Bongkoo, "Active Cell Balancing of Li-Ion Batteries Using LC Series Resonant Circuit," *Industrial Electronics, IEEE Transactions on*, vol. 62, no. 9, pp. 5491-5501, 2015.
- [9] M. Uno, and A. Kukita, "Single-Switch Single-Transformer Cell Voltage Equalizer Based on Forward Flyback Resonant Inverter and Voltage Multiplier for Series-Connected Energy Storage Cells," *Vehicular Technology, IEEE Transactions on*, vol. 63, no. 9, pp. 4232-4247, 2014.
- [10] L. Siqi, C. C. Mi, and Z. Mengyang, "A High-Efficiency Active Battery-Balancing Circuit Using Multiwinding Transformer," *Industry Applications, IEEE Transactions on*, vol. 49, no. 1, pp. 198-207, 2013.
- [11] H. Yi-Hsun, L. Tsong-Juu, S. M. O. Chen, H. Wan-Yi, and C. Yi-Yuan, "A Novel High-Efficiency Compact-Size Low-Cost Balancing Method for Series-Connected Battery Applications," *Power Electronics, IEEE Transactions on*, vol. 28, no. 12, pp. 5927-5939, 2013.
- [12] F. Mestrallet, L. Kerachev, J. C. Crebier, and A. Collet, "Multiphase Interleaved Converter for Lithium Battery Active Balancing," *Power Electronics, IEEE Transactions on*, vol. 29, no. 6, pp. 2874-2881, 2014.
- [13] A. M. Imtiaz, and F. H. Khan, "Time Shared Flyback Converter Based Regenerative Cell Balancing Technique for Series Connected Li-Ion Battery Strings," *Power Electronics, IEEE Transactions on*, vol. 28, no. 12, pp. 5960-5975, 2013.
- [14] "Battery Supervision and Cell Balancing Module for Li-Ion Battery Packs", Infineon Technologies AG, 2010.
- [15] "High Efficiency Bidirectional Multicell Battery Balancer," Linear Technology Corporation, 2013.

Battery-Less Short-Term Smoothing of Photovoltaic Generation Using Sky Camera

Mojtaba Saleh, *Student Member, IEEE*, Lindsay Meek, *Member, IEEE*, Mohammad A.S. Masoum, *Senior Member, IEEE*, and Masoud Abshar

Abstract— There is a growing concern over addressing the adverse effects of variations in the output power of distributed generators such as photovoltaic generation (PVG) systems that continue to be widely introduced into power networks. Nowadays, most network operators are requiring these intermittent energy resources to seek compliance with new regulations pertaining to the restriction of their export power fluctuations. This paper aims to investigate the smoothing of the export power fluctuations primarily attributed to clouds passing over the PVG plant which are traditionally compensated by integrating a battery storage (BS) system. The idea of incorporating short-term solar prediction information into the conventional smoothing approach is examined to indicate how it affects the engagement of BS in the smoothing process. Afterward, an enhanced solar forecasting scheme based on whole-sky imaging is proposed and its performance is demonstrated through several real-time experiments complemented with simulation studies. The results reveal that the proposed PVG smoothing strategy is capable of successfully filtering rapid export power fluctuations to an acceptable extent and the conventional generation reserves will experience a negligible amount of remaining undesired power variation. This clearly bears out the hypothesis of battery-less PVG regulation.

Index Terms—Cloud forecasting, photovoltaic systems, power smoothing, sky camera imaging.

I. INTRODUCTION

THE escalating deployment level of photovoltaic generation (PVG) systems and their growing contribution to meet the increasing energy demand has created emerging issues in the power systems planned to operate with conventional generation resources. The uncertainty of PVG which is primarily attributed to clouds obscuring the sun and substantial insolation variations can lead to an extra burden on the conventional operational reserve of the power system, in terms of the incidence of operation as well as required capacity [1]. This gives rise to a critical necessity for associated regulations on ramp rate (RR) of the variations in photovoltaic (PV) and wind generations, e.g. 10% of plant's rated capacity per minute is widely adopted by utility operators [2]–[4]. As an immediate solution, different energy storage technologies have been proposed and applied to address the intermittency

M. Saleh and M. A.S. Masoum are with the Centre for Smart Grid and Sustainable Power Systems at Department of Electrical Engineering, Curtin University, Perth, Australia. (Emails: mojtaba_saleh@hotmail.com, m.masoum@curtin.edu.au)

L. Meek and M. Abshar are with Magellan Powertronics Pty Ltd, Perth, Australia. (Emails: lmeek@magellanpower.com.au, mabshar@magellanpower.com.au)

Manuscript received November 15, 2016; revised August 10, 2017; accepted September 15, 2017.

of PVG, i.e. battery storage (BS) [5]–[10], ultra-capacitors [11], [12], superconducting magnetic energy storage (SMES) [13], [14], fuel cells [15], and flywheels [16]. Among these technologies, BS-based solutions have become more prevalent due to recent improvements in performance, declining trend in the cost, wide power range, and scalable capacity. Essentially, the backup storage system reacts to the erratic fluctuations in the PV export power termed as a "reactive" smoothing approach. Therefore, sufficient storage capacity proportional to the magnitude of the sudden PVG variations is required for a proper smoothing treatment. This also substantially raises the capital cost of the PVG system and consequently the generation cost of the solar electricity. On the other hand, the solar irradiance forecasting and projected generation information of the PV facilities enables a predictive approach which initiates the ramp down function sufficiently prior to the passing clouds shade the PV arrays. Therefore, upon the incidence of the shading event, the PV plant will not experience any severe fluctuation. This solution, termed as "proactive", significantly shrinks the required smoothing backup. Moreover, solar irradiance prediction approaches could offer remarkable reliability and power quality advantages to the power system, i.e. serve to improve the ability to dispatch utility-scale PV plants, enabling less variable PVG in urban feeders and alleviate the operation of voltage regulation equipment, and allow efficient and smart control of storage systems integrated into PV plants. There is a wide range of solar forecasting methods available; typically they differ in the temporal and spatial domain. Those range from a very short-term time frame of one minute to a full day ahead, with a spatial accuracy ranging from very coarse 50 [km] down to a more precise 1 [km] domain. Ground-based cloud imagery approaches offer comparatively higher resolutions in both the temporal and spatial domains, making them good candidates for PVG smoothing applications that require identifying rapid irradiance variations [17]. There are a series of publications available on solar irradiance forecasting [18]–[22] which to some extent describe the fundamentals. The acquired image is first captured by a whole-sky camera and transformed into a red-to-blue-ratio (RBR) image. Then, it is compared with a corresponding reference image of the clear sky, where the difference in RBR values is used to distinguish cloud regions. This is then processed to generate a cloud map, which in conjunction with the cloud base height (CBH) information yields a ground shadow map with a range of up to 5 [km] from the observation spot [18]–[20]. West *et al.* [21], have deployed an artificial neural network to make an estimation on the respective cloudiness

degree of each pixel while [22] proposed a fixed value RBR segmentation approach augmented by cloud texture filters. Another key element investigated in different approaches is the cloud motion, i.e. the cross-correlation of consecutive images [18]–[20] and dense optical flow [21] as well as a non-rigid registration method which takes the local deformation of clouds into account [22]. The insolation level is conclusively predicted according to the present cloud regions and their prevailing movements. In a traditional method as used by [18]–[20], the cloud map is advected by extrapolating the observed cloud motion elements to identify a projected cloud map and then by means of ray-tracing method a shadow map is calculated. However, [21] correlates the occlusion of the sun to the cloudiness figure of an annulus area with radii proportional to forecast range. Bernecker *et al.* [22], have defined and examined an area in which the clouds have a potential of obscuring the sun to generate an occlusion probability which is used to estimate the projected insolation level. Aside from the inherent inaccuracies arising from the cloud formation and evaporation, the perspective error, and the limited field of view, the extensive evaluative results presented in [20] implies an inconsistency in the incidence and magnitude of erroneous predictions from day to day. These inconsistencies call for a more robust and improved solution.

In this paper, an averaged cloud prediction approach is proposed that considers multiple historical observations to obtain a single projected cloud region. Furthermore, this method is applied to generate a series of equally spaced prediction information to improve the robustness while addressing the occasional inaccuracies of the algorithm in the identification of shape, dimensions, or motion of clouds. Ultimately, the cloud prediction information is incorporated into the conventional PVG regulation algorithm as an early warning of the upcoming shading events which starts the export ramp down to a reduced level so that it is not affected by the passing clouds.

The main contribution of this paper is a practical predictive solution addressing the short-term intermittency of the solar power to meet the RR regulations mandated by the utility grid operators. The experimental results confirm that the proposed approach effectively minimises the amount of required backup capacity which is tightly restricted to a certain level. Utility grid operators normally allow for the low amplitude generation variations to be accommodated by the existing spinning reserve capacity. This proves the hypothesis of a battery-less solution to the short-term PVG regulation in practice.

The remainder of the paper is organised into five sections. Sections II and III present the proposed imagery cloud prediction algorithm, and a detailed explanation on different cloud prediction-based smoothing approaches, respectively; followed the developed experimental testbed is described in section IV. The performances of several smoothing techniques are comparatively surveyed through experimental measurements and simulation studies in section V, followed by the conclusion.

II. PROPOSED AVERAGED CLOUD PREDICTION ALGORITHM

The cloud prediction procedure is primarily an image processing operation which considers successive whole sky

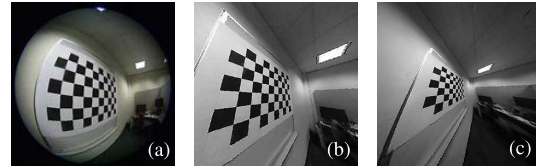


Fig. 1. (a) A sample fish-eye photo of a checkerboard and the undistorted images, (b) $F_p = 5$, (c) $F_p = 10$.

images captured by a fish-eye camera and generates projected cloudiness figures which are interpreted as a reliable indication of projected PVG power ramp downs. In this section, the major contribution is a multi-target prediction technique that examines cloud prediction information associated with a series of prediction instants within a prediction range of interest. This allows an averaged prediction that improves the overall performance of the algorithm in terms of robustness and accuracy.

A. Correcting Lens Distortion

Fish-eye lens produces an extremely wide field of view while the optical distortion is typical of the fish-eye images. For the purpose of motion analysis, the spherical perspective is projected onto the flat plane using the OCamCalib calibration toolbox [23]. The toolbox processes multiple sample photos of a chessboard template and obtains the coordinates of all corners and then calculates the corresponding inherent optical characteristics of the lens. Then a mapping lookup array is generated for instant conversion of the fish-eye hemispherical view into an undistorted image. The fish-eye lens normally creates a compressed artifact towards the periphery of the image. The calibration process is also significantly erroneous in marginal coordinates due to the non-linear characteristics of the lens towards the rim. Hence, the undistortion is conducted so that the poorly undistorted region with higher circular angle is projected outside the destination frame. This can be achieved by adjusting the projection factor F_p in the OcamCalib toolbox to ignore the calibration error at the price of limited view angle. As Fig. 1 points out, $F_p = 5$ produces relatively no distortion in the peripheries compared to $F_p = 10$. Therefore, $F_p = 5$ will be used hereafter to avoid the effect of the calibration error whereas the view angle is restricted to 136° .

B. Sun Positioning

The solar forecasting process mainly relies on the position of the sun in the sky images which is accurately indicated and updated over successive time intervals. Scanning the sky image for the brightest area does not work perfectly in practice as optically thin clouds can be intensely illuminated by the sun and considerably deviate the sun-locating process. Therefore, a computational approach is deployed which yields the angular position of the sun corresponding to the specific geographic information, date and time [24]. The fish-eye coordinates of the sun is obtained and then translated into undistorted coordinates using the calibration toolbox.

C. Cloud Segmentation

Different optical properties of atmospheric aerosols and constituent particles of the clouds create a relatively marked visual distinction between clear and cloudy regions of the sky. RBR value of each pixel has proven to be an effective approach to generate the cloud mask by discriminating the cloud pixels from the clear sky [25]. However, applying an ordinary thresholding on the RBR value of the pixels usually shows an unreliable performance in different regions of the sky. This is mainly attributed to the nonuniform luminance pattern of the sky due to the scattering effect of atmosphere on the sun beams [26] which is also shown in Fig.2(d). This effect can be compensated by comparing the real-time sky image against the corresponding clear sky reference (CSR) image in RBR values. The resulting differential array is then thresholded by Θ_{RBR} to identify the cloud areas. For this purpose, the sun position (zenith and azimuth angle) in the CSR has to be aligned with that of the real-time sky image. Therefore, a collection of clear sky images is created, where each element corresponds to a specific zenith angle considering the daily and seasonal variations of the sun trajectory. It ranges from minimum zenith angle of 7° at high noon on the summer solstice in Perth, Australia, to the maximum of 70° which corresponds to the extreme zenith angles at the start and end of the prediction algorithm at sunrise and sunset times, respectively. Moreover, each element of the clear sky collection (CSC) is centre rotated so that the sun is aligned to the azimuth angle of *zero*. This allows instant reconstruction of the CSR respective to any angular position of the sun; the element closest to the real-time zenith angle of the sun is chosen and centre rotated by its azimuth angle. To prevent computational burden, the sky image and the respective CSR are undistorted and averaged block-wise and the corresponding RBR value is calculated for each block instead of pixel-wise processing. Figs.2(c) and (f) illustrate the RBR images of the real-time sky view and the associated CSR represented in false colour, respectively. The resulting differential image is then thresholded to identify the cloud regions. The cutting value of Θ_{RBR} is tuned practically through observations and a satisfactory cloud detection process is achieved by the value of 0.176, as shown in Fig.2(h). The thresholding process produces a binary cloud mask representing the clear sky in *zero* and clouds in *one*. The shape of the clouds is then defined in a sequence of the coordinates on the outline of the respective area termed as "contours" which is illustrated in Fig. 2(i). Although, the CSR differentiation relatively avoids the severe illumination rise in the circumsolar area the cloud detection in this region is comparatively unreliable and only useful for relatively short-term sub-minute prediction range, e.g. 1 [min]. Therefore, for longer prediction ranges, i.e. 10 [min], the circumsolar area can be subtracted from the initially detected clouds. This operation is achieved by scattering the contours into small hexagons and those overlapped the circumsolar area are excluded, purple contours in Fig. 2(j).

D. Cloud Motion

The motion analysis of the observed clouds is a significant component of the prediction method. An optical-flow approach is deployed to identify the motion of the objects between two successive frames. It calculates an array of 2D displacement vectors respective to all pixels or blocks of pixels [27]. The vectors are then filtered by the binary cloud mask Fig. 2(h) to obtain the motion elements of the pixels inside the cloud regions. Fig. 2(j) gives an example of the motion vectors resulting from two successive samples. Using a simplifying assumption that all visible clouds are single layer making a uniform motion in a horizontal plane, the instantaneous velocity vector $\vec{V}(t_0)$ is obtained by averaging the validated collection of motion vector:

$$\vec{V}(t_0) = \frac{1}{t_c} \sum_{i=1}^n \frac{\vec{d}_i}{n} \quad (1)$$

where t_0 and t_c are sampling instant and cycling time of the algorithm, respectively, over which n displacement values of \vec{d}_1 through \vec{d}_n have been observed. Afterward, to smooth out the turbulent movement of the clouds or any occasional passing object within effective view of the camera, previous instantaneous motions corresponding to *three* recent cycles ($r=3$) of the algorithm are averaged to obtain the principal velocity vector $\vec{V}(t_0)$ which is introduced into the forecasting section of the proposed algorithm.

$$\vec{V}(t_0) = \frac{1}{r} \sum_{i=0}^r \vec{V}(t_0 - i \cdot t_c) \quad (2)$$

To ease the deployment of observation data for future predictions, in each cycle an observation structure containing the associated time tag t_r , cloud mask, and principal velocity vector is created as below:

$$obs(t_r) = \begin{cases} \text{reference time: } & t_r \\ \text{cloud outline: } & C \\ \text{velocity vector: } & \vec{V}(t_r) \end{cases} \quad (3)$$

E. Cloud Forecasting

Given the key assumption of the persistent movement of the clouds, the projected displacement value of $\vec{D}_{t_0}^{t_1}$, associated with a time interval of t_0 to t_1 , is obtained by extrapolating the principal velocity vector from the time origin.

$$\vec{D}_{t_0}^{t_1} = \vec{V}(t_0) \times (t_1 - t_0) \quad (4)$$

In order to make a more reliable prediction which is less susceptible to occasional errors in segmentation and optical-flow, a series of historical observations are incorporated. Respective to each prediction t_f a suitable range for the reference time of historic observation is defined as below:

$$t_0 + t_f - t_{h2} < t_r < t_0 + t_f - t_{h1} \quad (5)$$

Given the cloud segments neighboring the solar area are projected to create a shade in the very close future, eliminating the circumsolar clouds in the segmentation stage makes the very short-term cloud prediction impossible. Therefore, the

historic observations closer than t_{h1} to the target prediction time $t_0 + t_f$ doesn't contain useful cloud information and have to be excluded in the forecasting process. Moreover, due to the limited effective prediction range (viewing angle of the camera) the outdated observations spaced back farther than t_{h2} prior to the target prediction time $t_0 + t_f$ are projected out of the observation plane and have to be disregarded as well. Both t_{h1} and t_{h2} could be experimentally obtained:

$$t_{h1} = d_{min}/V_{avg} \quad (6)$$

$$t_{h2} = d_{max}/V_{avg} \quad (7)$$

where V_{avg} is the average motion amplitude over the available historic information, e.g. few months, recorded as 0.46[pix/sec]. Hence, $d_{min} = 55$ [pixel] is the circumsolar distance and $d_{max} = 339$ [pixel] is the longest radius of the frame as shown in Fig. 2(l). Therefore, it gives $t_{h1} \approx 120$ [sec] and $t_{h2} \approx 755$ [sec]. Afterward, the cloud outlines respective to the eligible observations (Eq. (5)) are displaced according to Eq. 4. A mean predicted cloud outline is then generated from the collection of the displaced cloud outlines which are then averaged pixel-wise and normalised to [0-255] to produce a single monochrome image. This image is then thresholded by the middle intensity value of $\Theta_{avg} = 256 \div 2 = 128$ to generate the averaged predicted cloud outline. Fig. 2(k) shows the result of the averaged prediction process as a binary cloud mask which is overlaid onto the solar disc templates to obtain the predicted cloudiness indexes. The solar disc template consists of a circle equal in size to the sun as observed in the undistorted image and centred on the calculated coordinate of the sun. The pixel count of the projected cloud mask that overlaps the solar disc template (highlighted in yellow) is then normalised by the solar disc area to produce the respective solar occlusion index, SOi , which is a fair indication of the predicted attenuation of solar insolation. Similarly, a circumsolar template is an annulus with an inner radius equal to the size of the solar disc, and an outer radius twice that size. The circumsolar occlusion index, COi , is the normalised conjunction of the circumsolar annulus and the cloud mask (highlighted in green), which could be interpreted as a moderate likelihood of sunlight obstruction in future time. However, when it comes to fast moving intermittent clouds, it is more challenging to predict a shading event that is occurring relatively far away from current time. The effective prediction range, T_P , is defined as the time a cloud segment takes to travel the effective displacement prediction, \vec{L}_P , at the velocity and orientation of the observed principal motion. As shown in Fig. 2(l), \vec{L}_P is the shortest trajectory from the margin of viewing field to the position of the sun.

$$T_P = |\vec{L}_P|/|\vec{V}(t_0)| \quad (8)$$

Hence, the cloud prediction algorithm is capable of indicating occlusion of the sun for a prediction time up to the effective range and fails when that time exceeds T_P . This is a motivation for proposing multi-point forecasting, as opposed to a single target, in which prediction is performed at a series of evenly spaced prediction instants:

$$\{t_0 + t_{sp}, t_0 + 2 \cdot t_{sp}, \dots, t_0 + n \cdot t_{sp}\} \quad (9)$$

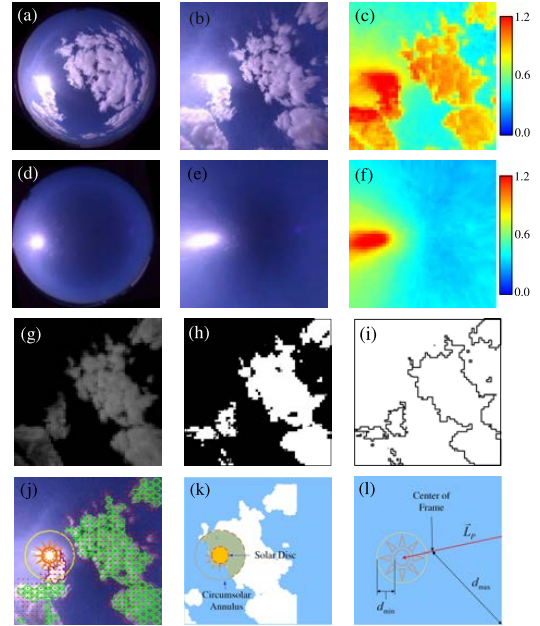


Fig. 2. Real-time captured image (a) fish-eye, (b) undistorted, (c) RBR in false color. Reconstructed clear sky image, (d) fish-eye, (e) undistorted, (f) RBR in false color. Cloud segmentation, (g) differential image, (h) thresholded by Θ_{RBR} , (i) cloud contours. (j) Cloud motion. (k) Cloud Forecast. (l) Observation ranges and effective range of displacement prediction.

$$n \times t_{sp} = t_f \quad (10)$$

where t_f and t_{sp} are total and split forecast ranges, respectively. Moreover, n stands for the total number of prediction instants. This is a solution to address the all-or-nothing nature of the individual target prediction i.e. a shading event out of an effective range will be still identified prior to its occurrence yet not at a perfect time. Therefore, pointing to a specific time forward, the multi-point prediction generates a series of SOi and COi values corresponding to the elements of prediction time series as per Eq. (9).

III. PROPOSED PVG SMOOTHING APPROACH

For grid-tied PVG systems compliance with operators RR requirements, i.e. 10% per minute RR tolerance as per [2], ensures that grid is not disturbed and power quality criteria are satisfied. Sudden under/over generation of a PV plant primarily attributed to passing clouds and their shading characteristics can be addressed in different ways. This section outlines the conventional non-predictive approach followed by cloud prediction aided proactive strategies. In the end, a new battery-less smoothing technique using conservative cloud prediction by the sky-camera is explained.

A. Conventional Non-Predictive Smoothing Strategy

This method works on the assumption that the PV plant is continuously operating at its maximum power point (MPP),

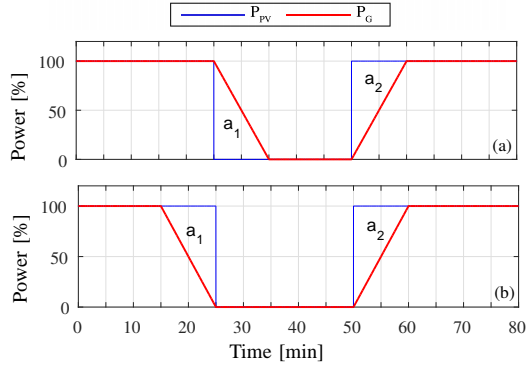


Fig. 3. Energy balance in PVG smoothing. (a) Conventional smoothing. (b) Based on cloud prediction.

while the generation is monitored and undue RR is compensated by means of a backup storage device such as BS. Eqs. (11)-(13) elucidate how the ramp function defines the PVG export power.

$$R(t_0) = \frac{P_{PV}(t_0) - P_G(t_0 - t_s)}{t_s} \quad (11)$$

$$R_r(t_0) = \begin{cases} R_s & \text{if } R(t_0) > R_s, \\ -R_s & \text{if } R(t_0) < -R_s, \\ R(t_0) & \text{otherwise.} \end{cases} \quad (12)$$

$$P_G(t_0) = P_G(t_0 - t_s) + R_r(t_0 - t_s) \times t_s \quad (13)$$

where P_{PV} and P_G are PV plant generation and the resulting smoothed power, respectively. t_0 and t_s stand for present time and sampling rate, respectively. Moreover, R and R_s represent instantaneous RR of the PVG and the associated extreme allowable RR, respectively.

Fig. 3(a) depicts a non-predictive smoothing process over a sudden 100% drop in the generation follows the full recovery. The upward and downward ramp functions are initiated upon the detection of sudden changes. During the ramp down period, the deficit energy marked by a_1 has to be injected while ramp-up smoothing requires energy absorption equal to area a_2 . This explains the critical role of a storage device such as BS of sufficient capacity to ensure an acceptable non-predictive PVG regulation. Given the upward ramps could be simply yet not utmost efficiently compensated by curtailment of the surplus power instead of energy absorption, battery-less PVG regulation is technically viable provided the ramp down procedures are started sufficiently prior to the occurrence of the PVG under generation period. This requires an algorithm that accurately predicts the timing and amplitude of sudden under generations caused by passing clouds. Fig. 3(b) illustrates the battery-less predictive regulation and as seen it only involves energy curtailment. Therefore, the mitigation of the storage doesn't disrupt the smoothing function.

In the following section, cloud prediction information is incorporated to the conventional smoothing algorithm to investigate whether a satisfactory storage-free smoothing approach is achieved, given the limitations and relative deficiencies of the imagery based cloud prediction methods.

B. Ideal Export Prediction Smoothing Strategy

Smoothing approach purely based on prediction is ideally defined on the assumption that valid projected PVG output is available all the time. The required prediction range t_f is inversely proportional to the maximum allowable RR.

$$t_f = 1/R_s \quad (14)$$

Eqs. (15)-(16) are applied to all projection points within the prediction range in order to generate the most critical RR and the appropriately restricted ramp for PVG is determined by Eq. (17).

$$R_i(t_0) = \frac{P_P(t_i) - P_G(t_0)}{t_i - t_0} \quad i \in (1 : n) \quad (15)$$

$$R_c(t_0) = \min\{R_1(t_0), R_2(t_0), \dots, R_n(t_0)\} \quad (16)$$

$$R_r(t_0) = \begin{cases} R_s & \text{if } R_c(t_0) > R_s, \\ -R_s & \text{if } R_c(t_0) < -R_s, \\ R_c(t_0) & \text{otherwise.} \end{cases} \quad (17)$$

$$P_G(t_0) = P_G(t_0 - t_s) + R_c(t_0 - t_s) \times t_s \quad (18)$$

where $R_i(t_0)$ is the required RR to bridge the present PVG value $P_G(t_0)$ to the expected generation level at the i^{th} prediction point $P_P(t_i)$ and n is the number of prediction instants. Moreover, $R_c(t_0)$ is the most critical RR which has to be followed in order to achieve a smooth P_G only by allowing energy curtailment and without any back up power injection. R_s and $R_r(t_0)$ are the extreme allowed RR and the RR command to the PV system, respectively. The plant export power is eventually defined by Eq. 18.

A practical storage-less PVG smoothing approach requires a precise prediction of P_{PV} by estimating the solar insolation, incidence angle, and temperature of the PV panels. Any inaccuracy arising from prediction process might need supporting power injection to be compensated. Alternatively, the lack of desired precision could be appropriately addressed to mitigate the required storage backup. In the following sections, two different attempts to develop a prediction based PVG output smoothing approaches are examined and compared in their effectiveness and functionality.

C. Proposed Smoothing Method-I: Using Output Estimation

The principle of this approach is to estimate the projected solar insolation according to the predicted cloudiness indices. Therefore, based on the specifications of the test system, we make few simplifying assumptions; virtually constant open-circuit voltage V_{OC} , PV panel temperature T , and fill-factor of FF . This results in the generated power being proportional to insolation S :

$$\begin{aligned} P_{MPP} &= FF \cdot V_{OC} \cdot I_{SC} \\ I_{SC} &\propto S @ T = 25^\circ, \\ V_{OC} &= 388.8[V] = cte, \quad FF = 0.73 = cte \\ \therefore P_{MPP} &\propto S \end{aligned} \quad (19)$$

where I_{SC} and P_{MPP} signify the short-circuit current and PV power at MPP, respectively. Furthermore, the angle of incident for the direct component of the solar irradiance can

TABLE I
SPECIFICATIONS OF TESTBED

	Parameter	Value
Camera	Model	ACTi E925
	Communication	TCP/IP
	Viewing Angle	189°(overview), 115.3°(high detail)
	Focal Length	Fixed, f1.19 [mm]
	Dynamic Range	Basic WDR 74 [dB]
Controller	Model	Raspberry Pi 2 Model B
	CPU	900MHz quad-core ARM Cortex-A7
	RAM	1 [GB]
	Storage	16 [GB]
Inverter #1	Model	SMA Sunny Boy 5000TL
	Rated power	4.6 [kW]
	Nominal AC voltage	210...230 [V]
	MPP voltage range	100...500 [V]
Inverter #2	Model	Solis-4K-2G
	Rated power	4 [kVA]
	Nominal AC voltage	180...270 [V]
	MPP voltage range	100...500 [V]
PV Array #1 / #2	Module	ESM200S-125 Monocrystalline
	Open Circuit Voltage- V_{OC}	388.8 [V]
	Short Circuit Current- I_{SC}	6.3 [A]
	Peak Power Watts- P_{MPP}	1.8 [kW] @ 314.1 [V] , 5.73 [A]
	Panel Azimuth Angle	0°N
Location	Panel Tilt Angle	34°
	Latitude	32.1°S
	Longitude	115.81°E
	Elevation	31 [m]

be obtained using the coordinates of the sun generated by the solar positioning procedure [24] and alignment of the PV array. Therefore, a rough approximation of P_{PV} forecast values, $P_P(t_i)$, are obtained in Eq. 20:

$$P_P(t_i) = P_{MPP}(t_i) = P_{STC} \cdot \cos(\alpha) \cdot SO_i \quad (20)$$

where P_{STC} is the PVG output in standard test conditions (STC), α is the solar incident angle, and SO_i is the respective solar occlusion factor. The simplified estimation of Eq. 20 is used to obtain the projected generation values, $P_P(t_i)$, and the governing principle of the ideal prediction, Eqs. (15)-(18), are applied to meet the appropriate RR requirement. As the smoothing control primarily relies on sudden variations, rather than precise estimation of the export power of the PV plant, in spite of the applied simplifications and resultant inaccuracies the prediction information effectively improved the smoothing process in terms of required backup power.

D. Proposed Method-II: Smoothing Using Binary Cloud Prediction

In order to address the limitations discussed earlier with respect to the PVG output estimation, a conservative PVG export smoothing strategy based on a binary cloud prediction is proposed. This proactive approach slowly lowers the export

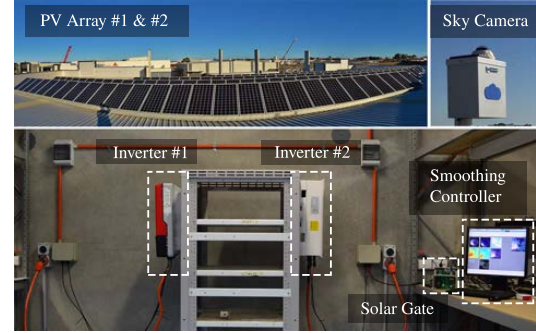


Fig. 4. Photo of the testbed for PVG smoothing based on the proposed cloud prediction technique.

power into a reduced value during the critical situations when it is highly likely that solar occlusion occurs and ramp that up when the clouds are passed. This is determined by the projected cloudiness figures SO_i and CO_i . Therefore, the projected plant export power at the prediction range is defined by Eq. (21).

$$P_P(t_f) = \begin{cases} P_{Base} & \text{if } \sum SO_i > \Theta_{SO}, \\ P_{Base} & \text{if } \sum CO_i > \Theta_{CO}, \\ P_{MPP} & \text{otherwise.} \end{cases} \quad (21)$$

where Θ_{SO} and Θ_{CO} are threshold values associated with aggregated SO_i and CO_i values, respectively. Furthermore, P_{Base} is the target amount of generated power during shut-off condition which is determined as a percentage of the nominal amount of expected generation in clear sky condition at the time ($P_{STC} \cdot \cos(\alpha)$). The transmissivity characteristic of the obscuring clouds is a decisive factor in subsequent incident radiation, which barely causes the PVG output to decline by more than 75%-80% [28]. Hence, the shut-Off coefficient of C_{Base} is assigned a value of 20% which enables efficient utilisation of the PVG yield while smooth power generation is maintained:

$$P_{Base}(t) = C_{Base} \cdot P_{STC} \cdot \cos(\alpha) \quad (22)$$

The projected export value $P_P(t_f)$ is then introduced to Eqs. (15)-(18) to determine the respective reference export power.

IV. DEVELOPED TESTBED AND EXPERIMENTAL SETUP

This section sets out the configuration of hardware components of the testbed developed for conducting a series of evaluative trials on the proposed PVG smoothing approach. The key component of the developed system is a weather proof fish-eye security camera with a wide dynamic range (WDR) to accommodate the extremely broad extent of pixel brightness in the sky image, ranging from the sun disc to relatively dark cloud regions, without a considerable level of saturation in the image. The IP camera is mounted upright facing the sky in an outdoor area and communicated through local area network (LAN). Based on the proposed strategy discussed in section III-D a cloud prediction software is developed and implemented on a Linux operating Raspberry

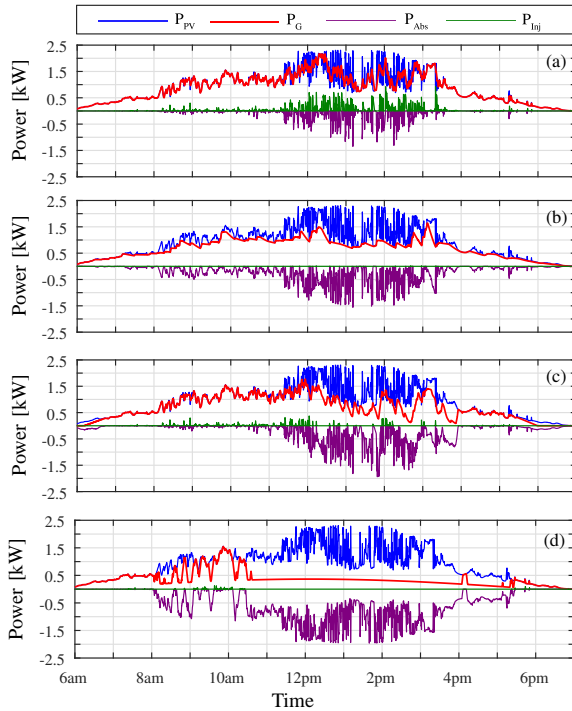


Fig. 5. Smoothing results for Dec. 4th, 2015. (a) Non-Predictive. (b) Ideal Prediction. (c) Estimation-based. (d) Binary Prediction.

PI computer which acquires snapshots from the sky camera in regular time steps and then generates and archives recent cloud segmentation and optical flow data used for the solar occlusion forecast. Meanwhile, for the purpose of future analysis all key data are logged, i.e. image processing results, SO_i and CO_i figures. Ultimately, the RR command is generated and sent out to a Solar-Gate [29], which is an intermediate device to enable external control of the PV power export by overriding the MPPT operation of the grid-tied solar inverter #1. The solar inverter #2 is used with no export smoothing control to allow a comparative evaluation of the proposed PVG smoothing algorithm. Fig. 4 makes a visual presentation of the composition of the testbed while Table I gives further details about that.

V. EVALUATION AND ANALYSIS

This section aims at establishing a benchmark to assess performance and eligibility of the previously discussed PVG smoothing schemes. Those are compared with the non-predictive method in terms of required capacity of the storage backup and the frequency of its usage. A preliminary trial experiment was conducted at Magellan Power in Western Australia, including different meteorological conditions, i.e. fully sunny, overcast, and partly cloudy. The collected data set includes all the critical prediction data including SO_i , CO_i , incident angle α , and the export power of the uncontrolled solar inverters #2. It allows trying different set points of Eq. (21) on the simulation model of the proposed PVG smoothing algorithm in Matlab/Simulink® to obtain the most suitable

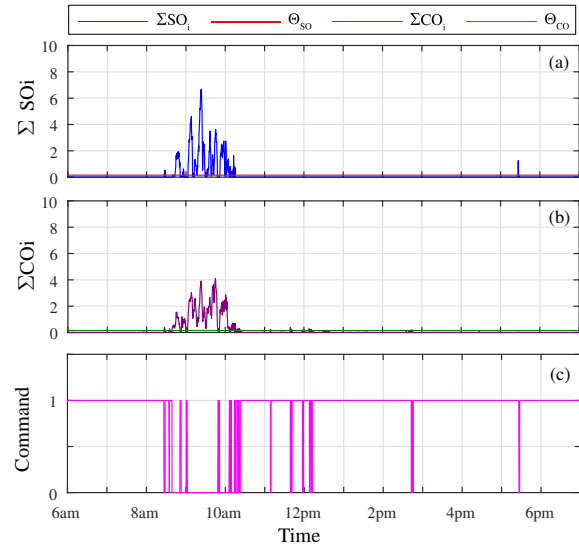


Fig. 6. Smoothing signals for Dec. 4th, 2015. (a) Total SO_i . (b) Total CO_i . (c) Export toggle command to solar inverter #1.

values. The lowest the cutting values Θ_{SO} and Θ_{CO} are, the more sensitive and conservative becomes the proposed cloud prediction algorithm. The optimised values of $\Theta_{SO} = 0.15$ and $\Theta_{CO} = 0.15$ ensure the best performance so that almost all of the cloud events are detected properly. Further reduction and narrowing down of the threshold values will not offer significant improvement in the prediction quality, but tends to create occasional erroneous ramp down commands during the clear sky periods. Afterwards, an evaluative trial was also carried out over 10 days in December 2015 to demonstrate the practical viability of the proposed smoothing algorithm. The 10 [min] prediction range is chosen according to the desired RR of 10% per minute. In this experiment, inverter #1 was subject to the export smoothing based on the proposed binary prediction approach of section III-D and the set points in Table II. Concurrently, inverter #2 was connected to the same size of PV array and operating normally at MPP with no smoothing controls and the critical real-time information is logged to provide the actual PVG data for the purpose of simulating the other smoothing approaches in exactly the same weather condition as the practical test of the proposed binary prediction approach. The simulation models of the other smoothing approaches are also developed in Matlab/Simulink® to conduct a comparative study. As representative samples, the measurement results of the proposed binary cloud prediction based PVG smoothing approach are presented accompanied with the simulation results associated with the other methods using the non-predictive approach, ideal export prediction, and output estimation. Figs. 5 and 7 illustrate the comparative results for 4th and 8th of December, 2015 with scattered fast-moving clouds, and mostly clear sky, respectively. Furthermore, the aggregated SO_i and CO_i figures and the resultant smoothing command are illustrated in Figs. 6 and 8, respectively. The energy balance profile, i.e. energy yield, smoothing power injection and absorption for different approaches are

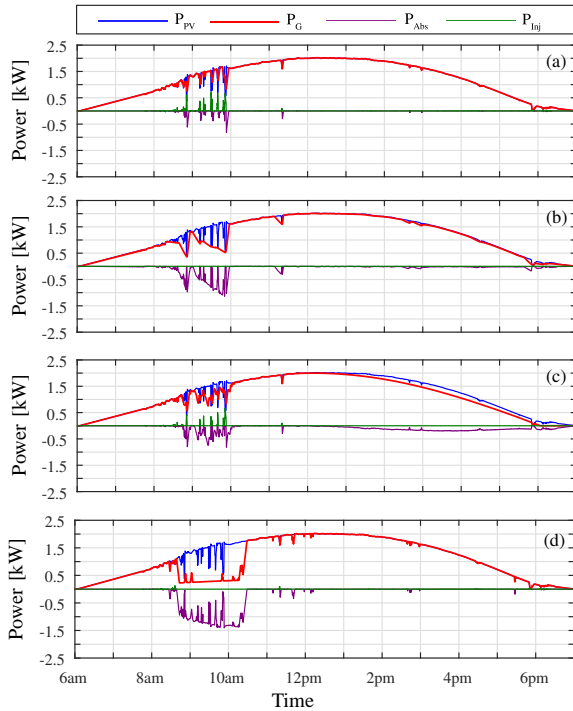


Fig. 7. Smoothing results for Dec. 8th, 2015. (a) Non-Predictive. (b) Ideal Prediction. (c) Estimation-based. (d) Binary Prediction.

summarised and compared in Fig. 9. To allow a more valid comparison it is assumed that the absorbed energy is not recovered into the grid while the injected energy is supplied to meet the RR criteria.

As discussed in section III and indicated by Eqs. (13) and (18), in the smoothing process the plant export power is governed so as to satisfy the RR requirements. Therefore, the sudden variations of the generated power have to be treated by a storage system such as BS of sufficient energy and power capacity. Incorporating the cloud prediction information, depending on how early the sudden variations are predicted and how accurately the projected PVG level is estimated, tends to mitigate the reliance on the required power injection (Fig. 3).

The following remarks could be concluded from the comparative results:

- The Non-predictive PVG smoothing (section III-A; Eqs. (11)-(13)) involves bidirectional supporting energy exchange during ramp events. Therefore, energy injection and absorption on ramp down and ramp up processes, respectively, are essential to maintain the RR requirement. This is illustrated in Figs. 5(a) and 7(a) where P_{Inj} and P_{Abs} represent the injected and absorbed power, respectively. Therefore, the storage support is inevitable in this approach which is a financial impediment to vast deployment of PV resources across the areas that RR requirement is a precondition for grid integration of PVG plants. In particular not all battery technologies are capable of delivering a cycle time as short as 10 [min], as the typical power density normally allows around 1[hr]

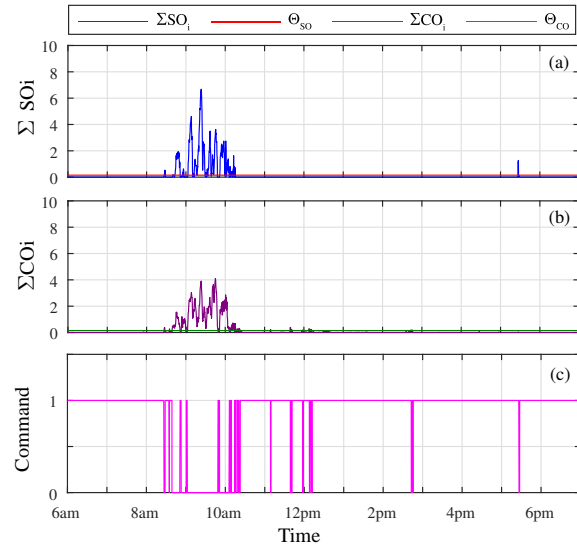


Fig. 8. Smoothing signals for Dec. 8th, 2015. (a) Total SO_i . (b) Total CO_i . (c) Export toggle command to solar inverter #1.

cycling time [30]. Hence, the BS has to be oversized in energy capacity to meet the power density of smoothing treatment. On the other hand, as Fig. 9(a) shows this approach exhibits a relatively high energy efficiency due to relatively less energy absorption. Nevertheless, the capital cost and the maintenance of BS has created a motivation for exploring more economical alternatives.

- As Figs. 5(b) and 7(b) imply, the ideal export prediction PVG smoothing (section III-B; Eqs. (15)-(18)) shifts the direction of smoothing energy exchange towards the absorption and it no longer involves power injection. Fig. 9(b) also confirms the fact that the energy injection could be totally mitigated provided the accurate prediction information determines the occurrence of the under/over generations and the resulting PV export power is precisely estimated. However, the utmost yield is achieved when the storage is deployed to handle the energy absorption P_{Abs} and deliver that slowly into the utility grid, meanwhile maintaining the RR requirement. Moreover, the unidirectional smoothing power allows for possible elimination of the storage at the cost of reduced energy efficiency of the smoothing process, as indicated in Fig. 9(a). The financial benefit of mitigating the storage distinctly outweighs the reduced financial revenue due to the lower yield. The capital price of the BS system normally accounts for a significant portion of the total cost of a BS assisted PV plant, e.g. it adds up to 50% to price of the PVG plant, as of 2012 in US [31]. Considering that, Perth, Western Australia, in average has only 30% cloudy days a year [32]. Given, the cloudy days are not of high yield compared to an ordinary sunny day and only a portion of the generation is curtailed in the smoothing process. The BS can recover less than 30% of annual yield while requiring up to 50% additional capital investment which is not financially justified compared to

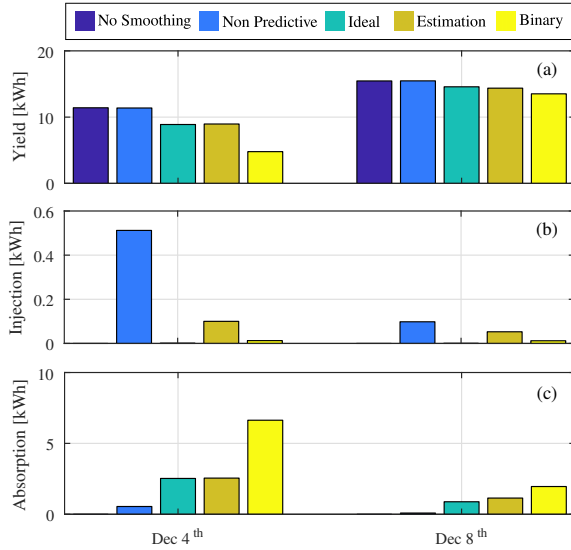


Fig. 9. Segregated energy balance for different smoothing approaches. (a) Energy yield, (b) injected energy, and (c) absorbed energy.

the prediction based PVG smoothing approach.

- The proposed PVG smoothing based on output estimation (section III-C; Eqs. (19)-(20)) shows virtually varying performance depending on the degree of cloudiness. As seen in Figs. 5(c) and 7(c) this method suffers from the lack of perfect accuracy in the presence of fast moving clouds. This is a typical drawback to the imagery based cloud prediction approaches. On the other hand, in highly cloudy days with substantially intermittent generation level, even a relatively inaccurate forecast makes a remarkable decrease in the energy and power injection backup for the smoothing. In contrast, in the case of occasional brief shadings on a mostly sunny day it fails to make a significant reduction in the smoothing energy injection either in terms of power, or occurrence frequency (Fig. 9(b)). This is mainly attributed to the estimation error during clear-sky periods. Moreover, the simplifications made in the calculation of projected generation level in Eq. 19 creates an offset estimation error during the clear sky periods and unnecessary energy absorption (Fig. 7(c)). Therefore, the output estimation method exhibits a relatively inferior energy yield compared to the ideal export prediction (Fig. 9(a)). Although it reduces the amount of injected smoothing energy, this smoothing approach involves bidirectional energy exchange which still makes the assistance of the storage unavoidable.
- The proposed binary prediction based PVG smoothing approach (section III-D; Eqs. (21)-(22)), in essence, operates on the principle that the PVG export power is restricted once passing clouds are projected to obscure the solar disc or the circumsolar region. This conservative solution compensates for the inherent imperfect accuracy of the cloud prediction process. Regardless of the magnitude of the projected export reduction, output

TABLE II
SMOOTHING SET POINTS.

Parameter	Symbol	Value
Permissible RR	R_s	180 [Wmin ⁻¹]
Min Observation Range	t_{h1}	120 [s]
Max Observation Range	t_{h2}	155 [s]
Forecast Range	t_f	10 [min]
Split Forecast Range	t_{sp}	30 [s]
SO_i Threshold	Θ_{SO}	0.15
CO_i Threshold	Θ_{CO}	0.15
Shut-Off Coefficient	C_{Base}	20%

power slowly ramps down to a reduced amount P_{Base} which will not be affected by the coming shading event. Hence a reduced energy harvest only during the cloudy days is typical of this approach compared to the ideal PVG export prediction (Fig. 9(a)). The simulation results suggest that during the passing clouds this method needs an inconsiderable amount of backup power injection P_{Inj} in only a very few instances day, which is negligible when compared with the conventional non-predictive method (Fig. 5 and Fig. 7). In practice, a slight deviations from the required RR up to a certain extent is allowed by most network operators, e.g. the Horizon Power Corporation in Western Australia permits for a 10% non-linearity in the RR of PVG power export [33]. The experimental results show that the supporting power exchange never exceeded the allowed non-linearity band ($10\% \times 1.8 = 0.18$ [kW]) which can be well accommodated by the existing spinning reserves of the utility grid. From the financial point of view, a justification similar to the ideal prediction methods holds for the practical proposed binary cloud prediction method as well. Therefore, given the minimum energy efficiency in the worst case scenario, the proposed binary cloud prediction method still exhibits a better financial profile compared to the conventional non-predictive BS-based approach.

VI. CONCLUSION

This paper proposes a predictive approach regulating the erratic PVG export variations attributed to the passing clouds to mitigate the extra burden on the operational reserve capacity of the utility grid. This smoothing method works on the principle of initiating a ramp down function sufficiently prior to the appearance of passing clouds over the PV array. Compared to the non-predictive approaches that react to the PVG intermittency issues upon the incidence, in the proposed method the sudden and disruptive PVG export variations are mostly avoided and the reliance on the backup power injection is significantly reduced accordingly. This highlights the "proactive" characteristics of the proposed smoothing approach as opposed to the "reactive" nature of the non-predictive solutions. The performance and practical viability of the proposed method are evaluated through a series of experimental tests on a prototype constructed at Magellan Power in Western Australia. The experimental results are also

compared with the associated results of the conventional non-predictive smoothing strategy simulated in Matlab/Simulink®. The main conclusions are:

- A perfectly accurate PVG output prediction enables a regulation method with no reliance on the back-up power injection while the amount of produced energy is not remarkably compromised.
- Given the inherent shortcomings of the imagery-based prediction approaches, a novel averaged cloud prediction scheme with improved robustness is proposed that is capable of indicating the erratic solar generation variations sufficiently ahead of its incidence.
- The proposed binary cloud prediction using a sky camera could significantly mitigate the reliance of the conventional PVG smoothing strategy on the supporting power injection.
- However due to the conservative nature of the cloud prediction algorithm, for some operating conditions the approach may suffer from an inferior energy harvest profile when compared with the ideal prediction technique.
- In the case of the proposed binary prediction based method, the financial benefit of mitigating storage support well outweighs the curtailed energy involves during the passing clouds.
- The experimental outcomes of the proposed prediction assisted PVG smoothing method support the feasibility of a reliable battery-less ramp rate smoothing solution.

ACKNOWLEDGMENT

The first author of this work has been awarded a competitive Australian Government Research Training Program Scholarships supported by Curtin University and Magellan Powertronics to support his research and the authors would like to acknowledge their contributions to this work as the result of the research program.

REFERENCES

- [1] E. Ela, M. Milligan, and B. Kirby, "Operating Reserves and Variable Generation," National Renewable Energy Laboratory (NREL), Report, Aug. 2011.
- [2] V. Gevorgian and S. Booth, "Review of PREPA Technical Requirements for Interconnecting Wind and Solar Generation," National Renewable Energy Laboratory (NREL), Report, Nov. 2013.
- [3] "National Electricity Rules Version 79," Australian Energy Market Commission (AEMC), Mar. 2016.
- [4] "Interconnection Requirements for Variable Generation," North American Electric Reliability Corporation (NERC), Atlanta, GA 30326, p. 121, 2012.
- [5] M. Bragard and N. Soltau and S. Thomas and R. W. De Doncker, "The Balance of Renewable Sources and User Demands in Grids: Power Electronics for Modular Battery Energy Storage Systems," *IEEE Trans. Power Electron.*, vol. 25, no. 12, pp. 3049–3056, Dec. 2010.
- [6] O. M. Toledo, D. O. Filhoa, and A. S. A. C. Dinizb, "Distributed PV Generation and Energy Storage Systems: A Review," *Renewable and Sustainable Energy Reviews*, vol. 14, no. 1, p. 506511, Jan. 2010.
- [7] J. Tant, F. Geth, D. Six, P. Tant, and J. Driesen, "Multiobjective Battery Storage to Improve PV Integration in Residential Distribution Grids," *IEEE Trans. Sustain. Energy*, vol. 4, no. 1, pp. 182–191, Jan. 2013.
- [8] J. Marcos, O. Storkl, L. Marroyo, M. Garcia, and E. Lorenzo, "Storage Requirements for PV Power Ramp-Rate Control," *Solar Energy*, vol. 99, pp. 28 – 35, Jun. 2014.
- [9] M. J. E. Alam, K. M. Muttaqi, and D. Sutanto, "Mitigation of Rooftop Solar PV Impacts and Evening Peak Support by Managing Available Capacity of Distributed Energy Storage Systems," *IEEE Trans. Power Syst.*, vol. 28, no. 4, pp. 3874–3884, Nov. 2013.
- [10] —, "A Novel Approach for Ramp-Rate Control of Solar PV Using Energy Storage to Mitigate Output Fluctuations Caused by Cloud Passing," *IEEE Transactions on Energy Conversion*, vol. 29, no. 2, pp. 507–518, Jun. 2014.
- [11] A. M. Gee, F. V. P. Robinson, and R. W. Dunn, "Analysis of Battery Lifetime Extension in a Small-Scale Wind-Energy System Using Supercapacitors," *IEEE Trans. Energy Convers.*, vol. 28, no. 1, pp. 24–33, Mar. 2013.
- [12] H. Zhou, T. Bhattacharya, T. Duong, T. S. T. Siew, and A. M. Khambadkone, "Composite Energy Storage System Involving Battery and Ultracapacitor With Dynamic Energy Management in Microgrid Applications," *IEEE Trans. Power Electron.*, vol. 26, no. 3, pp. 923–930, Mar. 2011.
- [13] Seung-TakKim and J.-W. Park, "Energy Management Strategy and Adaptive Control for SMES in Power System with a PV Farm," *Journal of Electrical Engineering & Technology*, vol. 9, pp. 742–747, 2014.
- [14] Z. Wang, Z. Zou, and Y. Zheng, "Design and Control of a Photovoltaic Energy and SMES Hybrid System With Current-Source Grid Inverter," *IEEE Trans. Sustain. Energy*, vol. 4, no. 2, pp. 464–473, Jun. 2013.
- [15] R. Naik, N. Mohan, M. Rogers, and A. Bulawka, "A Novel Grid Interface, Optimized for Utility-Scale Applications of Photovoltaic, Wind-Electric, and Fuel-Cell Systems," *IEEE Trans. Power Del.*, vol. 10, no. 4, pp. 1920–1926, Oct. 1995.
- [16] F. Capp, M. Lazarewicz, A. Arseneaux, P. Dresens, and H. Rojas, "Methods, Systems and Apparatus for Regulating Frequency of Generated Power Using Flywheel Energy Storage Systems With Varying Load and/or Power Generation," 2011.
- [17] M. Diagne, M. David, P. Lauret, J. Boland, and N. Schmutz, "Review of Solar Irradiance Forecasting Methods and a Proposition for Small-Scale Insular Grids," *Renewable and Sustainable Energy Reviews*, vol. 27, no. 0, pp. 65–76, Nov. 2013.
- [18] C. W. Chow, B. Urquhart, M. Lave, A. Dominguez, J. Kleissl, J. Shields, and B. Washom, "Intra-Hour Forecasting With a Total Sky Imager at the UC San Diego Solar Energy Testbed," *Solar Energy*, vol. 85, no. 11, pp. 2881–2893, Nov. 2011.
- [19] B. Urquhart, M. Ghonima, D. Nguyen, B. Kurtz, C. W. Chow, and J. Kleissl, "Sky-Imaging Systems for Short-Term Forecasting," in *Solar Energy Forecasting and Resource Assessment*, J. Kleissl, Ed. Boston, MA: Academic Press, 2013, ch. 9, pp. 195–232.
- [20] H. Yang, B. Kurtz, D. Nguyen, B. Urquhart, C. W. Chow, M. Ghonima, and J. Kleissl, "Solar Irradiance Forecasting Using a Ground-Based Sky Imager Developed at UC San Diego," *Solar Energy*, vol. 103, pp. 502–524, May. 2014.
- [21] S. R. West, D. Rowe, S. Sayeef, and A. Berry, "Short-Term Irradiance Forecasting Using Skycams: Motivation and Development," *Solar Energy*, vol. 110, pp. 188–207, Dec. 2014.
- [22] D. Bernecker, C. Riess, E. Angelopoulou, and J. Hornegger, "Continuous Short-Term Irradiance Forecasts Using Sky Images," *Solar Energy*, vol. 110, pp. 303–315, Dec. 2014.
- [23] D. Scaramuzza, "OCamCalib: Omnidirectional Camera Calibration Toolbox," 2006.
- [24] I. Reda and A. Andreas, "Solar Position Algorithm for Solar Radiation Applications," *Solar Energy*, vol. 76, no. 5, pp. 577 – 589, 2004.
- [25] R. W. Johnson, W. S. Hering, and J. E. Shields, "Automated visibility & cloud cover measurements with a solid state imaging system," Scripps Institution of Oceanography, UC San Diego, Report, 1989.
- [26] R. Kittler, M. Kocifaj, and S. Darula, "Propagation of Light in the Atmospheric Environment," in *Daylight Science and Daylighting Technology*. New York, NY: Springer New York, 2012, ch. 4, pp. 97–125.
- [27] R. Szeliski, "Dense Motion Estimation," in *Computer Vision: Algorithms and Applications*. Springer-Verlag New York, Inc., 2010, ch. 8, p. 812.
- [28] M. Paulescu, E. Paulescu, P. Gravila, and V. Badescu, "The Future of the Energy Mix Paradigm," in *Weather Modeling and Forecasting of PV Systems Operation*, ser. Green Energy and Technology, J. Kleissl, Ed. London: Springer London, 2013, ch. 1, pp. 1–15.
- [29] "Magellan Solar Export Control Solutions Solar Gate," Magellan Power, p. 8, 2015. [Online]. Available: <http://magellanpower.com.au/Products/Renewable-Energy-and-Energy-Storage-Systems/Solar-Gate>
- [30] National Research Council, *Meeting the Energy Needs of Future Warriors*. Washington, DC: The National Academies Press, 2004. [Online]. Available: <http://www.nap.edu/catalog/11065/meeting-the-energy-needs-of-future-warriors>

- [31] "Solar Photovoltaics," in *Renewable Energy Technologies: Cost Analysis Series*. The International Renewable Energy Agency (IRENA), 2012, p. 21, volume 1:Power Sector, Issue 4/5.
- [32] Bureau of Meteorology. (2016) Climate Statistics for Australian Sites. [Online]. Available: <http://www.bom.gov.au/climate/data/>
- [33] "Technical Requirements for Renewable Energy Systems Connected to the Low Voltage (LV) Network via Inverters," HPC-9FJ-12-0001-2012, Horizon Power Corporation, WA, Australia, p. 58, 2012. [Online]. Available: <http://horizonpower.com.au/media/1121/technical-requirements-for-renewable-energy-systems-connected-to-the-low-voltage-lv-network-via-inverters.pdf>

Appendix E

Statements of the Co-Authors

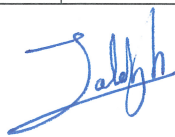
Publications

- "Control Algorithm for Bidirectional Fly-Back Active Cell Balancer with Interleaved Transformer Connections," in *2016 IEEE Power and Energy Society General Meeting (PESGM)*, July 2016, pp. 1-5.
- "Battery-Less ShortTerm Smoothing of Photovoltaic Generation Using Sky Camera," *Industrial Informatics, IEEE Transactions on*, 2017, unpublished, Manuscript No. TII-16-1373.R1.

Principal Author(Candidate)

Name of Principal Author	Mojtaba Saleh
Contribution to the Papers	<ul style="list-style-type: none">• Designed and coordinated the projects.• Developed the theory and designed the model.• Simulation analysis and interpretation of the results.• Developed the industrial prototype.▄ Designed and conducted the experiments.▄ Verified the results and drafted the manuscripts.
Overall percentage	75%

Signature:



Date: 31/01/2018

Co-Author Contributions

By signing the Statement of Authorship, each author certifies that:

- (i) The candidates stated contribution to the publication is accurate (as detailed above);
- (ii) Permission is granted for the candidate to include the publication in the thesis; and
- (iii) The sum of all co-author contributions is equal to 100% less the candidates stated contribution.

Name of Co-Author	Lindsay Meek
Contribution to the Papers	<ul style="list-style-type: none">● Developed the conceptual ideas.● Assisted and advised on development of the prototype.■ Provided critical feedback.

Signature: 

Date: 31/01/2018

Name of Co-Author	Mohammad A.S. Masoum
Contribution to the Papers	<ul style="list-style-type: none">● Planned and supervised the research works.● Provided critical feedback.● Revised the manuscripts.

Signature: 

Date: 31/01/2018

Name of Co-Author	Masoud Abshar
Contribution to the Papers	<ul style="list-style-type: none">• Developed the conceptual ideas.• Provided the logistics support to develop the prototype.• Advised on the development of the prototype.

Signature: 

Date: 31/01/2018

Bibliography

- [1] B. Tamimi, C. Caizares, and K. Bhattacharya, “System Stability Impact of Large-Scale and Distributed Solar Photovoltaic Generation: The Case of Ontario, Canada,” *Sustainable Energy, IEEE Transactions on*, vol. 4, no. 3, pp. 680–688, Jul. 2013.
- [2] A. G. Marinopoulos, M. C. Alexiadis, and P. S. Dokopoulos, “A Correlation Index to Evaluate Impact of PV Installation on Joule Losses,” *Power Systems, IEEE Transactions on*, vol. 26, no. 3, pp. 1564–1572, Aug. 2011.
- [3] M. McGranaghan, T. Ortmeier, D. Crudele, T. Key, J. Smith, and P. Barker, “Renewable Systems Interconnection Study: Advanced Grid Planning and Operations,” Sandia National Laboratories, Report, 2008.
- [4] M. Thomson and D. G. Infield, “Network Power-Flow Analysis for a High Penetration of Distributed Generation,” *Power Systems, IEEE Transactions on*, vol. 22, no. 3, pp. 1157–1162, Aug. 2007.
- [5] M. M. Haque and P. Wolfs, “A Review of High PV Penetrations in LV Distribution Networks: Present Status, Impacts and Mitigation Measures,” *Renewable and Sustainable Energy Reviews*, vol. 62, pp. 1195 – 1208, 2016. [Online]. Available: <http://www.sciencedirect.com/science/article/pii/S1364032116300429>
- [6] A. Toliyat, A. Kwasinski, and F. Uriarte, “Effects of High Penetration Levels of Residential Photovoltaic Generation: Observations From Field Data,” in *Renewable Energy Research and Applications (ICRERA)*, Nagasaki, Japan, Nov. 2012, Conference Paper.
- [7] M. Thomson and D. Infield, “Impact of Widespread Photovoltaics Generation on Distribution Systems,” *IET Renew. Power Gener.*, vol. 1, no. 1, p. 3340, Mar. 2007.

- [8] P. Denholm, M. OConnell, G. Brinkman, and J. Jorgenson, “Overgeneration from Solar Energy in California: A Field Guide to the Duck Chart,” National Renewable Energy Laboratory (NREL), Report, November 2015. [Online]. Available: <https://www.nrel.gov/docs/fy16osti/65023.pdf>
- [9] B. H. Chowdhury, “Effect of Central Station Photovoltaic Plant on Power System Security,” in *IEEE Conference on Photovoltaic Specialists*, May 1990, pp. 831–835 vol.2.
- [10] Y. Okumoto, N. Yorino, Y. Zoka, Y. Sasaki, T. Akiyoshi, and T. Isoya, “A Study on The Power System Security with Increased PV Penetration by Applying the Robust Power System Security,” in *IEEE PES Innovative Smart Grid Technologies, Europe*, October 2014, pp. 1–6.
- [11] J. V. Paatero and P. D. Lund, “Effects of Large-Scale Photovoltaic Power Integration on Electricity Distribution Networks,” *Renewable Energy*, vol. 32, no. 2, p. 216234, Feb. 2007.
- [12] R. Tonkoski, L. A. C. Lopes, and T. H. M. El-Fouly, “Coordinated Active Power Curtailment of Grid Connected PV Inverters for Over Voltage Prevention,” *Sustainable Energy, IEEE Transactions on*, vol. 2, no. 2, pp. 139–147, 2011.
- [13] M. Morjaria, D. Anichkov, V. Chadliev, and S. Soni, “A Grid-Friendly Plant: The Role of Utility-Scale Photovoltaic Plants in Grid Stability and Reliability,” *IEEE Power and Energy Magazine*, vol. 12, no. 3, pp. 87–95, May 2014.
- [14] J. P. Barton and D. G. Infield, “Energy Storage and Its Use With Intermittent Renewable Energy,” *Energy Conversion, IEEE Transactions on*, vol. 19, no. 2, pp. 441–448, 2004.
- [15] M. Bragard, N. Soltan, S. Thomas, and R. W. De Doncker, “The Balance of Renewable Sources and User Demands in Grids: Power Electronics for Modular Battery Energy Storage Systems,” *Power Electronics, IEEE Transactions on*, vol. 25, no. 12, pp. 3049–3056, 2010.
- [16] C. A. Hill, M. C. Such, D. Chen, J. Gonzalez, and W. Grady, “Battery Energy Storage for Enabling Integration of Distributed Solar Power Generation,” *Smart Grid, IEEE Transactions on*, vol. 3, no. 2, pp. 850–857, JUNE 2012.

- [17] S. Shivashankar, S. Mekhilef, H. Mokhlis, and M. Karimi, “Mitigating Methods of Power Fluctuation of Photovoltaic (PV) Sources A Review,” *Renewable and Sustainable Energy Reviews*, vol. 59, pp. 1170 – 1184, 2016. [Online]. Available: <http://www.sciencedirect.com/science/article/pii/S1364032116000897>
- [18] Y. Riffonneau, M. Seddik Bacha, F. Barruel, and S. Ploix, “Optimal Power Flow Management for Grid Connected PV Systems With Batteries,” *Sustainable Energy, IEEE Transactions on*, vol. 2, no. 3, pp. 309–320, Jul. 2011.
- [19] O. M. Toledoa, D. O. Filhoa, and A. S. A. C. Dinizb, “Distributed Photovoltaic Generation and Energy Storage Systems: A Review,” *Renewable and Sustainable Energy Reviews*, vol. 14, no. 1, p. 506511, Jan. 2010.
- [20] M. J. E. Alam, K. M. Muttaqi, and D. Sutanto, “Mitigation of Rooftop Solar PV Impacts and Evening Peak Support by Managing Available Capacity of Distributed Energy Storage Systems,” *Power Systems, IEEE Transactions on*, vol. 28, no. 4, pp. 3874–3884, 2013.
- [21] J. Tant, F. Geth, D. Six, P. Tant, and J. Driesen, “Multiobjective Battery Storage to Improve PV Integration in Residential Distribution Grids,” *Sustainable Energy, IEEE Transactions on*, vol. 4, no. 1, pp. 182–191, 2013.
- [22] Seung-TakKim and J.-W. Park, “Energy Management Strategy and Adaptive Control for SMES in Power System with a Photovoltaic Farm,” *Journal of Electrical Engineering & Technology*, vol. 9, pp. 742–747, 2014.
- [23] Z. Wang, Z. Zou, and Y. Zheng, “Design and Control of a Photovoltaic Energy and SMES Hybrid System With Current-Source Grid Inverter,” *Sustainable Energy, IEEE Transactions on*, vol. 4, no. 2, pp. 464–473, Apr 2013.
- [24] F. Capp, M. Lazarewicz, A. Arseneaux, P. Dresens, and H. Rojas, “Methods, Systems and Apparatus For Regulating Frequency of Generated Power Using Flywheel Energy Storage Systems With Varying Load and/or Power Generation,” US Generic US8 008 804 B2, 2011. [Online]. Available: <https://www.google.ch/patents/US8008804>

- [25] Z. Haihua, T. Bhattacharya, T. Duong, T. S. T. Siew, and A. M. Khambadkone, "Composite Energy Storage System Involving Battery and Ultracapacitor With Dynamic Energy Management in Microgrid Applications," *Power Electronics, IEEE Transactions on*, vol. 26, no. 3, pp. 923–930, 2011.
- [26] R. Naik, N. Mohan, M. Rogers, and A. Bulawka, "A Novel Grid Interface, Optimized for Utility-Scale Applications of Photovoltaic, Wind-Electric, and Fuel-Cell Systems," *Power Delivery, IEEE Transactions on*, vol. 10, no. 4, pp. 1920–1926, Oct 1995.
- [27] S. Rahman and K. S. Tam, "A Feasibility Study of Photovoltaic Fuel-Cell Hybrid Energy System," *Energy Conversion, IEEE Transactions on*, vol. 3, no. 1, pp. 50–55, 1988.
- [28] C. V. Nayar, M. Ashari, and W. W. L. Keerthipala, "A Grid-Interactive Photovoltaic Uninterruptible Power Supply System Using Battery Storage and a Back-Up Diesel Generator," *Energy Conversion, IEEE Transactions on*, vol. 15, no. 3, pp. 348–353, 2000.
- [29] M. Ashari, C. V. Nayar, and W. W. L. Keerthipala, "Optimum Operation Strategy and Economic Analysis of a Photovoltaic-Diesel-Battery-Mains Hybrid Uninterruptible Power Supply," *Renewable Energy*, vol. 22, no. 13, pp. 247–254, 2001. [Online]. Available: <http://www.sciencedirect.com/science/article/pii/S0960148100000136>
- [30] X. Huanhai, L. Yun, W. Zhen, G. Deqiang, and Y. Taicheng, "A New Frequency Regulation Strategy for Photovoltaic Systems Without Energy Storage," *Sustainable Energy, IEEE Transactions on*, vol. 4, no. 4, pp. 985–993, 2013.
- [31] X. Li, D. Hui, and X. Lai, "Battery Energy Storage Station (BESS)-Based Smoothing Control of Photovoltaic (PV) and Wind Power Generation Fluctuations," *Sustainable Energy, IEEE Transactions on*, vol. 4, no. 3, pp. 464–473, Apr. 2013.
- [32] W. Omran, M. Kazerani, and M. Salama, "Investigation of Methods for Reduction of Power Fluctuations Generated From Large Grid-Connected Photovoltaic Systems," *Applied Superconductivity, IEEE Transactions on*, vol. 26, no. 1, pp. 318 – 327, Mar. 2011.

- [33] S. Grillo, M. Marinelli, S. Massucco, and F. Silvestro, “Optimal Management Strategy of a Battery-Based Storage System to Improve Renewable Energy Integration in Distribution Networks,” *Smart Grid, IEEE Transactions on*, vol. 3, no. 2, pp. 950–958, 2012.
- [34] M. Braun, T. Stetz, R. Brndlinger, C. Mayr, K. Ogimoto, H. Hatta, H. Kobayashi, B. Kroposki, B. Mather, M. Coddington, K. Lynn, G. Graditi, A. Woyte, and I. MacGill, “Is The Distribution Grid Ready to Accept Large-Scale Photovoltaic Deployment State of The Art, Progress, and Future Prospects,” *Progress in Photovoltaics Research and Applications*, vol. 20, no. 6, p. 681697, 2012.
- [35] *Guide for Conducting Distribution Impact Studies for Distributed Resource Interconnection*, IEEE Standard 1547.7, 2013.
- [36] S. Eftekharnejad, V. Vittal, G. T. Heydt, B. Keel, and J. Loehr, “Impact of Increased Penetration of Photovoltaic Generation on Power Systems,” *Power Systems, IEEE Transactions on*, vol. 28, no. 2, pp. 893–901, May 2013.
- [37] M. Datta, T. Senjyu, A. Yona, and T. Funabashi, “Control of MW-class PV generation to reduce frequency and tie-line power fluctuations in three control area power system,” in *8th International Conference on Power Electronics - ECCE Asia*, May 2011, pp. 894–901.
- [38] H. Asano, K. Yajima, and Y. Kaya, “Influence of Photovoltaic Power Generation on Required Capacity for Load Frequency Control,” *IEEE Transactions on Energy Conversion*, vol. 11, no. 1, pp. 188–193, March 1996.
- [39] M. Datta, T. Senjyu, A. Yona, T. Funabashi, and C. H. Kim, “A frequency-control approach by photovoltaic generator in a pv-diesel hybrid power system,” *IEEE Transactions on Energy Conversion*, vol. 26, no. 2, pp. 559–571, June 2011.
- [40] E. Ela, M. Milligan, and B. Kirby, “Operating Reserves and Variable Generation,” National Renewable Energy Laboratory (NREL), Report, August 2011. [Online]. Available: www.nrel.gov/docs/fy11osti/51978.pdf
- [41] C. B. Martinez-Anido, B. Botor, A. R. Florita, C. Draxl, S. Lu, H. F. Hamann, and B.-M. Hodge, “The Value of Day-Ahead Solar Power

- Forecasting Improvement ,” *Solar Energy*, vol. 129, pp. 192 – 203, 2016. [Online]. Available: <http://www.sciencedirect.com/science/article/pii/S0038092X16000736>
- [42] T. KATO, Y. MANABE, T. FUNABASHI, K. MATSUMOTO, M. KURIMOTO, and Y. SUZUOKI, “A Study on Influence of Ramp Event of Aggregated Power Output of Photovoltaic Power Generation on Electric Power System Frequency,” *Electrical Engineering in Japan*, vol. 202, no. 3, pp. 11–21, 2 2018. [Online]. Available: <http://doi.org/10.1002/eej.23046>
- [43] A. Woyte, R. Belmans, and J. Nijs, “Fluctuations in Instantaneous Clearness Index: Analysis and Statistics,” *Solar Energy*, vol. 81, p. 195206, 2007.
- [44] W. Jewell and R. Ramakumar, “The Effects of Moving Clouds on Electric Utilities with Dispersed Photovoltaic Generation,” *Energy Conversion, IEEE Transactions on*, vol. EC-2, no. 4, pp. 570–576, 1987.
- [45] N. Kawasakia, T. Oozekia, K. Otania, and K. Kurokawa, “An Evaluation Method of The Fluctuation Characteristics of Photovoltaic Systems by Using Frequency Analysis,” *Solar Energy Materials and Solar Cells*, vol. 90, p. 33563363, 2006.
- [46] K. Otani, J. Minowa, and K. Kurokawa, “Study on Areal Solar Irradiance for Analyzing Areal-Totalized PV Systems,” *Solar Energy Materials and Solar Cells*, vol. 47, no. 1-4, pp. 281–288, Oct. 1997. [Online]. Available: <http://www.sciencedirect.com/science/article/pii/S0927024897000500>
- [47] I. de la Parra, J. Marcos, M. Garca, and L. Marroyo, “Storage Requirements for PV Power Ramp-Rate Control in a PV Fleet,” *Solar Energy*, vol. 118, pp. 426 – 440, 2015. [Online]. Available: <http://www.sciencedirect.com/science/article/pii/S0038092X15003102>
- [48] M. Datta, T. Senjyu, A. Yona, T. Funabashi, and C.-H. Kim, “Photovoltaic Output Power Fluctuations Smoothing Methods for Single and Multiple PV Generators,” *Current Applied Physics*, vol. 10, no. 2, Supplement, pp. S265 – S270, 2010, the Proceeding of the International Renewable Energy Conference and Exhibition 2008 (RE2008). [Online]. Available: <http://www.sciencedirect.com/science/article/pii/S1567173909005239>

- [49] D. S. Renne, “Emerging Meteorological Requirements to Support High Penetrations of Variable Renewable Energy Sources: Solar Energy,” in *Weather Matters for Energy*, A. Troccoli, L. Dubus, and S. E. Haupt, Eds. New-York: Springer-Verlag, 2014, pp. 257–273.
- [50] A. Kankiewicz, M. Sengupta, and D. Moon, “Observed Impacts of Transient Clouds on Utility-Scale PV Fields,” in *39th ASES National Solar Conference*, Boulder, Colorado, US, 2010, Conference Proceedings.
- [51] A. Ellis, D. Schoenwald, J. Hawkins, S. Willard, and B. Arellano, “PV Output Smoothing With Energy Storage,” in *Photovoltaic Specialists Conference (PVSC), 38th IEEE*, 2012, Conference Proceedings, pp. 001 523–001 528.
- [52] C. Abbey, K. Strunz, and G. Joos, “A Knowledge-Based Approach for Control of Two-Level Energy Storage for Wind Energy Systems,” *Energy Conversion, IEEE Transactions on*, vol. 24, no. 2, pp. 539–547, 2009.
- [53] X. Li, “Fuzzy Adaptive Kalman Filter for Wind Power Output Smoothing with Battery Energy Storage System,” *Renewable Power Generation, IET*, vol. 6, no. 5, pp. 340–347, 2012.
- [54] X. Li, Y. Lib, X. Hanb, and D. Huia, “Application of Fuzzy Wavelet Transform to Smooth Wind/PV Hybrid Power System Output with Battery Energy Storage System,” in *International Conference on Smart Grid and Clean Energy Technologies*, vol. 12, 2011, Conference Proceedings, p. 9941001.
- [55] M. J. E. Alam, K. M. Muttaqi, and D. Sutanto, “A Novel Approach for Ramp-Rate Control of Solar PV Using Energy Storage to Mitigate Output Fluctuations Caused by Cloud Passing,” *Energy Conversion, IEEE Transactions on*, vol. 29, no. 2, pp. 507–518, June 2014.
- [56] J. Marcos, O. Storkl, L. Marroyo, M. Garcia, and E. Lorenzo, “Storage Requirements for PV Power Ramp-Rate Control,” *Solar Energy*, vol. 99, pp. 28 – 35, 2014. [Online]. Available: <http://www.sciencedirect.com/science/article/pii/S0038092X13004672>
- [57] I. de la Parra, J. Marcos, M. Garca, and L. Marroyo, “Control Strategies to Use the Minimum Energy Storage Requirement for PV Power Ramp-Rate

- Control,” *Solar Energy*, vol. 111, pp. 332 – 343, 2015. [Online]. Available: <http://www.sciencedirect.com/science/article/pii/S0038092X14005258>
- [58] National Research Council, *Meeting the Energy Needs of Future Warriors*. Washington, DC: The National Academies Press, 2004. [Online]. Available: <http://www.nap.edu/catalog/11065/meeting-the-energy-needs-of-future-warriors>
- [59] I. Hadjipaschalis, A. Poullikkas, and V. Efthimiou, “Overview of Current and Future Energy Storage Technologies for Electric Power Applications,” *Renewable and Sustainable Energy Reviews*, vol. 13., no. 67, pp. 1513–1522, Aug./Sep. 2009.
- [60] T. Kinjo, T. Senjyu, N. Urasaki, and H. Fujita, “Output Levelling of Renewable Energy by Electric Double-Layer Capacitor Applied for Energy Storage System,” *Energy Conversion, IEEE Transactions on*, vol. 21, no. 1, pp. 221–227, 2006.
- [61] J. Simmins, “A Case Study on the Demonstration of Storage for Simultaneous Voltage Smoothing and Peak Shifting,” Electric Power Research Institute (EPRI), Report, Oct. 2012. [Online]. Available: <http://www.ecoult.com/case-studies/pnm-nm-usa-solar-power-smoothing-and-energy-shifting/>
- [62] S. T. Hung, D. C. Hopkins, and C. R. Mosling, “Extension of Battery Life Via Charge Equalization Control,” *Industrial Electronics, IEEE Transactions on*, vol. 40, no. 1, pp. 96–104, Feb 1993.
- [63] J. Ewanchuk and J. Salmon, “A Modular Balancing Bridge for Series Connected Voltage Sources,” *Power Electronics, IEEE Transactions on*, vol. 29, no. 9, pp. 4712–4722, 2014.
- [64] P. A. Cassani and S. S. Williamson, “Design, Testing, and Validation of a Simplified Control Scheme for a Novel Plug-In Hybrid Electric Vehicle Battery Cell Equalizer,” *Industrial Electronics, IEEE Transactions on*, vol. 57, no. 12, pp. 3956–3962, 2010.
- [65] L. Kyung-Min, C. Yoo-Chae, S. Chang-Hyeon, and K. Bongkoo, “Active Cell Balancing of Li-Ion Batteries Using LC Series Resonant Circuit,” *Industrial Electronics, IEEE Transactions on*, vol. 62, no. 9, pp. 5491–5501, 2015.

- [66] M. Uno and A. Kukita, "Single-Switch Single-Transformer Cell Voltage Equalizer Based on Forward Flyback Resonant Inverter and Voltage Multiplier for Series-Connected Energy Storage Cells," *Vehicular Technology, IEEE Transactions on*, vol. 63, no. 9, pp. 4232–4247, 2014.
- [67] L. Siqi, C. C. Mi, and Z. Mengyang, "A High-Efficiency Active Battery-Balancing Circuit Using Multiwinding Transformer," *Industry Applications, IEEE Transactions on*, vol. 49, no. 1, pp. 198–207, 2013.
- [68] M. Saleh, M. A. Masoum, L. Meek, and M. Abshar, "Control Algorithm for Bidirectional Fly-Back Active Cell Balancer with Interleaved Transformer Connections," in *2016 IEEE Power and Energy Society General Meeting (PESGM)*, July 2016, pp. 1–5.
- [69] P. Thanh Hai, A. Collet, and J. C. Crebier, "An Optimized Topology for Next-to-Next Balancing of Series-Connected Lithium-ion Cells," *Power Electronics, IEEE Transactions on*, vol. 29, no. 9, pp. 4603–4613, 2014.
- [70] K. Moon-Young, K. Chol-Ho, K. Jun-Ho, and M. Gun-Woo, "A Chain Structure of Switched Capacitor for Improved Cell Balancing Speed of Lithium-Ion Batteries," *Industrial Electronics, IEEE Transactions on*, vol. 61, no. 8, pp. 3989–3999, 2014.
- [71] K. Moon-Young, K. Jun-Ho, and M. Gun-Woo, "Center-Cell Concentration Structure of a Cell-to-Cell Balancing Circuit With a Reduced Number of Switches," *Power Electronics, IEEE Transactions on*, vol. 29, no. 10, pp. 5285–5297, 2014.
- [72] A. C. Baughman and M. Ferdowsi, "Double-Tiered Switched-Capacitor Battery Charge Equalization Technique," *Industrial Electronics, IEEE Transactions on*, vol. 55, no. 6, pp. 2277–2285, 2008.
- [73] Y. Ye, K. W. E. Cheng, and Y. P. B. Yeung, "Zero-Current Switching Switched-Capacitor Zero-Voltage-Gap Automatic Equalization System for Series Battery String," *Power Electronics, IEEE Transactions on*, vol. 27, no. 7, pp. 3234–3242, 2012.
- [74] H. Yi-Hsun, L. Tsorng-Juu, S. M. O. Chen, H. Wan-Yi, and C. Yi-Yuan, "A Novel High-Efficiency Compact-Size Low-Cost Balancing Method for Series-Connected Battery Applications," *Power Electronics, IEEE Transactions on*, vol. 28, no. 12, pp. 5927–5939, 2013.

- [75] A. M. Imtiaz and F. H. Khan, "Time Shared Flyback Converter Based Regenerative Cell Balancing Technique for Series Connected Li-Ion Battery Strings," *Power Electronics, IEEE Transactions on*, vol. 28, no. 12, pp. 5960–5975, 2013.
- [76] F. Mestrallet, L. Kerachev, J. C. Crebier, and A. Collet, "Multiphase Interleaved Converter for Lithium Battery Active Balancing," *Power Electronics, IEEE Transactions on*, vol. 29, no. 6, pp. 2874–2881, 2014.
- [77] M. Einhorn, W. Roessler, and J. Fleig, "Improved Performance of Serially Connected Li-Ion Batteries With Active Cell Balancing in Electric Vehicles," *Vehicular Technology, IEEE Transactions on*, vol. 60, no. 6, pp. 2448–2457, July 2011.
- [78] M. Diagne, M. David, P. Lauret, J. Boland, and N. Schmutz, "Review of Solar Irradiance Forecasting Methods and a Proposition for Small-Scale Insular Grids," *Renewable and Sustainable Energy Reviews*, vol. 27, no. 0, pp. 65–76, November 2013.
- [79] H. T. Yang, C. M. Huang, Y. C. Huang, and Y. S. Pai, "A Weather-Based Hybrid Method for 1-Day Ahead Hourly Forecasting of PV Power Output," *Sustainable Energy, IEEE Transactions on*, vol. 5, no. 3, pp. 917–926, July 2014.
- [80] H. T. Pedro and C. F. Coimbra, "Assessment of Forecasting Techniques for Solar Power Production with No Exogenous Inputs," *Solar Energy*, vol. 86, no. 7, pp. 2017 – 2028, 2012. [Online]. Available: <http://www.sciencedirect.com/science/article/pii/S0038092X12001429>
- [81] A. Yona, T. Senjyu, T. Funabashi, and C. H. Kim, "Determination Method of Insolation Prediction With Fuzzy and Applying Neural Network for Long-Term Ahead PV Power Output Correction," *Sustainable Energy, IEEE Transactions on*, vol. 4, no. 2, pp. 527–533, April 2013.
- [82] D. Bernecker, C. Riess, E. Angelopoulou, and J. Hornegger, "Continuous Short-Term Irradiance Forecasts Using Sky Images," *Solar Energy*, vol. 110, pp. 303–315, December 2014.
- [83] S. R. West, D. Rowe, S. Sayeef, and A. Berry, "Short-Term Irradiance Forecasting Using Skycams: Motivation and Development," *Solar Energy*, vol. 110, pp. 188–207, December 2014.

- [84] H. Yang, B. Kurtz, D. Nguyen, B. Urquhart, C. W. Chow, M. Ghonima, and J. Kleissl, “Solar Irradiance Forecasting Using a Ground-Based Sky Imager Developed at UC San Diego,” *Solar Energy*, vol. 103, pp. 502–524, May. 2014.
- [85] B. Urquhart, M. Ghonima, D. Nguyen, B. Kurtz, C. W. Chow, and J. Kleissl, “Sky-Imaging Systems for Short-Term Forecasting,” in *Solar Energy Forecasting and Resource Assessment*, J. Kleissl, Ed. Boston: Academic Press, 2013, book section 9, pp. 195–232, (Andu).
- [86] J. Bosch, Y. Zheng, and J. Kleissl, “Deriving Cloud Velocity from an Array of Solar Radiation Measurements,” *Solar Energy*, vol. 87, pp. 196 – 203, 2013. [Online]. Available: <http://www.sciencedirect.com/science/article/pii/S0038092X12003854>
- [87] A. T. Lorenzo, W. F. Holmgren, and A. D. Cronin, “Irradiance Forecasts Based On an Irradiance Monitoring Network, Cloud Motion, and Spatial Averaging,” *Solar Energy*, vol. 122, pp. 1158 – 1169, 2015. [Online]. Available: <http://www.sciencedirect.com/science/article/pii/S0038092X15005897>
- [88] V. P. Lonij, A. E. Brooks, A. D. Cronin, M. Leuthold, and K. Koch, “Intra-Hour Forecasts of Solar Power Production Using Measurements From a Network of Irradiance Sensors,” *Solar Energy*, vol. 97, pp. 58 – 66, 2013. [Online]. Available: <http://www.sciencedirect.com/science/article/pii/S0038092X13003125>
- [89] *EPRI-DOE Handbook of Energy Storage for Transmission and Distribution Applications*. EPRI, Palo Alto, CA and U.S. Department of Energy, Washington, DC, 2003, no. 1001834.
- [90] V. Gevorgian and S. Booth, “Review of PREPA Technical Requirements for Interconnecting Wind and Solar Generation,” National Renewable Energy Laboratory (NREL), Report, November 2013.
- [91] “National Electricity Rules Version 79,” Australian Energy Market Commission (AEMC), March 2016.
- [92] “Interconnection Requirements for Variable Generation,” North American Electric Reliability Corporation (NERC), Atlanta, GA 30326, p. 121, 2012.

- [93] R. A. Dougal, S. Liu, and R. E. White, "Power and Life Extension of Battery-Ultracapacitor Hybrids," *Components and Packaging Technologies, IEEE Transactions on*, vol. 25, no. 1, pp. 120–131, 2002.
- [94] J. Shen, S. Dusmez, and A. Khaligh, "Optimization of Sizing and Battery Cycle Life in Battery/Ultracapacitor Hybrid Energy Storage Systems for Electric Vehicle Applications," *Industrial Informatics, IEEE Transactions on*, vol. 10, no. 4, pp. 2112–2121, Nov 2014.
- [95] N. R. Tummuru, M. K. Mishra, and S. Srinivas, "Dynamic Energy Management of Renewable Grid Integrated Hybrid Energy Storage System," *Industrial Electronics, IEEE Transactions on*, vol. 62, no. 12, pp. 7728–7737, Dec 2015.
- [96] O. C. Onar and A. Khaligh, "A Novel Integrated Magnetic Structure Based DC/DC Converter for Hybrid Battery/Ultracapacitor Energy Storage Systems," *Smart Grid, IEEE Transactions on*, vol. 3, no. 1, pp. 296–307, March 2012.
- [97] A. Lahyani, P. Venet, A. Guermazi, and A. Troudi, "Battery/Supercapacitors Combination in Uninterruptible Power Supply (UPS)," *Power Electronics, IEEE Transactions on*, vol. 28, no. 4, pp. 1509–1522, April 2013.
- [98] M. E. Choi, S. W. Kim, and S. W. Seo, "Energy management optimization in a battery/supercapacitor hybrid energy storage system," *Smart Grid, IEEE Transactions on*, vol. 3, no. 1, pp. 463–472, March 2012.
- [99] L. Wei and G. Joos, "A Power Electronic Interface for a Battery Supercapacitor Hybrid Energy Storage System for Wind Applications," in *Power Electronics Specialists Conference (PESC)*, 2008, Conference Proceedings, pp. 1762–1768.
- [100] S. B. Kjaer, J. K. Pedersen, and F. Blaabjerg, "A Review of Single-Phase Grid-Connected Inverters for Photovoltaic Modules," *Industry Applications, IEEE Transactions on*, vol. 41, no. 5, pp. 1292–1306, 2005.
- [101] S. J. Chiang, K. T. Chang, and C. Y. Yen, "Residential Photovoltaic Energy Storage System," *Industrial Electronics, IEEE Transactions on*, vol. 45, no. 3, pp. 385–394, 1998.

- [102] A. A. Hussein, N. Kutkut, Z. J. Shen, and I. Batarseh, “Distributed Battery Micro-Storage Systems Design and Operation in a Deregulated Electricity Market,” *Sustainable Energy, IEEE Transactions on*, vol. 3, no. 3, pp. 545–556, 2012.
- [103] R. Hara, H. Kita, T. Tanabe, H. Sugihara, A. Kuwayama, and S. Miwa, “Testing the Technologies,” *Power and Energy Magazine, IEEE*, vol. 7, no. 3, pp. 77–85, 2009.
- [104] Q.-C. Zhong and T. Hornik, “Current proportional-integral control,” in *Control of Power Inverters in Renewable Energy and Smart Grid Integration*. Wiley-IEEE Press, 2012, ch. 15, pp. 250–258. [Online]. Available: <http://ieeexplore.ieee.org/xpl/articleDetails.jsp?arnumber=6381818>
- [105] S. Kouro, B. Wu, H. Abu-Rub, and F. Blaabjerg, “Photovoltaic Energy Conversion Systems,” in *Power Electronics for Renewable Energy Systems, Transportation and Industrial Applications*. John Wiley & Sons, Ltd, 2014, pp. 160–198. [Online]. Available: <http://dx.doi.org/10.1002/9781118755525.ch7>
- [106] T. Esmar and P. L. Chapman, “Comparison of Photovoltaic Array Maximum Power Point Tracking Techniques,” *Energy Conversion, IEEE Transactions on*, vol. 22, no. 2, pp. 439–449, June 2007.
- [107] P. Krause, O. Wasynczuk, S. Sudhoff, and S. Pekarek, “Reference-Frame Theory,” in *Analysis of Electric Machinery and Drive Systems*. John Wiley & Sons, Inc., 2013, ch. 3, pp. 86–120. [Online]. Available: <http://dx.doi.org/10.1002/9781118524336.ch3>
- [108] —, “Fully Controlled Three-Phase Bridge Converters,” in *Analysis of Electric Machinery and Drive Systems*. John Wiley & Sons, Inc., 2013, ch. 12, pp. 460–502. [Online]. Available: <http://dx.doi.org/10.1002/9781118524336.ch12>
- [109] M. Uno and A. Kukita, “Cycle Life Evaluation Based on Accelerated Aging Testing for Lithium-Ion Capacitors as Alternative to Rechargeable Batteries,” *Industrial Electronics, IEEE Transactions on*, vol. 63, no. 3, pp. 1607–1617, March 2016.

- [110] R. Ishizaki, L. Lin, and M. Fukui, “An Accurate SOC Estimation Method for Lithium-ion Batteries which Considers Thermal Variation,” *Electrochemistry*, vol. 83, no. 10, pp. 852–854, October 2015.
- [111] “Battery Supervision and Cell Balancing Module for Li-Ion Battery Packs,” Application Note, Infineon Technologies AG, 2010.
- [112] “High Efficiency Bidirectional Multicell Battery Balancer,” Datasheet, Linear Technology Corporation, 2013. [Online]. Available: <http://cds.linear.com/docs/en/datasheet/33001fb.pdf>
- [113] Z. Dong, D. Yang, T. Reindl, and W. M. Walsh, “Satellite Image Analysis and a Hybrid ESSS/ANN Model to Forecast Solar Irradiance in the Tropics,” *Energy Conversion and Management*, vol. 79, pp. 66 – 73, 2014. [Online]. Available: <http://www.sciencedirect.com/science/article/pii/S0196890413007644>
- [114] C. W. Chow, B. Urquhart, M. Lave, A. Dominguez, J. Kleissl, J. Shields, and B. Washom, “Intra-Hour Forecasting With a Total Sky Imager at the UC San Diego Solar Energy Testbed,” *Solar Energy*, vol. 85, no. 11, pp. 2881–2893, November 2011.
- [115] D. Scaramuzza, “OCamCalib: Omnidirectional Camera Calibration Toolbox,” 2006.
- [116] I. Reda and A. Andreas, “Solar Position Algorithm for Solar Radiation Applications,” *Solar Energy*, vol. 76, no. 5, pp. 577 – 589, 2004.
- [117] R. W. Johnson, W. S. Hering, and J. E. Shields, “Automated Visibility & Cloud Cover Measurements with a Solid State Imaging System,” Scripps Institution of Oceanography, UC San Diego, Report, 1989.
- [118] R. Szeliski, *Computer Vision: Algorithms and Applications*. Springer-Verlag New York, Inc., 2010.
- [119] M. Saleh, L. Meek, M. A. Masoum, and M. Abshar, “Battery-Less Short-Term Smoothing of Photovoltaic Generation Using Sky Camera,” *Industrial Informatics, IEEE Transactions on*, vol. 14, no. 2, pp. 403–414, Feb 2018.
- [120] M. Paulescu, E. Paulescu, P. Gravila, and V. Badescu, “The Future of the Energy Mix Paradigm,” in *Weather Modeling and Forecasting of PV*

Systems Operation, ser. Green Energy and Technology. London: Springer-Verlag, 2013, book section 1, p. 358.

- [121] “Magellan Solar Export Control Solutions Solar Gate,” Catalog, Magellan Power, p. 8, 2015. [Online]. Available: <http://magellanpower.com.au/Products/Renewable-Energy-and-Energy-Storage-Systems/Solar-Gate>
- [122] “Solar Photovoltaics,” in *Renewable Energy Technologies: Cost Analysis Series*. The International Renewable Energy Agency (IRENA), 2012, p. 21, volume 1:Power Sector, Issue 4/5.
- [123] Bureau of Meteorology. (2016) Climate Statistics for Australian Sites. [Online]. Available: <http://www.bom.gov.au/climate/data/>
- [124] “Technical Requirements for Renewable Energy Systems Connected to the Low Voltage (LV) Network via Inverters,” HPC-9FJ-12-0001-2012, Horizon Power Corporation, WA, Australia, p. 58, 2012. [Online]. Available: <http://horizonpower.com.au/media/1121/technical-requirements-for-renewable-energy-systems-connected-to-the-low-voltage-lv-network-via-inverters.pdf>
- [125] T. A. Clarke and J. G. Fryer, “The Development of Camera Calibration Methods and Models,” *The Photogrammetric Record*, vol. 16, no. 91, pp. 51–66, 1998. [Online]. Available: <http://dx.doi.org/10.1111/0031-868X.00113>

Every reasonable effort has been made to acknowledge the owners of copyright material. I would be pleased to hear from any copyright owner who has been omitted or incorrectly acknowledged.

Mojtaba Saleh
27/09/2017

A handwritten signature in blue ink, appearing to read 'Saleh' with a stylized flourish underneath.